UNIVERSITÀ DI GENOVA

ISTITUTO ITALIANO
DI TECNOLOGIA

DOCTORAL THESIS

Interplay between astrocytic and neuronal networks during virtual navigation in the mouse hippocampus

Author:
Pedro LAGOMARSINO DE LEON ROIG

Supervisor:
Dr. Tommaso FELLIN

Ciclo XXXIII

March 24, 2021

Abstract of thesis entitled

Interplay between astrocytic and neuronal networks during virtual navigation in the mouse hippocampus

Submitted by

Pedro LAGOMARSINO DE LEON ROIG

for the degree of Doctor of Philosophy

at The Università di Genova

in March, 2021

Encoding of spatial information in hippocapal place cells is believed to contribute to spatial cognition during navigation. Whether the processing of spatial information is exclusively limited to neuronal cells or it involves other cell types, e.g. glial cells, in the brain is currently unknown. In this thesis work, I developed an analysis pipeline to tackle this question using statistical methods and Information Theory approaches. I applied these analytical tools to two experimental data sets in which neuronal place cells in the hippocampus were imaged using two-photon microscopy, while selectively manipulating astrocytic calcium dynamics with pharmacogenetics during virtual navigation. Using custom analytical methods, we observed that pharmacogenetic perturbation of astrocytic calcium dynamics, through clozapine-n-oxyde (CNO) injection, induced a significant increase in neuronal place field and response profile width compared to control conditions. The distributions of neuronal place field and response profile center were also significantly different upon perturbation of astrocytic calcium dynamics compared to control conditions. Moreover, we found contrasting effect of astrocytic calcium dynamics perturbation on neuronal content of spatial information in the two data sets. In the first data set, we found that CNO injection resulted in a significant increase in the average information content in all neurons. In the second data set, we instead found that mutual information values were not significantly different upon CNO application compared to controls. Although the presented results are still preliminary and more experiments and analyses are needed, these findings suggest that astrocytic calcium dynamics may actively control the way hippocampal neuronal networks encode spatial information during virtual navigation. These data thus suggest a complex and tight interplay between neuronal and astrocytic networks during higher cognitive functions.

Interplay between astrocytic and neuronal networks during virtual navigation in the mouse hippocampus

by

Pedro LAGOMARSINO DE LEON ROIG
M.S. *Universidad de Buenos Aires*

A Thesis Submitted in Partial Fulfilment
of the Requirements for the Degree of
Doctor of Philosophy

at

Università di Genova
March, 2021

Acknowledgements

I would like to thank my mentor Tommaso Fellin for guiding me during these years. For his teachings and advise both in science and in life. For the discussions, the dedication and for always being available. I would like to thank Stefano Panzeri and Jacopo Bonato for collaboration and helpful comments. I would like to thank the people from Tommaso's group, a great and supportive team, for all the science and all the laughter. I would especially like to thank Sebastiano Curreli and Sara Romanzi, without whom this thesis would not exist. I would like to thank them not only for their exceptional experimental work, that produced all the data presented in this thesis, but most importantly for all the discussions, the support and for helping making the experience of doing science an exciting and enjoyable adventure. I would like to thank Camila for the support and the love. For *todo lo todo* that she is in my life.

My highest gratitude is for my parents, Carmen and Juan. I don't have the words to thank them enough. I would like to dedicate this thesis to them.

Pedro LAGOMARSINO DE LEON ROIG
Università di Genova
March 24, 2021

Contents

List of Figures

Chapter 1

Introduction

1.1 Spatial navigation

The interaction between organisms and the environment is the core of life and evolution. This interaction occurs at different levels with different objectives and outcomes. From the behavioural point of view, organisms have evolved to be able to perceive different aspects of the environment, interpret them, and act in consequence. The more we move forward in evolution, the more sophisticated and complex resources and behaviours we observe, with the nervous system being arguably one of the most prominent examples of this process.

One of the most fundamental aspects of such interaction consists of being able to move and navigate through the environment. An efficient navigation system has to achieve a series of very difficult tasks that include the integration of information from different sensory modalities and coordination with the motor system, together with higher-order cognitive processes such as proprioception and goal-directed activity ,in a flexible and dynamic way. In this thesis, we developed and applied an analytic pipeline for the analysis of two-photon imaging and cell-specific pharmacogenetic approaches aimed at testing the hypothesis that glial cell-type astrocytes modulate the neuronal representation of space. Given the interdisciplinary and multifaceted nature of the work presented, the introduction will focus on four major topics: spatial navigation, two-photon functional imaging, astrocyte physiology, and analytical methods based on information theory. For each of this four topics, we do not aim to provide an exhaustive description of the field; rather, we provide a general summary of the main concepts that are instrumental to the development of this project.

Spatial navigation has been extensively studied in the last 50 years, particularly in the mammalian brain. The seminal work of John O'Keefe during the 1970s on rats led to the confirmation of the *cognitive map* hypothesis [O'Keefe and Nadel, 1980], which is an idea that was first proposed by E. C. Toleman [Toleman, 1948], as the way the brain solves the challenge of spatial navigation, importantly, providing experimental corroborations of its possible neuronal implementation. Unexpectedly, such implementation

involved the activity of specialized cells in a restricted area of the brain: **the hippocampus**.

According to *cognitive map* theory, cells in the hippocampus receive inputs conveying information about sensory cues related to environmental stimuli, calculate the animal's position in space and consequently predict subsequent positions and trajectories depending on the goal, inferred distances and directions. The ability of the internal navigation system to calculate trajectories and predict future positions represents the essence of learning in the cognitive map and has several implications regarding the internal structure and what kinds of computations and types of cells should be found in the hippocampus.

In the next sections, I will summarize the anatomy and function of the hippocampus and the different types of information-encoding cells described as present in the hippocampal navigation system.

1.1.1 The Hippocampus

Although hippocampal anatomy and connectivity have been extensively studied for decades, the understanding of these characteristics and their relationships with functionality are far from completely elucidated [Cullen and J. S. Taube, 2017]. Here, we will briefly describe the canonical hippocampal circuit and it's constituents, structure and connectivity, paying special attention to the flow of information in this circuit.

The mammalian hippocampus is a seahorse-shaped (hence, the name) brain structure located underneath the temporal lobe of the neocortex. All mammals have a structure that can be identified as a hippocampus; moreover, putative homologs have been identified in most vertebrates [O'Keefe and Nadel, 1980; Kappers, Huber, and Crosby, 1936; Heier, 1948; Crosby, DeJonge, and Schneider, 1966].

In mice and rats, which are the mammalian species relevant to the work presented in this thesis, the hippocampus occupies a large portion of the forebrain. It consists primarily of excitatory neurons, pyramidal or granule cells, and various interneurons, among which basket cells are the most abundant subtype (Figure 1.1B). A horizontal section through the posterior arch of the hippocampus shows the three-layered hippocampal formation and the *subiculum* (Figure 1.1A).

The hippocampal structure can be divided into two U-shaped interlocking sectors: the *hippocampus proper* and the *dentate gyrus*. The hippocampus proper can, in turn, be divided into 4 subfields: CA1-4 [Lorente De Nó, 1934]. CA stands for *cornu ammonis*, which is another shape reference. Following the structured layer of principal neurons, CA1 appears first as the main output region of the hippocampus, followed by CA2-3 in the *regio inferior*, and finally, CA4 represents the scattered cells inside the hilus (or polymorphic zone, see bellow) of the dentate gyrus (see Figure 1.1A). With the exception of CA4, all regions of the hippocampus have a common simple structure: a compact and dense layer of cell bodies whose dendrites stretch in the same direction and

receive most of their inputs from perpendicularly running axons that make synapses with many neurons at constrained regions of the dendrites. Such a simple and preserved structure of the hippocampus represents one of the key aspects of it's function. The different subregions differ in the types of cells that they include, with CA3 having large pyramids, CA1 having smaller pyramids, and granule cells being present in the dentate gyrus.

The dentate gyrus is subdivided into three layers (Figure 1.1B right): the *granule* layer that contains the cell bodies of the mentioned granule cells, the *molecular* layer consisting of the apical dendrites of the granule cells and their afferents and finally the *polymorph* layer in the concave hilus of the dentate gyrus formed by the axons of the granule cells. These axons later conform the mossy fiber bundle that merges with CA4. Present in this last layer, there are also some scattered basket cell interneurons. Although the hippocampus proper, is basically a three-layered structure, it can be further divided to better describe pyramidal cells and their afferents (Figure 1.1B left). First, there is the *alveus* layer formed by the axons of the pyramidal cells that project to the subiculum, and then we find the *stratum oriens* containing the basal dendrites, some basket cells and afferents from the septum. Third, the *stratum pyramidale* contains the cell bodies, along with the *stratum radiatum* and the *stratum moleculare* with different parts of the apical dendrites. It is interesting to note that the main feature conveying the lamination of the hippocampal structure is the nature of the afferents, which are briefly described as follows.

Connectivity in the hippocampus is complex, with afferent fibers arising from many different regions of the brain. Here, we will describe only the canonical circuit (Figure 1.1A), starting with the **extrinsic afferents**. For a more detailed description of hippocampal connectivity, please refer to O'Keefe and Nadel, 1980. The main source of input to the hippocampus is the entorhinal cortex, which projects from its lateral and medial regions, passing by the upper layers of the subiculum to either the hippocampus proper through the perforant path or the dentate gyrus through the hippocampal fissure [Nafstad, 1967; Hjorth-Simonsen and Jeune, 1972; Van Hoesen, Pandya, and Butters, 1972; Hjorth-Simonsen, 1973; Van Hoesen and Pandya, 1975]. It is important to mention that the entorhinal cortex, as the main source of excitatory inputs to the hippocampus, integrates a plethora of inputs from different parts of the brain, among which are the prefrontal and cingulate cortices [Adey, 1951; Adey and Meyer, 1952; L. E. White, 1959; Cragg, 1965; Raisman, Cowan, and Powell, 1965; McLardy, 1971; Leichnetz and Astruc, 1975], the temporal cortex [Cragg, 1965], parietal areas [Pandya and Kupyers, 1969; Pandya and Vignolo, 1969; Petras, 1971], pyriform cortex [Powell, Cowan, and Raisman, 1965], and olfactory [Cragg, 1960; Cragg, 1961; Heimer, 1968; L. E. White, 1965; Price and Powell, 1971; D. I. B. Kerr and Dennis, 1972] and visual systems [Casey, Cuenod, and Maclean, 1965,Cuenod, Casey, and MACLEAN, 1965] and the amygdala [Krettek and Price, 1974].

In the hippocampus the major **interconnections between sectors** are primarily

unidirectional, starting from the dentate gyrus, moving through CA3 and ending in CA1 [Lorente De Nó, 1934; Raisman, Cowan, and Powell, 1965; Hjorth-Simonsen, 1973; Andersen, Blackstad, and Lomo, 1966; Fujita and Sakata, 1962; Gloor, Vera, and Sperti, 1963]. Cells in the dentate gyrus have axons that gather together in the hilus, forming the mossy fibers. The mossy fibers split into two bundles that project to the hippocampus proper. One bundle innervates the dendrites of pyramidal neurons in the stratum oriens. The second bundle runs above the pyramidal cells of CA3 through the stratum lucidum and continues until the border of CA1. CA3 and CA4 neurons make powerful excitatory connections with pyramidal cell dendrites in the stratum radiatum of CA1 called *Schaffer collaterals* [Lorente De Nó, 1934; Hjorth-Simonsen, 1973; Andersen, Blackstad, and Lomo, 1966]. Collaterals from CA3 and CA4, which are potentially the same as those that form the *Schaffer collaterals*, bend and project back to the proximal dendrites of the granule cells in the dentate gyrus [Zimmer, 1971]. Interestingly, CA1 and the dentate gyrus receive inputs from the CA3 of both hippocampi, the ipsilateral hippocampus and the contralateral hippocampus. Information flows out of the hippocampus through CA1 cell axons that project to the septum and the subiculum, which in turn project back to the entorhinal cortex, closing the loop in the information flow (a schematic of this connection can be seen in Figure 1.1A).

Moreover, the hippocampus is characterized by a certain amount of **intrinsic afferents from the same sector**; that is, within each region of the hippocampus, there is local connectivity. Local connectivity comes mostly in two flavors: excitatory monosynaptic connections between neighboring pyramidal neurons [Lebovitz, Dichter, and Spencer, 1971] and inhibitory polysynaptic connections due to the instrinsic pyramidal - interneuron - pyramidal loops [Kandel, Spencer, and Brinley, 1961; Spencer and Kandel, 1961; Andersen, Eccles, and Loyning, 1964a; Andersen, Eccles, and Loyning, 1964b].

Thus, in this general scheme, information flows from several regions of the neocortex and other brain areas to the entorhinal cortex, next to the dentate gyrus, and then to CA3-4, finalizing in CA1 that projects back to the subiculum and entorhinal cortex (and the septum) to close the loop. Interestingly, hippocampal projections can be topographically precise in the sense that, for example, a small number of cells in the dentate gyrus project to a small number of cells in CA3 [Witter et al., 1993; Tamamaki and Nojyo, 1995].

A major question in the field has been how does such a well-defined anatomy and connectivity structure compute spatial information to provide a substrate for spatial navigation? When O'Keefe first elaborated the *cognitive map* theory, he hypothesized that each of the three regions of the hippocampus accounted for a stage in the mapping system [O'Keefe and Nadel, 1980]. The first stage, occurring in the dentate gyrus, would consist of organizing the environmental inputs from the entorhinal cortex and subiculum into a scheme required by the mapping system. This complex integration would then be transmitted to CA3-4, where the second stage of the map would take

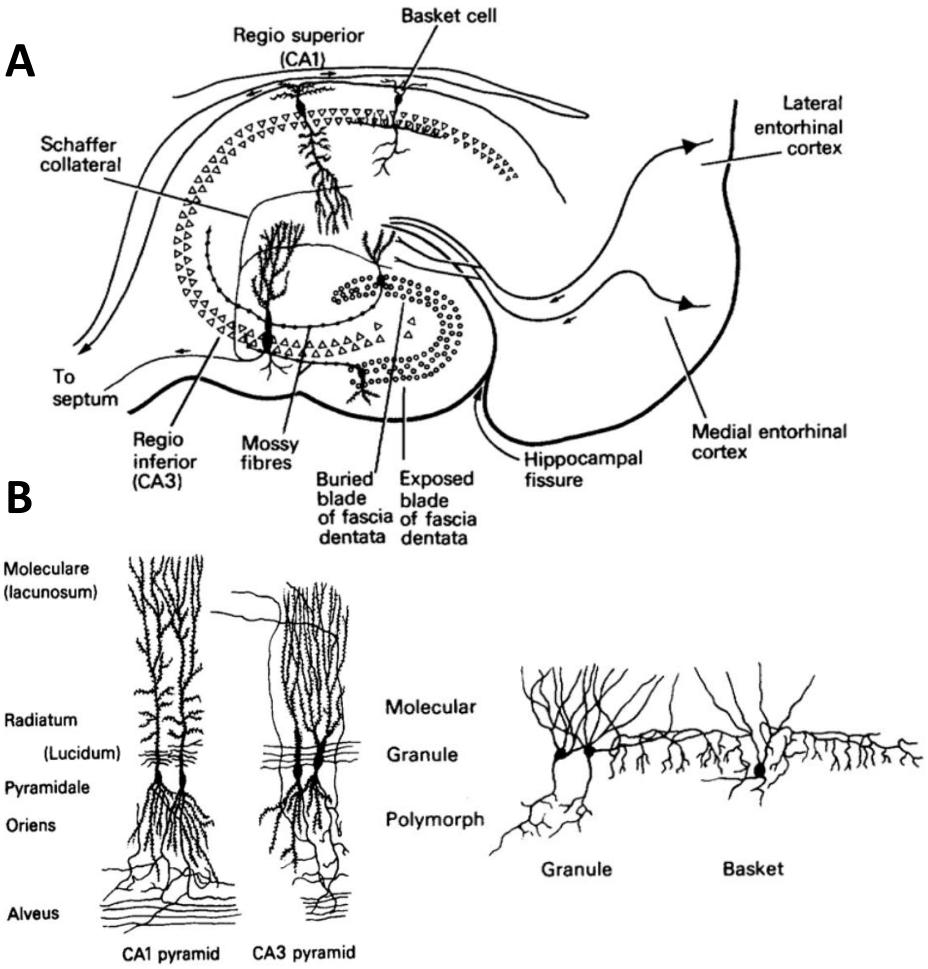

Figure 1.1: Hippocampal anatomy. A) Schematic representation of the mouse hippocampus and the connections between regions, adapted from [O'Keefe and Nadel, 1980]. B) Examples of CA1 and CA3 pyramidal cells (Cajal 1911, Figure 475) and dentate granule and basket cells [Lorente De Nó, 1934, Figure 10].

place, by representing locations in an environment and the relationships between locations. Finally, in CA1, the map would be represented together with a mismatch system that would account for novelty or changes in location information.

This simple schematic has been supported by several experimental studies [O'Keefe, 2014]. However, over the course of 40 years of experimental research, this initial model has been improved and further completed. For example, it is now well established that the subiculum and the entorhinal cortex are important parts of the greater formation that processes and integrates spatial information. In fact, in each of the aforementioned regions, a set of highly specialized neurons has been discovered. Interestingly, the existence of many of these neurons was predicted in the 1970s by *cognitive map* theory. In the next section, the main types of space-informative cells and their contributions to the overall model are presented.

1.1.2 Spatial information encoding neurons

The main type of cells that conform to the cognitive map model was found by O'Keefe and Dostrovsky in 1971. Using electrophysiological recordings in the hippocampus, cells that fire predominantly in a specific location of a familiar environment (Figure 1.2A) were observed. These cells were called *place cells*. Here, we will focus only on the main characteristics of place cells. We point to these fundamental reviews for an in-depth description of place cell function [M.-B. Moser, D. C. Rowland, and E. I. Moser, 2015; P. J. Best, A. M. White, and Minai, 2001].

Place cells are mainly found in the hippocampus proper, and their firing rate is modulated purely by spatial location; that is, they fire maximally when the animal's head is in a specific region of the environment (Figure 1.2A). This region of the space is called the *place field* of the cell (Figure 1.2B). Here, we use the term environment in a generic way, but place cells have been mainly studied in constrained laboratory environments. Interestingly, place cells have different characteristics, depending on the nature of the space that the animal explores. In a two-dimensional space, such as the square/rectangular or circular boxes used in the early O'Keefe experiments [O'Keefe, 1976], place cells fire at their place field location regardless of the direction of motion or speed of the animal. However, in a one-dimensional environment (e.g., a linear track), place cells display a preferred direction of firing and fire much less, not at all or in a different location depending on the direction of motion on the linear track [B. McNaughton, Barnes, and O'Keefe, 1983; O'Keefe and Recce, 1993]. Place cells have also been found in three-dimensional environments, with three-dimensional place fields [Yartsev and Ulanovsky, 2013; R. Grieves et al., 2020]. The latter type of place cell has been observed in bats flying through a familiar environment [Yartsev and Ulanovsky, 2013] and, more recently, in rodents exploring three-dimensional environments [R. Grieves et al., 2020].

The way that place cells represent position is not limited to the firing rate but also involves the temporal aspect of their firing. Place cell firing is locked to the phase of the sinusoidal local field potential (LFP), which is called the theta rhythm, and hence to the population activity in the hippocampus [O'Keefe and Recce, 1993]. The theta rhythm works as a sort of clock against which the network can measure time and temporally locate cell spikes, allowing place cells to identify locations in an environment with much finer precision than if only the rate code were used. This is called *temporal coding* [O'Keefe and Recce, 1993; Huxter, Burgess, and O'Keefe, 2003; G. Buzsáki and Draguhn, 2004; G. Buzsáki, 2002].

Neighboring place cells do not necessarily have similar or adjacent place fields. Furthermore, groups of anatomically close place cells typically have place fields that span the whole space, suggesting that place cells represent a complete and highly redundant representation of the environment [O'Keefe, 1976; Wilson and B. L. McNaughton, 1994]. Once formed, these representations can be stable across days [Hill, 1978; R. Muller, Kubie, and Ranck Jr., 1987] or even weeks [Thompson and P. Best,

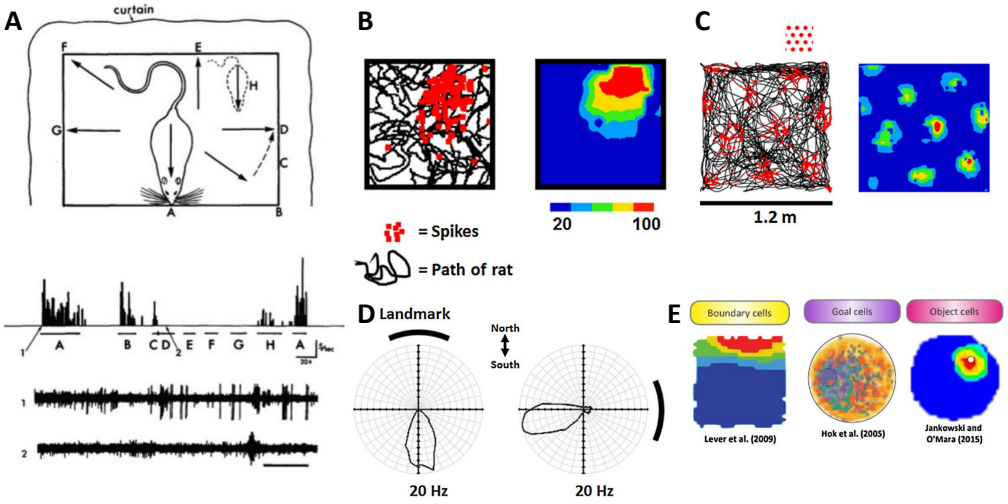

Figure 1.2: Spatial information-encoding cells. A) The first report of a place cell in the hippocampus of a freely moving rat. The animal navigated a box (top). The cell fired only when the animal was in locations A and B. From O'Keefe and Dostrovsky (1971). B) Spikes (red squares) from a single hippocampal cell and the path of the animal (black line) in a single trial (left). On the right, the same data are shown as a heat plot of the dwell-time-adjusted firing rate (between peak and 20% peak amplitudes), displaying the place field of the neuron. C) Grid, close-packed hexagonal firing pattern of a single entorhinal grid cell. Firing is depicted as in B). Characteristic distances from the lattice are specific to each cell and relatively constant in different environments, suggesting the encoding of distances. D) Two trials recorded from a postsubicular head direction cell in a symmetrical environment with a single polarizing landmark. Polar plots show the firing rate as a function of the direction of the animal's head. When the landmark is positioned north (left), the cell fires maximally when the animal's head faces south. When the landmark is rotated to the east (right), the cell fires to the west, maintaining an equivalent relationship to the landmark. This shows that cells are influenced by local cues and not by geocentric cues such as the Earth's magnetic field. B), C), and D) are adapted from R. M. Grieves and K. J. Jeffery, 2017. E) Examples of other types of navigation cells; references are indicated in the figure.

1990]. However, not all place fields are stable, and plasticity of this neuronal representation of spatial information has been reported [Mankin et al., 2015; Ziv et al., 2013].

How does this spatial representation arise in hippocampal cells based on the synaptic inputs that these cells receive? A large number of studies have focused on this question and provided important hints. It is clear that visual information is important, as distal cues or landmarks surrounding the environment can influence place field formation [R. Muller and Kubie, 1987; O'Keefe and Conway, 1978; Yoganarasimha and Knierim, 2005]. However, these inputs are not necessary. In fact, place cells fire in the same location in the dark in a familiar environment [Save, Nerad, and Poucet, 2000; S. Zhang et al., 2014; C. Markus E. B., B. McNaughton, and Gladden, 1994; Quirk, R.

Muller, and Kubie, 1990], provided that other sensory cues are available, such as olfaction or tactility. These different sensory modalities are integrated outside of the hippocampus [K. Jeffery, 2007]. This indicates that place fields are higher order representations that integrate more primitive spatial constructs such as direction, self-motion, and boundaries. If sensory cues signal that the environment changes, a new and unique representation is formed in the hippocampal circuit [Anderson and K. Jeffery, 2003; O'Keefe and Conway, 1978] in a process called remapping [R. Muller and Kubie, 1987]. Importantly, in rats and mice, the animal must directly explore the physical space for place cells to form a spatial representation [D. Rowland, Yanovich, and Kentros, 2011]. In contrast, other mammals (e.g., primates) can form inferred allocentric representations of remote space if observed [Rolls, 1999; Rolls, Robertson, and Pierre, 1997; Rolls and O'Mara, 1995].

To define a place cell and its place field, several criteria related to the firing rate, consistency of firing, and reliability have been used [O'Keefe, 1976; Thompson and P. Best, 1990; D. A. Dombeck, Harvey, et al., 2010]. Throughout this thesis, we will define a place cell as a cell in the hippocampus proper that carries a *significant amount of information* about the animal's position in its firing activity (see also methods and later sections of the introduction for more details about the contextual definition of the word information).

A key cell type in the spatial representation is **head direction cells** (Figure 1.2D). Head direction cells are located in the presubiculum, and their firing is modulated by the facing direction of the head. They were first found by Rank [Ranck Jr., 1984; Ranck Jr., 1985] and characterized in detail later [J. Taube, R. J. Muller R., and J.B., 1990; J. Taube, R. Muller, et al., 1990; J. Taube, R. Muller, et al., 1987]. Here, by the term *head direction*, we refer to the orientation of the head in the horizontal plane. Head direction cells are similar in their characteristics to place cells. They have a preferred direction of firing that is independent of other behavioral factors. Each head direction cell has a different preferred direction. Preferred directions are equally distributed in the circle, meaning that there is no overall preferred direction of the network [J. Taube, R. Muller, et al., 1990]. Similar to place cells, the angular orientation of environmental cues is an important modulator of head direction cell activity (Figure 1.2D) [Goodridge and J. Taube, 1995; J. Taube, 1995; J. Taube, R. Muller, et al., 1990; Zugaro, Tabuchi, and Wiener, 2000; Knierim, H. Kudrimoti, and B. McNaughton, 1995] but is not necessary [Mizumori and J. Williams, 1993; Yoder, Clark, Brown, et al., 2011; Yoder, Clark, and J. Taube, 2011]. An interesting characteristic of head direction cells is that the angular relationship between preferred directions of different cells is preserved [W. Skaggs, Knierim, and B. Kudrimoti H. a., 1995; Yoganarasimha and Knierim, 2005]. Hence, when remapping of the environment occurs in which one cell changes its orientation, the rest of the cells coherently change their functional properties [W. Skaggs, Knierim, and B. Kudrimoti H. a., 1995; Yoganarasimha and Knierim, 2005].

With the information encoded in place cells and head direction cells, the cognitive

map model can build positions and measure angles. However, another crucial requirement for the map to be completed is a way of measuring distances, i.e. to establish the metric of the map. In 2005, a cell type that could achieve this task was identified in the Moser's lab: **grid cells**. Grid cells are cells that fire in multiple discrete and regularly spaced locations. Grid cells form a triangular or, equivalently, a hexagonal lattice (Figure 1.2C). These cells are found in the medial entorhinal cortex (mEC), in the postrhinal cortex [Fyhn, Molden, et al., 2004; Hafting et al., 2005; Fyhn, Solstad, and Hafting, 2008] and in the pre- and para-subiculum [Boccara et al., 2010].

Grid cells share some characteristics with place cells and head direction cells. Their pattern of firing arises in familiar environments and partially relies on distal visual cues [Hafting et al., 2005]. If environmental cues rotate, grid patterns consistently do so too [Hafting et al., 2005]. Deformation of the environment causes deformation of the grid patterns [Barry, Hayman, et al., 2007; Stensola et al., 2012]. Similar to head direction cells, the angles and distances between grid patterns of different grid cells are preserved, and when the environment rotates or moves, the patterns adapt in a coherent fashion, maintaining a stable relationship [Fyhn, Hafting, et al., 2007] across grid cells. This suggests that grid cells work cooperatively, as an interconnected matrix known as an attractor network [B. McNaughton, Battaglia, et al., 2006]. Moreover, the spacing between peaks of grid patterns varies as a function of location in the entorhinal cortex. The scales of the patterns increase in discrete jumps from the dorsal to ventral sides of the entorhinal cortex [Brun et al., 2008]. Each animal can display 3 or 4 different scales[Brun et al., 2008].

An additional functional class of cells that contain spatial information about the outer environment is **boundary cells** (Figure 1.2E left). Boundary cells, or boundary vector cells, are located in the subiculum and selectively respond to environmental boundaries. Boundaries can be walls, low ridges, and vertical drops. The color, texture, and odor of these boundaries do not seem to influence the firing of boundary cells [Lever et al., 2009]. Interestingly, the existence of boundary cells was first hypothesized to explain the observation that after elongating one side of a rectangular box, place fields stretched accordingly [O'Keefe and Burgess, 1996]. This led researchers to hypothesize the existence of cells that fire in relation to environmental boundaries and that place cell firing could arise as a thresholded sum of a subpopulation of such neurons [Barry, Lever, et al., 2006; Burgess et al., 1997; Hartley et al., 2000]. Cells that partly fit this theoretical description were later found in several regions of the brain, including the subiculum [Barry, Lever, et al., 2006], presubiculum and parasubiculum [Boccara et al., 2010], medial entorhinal cortex [Bjerknes, E. Moser, and M.-B. Moser, 2014; Savelli, Yoganarasimha, and Knierim, 2008; Solstad et al., 2008], anterior claustrum [Jankowski and O'Mara, 2015], and rostral thalamus [Jankowski, Passecker, et al., 2015].

In a more formal definition, boundary vector cells can be defined as neurons that i) fire when the animal encounters an environmental boundary in its preferred direction, and ii) their firing is driven by the memory of the boundary's position relative to the

animal, based not only on perceptual cues but also on self-motion information [Lever et al., 2009; Raudies, R. Florian, et al., 2012; Raudies and Hasselmo, 2012]. Notably, boundary cells fire at a specific distance from the boundary, and this distance is different for boundary cells in different brain regions [Bjerknes, E. Moser, and M.-B. Moser, 2014; Solstad et al., 2008; Jankowski, Passecker, et al., 2015; Lever et al., 2009].

Altogether, place cells, head direction cells, grid cells, and boundary vector cells lie at the core of the cognitive map model and are the most relevant and studied type of cells in the context of spatial navigation. This obviously does not imply that other types of spatially informative cells might not be present; therefore, there is room for more *types* of these cells to be discovered in future investigations. In particular, cells in which the firing activity is modulated by more abstract or complex information have been described, including **object cells**, **goal cells**, **boundary-off cells**, **perimeter cells**, and **band cells**, among others (Figure 1.2E center and right).

What is the relation between the firing patterns of all these functional classes of cells? Mathematically, it can be shown that place cells can be formed by summing two grids with different spacings or, equivalently, by summing two border cells. Similarly, it has been demonstrated that grid cells can be built by combining the activity of band cells. However, a complete understanding of the function and implication of each of these functional classes of cells and their interactions in contributing to spatial navigation has not yet been achieved. Moreover, as mentioned earlier, the functional classes listed above could be only the tip of the iceberg. The more the extended hippocampal formation is studied, the larger the number of new cell classes that are described will be.

1.1.3 Calcium as a proxy of spiking activity

With a few exceptions, the large majority of the research presented in the previous sections has relied on electrophysiological recordings of neuronal activity. Electrophysiology has long been the preferred technique by which to interrogate brain activity, mostly because of its versatility, high signal-to-noise ratio, high temporal resolution, and ability to capture a large spectrum of neuronal signals, from individual action potentials (AP) and subthreshold membrane potential to network oscillations [C. Buzsáki, Anastassiou, and Koch, 2012; Margrie et al., 2003; Hubel and Wiesel, 1959]. In the last few decades, huge technological improvements in micro- and nanofabrication techniques for multielectrode arrays [Bareket-Keren and Hanein, 2012; Spira and Hai, 2013; Viventi and Blanco, 2012; Jun, Steinmetz, and Siegle, 2017] have helped improve the yield, sampling density, and biocompatibility of electrical probes. At the same time, the development of modern analytical methods has permitted the extraction of many types of information from this kind of recording [Agarwal et al., 2014; Shein-Idelson et al., 2017]. Although electrophysiologial approaches have come a long way and are a reliable and versatile way of studying neuronal activity, they also suffer from limitations. For example, in unit recordings, they are biased towards the detection of cells with high firing

rate; at the microcircuit level, they allow limited structure-function correlations [D. A. Dombeck, Harvey, et al., 2010], and importantly, they poorly discriminate between genetically selected neuronal populations. Moreover, electrophysiological recordings are blind to the form of excitability that does not generate electrical signals, such as the calcium excitability of certain glial cells. Alternative experimental methods partially overcome some of these limitations. In the last 3 decades, optical imaging methods and fluorescent activity reporters have provided an additional and efficient tool with which to study neural networks and their functions, overcoming some of the limitations of the methods described above [Ohki et al., 2005,Shoham et al., 1999; Grienberger and Konnerth, 2012; Bovetti, Moretti, and Fellin, 2014; W. Yang and Yuste, 2017]. The current success of these optical methods relies on two main technical advances: the synthesis of fluorescent calcium indicators and the development of nonlinear microscopy. The latter technique made it possible to record large ensembles of neurons (up to 10.000) at subcellular spatial resolution in the intact brain [Bovetti, Moretti, and Fellin, 2014; W. Yang and Yuste, 2017; Svoboda and Yasuda, 2006].

Action potential firing, as well as strong synaptic inputs, leads to the opening of voltage-gated calcium channels in neurons, which induces transient elevations in cytoplasmic Ca^{2+} concentration. These variations are typically in the range of 50-100 nM to 5-10 μM and can be detected by fluorescence calcium indicators. In this approach, neurons stained with these fluorescent compounds change the fluorescence emitted from the somatic region upon AP firing [Yuste and Katz, 1991]. Calcium transients decay over 100–500 ms through diffusion, the activity of calcium extrusion mechanisms, and internal buffering processes [Grienberger and Konnerth, 2012]. Importantly, cells that are not electrically excitable may display intracellular calcium transients. This is the case, as seen in the next section (1.2.2), for glial cells, particularly astrocytes. Astrocytes display variations in their intracellular calcium levels that correlate with neuronal activity.

The first calcium indicators developed were synthetic [Grienberger and Konnerth, 2012; Tsien, 1981]. These dyes typically have high signal-to-noise ratio [Stosiek et al., 2003; Grienberger and Konnerth, 2012; Wiederschain, 2011; Helmchen and Waters, 2002]; however, they do not easily allow labeling of genetically identified cell populations. An important breakthrough in overcoming this limitation was developed by the laboratory of the Nobel Prize winner Roger Tsien [Miyawaki et al., 1997] who developed the first versions of protein-based genetically encoded calcium indicators (GECIs).

By combining these fluorescent calcium binding proteins with cell-type specific promoters, subcellular targeting sequences, and transgenic technology, stable expression in distinct cell subpopulations (Figure 1.5) over prolonged periods of time is possible [Grienberger and Konnerth, 2012; Knöpfel, Díez-García, and Akemann, 2006; Looger and Griesbeck, 2012; T.-W. Chen et al., 2013]. The applications of GECIs were initially restricted due to their limited signal-to-noise ratios and slow response kinetics

[Ohkura, Matsuzaki, et al., 2005; Tallini et al., 2006; Tian et al., 2009]. However, incredible progress in the development and refinement of brighter and more sensitive variants has been achieved during the last 15 years, and newer GECIs rival synthetic calcium indicators in many respects [Horikawa et al., 2010; Palmer et al., 2011; Akerboom, T.-W. Chen, et al., 2012]. For example, ultrasensitive genetically encoded calcium indicators of the GCaMP6, GCaMP7 family [T.-W. Chen et al., 2013; Dana, Y. Sun, et al., 2019] and RCaMP family [Akerboom, Carreras Caldéron, et al., 2013; Dana, Mohar, et al., 2016; Ohkura, Sasaki, et al., 2010; Forli et al., 2018] can report, under optimized experimental conditions, the calcium transients associated with the discharge of a single AP in vivo.

1.1.4 2-photon calcium imaging

The design, development, and optimization of fluorescent activity indicators opened the door to a wide range of possibilities and demonstrated that it was possible to monitor neural activity indirectly by capturing changes in the intracellular concentrations of certain ions. However, fundamental advances in **optical imaging** are also needed for the application of fluorescent calcium indicators to the study of neural or glial network function in the intact CNS [Grienberger and Konnerth, 2012; Bovetti, Moretti, and Fellin, 2014; W. Yang and Yuste, 2017]. One of these fundamental advances is multiphoton microscopy-in particular, two-photon laser-scanning microscopy (2PLSM). 2PLSM saw its first experimental validation approximately 30 years ago, and since then, it has revolutionized biological imaging due to its unprecedented combination of high resolution and high contrast, even when imaging hundreds of microns deep inside intact tissue [Denk, Delaney, et al., 1994; Helmchen and Denk, 2005]. Briefly, 2PLSM is a laser-scanning method that exploits localized 'nonlinear' excitation to stimulate fluorophores only within the thin raster-scanned plane [Zipfel, R. M. Williams, and Webb, 2003]. Two-photon (2P) fluorophore excitation was first conceived by Marie Goeppert-Mayer [Göppert-Mayer, 1931] and relies on the idea that when two photons arrive "quasi-simultaneously", that is, within fractions of a fs, at the fluorophore, their energy is absorbed to promote the transition of one electron of the fluorophore from the ground state to the excited state. The electron in the excited state then decays following the normal fluorescence-emission pathway, as in single-photon fluorescence excitation (Figure 1.3A) [Pawley, 2006]. In this process, fluorophore excitation relies on higher-order light-matter interactions, thus having a nonlinear dependency on the incident light intensity [Svoboda and Yasuda, 2006; Helmchen and Denk, 2005]. 2PLSM represents an improvement with respect to standard wide-field fluorescence, wherein excitation is due to the absorption of a single photon and therefore depends linearly on the light intensity.

Three characteristics of 2P microscopy provide a comparative advantage with respect to other approaches when imaging thick samples in vivo [Helmchen and Denk, 2005]:

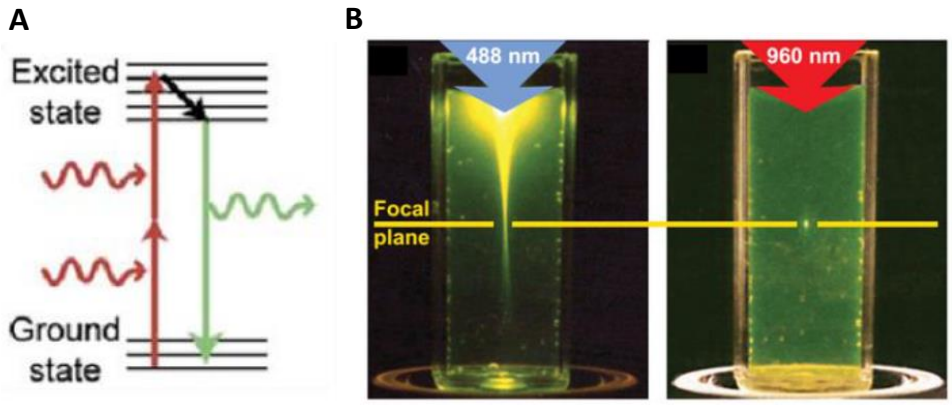

Figure 1.3: Two-photon excitation of fluorescent molecules. A) Simplified Jablonski diagram of the two-photon emission process. Adapted from Svoboda and Yasuda, 2006. B) Experimental demonstration of the localization of excitation in 2P imaging using focused (0.16 NA) fs pulses of 960 nm light (right) in comparison to single-photon excitation of fluorescein by focused 488 nm light (0.16 NA) (left). Adapted from Zipfel, R. M. Williams, and Webb, 2003.

1. **Imaging depth and phototoxicity**: 2P absorption in commonly used fluorophores occurs in the near-infrared wavelength range (700-1100nm). This wavelength range is generally less phototoxic and penetrates deeper into scattering tissue compared to visible light.

2. **High resolution**: The fluorescence signal (S) depends on the square of the light intensity ($S \propto I^2$). Thus, when focusing the laser beam through a high NA objective, 2P absorption under unsaturated conditions is limited to the perifocal region (Figure 1.3B) [Nagy, J. Wu, and Berland, 2005].

3. **No pixel cross-talk**: Because the sample is sequentially excited, meaning that the signals are collected point-by-point, the pixel cross-talk observed in wide-field imaging is virtually absent.

Since the first validation of 2PLSM [Denk, Strickler, and Webb, 1990], several advancements have been made in several aspects, leading to higher signal-to-noise ratios, better temporal resolutions, and larger field-of-view dimensions, penetration depths and accessible volumes for in vivo imaging (reviewed in W. Yang and Yuste, 2017). Combining 2PLSM with fluorescent activity reporters constitutes one of the most powerful approaches to investigating neuronal networks in the intact CNS at cellular resolution over mm of brain tissue.

Thanks to its unique advantages, researchers in the spatial navigation field have increasingly used 2P calcium imaging for the interrogation of hippocampal circuits [Gauthier and Tank, 2018; Rubin et al., 2015b; D. A. Dombeck, Harvey, et al., 2010]. Together with appropriate analytical tools [Sheintuch et al., 2017a], these approaches

allow the study of anatomically and genetically identifiable ensembles of cells across days in awake, behaving animals, opening the door the a whole range of new investigations that wold not be possible otherwise.

All the aforementioned research has focused only on neuronal networks. However, neurons represent approximately half of the cells in the mammalian brain. The main nonneuronal population of cells in the mammalian brain is called **glial cells**. Although glial cells do not have electrical activity similar to neurons, they express rich intracellular calcium dynamics and interact with neuronal cells in active ways. In this thesis, we will approach the question of whether glial cells play a role in spatial navigation in the mouse brain and what that role may be.

We will briefly describe the types of glial cells that can be found in the brain, focusing on a particular subtype, **astrocytes**, their characteristics and their role in modulating neuronal activity.

1.2 Glia

Glial cells were first observed as early as the mid 19th century by Virchow [Virchow, 1856], and were better described and brought to wider attention by Santiago Ramón y Cajal and Pío del Río Hortega a few decades later thanks to the development of the chloride-sublimate technique, which is a staining technique that specifically targets astrocytes [Ramón y Cajal, 1895; Río Hortega, 1921]. At this time, glial cells were thought to play a strictly structural role in the brain. If anything, the terminology used to describe them would be sufficient to understand the hypothesized role—glial cells were described as *Zwishchenmass*, which is German for *in between mass*; *Nervenkitt*, or *nerve glue* in English; and finally, the current terminology *glial cell* comes from the Greek word *glía*, meaning *glue*. It was not until the second half of the 20th century when electrophysiological characterizations and physiological studies of glial cells permitted the understanding of the wide range of vital functions that glial cells have in the functioning of the central nervous system [Morrison and De Vellis, 1981; Bowman and Kimelberg, 1984; Kettenmann, Backus, and Schachner, 1984a; Kettenmann, Backus, and Schachner, 1984b; Cornell-Bell et al., 1990; Araque, Sanzgiri, et al., 1998; Bezzi et al., 1998]. Phylogenic studies show that all organisms with a central nervous system have glial cells, and interestingly, the ratio of astrocytes to neurons is different depending on the animal species and on the brain region, with intriguing correlations with the brain complexity and neuronal density [Herculano-Houzel, 2011; Herculano-Houzel, 2014]. Throughout evolution, glial cells have diverged into specialized subgroups with different characteristics and functions. In mammals, glia can be divided into two large groups based on their size: **microglia** and **macroglia**. Macroglia can be further subdivided into three major groups: **oligodendrocytes**, **NG2-positive cells**, and **astrocytes**.

Unlike the rest of the glial cells, **microglia** originate from yolk-sac progenitors that only populate the brain during development (reviewed in S. U. Kim and Vellis, 2005;

Kettenmann, Hanisch, et al., 2011). They represent the main immunocompetent and phagocytic cells of the central nervous system [Filiano, Gadani, and Kipnis, 2015] and cover a major part of the adult brain in individual nonoverlapping domains. Microglia sense the environment through the movement of their filopodia, which rapidly reacts to abnormalities or damage [Nimmerjahn, Kirchhoff, and Helmchen, 2005; Cronk and Kipnis, 2013]. In adition to the immune role, microglia have recently been hypothesized to have an active role in the healthy brain. Opinions on this matter are, however, controversial. Some studies show that microglia could be involved in motor-dependent synapse formation [Parkhurst et al., 2013] and in features as high-order as learning or social behavior [Torres et al., 2016; Kierdorf, Prinz, et al., 2017], while others have shown that ablation of microglia barely produces any alterations or pathologies in healthy adult mice [Elmore, Najafi, et al., 2014; Elmore, R. J. Lee, et al., 2015; Bruttger et al., 2015]. When comparing the results of these studies, it should be considered that these discrepancies might be due to the major methodological differences in those studies [Jäkel and Dimou, 2017].

Oligodendrocytes are large macroglial cells that were first observed by Pío del Río Hortega in the first half of the 20th century. Their function is to insulate axons with self-produced myelin to allow fast saltatory conduction and provide trophic support to axons [Nave, 2010]. However, oligodendrocytes have also been found in sparsely myelinated brain regions, and presumably, nonmyelinating oligodendrocytes might have other overlooked functions.

The more recently discovered **NG2-positive cells** are oligodendrocyte precursors [Ffrench-Constant and Raff, 1986]. Their first evident function is to form and maintain a homeostatic network, preserving stable cell numbers stable by generating mature myelinating oligodendrocytes throughout their lifetime [Dimou et al., 2008; Rivers et al., 2008; Psachoulia et al., 2009; Simon, Götz, and Dimou, 2011; Hughes et al., 2013] under physiological conditions. NG2-positive cells form functional synapses with neurons. An associated phenomenon was first observed in the hippocampus [Bergles et al., 2000] but later described in other brain regions [Káradóttir et al., 2005; reviewed in W. Sun and Dietrich, 2013]. Such synapses are uniderectional in the sense that they can only receive neuronal signals but cannot generate action potentials on their own and further propagate them [De Biase, Nishiyama, and Bergles, 2010]. This shows that NG2-positive cells can accurately sense synaptic activity and suggests that this process may modulate their functions.

The last large group of glial cells in the brain is **astrocytes**. As mentioned before, astrocytes and their intracellular calcium signals are a key aspect of this thesis work. For this reason, within the next few sections, we will focus on their function, anatomy and known relationship with neuronal activity.

1.2.1 Astrocytes

Astrocytes are the most abundant type of glial cell in the mammalian brain [Herculano-Houzel, 2014]. Despite being one of the first glial cells discovered approximately 150 years ago, their description and the understanding of their role in brain function are still far from complete. Astrocytes do not represent a single homogeneous cell type and can be subdivided into several types depending on their morphology, molecular profile or function [Batiuk et al., 2020].

From a morphological point of view, astrocytes can be roughly divided into two types: **fibrous** and **protoplasmic**. The first is a star-shaped cell with regular contours present mainly in the white matter of the brain and spinal cord and in the optic nerve and the retina fiber layer. Fibrous astrocytes are characterized by their elongated morphology, with long processes running parallel to the axon bundles that make contact with myelinated axons and with oligodendrocytes. They have fewer processes than protoplasmic astrocytes. Their processes spatially overlap in their domains and extend to perivascular, subpial, and axonal endfeet [Lundgaard et al., 2014].

Protoplasmic astrocytes, on the other hand, have a "bushy" and irregular morphology, with a small round somata of $\sim 10\mu m$ in diameter (Figure 1.4). They present $5-10$ primary processes that further branch into thousands of branchlets and leaflets to form dense arborizations that contact neurons at synapses [Bushong et al., 2002]. Astrocytic processes also end in large endfeet that contact the vasculature [Nagelhus and Ottersen, 2013; Verkhratsky, Nedergaard, and Hertz, 2015] (schematically represented in Figure 1.4). Unlike fibrous astrocytes, protoplasmic astrocytes mainly populate the gray matter in the brain and have domains with well-defined borders that minimally overlap with each other [Bushong et al., 2002]. A single astrocyte arborization can cover 20,000 to 80,000 μm^3, contacting 300 to 600 dendrites and potentially 100,000 individual synapses [Bushong et al., 2002; Halassa, Fellin, et al., 2007]. This dense connectivity allows astrocytes to control several processes, including ion homeostasis, neurotransmitter clearance, trophic support to neurons, and neuromodulation. Interestingly, astrocytic domain boundaries have been proposed to be functional units [Perea, Sur, and Araque, 2014; Fellin, 2009]. For example, astrocytes could play the role of controlling and modulating *functional islands* formed by synapses confined within the area of influence of a single astrocyte (Figure 1.6C) [Halassa, Fellin, et al., 2007; Fellin, 2009]. Indirect support for this hypothesis comes from the observation that branching and position processes are dynamic [Kacerovsky and Murai, 2016], strongly dependent on neuronal activity [Genoud et al., 2006], and brain region-dependent [Chai et al., 2017]. For example, when comparing striatal and hippocampal astroglial populations, it was noted that despite having the same somatic volume, equivalent number of primary branches, and total cell volume, hippocampal astrocyte territories are more constrained and display a tighter physical interaction with excitatory synapses [Chai et al., 2017] compared to striatal territories.

If astrocytes are so closely related to neuronal function and, as said before, have

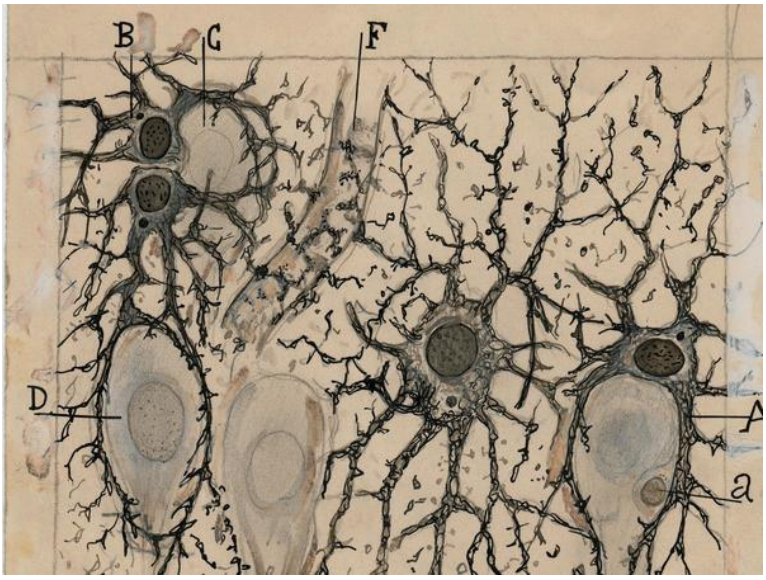

Figure 1.4: One of Cajal's original drawings of astrocytes in the hippocampus of a man three hours after death. This beautiful representation exemplifies several of the properties of astrocytes discussed herein. Note the connections with blood vessels, the small overlapping areas of domains, the somas, the large and distal processes and how astrocytic processes surround neuronal cell bodies. Adapted from Swanson et al., 2017.

large and dense areas of influence, what are astrocyte's functions in the brain? This question still represents a very active area of research. Here, we will enumerate some of the known functions that have been ascribed to astrocytes.

Astrocytes are involved in the **control of cerebral blood flow** through **gliovascular coupling**. Matching the blood flow to the neuronal metabolic needs is crucial for healthy brain functioning, which is achieved by astrocytes in a twofold manner. First, by regulating the dilation of blood vessels, it has been proven that synaptic activity mediates cytoplasmic calcium increases in astrocytes, which, in turn, promote the dilation of neighboring arterioles [Zonta et al., 2003; Attwell, Buchan, et al., 2010]. At the same time, astrocytes regulate vasoconstriction through the release of 20-hydroxyeicosatetraenoic acid (20-HETE) [Metea and Newman, 2006; Attwell, Buchan, et al., 2010]. Interestingly, astrocytes seem to *decide* drive dilation or constriction based on local oxygen levels and metabolic states [MacVicar and Newman, 2015].

Given the enormous energy consumption in the brain, the regulation of oxygen and glucose availability must be tightly controlled. This is, of course, in part regulated by blood flow. However, while oxygen freely diffuses in the brain, glucose and other metabolites need specialized transporters to travel through cell membranes. The need for energy depends on neuronal activity, which can go from completely silent to a high firing rate in milliseconds, in turn demanding up to a 30-fold increase in metabolic consumption [Attwell and Laughlin, 2001]. It has been demonstrated that astrocytes, which are in contact with both blood vessels and synapses, strongly and tightly control

active **metabolic support** to neurons. This can be achieved through a variety of processes that are still the subject of intense research. Glucose is preferentially taken up by astrocytes rather than neurons [Pellerin, Bouzier-Sore, et al., 2007]. Within astrocytes glucose enters glycolysis, producing lactate. Lactate is then delivered to neurons via the astrocyte-neuron lactate shuttle (ANLS) [Pellerin and Magistretti, 1994]. Thus, astrocytes are involved in the metabolic support of neurons not only through blood flow regulation but also through direct delivery of energy substrates.

Astrocytes, together with microglia, have a key role in the **immune response** of the brain under both physiological and pathological conditions. Upon brain injury or disease, astrocytes become reactive, drastically changing gene expressions [Zamanian et al., 2012]. These changes induce morphological and functional alterations that lead astrocytes to enter one of two distinct reactivity profiles, depending on the nature of the insult. Inflammatory insult leads astrocytes to enter what has been called *A1*, which is a reactivity profile leading to synapse pruning. On the other hand, ischemic injury leads to activation of reactivity profile *A2*, which is responsible for the growth and survival of neurons and synapses. These contrasting mechanisms coexisting in the same cell type prove once more the complexity and diversity of astrocytic function. Moreover, under physiological conditions, astrocytes continue to play a role in immune protection of the brain by controlling the functionality of the blood-brain barrier (BBB)[Almutairi et al., 2016]. Interestingly, astrocytes have been shown to be involved in BBB formation during development [Hayashi et al., 1997].

In addition to the aforementioned functions, astrocytes play key roles in ionic [Sibille, Pannasch, and Rouach, 2014; Nwaobi et al., 2016], water [Nielsen et al., 1997; Risher, Andrew, and Kirov, 2009] and neurotransmitter [Danbolt, 2001; Herman and Jahr, 2007] homeostasis. Astrocytes can rapidly change their volume and intercellular communicative capacity, which allows them to redistribute water across astrocytic networks. They can redistribute K^+ ions through K^+ spatial buffering and are the only cells in the central nervous system that can synthesize glutamate and GABA from glucose. Astrocytes are thus an incredibly versatile and complex cell in the brain. A key aspect of astrocyte physiology is their excitability based on intracellular calcium signals and the relation of this process to neuronal function. We will discuss these aspects in the next sections.

1.2.2 Calcium signaling in astrocytes

Astrocytes, unlike neurons, are electrically nonexcitable cells. However, astrocytes display changes in the intracellular concentration of calcium ions and Ca^{2+} fluctuations have been considered the main form of excitability for this type of glial cell. An extensive amount of work in the last few decades has been dedicated to understanding the origin of Ca^{2+} transients, as well as whether these fluctuations are somehow relevant for neuronal regulation, and if so, how. To date, many of these questions remain

largely unanswered. However, increasing evidence points to calcium signaling in astrocytes being involved in several processes [Araque, Carmignoto, Haydon, et al., 2014; Volterra, Liaudet, and Savtchouk, 2014; Khakh and Deneen, 2019].

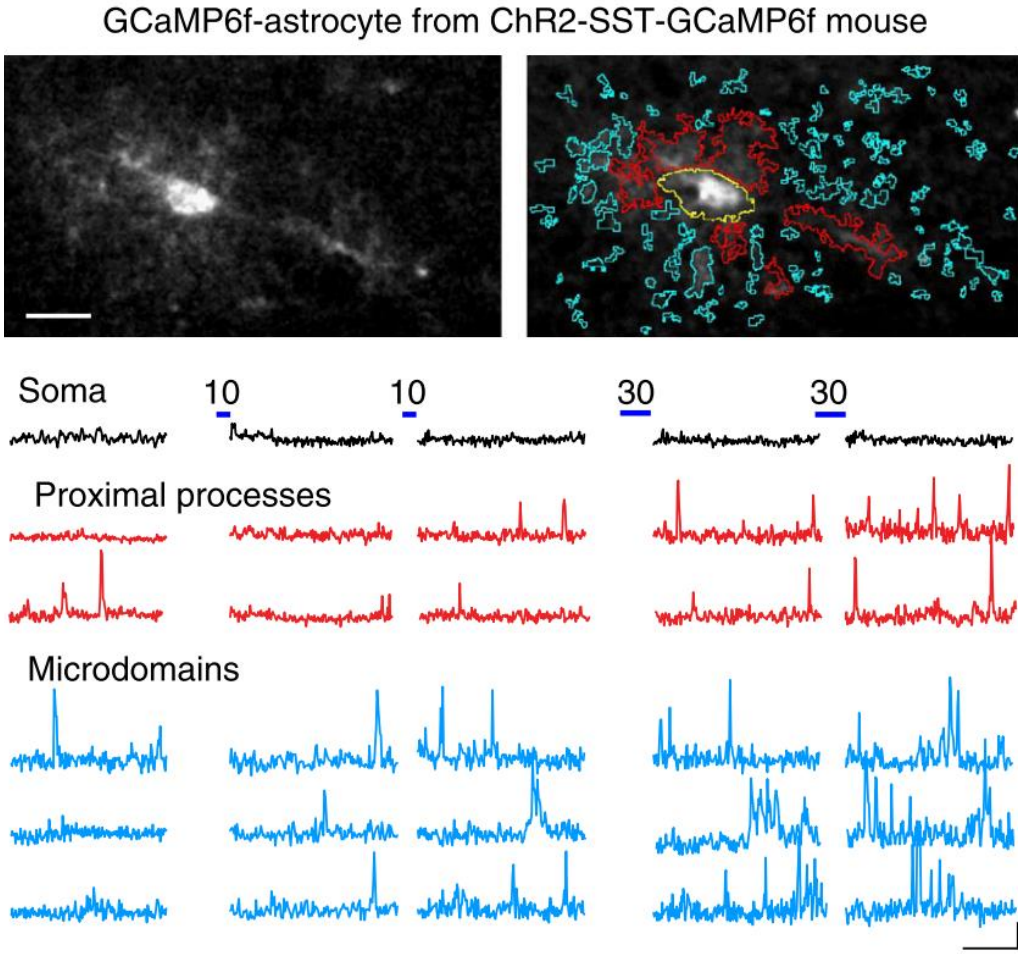

Figure 1.5: Astrocytes present complex calcium transients in their somas and processes. Image of GCaMP6f astrocytes in layer 2/3 SSCx from an adult ChR2-SST-GCaMP6f mouse that underwent SST interneuron optogenetic stimulation. ROIs are depicted for the soma (yellow), proximal processes (red) and more distal processes (blue); scale bar, is 20 μm (top). Calcium signal dynamics in example compartments show the difference between transients depending on the region of the astrocyte; scale bars are 50 s, 20% $\frac{dF}{F0}$. Adapted from Mariotti et al., 2018.

Baseline levels of Ca^{2+} in astrocytes are higher than those in neurons, and this concentration varies inside each cell, being higher in processes than in the soma [Zheng et al., 2015]. This already indicates its within-cell complexity (Figure 1.5). In astrocytes, Ca^{2+} fluctuations can have different sources, the first of which is intrinsic. In fact, 65% of astrocytes in hippocampal slices exhibit asynchronous and localized Ca^{2+} transients, even in the absence of neuronal activity [Nett, Oloff, and Mccarthy, 2002; Hirase et al., 2004]. The role and relevance of these untriggered events are still largely undefined.

In addition to spontaneously, calcium signals in astrocytes can also be triggered by neurotransmitter release through the activation of mostly metabotropic receptors for neurotransmitters. For example, glutamate has been shown to evoke calcium concentration increases in astrocytes in several contexts-in culture [Cornell-Bell et al., 1990], in brain slices [Dani, Chernjavsky, and Smith, 1992], in whole retina [Newman and Zahs, 1997], and *in vivo* [X. Wang et al., 2006]. These calcium transients can propagate along astrocyte processes and even between glial cells in the form of waves [Cornell-Bell et al., 1990,Dani, Chernjavsky, and Smith, 1992; Hirase et al., 2004 Nimmerjahn, Kirchhoff, J. N. Kerr, et al., 2004]. Astrocytic calcium waves have been observed in cultures, e.g., [Cornell-Bell et al., 1990], as well as *in vivo*, e.g., in the frontal and parietal cortices upon sensory stimulation [Ding et al., 2013] and in the cerebellum during locomotion [Nimmerjahn, Mukamel, and Schnitzer, 2009]. These observations further support the possibility that glial Ca^{2+} waves might constitute an extraneuronal signaling system in the CNS and, importantly, that it can be driven by neuronal activity (reviewed in Araque, Carmignoto, Haydon, et al., 2014; and Bazargani and Attwell, 2016). As stated above, calcium transients in astrocytes can be triggered by neurotransmitter release and can originate in neuronal activity-dependent processes. For example, in hippocampal dentate gyrus astrocyte action potential–driven synaptic transmitter release triggers large and long-lasting ($\sim 3s$) spatially broad ($\sim 12\mu m$) events, while spontaneous synaptic transmitter release produces brief ($\sim 0.7s$) and spatially localized ($\sim 4\mu m$) transients [Di Castro et al., 2011]. It has been observed that whisker stimulation increases the Ca^{2+} concentration in astrocytic cytoplasm in the barrel cortex [X. Wang et al., 2006] in a frequency-dependent manner [Perea and Araque, 2005; Sherwood et al., 2017]. Other behavioral variables, such as locomotion or the arousal state, have been observed to evoke Ca^{2+} elevation over broad spatial areas mediated by noradrenaline signals in the frontal and parietal cortex [Ding et al., 2013; Paukert et al., 2014].

To begin to understand the complexity of astrocytic Ca^{2+} activity, it is important to keep in mind that calcium transients occurring in the astrocytic cell body are very different (Figure 1.5) from those in fine astrocytic processes. Ca^{2+} events in processes can occur independently of somatic calcium events and usually display a higher frequency. These local events in processes can, however, propagate to neighboring intracellular areas [Di Castro et al., 2011] or even synchronize with neighboring cells [Takata et al., 2013]. Importantly, it has been shown that such events correlate with the strength of neuronal activity [Panatier, Vallée, et al., 2011].

Ca^{2+} events in the soma and processes also differ in their temporal profile. Somatic calcium transients are several orders of magnitude longer than neuronal action potentials, which has been a historical argument against the hypothesis that astrocytes could be involved in real-time information processing in the brain. However, smaller-amplitude calcium events occur in astrocytic processes even on the subsecond scale [Winship, Plaa, and Murphy, 2007; Lind, Brazhe, et al., 2013; Lind, Jessen, et al., 2018; Stobart et al., 2018].

It has been suggested that the release of Ca^{2+} from internal stores could be the main source of Ca^{2+} somatic transients, while in astrocyte processes, transmembrane entry of Ca^{2+}, presumably through endogenously active channels such as TRPA1 [Shigetomi, Tong, et al., 2012] or receptor-gated Ca^{2+}-permeable ion channels, generates 30–40% of Ca^{2+} concentration elevations. In this way, while Ca^{2+} increases in astrocyte somata may be too slow [Schummers, H. Yu, and Sur, 2008; Schulz, Kroner, and David, 2012] to generate rapid blood flow increases, Ca^{2+} transients in processes that are faster than those in the soma [Tang et al., 2015] occur before or with a similar time course to the increase in blood flow [Lind, Brazhe, et al., 2013; Otsu et al., 2015].

1.2.3 Astrocytic modulation of neuronal activity

In the late 1980s, Muller and Best [Müller and J. Best, 1989] provided some of the earliest evidence that astrocytes are signaling cells in the sense that astrocytes can release chemical messengers that affect neuronal activity and function. They showed that injecting immature astrocytes into the adult cat visual cortex *in vivo* reopens ocular dominance (OD) plasticity. The visual cortex in higher mammals is organized into columns of neurons that respond preferentially to one eye (OD columns). Imbalances in visual inputs, such as depriving one eye of vision, result in dramatic changes in OD column neuronal circuits. This effect is present only during a precise postnatal time period, called the critical period [Wiesel and Hubel, 1963], after which visual deprivation has little or no effect on neuronal plasticity. Muller and Best demonstrated that immature astrocyte injection in adult cats reopens the critical window, leading to the hypothesis that immature astrocytes can release a permissive factor that allows OD plasticity to occur [Müller and J. Best, 1989]. Importantly, this result suggested that astrocytes are not only supportive but also signaling cells that can release neuroactive molecules, affecting neuronal function. Astrocytic molecule release or gliotransmission, has been extensively studied since, and astrocytes have been found to release, among others, glutamate [Parpura et al., 1994; Bezzi et al., 1998], ATP [Cotrina et al., 1998; Coco et al., 2003], D-serine [Mothet, Parent, et al., 2000] and TNF [Stellwagen and Malenka, 2006]. Some of these molecules are involved in the regulation of the astrocytic cytosolic calcium concentration. Moreover, astrocytes have been observed to display Ca^{2+} concentration dynamics spontaneously or driven by neuronal activity [Cornell-Bell et al., 1990; Charles et al., 1991; Parri, Gould, and Crunelli, 2001; Stobart et al., 2018; Mu, Bennett, Rubinov, Narayan, C.-T. Yang, et al., 2019]. Ca^{2+} concentration dynamics can trigger the release of gliotransmitters, such as glutamate [Parpura et al., 1994], D-serine [Mothet, Pollegioni, et al., 2005] and ATP [Coco et al., 2003; Achour and Pascual, 2012]. What are the roles of astrocytic calcium dynamics in the processing of information by neuronal networks? Does astrocytic calcium activity modulate neuronal functioning?

Astrocytes extend processes that are ideally positioned to chemically interact with neurons at synapses (Figure 1.6A), where the astrocytic process comes into contact with both the pre- and postsynaptic neuronal terminals. Indeed, many experimental observations relate to astrocyte calcium signaling influencing synaptic activity. This

astrocyte-to-neuron communication modulates three main aspects of synaptic physiology: **presynaptic release probability** through the activation of presynaptic receptors, **postsynaptic excitability** through the activation of post-synaptic receptors, and **synaptic plasticity**. One important way in which calcium signaling in astrocytes controls synaptic function is through the release of neuroactive molecules, which are frequently called gliotransmitters (for review see Araque, Carmignoto, and Haydon, 2001; Araque, Carmignoto, Haydon, et al., 2014; Volterra, Liaudet, and Savtchouk, 2014). While astrocytes can release a plethora of transmitters, here, we will focus on a few prototypical examples of astrocyte-to-neuron communication. We refer to a previously mentioned review for an in-depth description of the complexity of chemical messaging between astrocytes and neurons.

At the **presynaptic level**, it has been observed that in the dentate gyrus, glutamate release from astrocytes activates presynaptic NMDA receptors, potentiating excitatory transmission [Jourdain et al., 2007]. Ca^{2+} uncaging-mediated glutamate release from astrocytes activates NMDA receptors to increase the frequency of miniature synaptic currents [Araque, Sanzgiri, et al., 1998] Astrocytic glutamate potentiates transmitter release by activating presynaptic mGluRs in the absence of NMDA receptor activation [Perea and Araque, 2007; Navarrete and Araque, 2010]. Astrocyte release of glutamate not only mediates an overall excitatory effect, but can also lead to inhibitory effects. For example, astrocytic glutamate binds presynaptic kainate receptors that strengthen inhibitory synaptic transmission [J. Kang et al., 1998; Liu et al., 2004]. Interestingly, it has been recently shown that a single astrocyte may release different gliotransmitters [Covelo and Araque, 2018], which can induce more complex modulation of synapses. For example, high-frequency stimulation of the CA3-CA1 projection in the hippocampus produced finely tuned release of both glutamate and adenosine from astrocytes, modulating synapses in a biphasic way. Initial glutamate release induces potentiation followed by adenosinergic-mediated depression of neurotransmitter release, which represents an elegant example of the subtle and complex modulation effects of neuronal communication by astrocytes (Figure 1.6B).

At the **postsynaptic level**, it has been suggested that spontaneous Ca^{2+} activity can mediate the release of glutamate from astrocytes, modulating neuronal excitability by inducing slow inward currents (SICs) mediated by the NMDA receptor [Parri, Gould, and Crunelli, 2001; Gómez-Gonzalo et al., 2018]. These slow inward currents have been extensively studied. Ca^{2+} signaling stimulation by different protocols has been observed to increase the SIC frequency in neurons through pharmacological stimulation [Angulo et al., 2004; N. Kang et al., 2005; Kozlov et al., 2006; Fellin, Pozzan, and Carmignoto, 2006; Nestor et al., 2007; Navarrete and Araque, 2008; Shigetomi, Bowser, et al., 2008], single-cell stimulation [D'Ascenzo et al., 2007; Fellin, Pascual, Gobbo, et al., 2004; Perea and Araque, 2005] and extracellular stimulation of neuronal afferents [Fellin, Pascual, Gobbo, et al., 2004]. Moreover, it has been shown that the generation of SICs by glutamate release from astrocytes is due to the activation of a particular set of NMDA receptors located at extrasynaptic sites and preferentially containing the

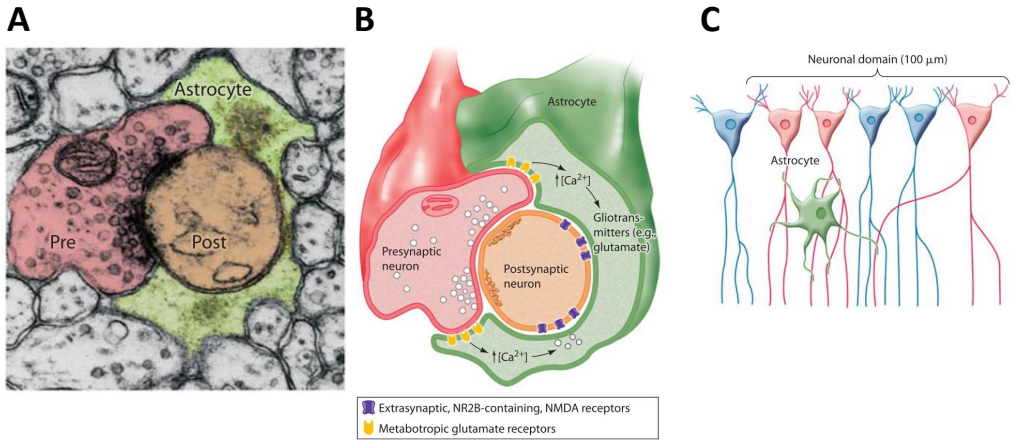

Figure 1.6: The tripartite synapse model. A) Electron microscopy shows the tripartite nature of synaptic structures with astrocytic processes (green) associated with pre- and postsynaptic terminals. Adapted from Mariotti et al., 2018. B) Schematic representation of A), where, in the hippocampus, metabotropic receptors in the plasma membrane of the nearby astrocytic processes are activated by glutamate released from the presynaptic Schaffer collateral terminals. As a result of this activation, intracellular Ca^{2+} increases in the astrocytes, which, in turn, leads to the release of glutamate from glial cells through the fusion of tetanus toxin-sensitive vesicles. Astrocytic glutamate selectively acts on extrasynaptic NR2B-containing NMDA receptors to trigger slow inward currents (SICs) in pyramidal CA1 neurons. C) Schematic representation of the mechanisms by which a single astrocyte (green cell) can lead to neuronal synchronization of local clusters of neurons or neuronal domains (red cells) through glutamate release. B) and C) are adapted from Fellin, Pascual, and Haydon, 2006

NR2B subunit [Fellin, Pascual, Gobbo, et al., 2004], and the level of SIC synchronization is neuronal type-dependent [Fellin, Pascual, Gobbo, et al., 2004; Angulo et al., 2004; Kozlov et al., 2006]. NMDA receptor binding has been shown to be modulated by astroglial D-serine release, which in turn modulates glutamatergic synaptic transmission [Panatier, Theodosis, et al., 2006; Henneberger et al., 2010] (for controversial results, see Wolosker, Balu, and Coyle, 2016). Moreover, it has been observed that disrupting gliotransmission in a dnSNARE mouse model produces a hypofunction of postsynaptic NMDA receptors, which has effects at the network level affecting cortical slow oscillations (see below) [Fellin, 2009].

Gliotransmission has been observed to modulate **synaptic plasticity**. For example, astrocytes have been shown to be involved in heterosynaptic depression in the hippocampus [Pascual et al., 2005; Serrano et al., 2006; Andersson, Blomstrand, and Hanse, 2007; J. Chen et al., 2013]. Moreover, clamping Ca^{2+} in individual CA1 astrocytes blocks LTP induction at nearby excitatory synapses by decreasing the occupancy of NMDAR coagonist sites [Henneberger et al., 2010]. Exogenous D-serine or glycine application reverse this effect. However, the release of D-serine from astrocytes is controversial, and a novel hypothesis is that astrocytes release l-serine rather than D-serine and shuttle it to neurons for D-serine synthesis [Wolosker, Balu, and Coyle, 2016]. Astrocytes can also modulate synaptic depression. Ca^{2+} clamping in rat barrel

cortex astrocytes during development showed impaired t-LTD [Min and Nevian, 2012]. Moreover, simultaneously stimulating an astrocyte with depolarizing pulses and afferent fibers resulted in LTD [Min and Nevian, 2012].

As described above, a large amount of data supports the view that astrocytes are crucial modulators of synapses and that their activity can regulate synaptic transmissions and plasticity. The next obvious question is whether astrocytes can modulate neuronal network activity, brain rhythmogenesis in vivo, and behavior. The development of mouse models of impaired gliotransmission and new more precise genetic tools for cell-specific manipulation offered the opportunity to test these hypotheses. By using extracellular and patch-clamp recordings in anesthetized animals, Fellin et al. showed that the selective expression of a dominant-negative form of synaptobrevin 2 in astrocytes to inhibit gliotransmission [Pascual et al., 2005; Q. Zhang et al., 2004] results in decreased slow oscillations in the somatosensory cortex [Fellin, Halassa, et al., 2009]. The decreased slow oscillation activity is due to the astrocytic modulation of cortical synapses at least at two different sites. First, there is a loss of the tonic level of extracellular adenosine activating A1 receptors, and second there is decreased function of neuronal NMDA receptors. Alterations in astrocytic calcium dynamics inhibit slow wave activity, showing the fine causal interplay between both types of cells during brain oscillations [Szabó et al., 2017]. Interestingly, it has been recently proposed that astrocytes might play a role in the regulation of neuronal membrane potential oscillations at a wide range of frequencies [Bellot-Saez et al., 2018]. Indeed, the blockade of K^+ uptake or astrocytic connectivity enhances the network excitability and forms high-power network oscillations. This could be due to changes in the oscillatory behavior of individual neurons, which is a well-known effect in the system dynamics field. More recently, astrocytes have been shown to modulate behavior. For example, astrocytes control sleep behavior [Halassa, C. Florian, et al., 2009], enhance performance in memory tasks [Adamsky et al., 2018], and sustain goal-directed behavior [Mederos et al., 2020].

Overall, the data presented in this section point to astrocytes as key regulators of neuronal function, from individual synapses, to network activity and behavior.

1.2.4 Astrocytes accumulate evidence

In the previous sections, we discussed how astrocytes are involved in the way in which neurons process information, focusing mainly on the mechanisms by which these interactions may take place. However, to further explore the hypothesis that the brain works through the concerted action of an extended network of both neurons and glial cells, the next question is whether astrocytes or astrocytic networks process information themselves and, if so, how.

Some very recent findings, started addressing this question [Mu, Bennett, Rubinov, Narayan, C.-T. Yang, et al., 2019; Mederos et al., 2020; S. Kang et al., 2020]. Here we will focus on one of them [Mu, Bennett, Rubinov, Narayan, C.-T. Yang, et al., 2019]. The

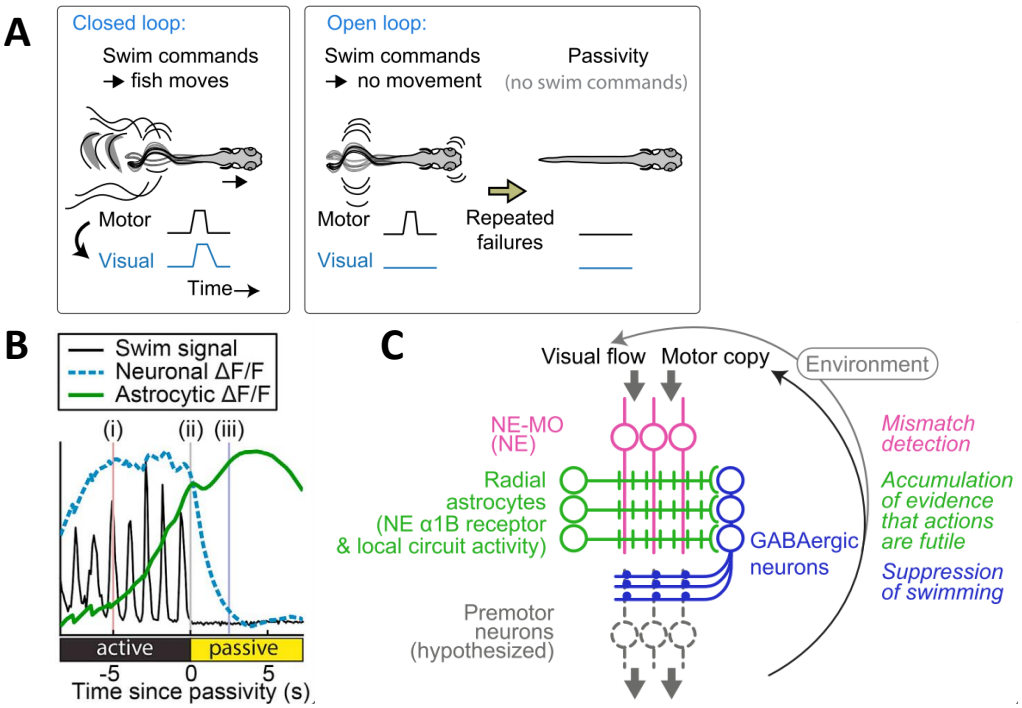

Figure 1.7: Astrocytes in zebrafish accumulate evidence. A) Locomotion in closed loop versus open loop. Zebrafish entered a passive behavioral state after repeated swim failures. B) Averaged neuronal and glial signals near passivity onset for one representative animal. The average neuronal calcium activity decayed after passivity onset, while the glial calcium activity increased before passivity onset and peaked soon after. C) Schematic representation of the circuit hypothesized by the authors: mismatch signals computed from visual and motor efferent inputs are represented by specific neuronal circuits. Noradrenergic axons excite glial processes belonging to astrocytes that integrate mismatch signals and suppress swimming through the activity of downstream GABAergic neurons. Adapted from Mu, Bennett, Rubinov, Narayan, C. T. Yang, et al., 2019.

Misha Ahrens group studied the interplay of astrocytic and neuronal networks during swimming adaptation strategies and information integration in larval zebra fish [Mu, Bennett, Rubinov, Narayan, C.-T. Yang, et al., 2019]. In this task, animals were exposed to a virtual reality environment where visual feedback was decoupled from motor actions so that swim behavior failed to trigger the expected visual flow. The animals, after becoming aware of the futility of their efforts, became passive and stopped moving, trying again a few seconds later (Figure 1.7A). When the animals switched from the active to the passive behavioral state, the whole-brain average neuronal activity decreased, while the glial activity increased. In this case, activity refers to Ca^{2+} transients that started seconds before and peaked after passivity onset (Figure 1.7B).

The availability of chemical, optical, and genetic tools allows interventional approaches that can test the causal role of astrocytes in this process. On one hand, the reduction of astrocytic Ca^{2+} activity by two-photon laser ablation of glial cells or blocking the inositol 1,4,5-trisphosphate receptor to reduce Ca2+ release from intracellular stores led to a reduction in futility-induced passivity. On the other hand, using a chemogenetic approach to increase intracellular Ca^{2+} in glia led to an increase in the time spent in the passive state. This effect was temporally tuned as shown by optogenetic activation of radial astrocytes (using either CoChR or Opto-a1-AR), suggesting that astrocytic Ca^{2+} signals are necessary and sufficient for the expression of this behavior.

Interestingly, the way astrocytes exert this effect on behavior is achieved through finely tuned interplay between neuronal and astrocytic networks. More precisely, during futility-induced passivity, signals from noradrenergic (NE) neurons together with local circuit activity triggered glial responses, as proven by optogenetically activating NE neurons, showing that astrocytes integrate both behavioral information and NE signals. Astrocytes, in turn, activated GABAergic neurons that would most likely suppress swimming.

Importantly, through a series of complex but very elegant probabilistic experiments, the group demonstrated that NE neuron signals encode sensory-motor mismatch signals. Signals are transmitted to astrocytes, which in turn *accumulate evidence* that actions are futile and control swimming behavior through GABAercig neurons (Figure 1.7C).

This study is a beautiful example of the complexity of astrocytic physiology, and it commbines several of the characteristics of astrocytes discussed in the previous sections in an orchestrated mechanism and behaviorally relevant context. This study shows how astrocytes are involved in network state changes, integrate neuronal activity, modulate downstream circuits, influence behavior and, importantly, process information in multiple ways.

1.3 Astrocytes encode spatial information in their Ca^{2+} dynamics

In the following sections, we introduce recent unpublished work from my supervisor's laboratory in collaboration with Jacopo Bonato and Stefano Panzeri. These results significantly contributed to the conceptual development of the work presented in this thesis. As we previously introduced, astrocytes are involved in the processing of information in the brain, both by encoding specific aspects of behavioral variables and their relations with the environment and by interacting with neuronal networks. Astrocytes and their interactions with neurons have been extensively studied in the hippocampus [Perea and Araque, 2007; Pascual et al., 2005; Serrano et al., 2006; Andersson, Blomstrand, and Hanse, 2007; J. Chen et al., 2013; Covelo and Araque, 2018; Fellin, Pascual, Gobbo, et al., 2004; Fellin, Pozzan, and Carmignoto, 2006]. However as discussed in the

first part of this introduction, one of the most interesting and thoroughly studied functions of hippocampal networks is the encoding of spatial information and the building of a cognitive map for spatial navigation. The questions of whether navigational information is encoded exclusively in neuronal cells or whether it involves the extended brain network comprising glial cells as well as neurons and whether hippocampal astrocytes intervene in, alter, or modulate spatial information encoding in neurons are still open. In my mentor's laboratory, we have started tackling these questions. Given that the experimental results that we obtained required precise quantification of spatial information, in the next section, I will introduce information theory and its main statements.

1.3.1 Information Theory

C. E. Shannon critically contributed to the development of Information theory. In his landmark paper *A Mathematical Theory of Communication* [Shannon, 1948], Shannon developed a mathematical formalism of communications, considering the coding and decoding problem of information in noisy channels. This theory extended to many fields with several practical and theoretical applications-notably, modern computation, quantum mechanics, quantum computation, and neuroscience. There are several ways of approaching the notion of information, as in Shannon's theory, and here, we will expose a modified version of the one exposed in his original paper. We will start by initially taking his approach because it relates information to probability distributions in an intuitive way. However, it's useful to keep the objective in mind, which is what we are trying to use information theory to address. The question that we'll try to answer is as follows: if we look at neuronal activity, how much information do we gain from a certain behavioral variable (for example, in the context of spatial navigation, the position of the animal)?

Let us first try to formalize the problem-neurons can be in several states, depending on how we describe them. We can think of a neuron as a variable with two states, either firing or not, or with a continuum of states, such as all the possible values of its membrane potential or of the calcium concentration inside the cell. Let us then consider, in a general way, that each state of the neuron has a certain probability, namely, state x has probability p_x of occurring. When we observe a neuron we gain information about its state, e.g., whether or not the neuron is firing. However, before measuring it, we can ask the question of **how uncertain we are about the state of the neuron if we know the set of probabilities** $\{p(x)\}$. This is equivalent to asking the question concerning *how much* information we will gain when we learn the state of the neuron. In this example, we use the state of a neuron, but the approach can be generalized to any probability distribution. To answer a 'how much' question (either how much uncertainty we have or how much information we gain), we need a quantitative measure. Let us call this measure H. There are three reasonable properties that H should have, as follows:

- H **should be a function only of the probabilities**, regardless of the identity of the object to which H refers (e.g., if the object is a cell, then it does not matter whether the cell is a principal neuron, an interneuron, an astrocyte). What is important is that the probabilities of states are the same; therefore we can write $H(p_x)$. In addition, H **should be continuous in** p_x.
- If all events are equally possible, that is, $p_i = \frac{1}{n}$, with n being the number of states, then H **should be a monotonically increasing function of** n. Intuitively, this can be understood as follows: when there are more possible states and all the states are equally possible, there is more uncertainty.
- The information gained when two independent events occur with individual probabilities p and q is the sum of the information gained from each event alone.

It can be shown [Shannon, 1948] that the only H that satisfies all three properties is of the form:

$$H = -K \sum_{x=1}^{n} p_x \, log(p_x) \tag{1.1}$$

where K is a positive constant that determines the choice of units of measure. This definition of H falls under the name of **entropy**. We select the logarithm to be in base 2 (all logarithms in this thesis will be in base 2 unless otherwise specified), which is achieved by appropriately selecting the constant K, and define the entropy of the probability distribution $p_1, p_2, ..., p_n$ of an n state variable as:

$$H = - \sum_{x=1}^{n} p_x \, log_2(p_x) \tag{1.2}$$

This definition is intuitive and has the advantage that it can be used to *quantify the resources needed to store information*. It can be shown that Shannon's entropy represents the minimal physical resources required to store the information being produced by a source in such a way that at a later time, the information can be reconstructed. This result is known as *Shannon's noiseless coding theorem* [Shannon, 1948].

To illustrate some of the properties of H, we provide an example. Let us consider a simplified neuron with two possible functional states: firing and not firing. The neuron fires with probability p and is silent with probability $q = 1 - p$. Its entropy is given by:

$$H = -(p \, log(p) + (1 - p) \, log(1 - p)) \tag{1.3}$$

We can see the values of H as a function of p in Figure 1.8A. If the neuron is always silent and never fires, we have no uncertainty regarding its state, and we gain no information by measuring its state. Under these conditions, $p = 0$, and therefore, $H = 0$. If, on the other hand, the neuron randomly fires half of the time, we have maximal uncertainty about its state before measurement, and therefore, we gain the maximum amount of information after measurement. Thus, $p = 0.5$, and the entropy is $H = 1$.

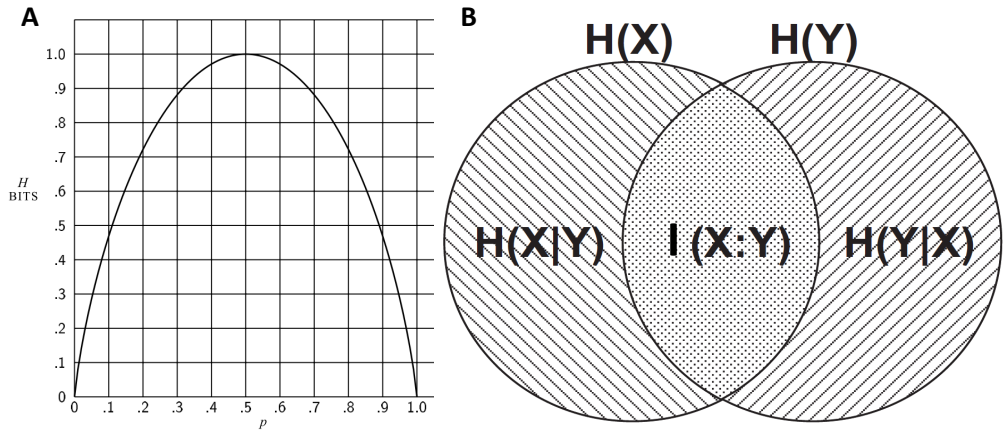

Figure 1.8: Entropy and information theory. A) Entropy of a binary variable as a function of the probability p, adapted from Shannon, 1948. B) Schematic entropy and information Venn diagram, adapted from Nielsen and Chuang book, 2010.

In other words, this means that knowing the state of the neuron gives us 1 bit of information. In general, we have $H = 0$ if and only if all $p_i = 0$ except one, which is 1. The uniform distribution is the probability distribution with the maximum entropy, and in this case, the entropy is the logarithm of the number of states. That is, $H = log(n)$, and it is maximum if and only if $p_i = \frac{1}{n} \; \forall \, i$.

In addition to H, there are other important quantities to define in information theory. Let us hypothesize that we have another variable, Y, with its own states and probability distribution $p(y)$, that can represent another neuron or set of neurons, or a behavioral variable such as the position of the animal. We define the **joint entropy** of variables X and Y as

$$H(X,Y) \equiv -\sum_{x,y} p(x,y) \; log(p(x,y)) \tag{1.4}$$

The joint entropy measures the total uncertainty about the pair (X, Y). A third important quantity applies to the following situation: suppose that we learn the value of Y, meaning that we gain $H(Y)$ bits of information about the pair (X, Y). How much uncertainty remains about the pair (X, Y)? Or in other words, how uncertain are we about X, given that we know the value of Y? This quantity is called the *entropy of X conditioned on knowing Y* and is defined as:

$$H(X \mid Y) \equiv H(X,Y) - H(Y) \tag{1.5}$$

With the definition provided above, we now have everything we need to define the quantity that addresses our initial question, i.e., if we look at neuronal activity, how

much information do we gain from a certain behavioral variable (for example, the position of the animal)? Alternatively, how much information is shared between neuronal activity and the behavioral variable? We can formalize this situation as follows. Let us consider two variables X and Y, and suppose that we add the information content of X, $H(X)$ to that of Y, $H(Y)$. If there is information shared between the two variables, then we will count it twice, and information that is not common will be counted only once. Therefore, if we subtract from the sum of $H(X)$ and $H(Y)$, the total amount of information of the pair, which is nothing but the joint entropy $H(X,Y)$, what remains is the common or **mutual information** of X and Y:

$$I(X:Y) \equiv H(X) + H(Y) - H(X,Y) \tag{1.6}$$

In the last paragraph, we have been using *information* and entropy as somewhat interchangeable concepts. This is because, as we said at the beginning of this section, entropy quantifies the amount of uncertainty about a variable before knowing its state or, equivalently, how much *information* we gain about that variable when we measure its state. However, we could arrive, at the expression for mutual information in a slightly different but equivalent way. As we saw before *conditional entropy* $H(X \mid Y)$ represents the uncertainty that remains in X given that we learned the value of Y. Thus, the complement of the uncertainty that remains is the *information that we gained* about X by knowing Y. Formally, we can then define *mutual information* as:

$$I(X:Y) \equiv H(X) - H(X \mid Y) \tag{1.7}$$

The equivalency of expressions 1.6 and 1.7 is trivially shown simply by replacing 1.5 in 1.6. A useful way of visualizing the various definitions of entropic quantities is the 'entropy Venn diagram' shown in figure 1.8B.

Information theory has been widely applied in neuroscience, starting from the works of Richmond and Optican in 1990 [Richmond, Optican, and Spitzer, 1990; Richmond and Optican, 1990] on the primate visual cortex and the Skaggs formula for spiking activity in 1992 [W. E. Skaggs et al., 1992]. There are several reasons for the success and usefulness of information theory approaches for studying the brain. First, information theory is model-independent in the sense that there is no a priori model of the interaction between the variables of the system under study. This does not mean that information theory is *assumptions*-free. Rather, there are several assumptions about the data that need to be made. For example, it is required to assume the data to be stationary, i.e., if a neuron encodes information about a behavioral variable at the beginning of the experiment, it will do so at the end. Second, because of its probabilistic nature, information theory is applicable regardless of the data type, meaning that we can use it if one of the variables is represented by a binary signal, as in the case of spikes in a neuron, or if it is a continuous variable, as in the speed of an animal in cm/s. Third, information theory can uncover nonlinear relations between variables. Finally, all the

quantities presented so far are easily scalable to many variables and are therefore applicable to many neurons or combinations of a neuron and several behavioral variables.

Information theory also has limitations when applied to neuroscience. For example, information theory would require knowledge of the true probability distributions of considered variables, but this information is not available in the experimental neuroscience setting. Most of the time, experimentally measured probability distributions are only good approximations of true distributions. The bias implied by using empirical probability distributions has been extensively studied, and several alternatives for correcting such bias have been proposed [Panzeri, Senatore, et al., 2007; Panzeri and Treves, 1996; Treves and Panzeri, 1995].

Information theory approaches have been traditionally used for studying spiking trains and therefore electrophysiological data [W. E. Skaggs et al., 1992]. However, as we said before, this approach can be used regardless of the nature of the data types, and more recently, it has been used for analyzing the information content and correlations in calcium activity as recorded by 2-photon imaging [Shuman et al., 2020; Stefanini et al., 2020; Rubin et al., 2015a; Sheintuch et al., 2017b; Runyan et al., 2017].

1.3.2 Astrocytes and spatial information

In the context of information theory and spatial navigation, the first outstanding question is whether astrocytes encode spatial information about the position of the animal in the dynamics of intracellular calcium signals. Here, we will summarize recent unpublished data from my mentor's laboratory that contribute to answering this question. To test this hypothesis, mice were trained to run head-fixed in a virtual reality corridor (Figure 1.9A) [Gauthier and Tank 2018]. Astrocyte-specific expression of the genetically encoded calcium indicator GCaMP6f [T.-W. Chen et al., 2013; Haustein et al., 2014] was used together with two-photon functional imaging to capture the subcellular calcium dynamics of hippocampal CA1 astrocytes (Figure 1.9C). It was found that a fraction of subcellular regions carried significant information about the spatial position of the animal in the virtual track (Figure 1.9B,D). In this context, *significant amount of information* is related to how the mutual information value compares to surrogate distributions of MI values built by temporally shuffling the data (see methods for details). The distribution of response field positions covered the entire length of the virtual corridor (Figure 1.9D), suggesting a full map of the environment produced by astrocytes, which was parallel (or complementary) to that of the neuronal network. Similar to neurons, when exposed to a bidirectional environment, astrocytic ROIs showed significant direction selective spatial modulation in their response field.

It was found that both cell bodies and processes encoded spatial information and that a similar fraction of somas and processes were modulated by the spatial position of the animal (Figure 1.10A,B). The preferred field position of astrocytes was not entirely random. This was observed first because the correlation between the calcium

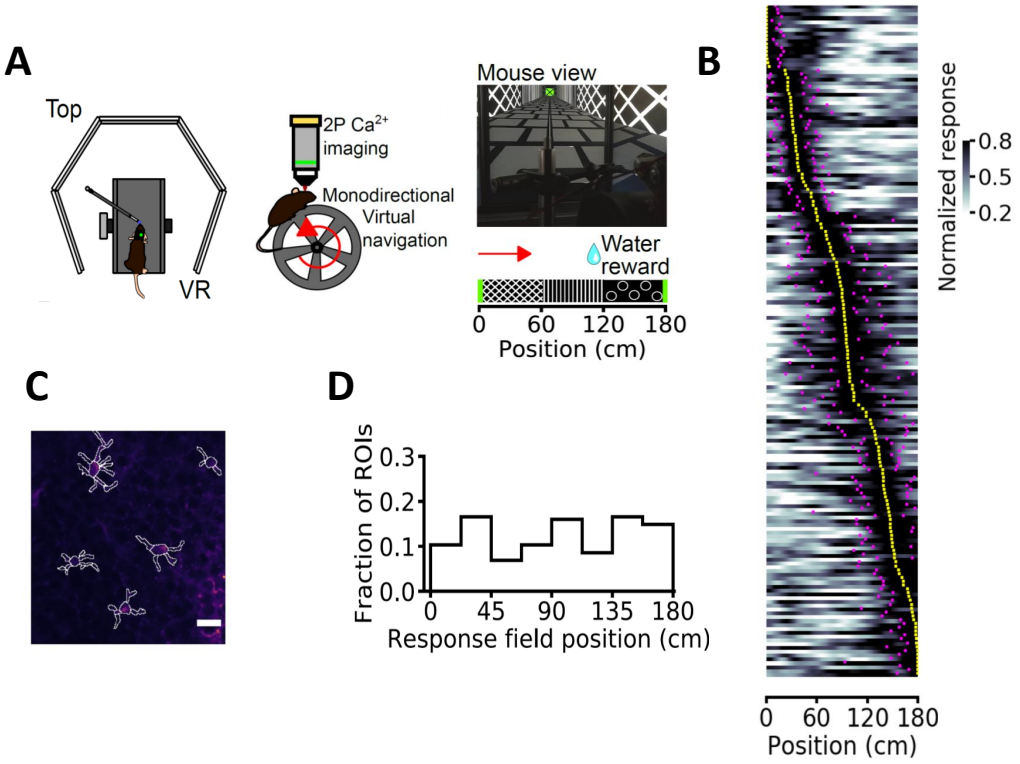

Figure 1.9: Calcium dynamics in astrocyte networks in the hippocampus encode spatial information. A) Schematics of the experimental setup. Head-restrained mice run on a treadmill while navigating a virtual corridor. B) Normalized astrocytic calcium responses as a function of position for astrocytic ROIs that contain significant amount of spatial information. Yellow dots indicate the center position of the response field, and magenta dots indicate its width (vertical scale: 50 ROIs) C) Median projection of GCaMP6f-labeled astrocytes in the CA1 pyramidal layer. Segmented ROIs are shown in white; scale bar, 20 μm. D) Distribution of response field positions. Adapted from Curreli, Bonato, Romanzi, Panzeri and Fellin, submitted.

activity of pairs of informative ROIs decreased as a function of the pair distance (Figure 1.10D). Second, the difference between the field positions of the two informative ROIs in a given pair increased as a function of the pair distance within $0 - 40\mu m$ and reached a constant value, indicating that informative calcium signals were coordinated across cells (Figure 1.10C). Similarly, when looking at the single cell-level, the difference between the field position of an informative process and the corresponding somas increased as a function of the process distance from the soma (Figure 1.10E), demonstrating that spatial information is differentially encoded in topologically distinct locations of the same astrocyte. Overall, these results demonstrate that astrocytes encode spatial information in the hippocampus during virtual navigation, and that a complete map (at least in a unidimensional virtual track) could be encoded in the astrocytic network (meaning that the place fields of all astrocytes observed spanned the whole length of the virtual corridor).

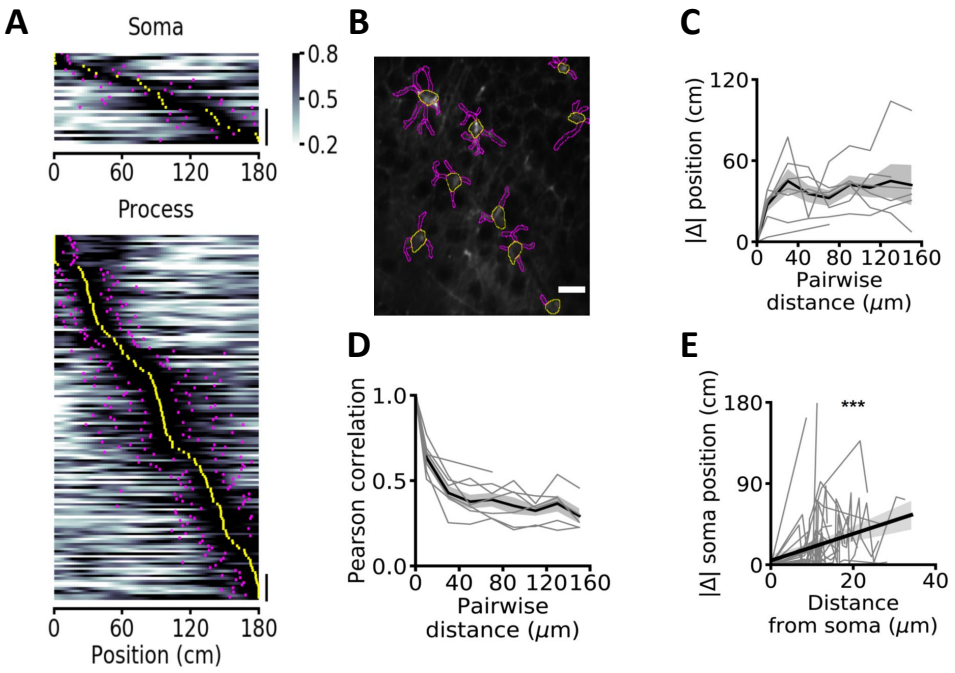

Figure 1.10: Spatial information is encoded differentially in astrocyte somas and processes. A) Normalized astrocytic calcium responses as in 1.9B for ROIs corresponding to somas (top) and processes (bottom) (vertical scale: 10 ROIs). B) Median projection of a t-series displaying GCAMP6f-labeled astrocytes in the CA1 pyramidal layer. ROIs are separated into somas (yellow) and processes (magenta). Pairwise Pearson's correlation (D) and difference between response field positions (C) for pairs of astrocytic ROIs across the whole FOV as a function of the ROI pairwise distance. E) Difference in the response field position of a process with respect to the field position of the corresponding soma as a function of the process distance from the cell soma. Adapted from Curreli, Bonato, Romanzi, Panzeri and Fellin, submitted.

1.3.3 Decoding of position

Is it possible to decode the animal's position based on the calcium dynamics of astrocytes during navigation in the virtual corridor? To answer this question, a support vector machine (SVM) was trained to solve the classification problem of decoding the mouse's position using single-trial astrocytic calcium signals according to a set of discrete locations. Decoder performance was tested for different granularities; that is, for different number of discrete locations used for the decoder. Animal's spatial location was predicted across granularities as shown in the confusion matrices (Figure 1.11A). The decoder decoded spatial information was significantly above chance level, regardless of how many discrete locations were available in the space domain (Figure 1.11B, chance bars are not visible because chance decoded information was 0 bits for all granularities). Disrupting temporal coupling within astrocytic population vectors while preserving single-ROI activity patterns and spatial information, which was achieved by shuffling calcium events occurrences for each spatial bin between different passes

in other trials through that same location (as in Stefanini et al., 2020), consistently decreased decoded spatial information (Figure 1.11B). This is important because it means that a downstream neuron (or network) would be able to decode animal's position by integrating astrocytic calcium transients information, suggesting the potential behavioral relevance of this process. Misclassifications were more likely to occur among nearby locations across all granularity conditions (Figure 1.11C), meaning that decoder errors are not uniformly distributed and suggesting that errors made are *reasonable errors* and not random misclassifications.

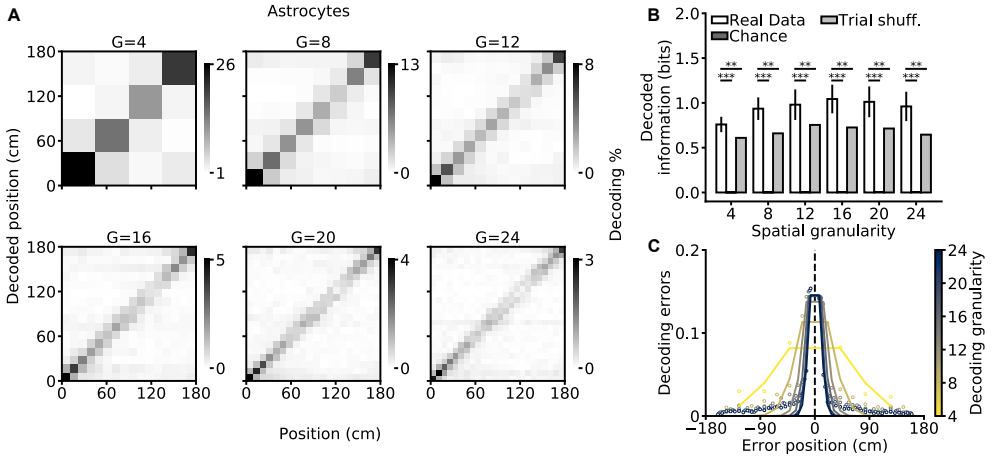

Figure 1.11: Animal spatial location can be efficiently decoded from astrocytic calcium signals. A) Confusion matrices of a SVM classifier for different decoding granularities (number of spatial bins used, G = 4, 8, 12, 16, 20, 24). The actual position of the animal is shown in the x axis, the decoded position in the y axis. The grey scale indicates the number of events in each matrix element. B) Amount of information in bits retrieved by the SVM decoder as a function of the granularity on real (white), chance (dark gray, chance levels computed were 0 across granularity and therefore not visible in the plot), and trial shuffled (grey) data. Trial-shuffling disrupts temporal coupling within astrocytic population vectors, while single-ROI activity patterns are preserved. C) The decoding error (fraction of misclassifications) as a function of the error position (distance between the true position and the classified one) within a confusion matrix. The decoding granularity is represented as different lines. Adapted from Curreli, Bonato, Romanzi, Panzeri and Fellin, submitted.

Chapter 2

Rational and Aim

Neural place cells in the hippocampus encode navigational information through the modulation of their firing rate as a function of the animal's spatial location [O'Keefe, 1976], providing a cellular substrate for spatial cognition. Whether navigational information is processed exclusively in neuronal cells or it involves other cell types in the brain is currently unknown. Astrocytes, a major class of glial cells in the brain, display complex dynamics in their intracellular calcium concentration [Bazargani and Attwell, 2016]. These intracellular signals can be spatially restricted to individual subcellular domains (e.g., cellular processes vs somas), be coordinated across astrocytic cells, and trigger the release of neuroactive molecules which deeply influence synaptic transmission and neuronal excitability. Recent unpublished work from my mentor's laboratory in collaboration with Jacopo Bonato and Stefano Panzeri shows that astrocytes encode navigational information in their intracellular calcium dynamics, suggesting that astrocytes may contribute to the modulation of the neuronal representation of space. In this thesis work, I developed an analysis pipeline to directly test this hypothesis using statistical methods and Information Theory approaches. The developed analytical tools were applied to two experimental data sets in which neuronal place cells in the hippocampus were imaged using two-photon microscopy while selectively manipulating astrocytic calcium dynamics with pharmacogenetics during virtual navigation.

Chapter 3

Materials and Methods

3.1 Experimental procedures

3.1.1 Animals

All experiments involving animals were approved by the National Council on Animal Care of the Italian Ministry of Health and carried out in accordance with the guidelines established by the European Communities Council Directive authorization (61/2019-PR). From postnatal days 30, animals were separated from the original cage and group housed (2–5 per cage) in a 12-hours light-dark cycle with *ad libitum* access to food and water. Only animals older than 10 weeks underwent experimental procedures.

3.1.2 AAV injection and surgery for chronic hippocampal imaging

Neuronal-specific GCaMP6f expression was obtained using AAV1.CamKII.GCaMP6f.WPRE.SV40 (Addgene viral prep # 100834-AAV1). Astrocytic-specific GCaMP6f expression was obtained using pZac2.1 gfaABC1D-cyto-GCaMP6f (Addgene viral prep # 52925-AAV5 a gift from Dr. Khakh, Haustein et al., 2014; Srinivasan et al., 2015). Astrocytic-specific DREADD expression was obtained using AAV-GFAP-hM3D(Gq)-mCherry (Addgene viral prep # 50478-AAV5)

Male C57Bl6/j mice were placed into a stereotaxic apparatus (Stoelting Co, Wood Dale, IL), maintained on a warm platform at 37°C and anesthetized with 2% isoflurane/0.8% oxygen. Before surgery, a bolus of Dexamethasone (4 mg/kg, Dexadreson, MSD Animal Health, Milan, IT) was provided with an intramuscular injection. A small circular craniotomy (diameter, 0.5 mm) was drilled on the right hemisphere (1.75 mm posterior, 1.35 mm lateral to bregma) after scalp incision. A micropipette loaded with AAV was then lowered into the CA1 region of the hippocampus (1.40 mm deep to bregma). 800 nl of solution containing the two AAVs for GCaMP6f (dilution, 1:5) and DREADD (dilution, 1:8) was injected at 100 nL/min using a hydraulic injection apparatus driven by a syringe pump (UltraMicroPump, WPI, Sarasota, FL). After viral injection, a stainless-steel screw was positioned on the skull of the left hemisphere and a chronic hippocampal window was implanted following (D. A. Dombeck, Harvey,

et al., 2010, Sheffield and D. Dombeck, 2015). A 3 mm craniotomy centered at coordinates 2.00 mm posterior and 1.80 mm lateral to bregma was opened using a drill and the dura was removed using fine forceps. A blunt needle coupled to a vacuum pump was used to carefully aspirate the cortical tissue overlaying the hippocampus. The exposed tissue was continuously irrigated during aspiration with HEPES-buffered artificial cerebrospinal fluid (ACSF). Aspiration was interrupted when the thin fibers of the external capsule were visible. A cylindrical cannula-based optical window was then positioned at the craniotomy touching the external capsule. A thin layer of silicone elastomer (Kwik-Sil, World Precision Instruments, Sarasota, FL) was used to fill and isolate the space between the steel surface of the optical window and the brain tissue. Epoxy glue was used to attach a custom stainless-steel headplate to the skull. Black dental cement was used to secure each component in place. An intraperitoneal bolus of antibiotic (BAYTRIL, Bayer, DE) was administrated to animals after surgery.

Optical windows consisted of stainless-steel cannula segments with thin walls (outer diameter, 3 mm; inner diameter, 2.77 mm; height, 1.50 - 1.60 mm). At one end of the cannula a 3.00 mm diameter round coverslip was attached by means of UV curable optical epoxy (Norland optical adhesive 63, Norland, Cranbury, NJ). Bonding residues and Edges were smoothed with a diamond coated cutter.

3.1.3 Two-photon imaging

Two-photon calcium imaging was performed using an Ultima Investigator or an Ultima II scanheads (Bruker Corporation, Milan, IT) equipped with raster scanning galvanometers (mirror dimension, 6 mm or 3 mm) a 16x/0.8 NA objective (Nikon, Milan, IT), and multi-alkali photomultiplier tubes. For GCaMP6f imaging, the excitation pulsed laser sources were either a Chameleon Ultra or a Chameleon Ultra II, both tuned at 920 nm (repetition rate, 80 MHz; Coherent, Milan, IT). Before every experimental session, each FOV was imaged at 740 nm to confirm the expression of DREADD-mCherry construct. Laser beams intensity was adjusted using Pockel cells (Conoptics Inc, Danbury, CT). Imaging average power at the objective focus was $\sim 80 - 110mW$. Fluorescence emission was collected using multi-alkali PMT detectors downstream of appropriate emission filters (525/70 nm for GCaMP6f, 595/50 nm for red reporter fluorophores). Detector signals were digitalized at 12 bits. Imaging was conducted in raster scanning mode at $\sim$ 3 Hz using 5x optical zooming factor. Images contained 256 pixels x 256 pixels field-of-view (FOV). The pixel dwell-time was set at $4\mu s$. The pixel size was $0.634\mu m$ for the Investigator scanhead and $0.509\mu m$ for the Ultima II scanhead. For recordings in which we imaged the same FOV over days (longitudinal recordings), imaging was performed at 9.972 Hz with 3x optical zoom factor. Images contained 128 x 128 pixels, dwell-time was set at $2.8\mu s$ and pixel size was $2.144\mu m$.

3.1.4 Longitudinal recordings

To perform longitudinal recordings, we implemented a protocol to precisely image the same FOV over different days based on a series of acquired coordinates and images. More specifically, we first head fixed using a *Luigs&Neumann* apparatus, which allowed movements according to 5 coordinates. These coordinates were chosen to minimize the tilting of the cannula relative to the wheel, annotated, and saved for the following sessions. Moreover, a laser pointer was attached close to the mouse head and the position of the laser spot projected $\sim$ 40 cm away from the mouse was also annotated and used as an additional spatial reference. Several two-photon images at high resolution (1024x1024) of the FOV were acquired. Images were taken at the level of the fibers of the corpus callosum where the Z axis was zeroed and at the level of the hippocapal stratum pyramidale without zoom and at 3x zoom. Functional imaging was then performed in the first session of a longitudinal imaging experiment. During subsequent imaging sessions, the mouse was positioned according to the previously annotated coordinates and the projection of the laser pointer was aligned with the reference position. A wide field image of the FOV was acquired with a basler camera both with a 5x objective and the 16x objective. This images were used to finely re-positioning the FOV, mostly based on the position of the vasculature, which provided clear and stable landmarks. Fine and final re-positioning was obtained using the median projection of short t-series.

3.1.5 Animal habituation

After 7-14 days from surgery, animals were subjected to water restriction and delivered 1 ml of water per day. Mouse weight was monitored on a daily basis to maintain the animal's weight between 80 % and 90 % of the *ad libitum* weight throughout the complete duration of the experiments. A minimum of two sessions of "handling" (i.e. mouse habituation to the experimenter) was performed two days after water scheduling. In subsequent training sessions, mice were then habituated to the VR setup. This was achieved by head-restraining the animals for progressively longer periods (up to 1 hour) in multiple training sessions (one per day). In each training/habituation session, mice were exposed to the noise generated by the two-photon imaging setup (galvanometer scanning noise, shutter noise), even when no imaging was performed. Training in the setup was performed until animals routinely ran along the linear track. On experimental days, mice were head-tethered, and VR session begun after a suitable FOV was identified. 3 to 6 t-series (750 frames/series, $\sim$ 250s), interleaved by 5 minutes breaks, were acquired during $\sim$ 1 hour virtual navigation session. At the end of each imaging session, animals were returned to their home cage.

3.2 Data acquisition and pre-processing

3.2.1 Virtual reality Linear track

A custom virtual reality (VR) setup was design and implemented using Blender, an open source 3D creation suite (blender.org, version 2.78c). VR was rendered with Blender Game Engine and displayed at a video rate of 60 Hz. The VR environment was a linear corridor with lateral walls depicting three different white textures (vertical lines, mesh, and circles) on a black background (see Figure 1.9A). Extremes of the corridor were represented as green walls labeled with a black cross. The corridor was 180 cm long and 9 cm wide. The animal was represented in the VR environment with a spherical avatar of radius 2 cm. To simulate touch-interactions with the environment, a touch sensor represented with a rectangular cuboid of dimensions ($x = 5, y = 1, z = 1cm$) was included, protruding the animals avatar parallel to the corridor floor. The avatar was used to emulate the real dimensions of the animal in the virtual environment and was never visible to him. Practically, when arriving to a location in the track (reward position, the end of the track or any other position) the animal saw that position at a 7 $(5 + 2)$ cm distance. Composite tiling of five thin-bezel led screens were used to project the avatars point of view in the VR environment (220° horizontal, 80° vertical) (see Figure 1.9A). Mice could virtually navigate the environment by running on a custom 3D printed wheel (radius 8 cm, width 9 cm). Motion was captured with an optical rotary encoder (Avago AEDB-9140-A14, Broadcom Inc., San Jose, CA), whose signal was converted into a serial mouse input by a single board microcontroller (Arduino Uno R3, Arduino, Ivrea, Italy). Physical motion performed by the animal and measured by input devices was then mapped with a 1:1 correspondence to the virtual environment. To motivate mice to explore and navigate the virtual corridor, a $\sim 4\mu l$ water reward was delivered when the mouse reached the position $115cm$ along the VR corridor. Rewards were delivered through a custom steel lick-port controlled by a solenoid valve (00431960, Christian Bürkert GmbH & Co., Ingelfingen, DE) and licks were monitored using a capacitive sensor (MTCH102, Microchip Technology Inc., Chandler, AZ). Upon reaching the end of the corridor, animals were teleported back to the beginning of the track and a new trial was started. If instead the mouse failed to reach the end of the track within 120 s, the trial was automatically terminated and the animal teleported to the beginning of the track. After trial termination, either by reaching the end of the track or in terminated runs, a timeout interval of $5s$ was applied before a new trial started. VR rendering and two-photon imaging acquisition were synchronized using the command signal of the x galvanometer.

3.2.2 Motion correction

2-photon microscopy experiments produced t-series consisting of sequential *.tiff* images. All images corresponding to a t-series were first concatenated to produce an *.avi* video with no compression. Motion correction was performed using the *NoRMCorre* algorithm [Pnevmatikakis and Giovannucci, 2017], that corrects non-rigid motion

artifacts by estimating motion vectors with subpixel resolution over a set of overlapping patches within the FOV. These estimates were used to infer a smooth motion field within the FOV for each frame. The inferred motion fields were applied to the original data frames. For *NoRMCorre* correction the following characteristics was used: patch size $(48, 48)$ pixels, maximum overlap of $(24, 24)$ pixels between patches, max rigid shift of $(6, 6)$ pixels, and a maximum relative shift of each patch with respect to rigid shifts of 3 pixels.

Motion correction was applied in two steps, first each t-series was motion corrected individually. Then, all t-series from the same day and same animal were concatenated and motion corrected again. For longitudinal recordings a third step of motion correction was included. After each day was motion corrected, all days belonging to the same FOV were concatenated and motion correction was performed again to maximize the correspondence across days. Motion corrected recordings were finally split again and analyzed separately for each day.

3.3 Video Segmentation

To infer neuronal activity, imaging data were first segmented using the customized algorithm CITE-on (Cell Identification and Trace Extraction online). CITE-on was a convolutional neural network-based algorithm for automatic online cell identification, segmentation, identity tracking, and trace extraction in two-photon calcium imaging data. The off-line cell identification suit was used on the median projection of the full length concatenated recordings. By using the median projection of the full motion corrected concatenated recordings, the amount of detected neurons was maximized. CITE-on implemented an image detector based on the publicly available convolutional neural network (CNN) RetinaNet [Lin et al., 2020]. The output of the CNN image detection was a set of boxes tightly surrounding each detected neuronal soma, from here on called *bounding boxes*. Coordinates and identity of the bounding boxes were saved and used in the following steps. Because the motion correction was performed across t-series and the median projection was calculated on the full-length recording, the coordinates and identities of the bounding boxes were preserved across frames and t-series and did not require any adjustment or tracking across frames. CITE-on required an upscaling factor that depended on the ratio between the FOV surface and the average surface of the neuronal somata. This parameter was optimized to obtain the tightest fit of bounding boxes to cell somatas. in all recordings presented in this work this parameter was set to 0.7.

3.4 Longitudinal tracking

In longitudinal recordings, video segmentation was applied separately for each day, and cell identities were matched *a posteriori*. To compare sets of bounding boxes, we computed the intersection over union (*iou*) for all pairs of boxes. Pairs with $iou > 0.5$

were considered matching identities, if a box from one set satisfied this condition with more than 1 box from the other set, then the pair with the biggest *iou* was considered as matching identities. Matching procedure was applied between the set of bounding boxes from first day of recording and the second and then between the first and third day of recordings. The intersection between both matching sets were the cells that we considered as **tracked**. All cells that had not a matching identity between first and second day and/or first and third day were considered as **non tracked** cells.

3.5 Trace extraction

After cell identification, the following step to infer neuronal activity consisted in extracting functional calcium traces from identified cells. This was achieved using the algorithm CaImAn, a popular state-of-the-art method based on Constrained Non-Negative Matrix Factorization (CNMF) [Giovannucci et al., 2019]. We used the bounding boxes generated offline by CITE-On to build binary masks that were used as seeds to initialize the seeded-CNMF algorithm. Seeded-CNMF calculated first the temporal background component of the recording using pixels that were not included in any mask. This background component was later subtracted from each neuronal factor. It represented the background noise shared across all signals, including the neuropil activity. The seeded-CNMF algorithm then estimated the temporal component and spatial footprint for each bounding box, constrained to be non-zero only at the location where the binary masks were positioned. Parameters for seeded-CNMF were explored and tuned manually. Specifically: the number of global background components was 2; no merging was performed; the expected half size of neurons in pixels was $= (7, 7)$; no spatial or temporal subsampling was performed. Finally, for each component the $\Delta F/F_0$ was computed with the CaImAn **detrend_df_f** function (see Giovannucci et al., 2019), using the 50^{th} quantile as baseline and a 2000 frames running window to compute quantiles. At the end of the trace extraction procedure a spatial footprint and a temporal $\Delta F/F_0$ trace was obtained per bounding box.

The combination of off-line CITE-on and CaImAn presented several advantages for the analysis of our dataset. Off-line CITE-on localized putative neurons considering only anatomical aspect, regardless of their activity profile. CaImAn then refined the segmentation for each binding box and provided denoised calcium traces. Neither deconvolution nor spike inference were used.

3.6 Event detection

For each component obtained after trace extraction, statistically significant calcium events were detected on the $\Delta F/F_0$ traces with a modified implementation of the algorithm described in [D. A. Dombeck, Khabbaz, et al., 2007]. Briefly, the standard deviation σ_1 of the signal was computed and points with absolute value larger than σ_1 were removed from the trace. This procedure automatically excluded large transients.

Then, the standard deviation, σ_2, of the resulting trace was computed. Fluorescence transients were identified as events in the original $\Delta F/F_0$ that:

i) were bigger in absolute value than 3 σ_2

ii) didn't return within 2 σ_2 before 0.5 s [D. A. Dombeck, Khabbaz, et al., 2007].

These criteria were selected to obtain a false discovery rate $< 5\%$. False discovery rate was defined as:

$$FDR = \frac{N_{E_n}}{N_{E_p} + N_{E_n}} \tag{3.1}$$

where N_{E_p} and N_{E_n} were the numbers of identified positive and negative deflections of the $\Delta F/F_0$ trace, respectively. As described in D. A. Dombeck, Khabbaz, et al., 2007, out-of-plane motion would be expected to cause an equal number of positive and negative false fluorescence transients. With this procedure we reduce the number of positive deflection detected as events due to out-of-plane motion, which should be similar in number to the negative ones. An **event trace** could be obtained by setting all fluorescent values from the $\Delta F/F_0$ trace that did not belong to a positive event to 0. We called such trace the *event trace*.

3.7 Place Cell detection

3.7.1 Response profiles and response fields

Only instants in which the animal was running at a speed $> 1cm/s$ were considered for the analysis. The virtual corridor was binned using 81 equally spaced bins and the occupancy map was calculated for each animal. The occupancy map represented the total amount of time spent in each spatial bin. The activity map was then computed for each ROI as the average fluorescence value from the event trace in each spatial bin. Both the activity and the occupancy maps were independently normalized to sum 1 and convolved with a Gaussian kernel with a width of 3 spatial bins. We defined the response profile of a ROI (RP) as the ratio of its activity map over the occupancy map. For each RP, we defined and computed a response field (RF) as follows:

i) we identified all local maxima greater than the 25^{th} percentile of the response profile values $C = (c_0, c_1, ..., c_n)$

ii) we fitted the response profiles as the sum of n parametrized Gaussian functions, with means equal to the elements of C. The amplitude, a_i, and standard deviations, σ_i, were constrained to take values $0 \leq a \leq 1$ and $0 \leq \sigma \leq 90cm$, respectively. The fitting was performed by solving a non-linear least squares problem using the function *curve_fit*, from scipy, `www.scipy.org`). Formally,

$$RP \cong \sum_{c_i \in C} a_i \exp \frac{-(x - c_i)^2}{2\sigma_i^2} \tag{3.2}$$

With the following constrains:

$$\begin{cases} 0 \leq c_i \leq 180 \; \forall \; c_i \in C \\ 0 \leq a_i \leq 1 \; \forall \; a_i \in A \\ 0 \leq \sigma_i \leq 90 \; \forall \; \sigma_i \in S \end{cases} \tag{3.3}$$

iii) the RF was defined as the fitted gaussian with the highest amplitude, and its width as 2 σ_i

$$RF = a_i \exp \frac{-(x - c_i)^2}{2\sigma_i^2} \quad \text{with} \quad i = argmax(A) \tag{3.4}$$

In this way we considered only the main response area of each neuron and, in the case of place cells, the main place field [Turi et al., 2019]. Other properties of neuronal activity such as secondary peaks were not included in the analysis, however no hypothesis was done on the firing profile of the neurons analyzed, meaning that neurons with complex or noisy response profiles were studied by only looking at their main area of response.

3.7.2 Place cells analysis

Only periods in which the animal running speed was $> 1cm/s$ were used to analyze the spatial modulation of neuronal cell activity. We defined spatial modulation based on information theory (see section 1.3.1, Shannon, 1948, Quiroga and Panzeri, 2013). We computed the mutual information between position in the linear track P and the neuronal calcium event trace F using equation 1.6:

$$I(F \; : \; P) = H(F) + H(P) - H(F, P) \tag{3.5}$$

Where H is the Shannon entropy as defined in equation 1.2:

$$H(X) = -\sum_{x \in X} p(x) \; log_2(p(x)) \tag{3.6}$$

Here $X = (x_0, x_1, ..., x_n)$ represented all possible discrete values of either F or P. And $H(F, P)$ is the joint entropy as defined in equation 1.4.

To answer the question of whether a cell carried **significant amount of information** in its calcium activity, we compared the mutual information of that cell with a surrogate distribution of mutual information values. These values were obtained by calculating the mutual information of surrogate traces that were cyclic permutations of the temporally inverted original trace. The permutations were done shifting the traces by a random amount of time bigger than the 5% of the length of the trace and smaller than the 95%. Importantly, this surrogate method preserved many features of the trace,

such as auto-correlation, temporal structure, mean value, etc.., but destroyed the temporal relationship between neuronal activity and position. This procedure was perform 1000 times for each ROI to build the null distribution of mutual information values. A cell whose mutual information value was higher than the 95^{th} percentile of the null distribution was considered a **place cell**.

It is important to note that with this definition, cells with multi-modal, or more complex response profiles could also be detected as place cells. The use of mutual information to detect place cells has been widely used and represents a model free notion of place cell that we preferred to other more post-hoc alternatives, e.g. using width, amplitude, reliability or other properties of response profiles.

3.7.3 Bias correction and parameter selection

As mentioned in the introduction (see section 1.3.1), using an empirical probability distribution as approximation of the true underlying probability distribution produced biased values of mutual information (MI). The contribution of the bias to the MI value strongly depended on how we binned the variables; higher number of bins better described the data but produces bins with less counts and therefore worst estimates of their probabilities. To account for this bias, we first computed the parameter:

$$NsR = log_2(\frac{N_s}{R}) \tag{3.7}$$

with N_s being the average number of counts in position bins, and R the number of stimulus bins (that is the amount of steps in which we binned calcium intensities). NsR gave a quantitative measure of how well we could estimate the probability distributions: the larger it is, the smaller the bias. We considered $NsR = 3$ as a conservative threshold, above which the description quality was good. For each recording, we calculated NsR for different number of intensity bins ($r_{bins} = [2, 3, 4, 5, 8, 10, 20]$) and position bins ($s_{bins} = [4, 8, 12, 16, 20, 24, 40, 60, 80, 100, 160]$). We then calculated the contribution of the bias for each ROI as the mean of the null distribution, that is, the mean of the MI values calculated between position and surrogate responses obtained by shuffling as described in the previous section. The **unbiased value of MI** was thus defined as the MI value calculated as in equation 3.5 minus the bias:

$$MI_{unbiased} = I(F\ :\ P) - \langle I(F_s\ :\ P)\rangle_{surrogates} \tag{3.8}$$

We calculated the average unbiased MI value across ROIs for each combination of numbers of intensity and position bins and their standard deviation. We then split these averages in place cells and non-place cells. By doing so, we studied the contribution of the bias as a function of the binning of the variables. Higher contribution of the bias decreased the value of the unbiased MI. At the same time, we expected that if the bias was correctly subtracted, the non place cells had unbiased MI values close to zero, while place cells had positive MI values. We therefore selected the appropriate combination

of space and intensity binning as that with the highest number of bins which had a $NsR > 3$ and which maximized the unbiased MI. This procedure allowed comparison of MI values across recordings, experimental conditions, and ROIs. We performed all the aforementioned steps for two binning procedures for space: *i*) uniform width bins; *ii*) uniform count bins yielding a uniform distribution of space occupancy. This last computational step served as a control for the consistency of the unbiased MI values across binning procedures.

3.8 Statistical testing

To compare distributions we first performed normality tests and, when negative, the non parametric test Mann-Whitney U was used for independent samples. For related paired samples we used the Wilcoxon signed-rank test. All test were implemented with the Scipy [`www.scipy.org`] ecosystem for python.

The question whether CNO application had an effect on information content in place cells involved comparisons across conditions for different animals and with different numbers of cells for each recording. The contribution of animal variability could in principle mask the statistical significance of the condition effect, and the difference in counts broke the symmetry needed for some standard statistical tests. For these reason, to explore the difference in the information content of cells in both conditions, but excluding the animal variability, we used a Linear Mixed Effects Model (LMEM) with treatment (CNO or Saline injection) as the fixed effect, and animal (or FOV depending on the experimental paradigm) as the random effect. LMEM was fitted using the *lme4* and *lmerTest* and *car* libraries from **R** [R Core Team, 2017]. We compare two models described as follows:

$$MI \sim treatment + (1|animal) \tag{3.9}$$

$$MI \sim treatment + (1 + treatment|animal) \tag{3.10}$$

Equation 3.9 represents a model with one fixed effect and a random intercept for the animal. Equation 3.10 adds a random slope to the previous model. To compare both models, an ANOVA test was performed. If the more complex model described significantly more variance, then model 3.10 was used. If, on the other hand, there was no significant difference across models, the simpler one (3.9) was preferred. After fitting the model, statistical significance of the fixed effect was tested using a Type II Wald chi-square tests implemented as in the *car::Anova* function.

Chapter 4

Results

4.1 Pharmacogenetic manipulation of astrocytic calcium activity in vivo

In this thesis, we developed an analysis pipeline to investigate the effects of the manipulation of astrocytic calcium signals on neuronal spatial information encoding. Astrocytic calcium signals were manipulated by pharmacogenetic intervention using designer receptors exclusively activated by designer drugs (DREADD) technology [B. L. Roth, 2016; B. Armbruster and B. Roth, 2005; B. N. Armbruster et al., 2007]. DREADDs (Figure 4.1) perform signal transduction upon binding with their specific designer drugs. The DREADD receptor agonist is clozapine-n-oxyde (CNO), which is an endogenous product of the oxidative metabolism of clozapine. Upon binding, DREADDs activate

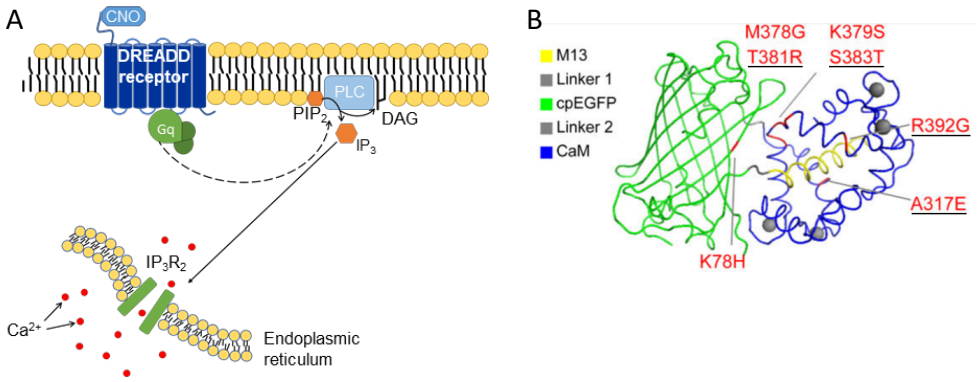

Figure 4.1: Tools used to manipulate and visualize astrocytic calcium signaling. A) DREADDs (designer receptors exclusively activated by designer drugs) are engineered GPCRs that can be activated by inert chemicals and not by endogenous ligands. We used the hM3Dq-receptor moiety, which is designed to bind CNO, mediating the activation of the Gq GPCR pathway. In astrocytes, this pathway activates the signaling cascade of inositol 1,4,5-trisphosphate receptor (IP3R), mediating Ca^{2+} release from the endoplasmic reticulum (ER). B) GCaMP6f is a fast variant of the GCAMP family of genetically encoded calcium indicators (adapted from T.-W. Chen et al., 2013) (Kd 375 nM). To investigate calcium dynamics either in astrocytes or neurons, we relied on cell-specific promoters and optimized rAAV tropism (see methods 3.1.2).

G-protein coupled receptor (GPCR) signaling pathways (Figure 4.1). DREADDs were generated in two classes to selectively manipulate either the Gq or Gi intracellular pathway. We selected the hM3Dq version of the DREADD receptor because it allowed specific action on the Gq pathway. This manipulation was previously shown to promote calcium elevations in astrocytes [Mu, Bennett, Rubinov, Narayan, C. T. Yang, et al., 2019; Adamsky et al., 2018]. Throughout this thesis, hM3Dq activation was mediated via intraperitoneal injection of CNO (see methods 3.1.2). In both astrocytes and neurons (see methods 3.1.2) calcium activity was monitored using the fast genetically encoded calcium indicator GCaMP6f (Figure 4.1B).

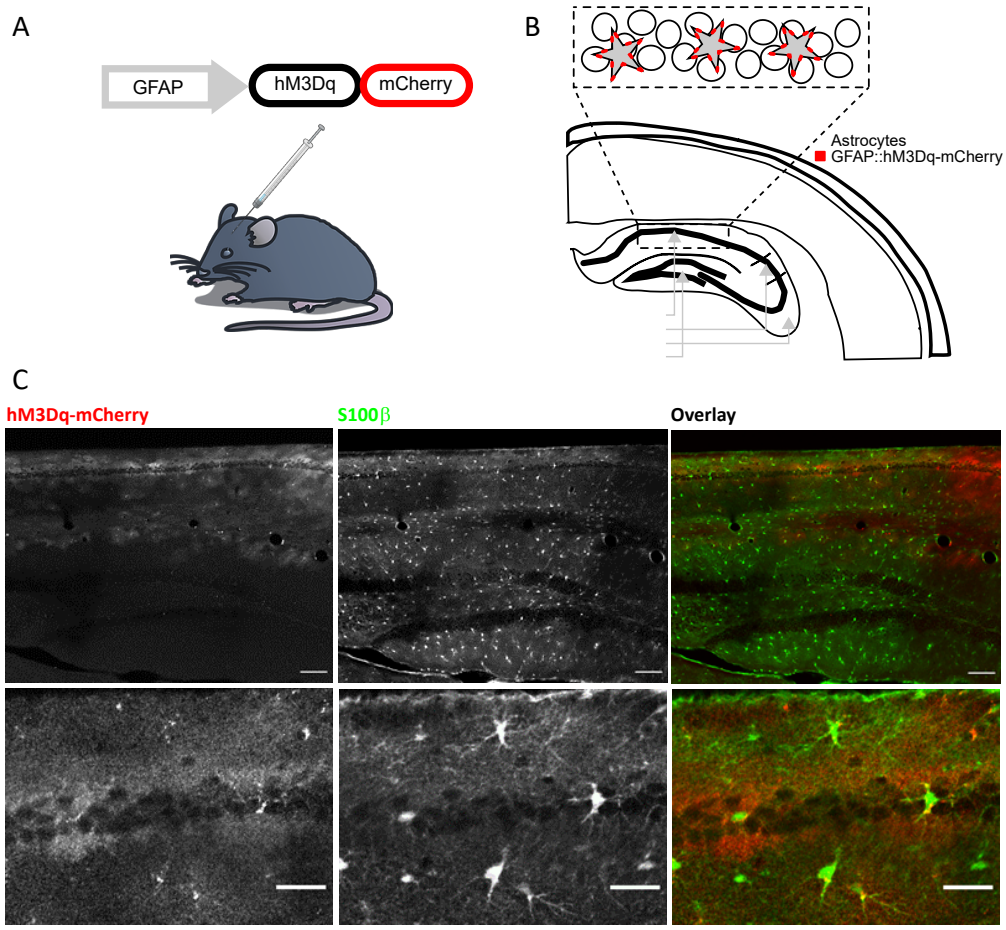

Figure 4.2: Viral strategy to perform temporally restricted pharmacogenetic perturbation of astrocytic calcium signaling. A) Adult mice were injected with serotype 5 rAAV encoding for the fusion construct hM3Dq-mCherry under the control of the astrocyte-specific promoter GFAP. Injection was performed using stereotaxic coordinates to target the right hippocampus. B) Schematic of virally transduced astrocytes in hippocampal CA1 area. C) Confocal micrographs of CA1 area of mice expressing hM3Dq-mCherry construct. Astroglia was immunolabeled with the astrocyte-specific marker $S100\beta$. Top: low magnification micrographs highlighting infection diffusion (scale $= 100\ \mu m$). Bottom: high magnification micrographs show that the expression of hM3Dq-mCherry construct is restricted to astrocytic cell membrane (scale $= 30\ \mu m$).

We used recombinant adeno-associated viral particles (rAAV) to deliver a DREADD-hM3Dq-mCherry fusion construct (hM3Dq-mCherry) into astrocytes. The construct was under the control of the astrocyte-specific promoter GFAP (Figure 4.2A), and rAAV particles were pseudotyped with serotype-5 capsid proteins to improve astrocytic tropism. Viral delivery was performed via stereotaxic injection into the CA1 area of the right

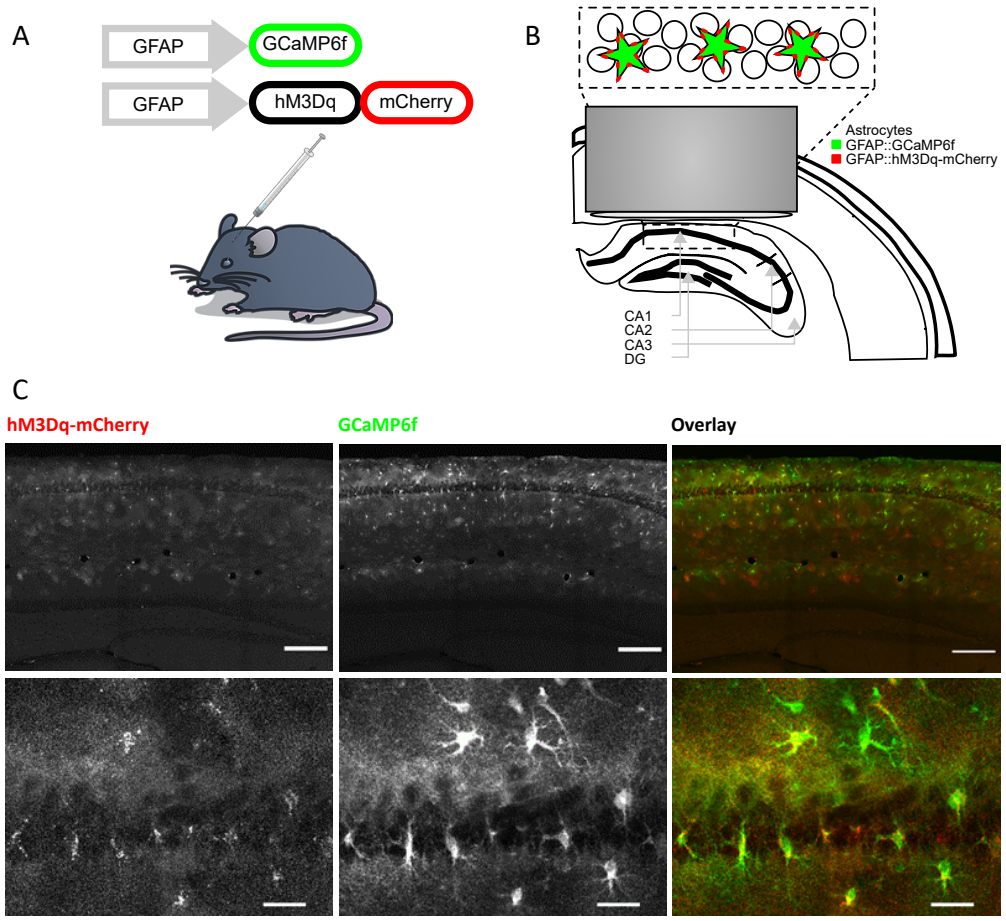

Figure 4.3: Viral strategy to investigate astrocytic calcium signaling upon pharmacogenetic intervention. A) Adult mice were injected with two serotype 5 rAAV. One vector encoded for the genetically encoded calcium indicator GCaMP6f. The second vector encoded for the fusion construct hM3Dq-mCherry. Both constructs were under the control of the astrocyte-specific promoter GFAP. Injection was performed using stereotaxic coordinates to target the right hippocampus. B) Schematic of the chronic optical access to hippocampal CA1 area. Optical access was granted by the implant of a chornic hippocampal imaging window above CA1 area. C) Confocal micrographs of CA1 area of mice transduced with GFAP::GCaMP6f and GFAP::hM3Dq-mCherry rAAVs. Images show astrocytes-specific co-expression of the two viral constructs in large volumes of hippocampal CA1 area. Top: low magnification micrographs highlighting infection diffusion (scale $= 200\ \mu m$). Bottom: high magnification micrographs showing in detail that the vast majority of astrocytes expressed simultaneously hM3Dq-mCherry fusion protein and GCaMP6f indicator (scale $= 30\ \mu m$).

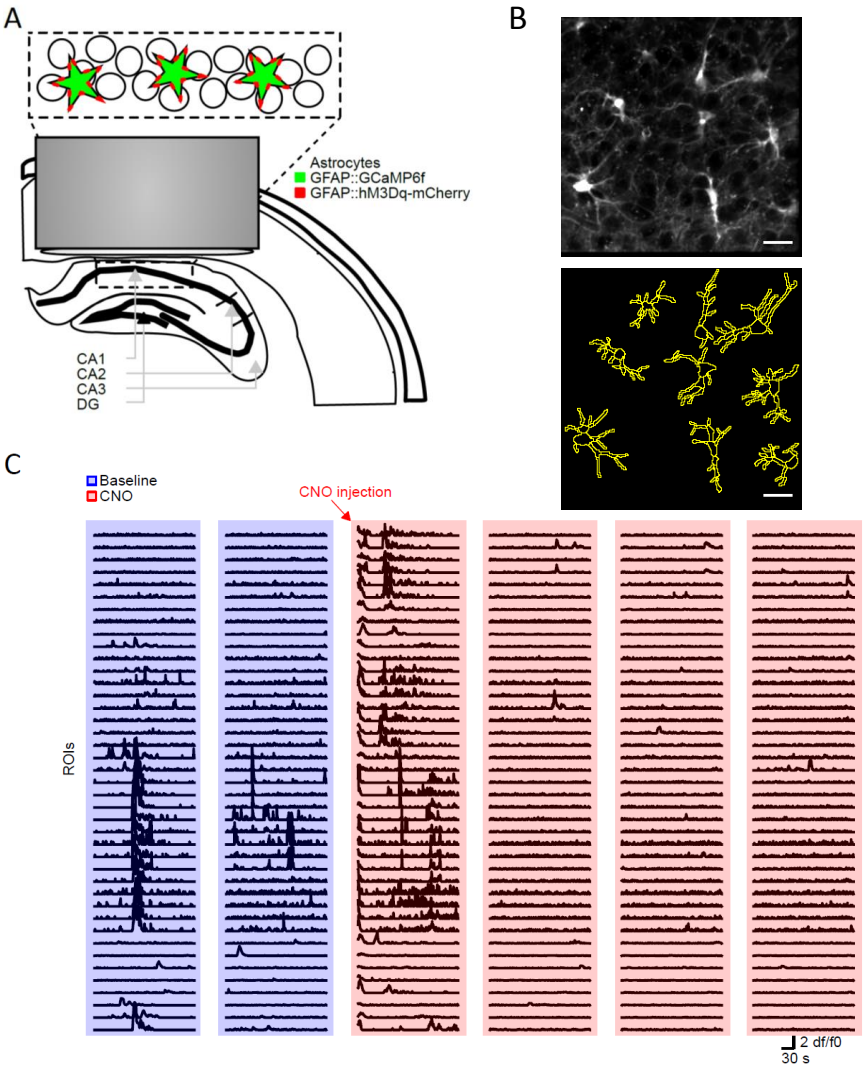

Figure 4.4: In vivo two-photon calcium imaging of CA1 astrocytes during pharmacogenetic intervention. A) Schematic of the optical preparation to perform two-photon calcium imaging in astrocytes expressing the genetically encoded calcium indicator GCaMP6f and the pharmacogenetic actuator hM3Dq. B) Temporal median projection of a sample field of view (top, scale 30 μm, field of view size approx $(160\ \mu m)^2$). Astrocytic regions of interest (ROIs) have been manually selected on the median projection according to anatomical structures (bottom). C) Representative calcium traces for 40 out of 135 ROIs shown in panel B. We performed six·248s temporal serieses interleaved by 300s intervals. Blue shaded areas indicate baseline spontaneous activity. CNO was administered intraperitoneally few seconds before starting the third temporal series (red arrow). Red shaded areas indicate recordings under putative activation of hM3Dq-receptor. CNO administration resulted in a sudden increase of calcium activity (third temporal series), followed by a phase in which astrocytes decreased their calcium dynamics (fourth to sixth temporal series).

hippocampus (Figure 4.2B). This strategy resulted in the vast majority of CA1 astrocytes expressing the hM3Dq fusion construct, as verified by immunolabeling with the

astrocyte specific marker $S100\beta$ (Figure 4.2C). Importantly, within the virally transduced region, hM3Dq expression was limited to the astrocytic outer membranes (Figure 4.2C).

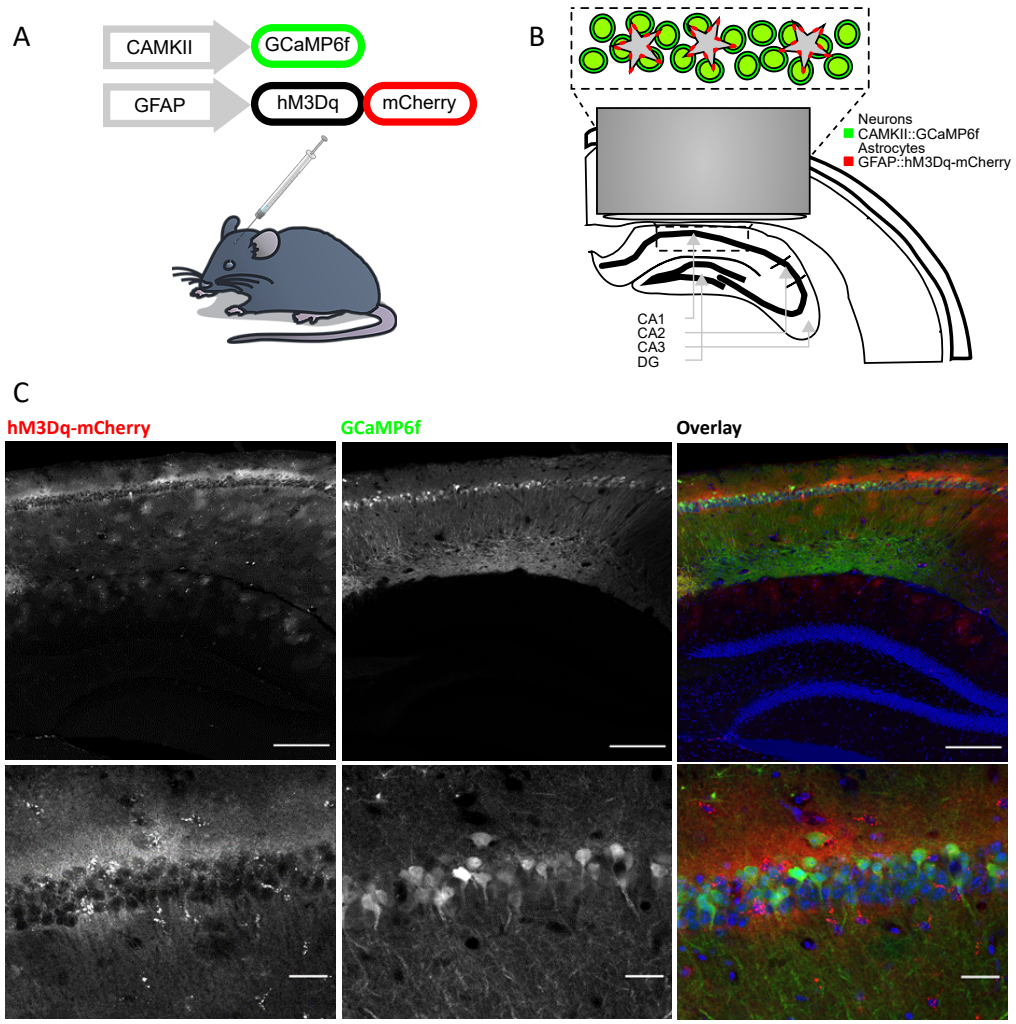

Figure 4.5: Viral strategy to investigate neuronal calcium signaling under pharmacogenetic manipulation of astrocytic calcium signaling. A) Adult mice were injected with two viral vectors: i) one vector encoded for the genetically encoded calcium indicator GCaMP6f under the control of the neuronal specific promoter CAMKII; ii) serotype 5 rAAV encoding for the fusion construct hM3Dq-mCherry. Injection was performed using stereotaxic coordinates to target the right hippocampus. B) Schematic of the chronic optical access to hippocampal CA1 area. Optical access was granted by the implant of a chornic hippocampal imaging window above CA1 area. C) Confocal micrographs of CA1 area of mice transduced with CAMKII::GCaMP6f and GFAP::hM3Dq-mCherry rAAVs. Images show astrocytes-specific expression of hM3Dq-mCherry fusion construct and neuronal specific expression of GCaMP6f. Infection spread in large volumes of hippocampal CA1 area. Top: low magnification micrographs highlighting infection diffusion (scale = 200 μm). Bottom: high magnification micrographs showing in detail astrocytic expression of hM3Dq-mCherry fusion protein and neuronal specific expression of GCaMP6f indicator (scale = 30 μm).

To validate the effects of hM3Dq activation in vivo, we simultaneously labeled astrocytes with GCaMP6f and hM3Dq-mCherry. Coexpression was obtained by coinjection of two viral constructs under the control of the GFAP promoter and packaging in pseudotyped type-5 viral particles (Figure 4.3A-B). Under these conditions, coinfection was optimal, and it resulted in most hM3Dq-mCherry-expressing astrocytes being colabeled with GCaMP6f (Figure 4.3C).

We performed in vivo 2-photon calcium imaging in animals coexpressing hM3Dq and GCaMP6f. Optical access to the CA1 area of the hippocampus was obtained through a chronic hippocampal window [D. A. Dombeck, Harvey, et al., 2010] (Figure 4.4B). In anesthetized mice, we recorded the astrocytic calcium activity, which was characterized by heterogeneous dynamic signals involving astrocytic somata and processes (Figure 4.4C). We observed that CNO administration resulted in a sudden and synchronous increase in GCaMP6f fluorescence in astrocytes at the beginning of CNO application. This GCaMP6f signal increase was followed by a prolonged phase in which astrocytes showed decreased calcium dynamics (Figure 4.4C).

We used a viral delivery strategy to investigate the effects of the perturbation of astrocytic calcium dynamics on spatial information encoding in hippocampal neuronal cells. To monitor neuronal activity, we used a viral construct under the control of the CAMKII-promoter to express GCaMP6f in CA1 neurons (Figure 4.5A). CA1 astrocytes expressed hM3Dq-mCherry under the control of the GFAP promoter (Figure 4.5A). Within the virally transduced region, we reliably obtained GCaMP6f-labeled neurons and hM3Dq-mCherry-labeled astrocytes (Figure 4.5C).

4.2 Imaging neuronal place cells during pharmacogenetic manipulation of astrocytes in vivo: nonlongitudinal recordings

To investigate the effects of the perturbation of astrocytic calcium dynamics on spatial information encoding in hippocampal neuronal cells, we trained head-tethered mice to navigate in a unidirectional virtual environment while we performed two-photon functional imaging of neuronal cells (Figure 4.6, Saleem, Diamanti, et al., 2018). We combined astrocyte-specific expression of hM3Dq and neuronal-specific expression of the genetically encoded calcium indicator GCaMP6f (Figure 4.7A) to capture hippocampal CA1 neuron activity.

To extract the calcium activity traces of neurons in CA1, we first computed the median temporal projection of the field of view on motion-corrected two-photon calcium imaging t-series (Figure 4.8A top). We used CITE-on (see methods 3.3 and appendix B), which is a deep learning-based algorithm for fast segmentation of neurons in two-photon imaging data (see appendix B), to detect neuronal cells in the median projections, obtaining rectangular regions of interest (bounding boxes) tightly surrounding

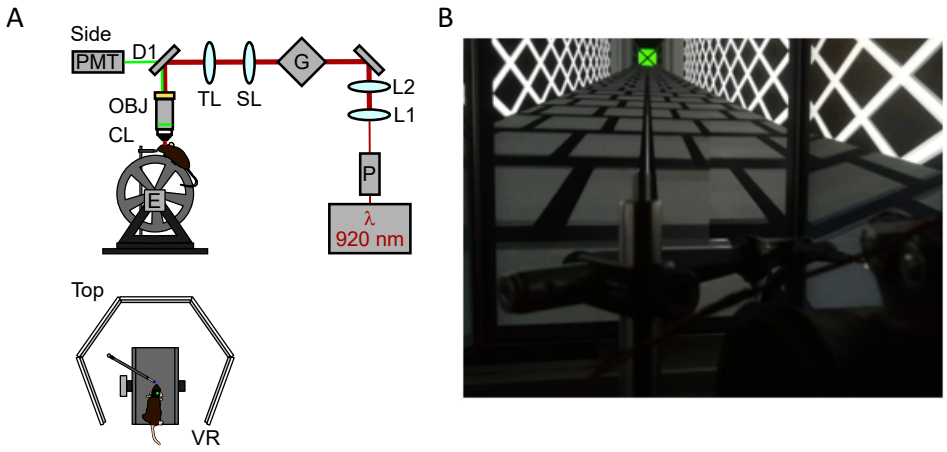

Figure 4.6: Two photon functional imaging during virtual spatial navigation. A) Schematic of virtual reality and imaging setup. Mice run along a virtual corridor provided with visual features (B), at the end of each run they get teleported back to the beginning of the track. B) Sample of mouse visuals from the beginning of the linear track.

putative neuronal somas (Figure 4.8A bottom). To perform segmentation on bounding boxes, we used a spatially confined version of the nonnegative matrix factorization algorithm (seeded-CaImAn, Giovannucci et al., 2019). Seeded-CaImAn was initialized on each bounding box, yielding precise segmentation of the putative neuronal source and its respective calcium activity trace. For each calcium trace, $\Delta F/F_0$ was computed

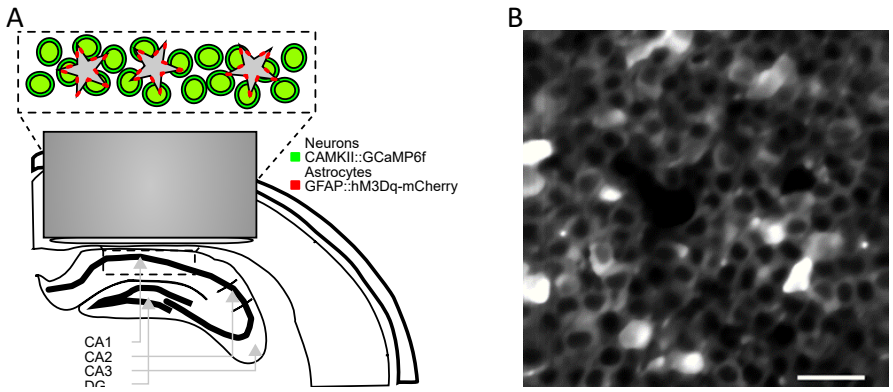

Figure 4.7: In vivo two-photon calcium imaging of CA1 neurons and pharmacogenetic astrocytic manipulation during virtual navigation. A) Schematic of the optical preparation to perform two-photon calcium imaging in CA1 neurons labeled with the genetically encoded calcium indicator GCaMP6f while astrocytic activity was manipulated using the pharmacogenetic actuator hM3Dq. B) Temporal median projection of a sample field of view (scale = 30 μm, field of view size approx $(160\ \mu m)^2$).

(Figure 4.8B top), and calcium events were detected with a threshold criterion based on

the $\Delta F/F_0$ trace (see Methods 3.6). To build the *event trace*, all time instants that did not belong to an event were set to zero. Calcium events corresponded to above-threshold calcium transients generated by putative neuronal spikes (Figure 4.8B zoom-in).

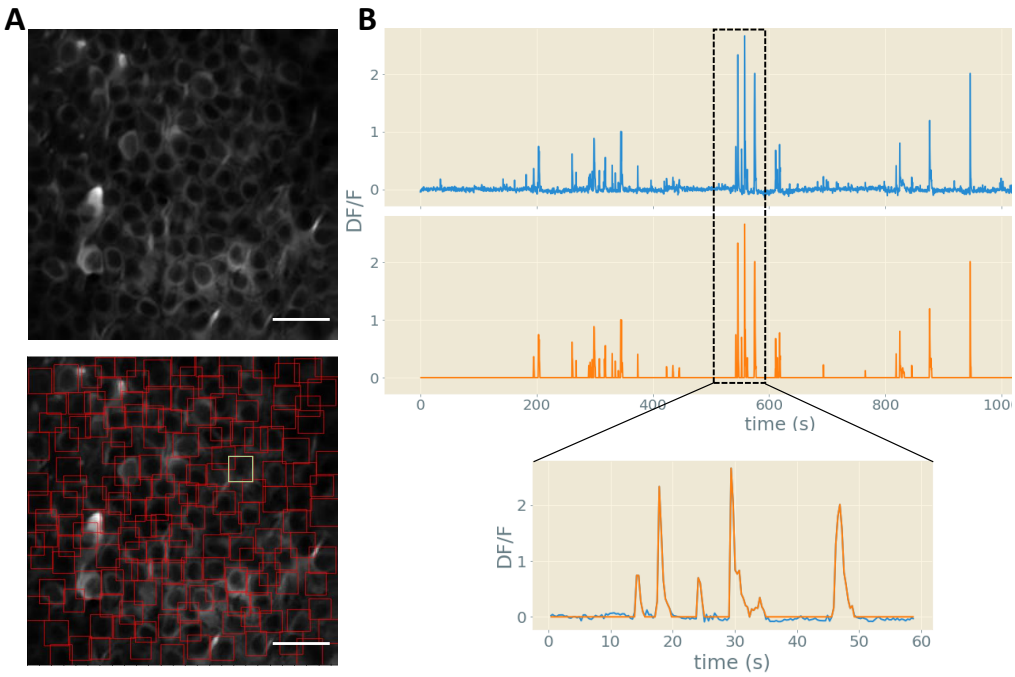

Figure 4.8: Segmentation and trace extraction of 2-photon imaging data. A) Median projection of a representative recording of CA1 neurons (top) and the detected boxes segmented with CITE-on in red (bottom) (scale 30 μm, field of view size approx $(160\ \mu m)^2$). B) Representative $\Delta F/F_0$ trace extracted using seeded-CaImAn in blue, and the event trace in orange. A zoom of one minute of recording is shown in the bottom panel. The trace corresponds to the green box in bottom panel A.

To study how neuronal activity is related to the animal position, calcium traces from neuronal populations were analyzed in the context of mice running in a 1-dimensional virtual corridor (or linear track). $\Delta F/F_0$ traces were averaged across trials (runs in the linear track) to obtain the average calcium intensity as a function of position in the track, which is hereafter termed the *response profile*. Response profiles were modeled as a sum of gaussians with different centers, widths (or sigmas), and amplitudes (see methods 3.7.1). For each response profile, we considered the gaussian component with the highest amplitude as the *response field* (RF). Intuitively, this is the fraction of the linear track in which each cell showed the highest average activity. Five representative response profiles are shown in Figure 4.9, together with the corresponding response field functions (gray dashed lines) and response field *widths* (gray shadowed areas). Modeling, fitting, and estimation of the centers and widths of response profiles were performed for all detected regions of interest.

We studied how neuronal activity is related to the animal position in the linear track as a function of the pharmacogenetic perturbation of astrocytic calcium activity.

In detail, 20 recordings from 7 animals were analyzed. Animals received an intraperitoneal injection of either saline solution (control; $n = 10$) or clozapine-n-oxyde (CNO; $n = 10$). Saline or CNO injection experiments were performed in different days. After injection, animals were positioned under the two-photon microscope and imaging started 30 minutes after injection. Experimental timeline was defined as in Adamsky et al., 2018. In this first dataset, imaging was performed in different field of view for each condition. This meant that the same cell could not be monitored across conditions (nonlongitudinal recordings). 3 to 6 t-series (750 frames/series, $\sim$ 250s), interleaved by 5 minutes breaks, were acquired during $\sim$ 1 hour virtual navigation session. One recording of each treatment (CNO or saline) was analyzed for each animal, with the exception of animal *0001* (2 recordings for each condition) and animal *0002* (3 recordings for each condition). On average, 109 cells were detected *per* FOV (min 50; max 165), resulting in a total of 2193 cells studied. Further imaging sessions were performed in all animals, but they were discarded due to technical issues (e.g., large movement artifacts).

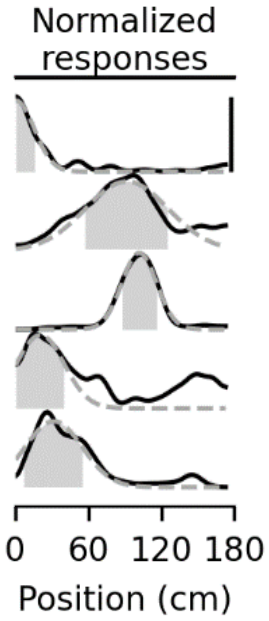

Figure 4.9: Place field estimation. Representative examples of the normalized response profiles of five cells (black line) with their gaussian fit (dotted gray lines) to estimate place fields. The gray-shadowed areas show the width of the place fields, which is defined as $\mu \pm \sigma$, with μ and σ being the mean and standard deviation of the fit, respectively. Vertical scale bar = 1

We then applied an information theory approach (see introduction) to compute the amount of spatial information contained in each identified neuron. More specifically, we computed the Shannon entropy (eq. 1.2 of the introduction) and then the mutual information (eq. 1.7 of the introduction) about the spatial variable contained in the calcium signal extracted from each identified neuron. To correct for biases in MI values, we first computed the NsR parameter (eq. 3.7) for all recordings as a function of the number of response (calcium activity) and stimulus (position) bins (Figure 4.10A). Note that NsR parameter depends only on spatial occupancy map and binning choice and not in cell activity, therefore it has to be computed once for each experimental session (and not for each cell). $NsR = 3$ was considered a threshold above which description

of the variables with respect to the number of trials was acceptable (red squares). We then computed average mutual information values for different binning of response and stimulus (Figure 4.10B). Without bias correction values of mutual information increased with higher number of bins in both variables. We then calculated the contribution of the bias computed as described in section 3.7.3 of the methods (Figure 4.10C). As expected, the bias increased with higher number of bins, which was represented in the raw mutual information values. We calculated the average mutual information values after bias subtraction (eq. 3.8) for different configurations of binning (Figure 4.10D). Bias-corrected mutual information values initially increased, then plateaued, and finally decreased with the number of spatial bins (Figure 4.10D). In those cases, the bias term highly contributed to the mutual information value, and its subtraction resulted in a strong decrease in the bias-corrected MI values, which, in turn, was observed as a negative change in the slope of the curves. For each ROI and each binning combination, we calculated whether the amount of spatial information was significant by comparing the mutual information of that cell with a surrogate distribution of mutual information values (see methods 3.7.2). Separating the bias-corrected MI values

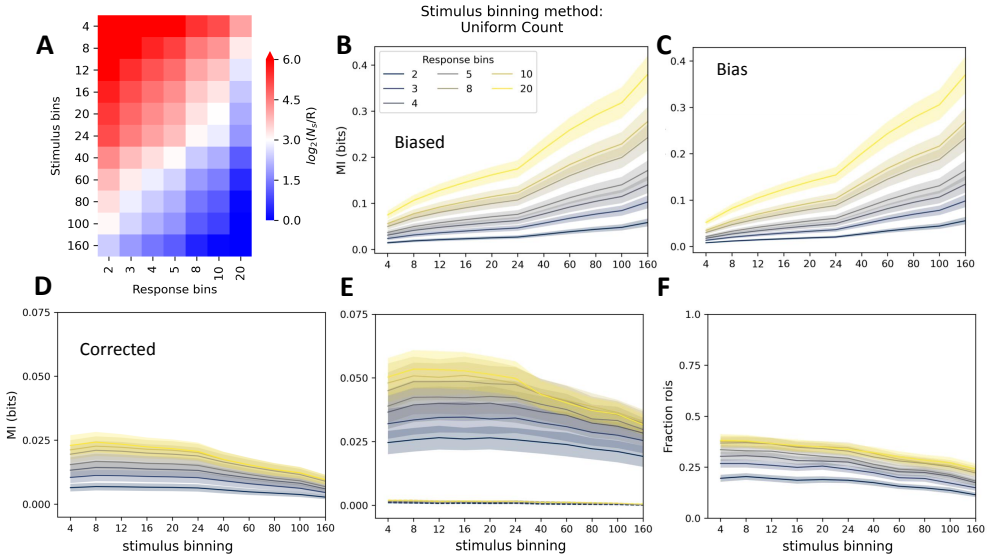

Figure 4.10: Bias correction and binning selection for mutual information calculation. A) Matrix of $log(N_sR)$ parameter values averaged across FOVs for different response and stimulus binning. $log(N_sR) = 3$ was considered an adequate quality threshold. B) Across ROIs average MI values before bias correction as a function of spatial binning, each line corresponds to a different response binning. C) Average contribution of the bias in MI values in (B) calculated as described in methods 3.7.3, colors and axis as in (B). D) Across ROIs average bias-corrected MI values as a function of spatial binning, colors as in (B). E) Bias corrected MI values as in (D) separated in cells with significant information content (filled lines) and without (dotted lines). F) Fraction of ROIs with significant information content as a function of binning as in (B).

for ROIs with significant information content from those without implies a clear split in the bias-corrected MI values (Figure 4.10E), with non-place cells having distributions

close to zero. Finally, we calculated the average fractions of significant ROIs as a function of binning (Figure 4.10F). Plots 4.10A,D,E and F were performed and inspected separately for each dataset, and appropriate binning was selected such that the level of description was as high as possible (higher number of bins) while having $SnR > 3$ and maximized bias corrected MI values (before the change in slope). The same selected binning parameters where used for all recordings and all FOVs from the same dataset.

After appropriate selection of response and stimulus binning, we calculated, for each neuron, whether the amount of spatial information was significant by comparing the mutual information of that cell with a surrogate distribution of mutual information values (see methods 3.7.2). In figure 4.11, we show the normalized calcium responses of all neurons with significant information content about space (see methods 3.7.2) ordered according to the position of the center of the response field in increasing order. The left panel shows recordings after saline injection, and the right panel shows recordings after CNO injection (193 and 261 informative ROIs out of 1192 and 1001 total, respectively). In both cases, the place field of neurons spans the whole virtual corridor, allowing for complete mapping of the space, regardless of treatment. In the case of place cells, the centers μ and widths σ of the principal gaussian component had a straightforward interpretation as the center and width of the **principal** place field. For cells without significant information content about space, the μ and σ parameters give us information about where the cells responded maximally on average and how spread out the response was in space (Figure 4.9). This information is relevant when trying to uncover the effects of alterations in calcium activity in astrocytes on neuronal networks in the hippocampus beyond place cell encoding.

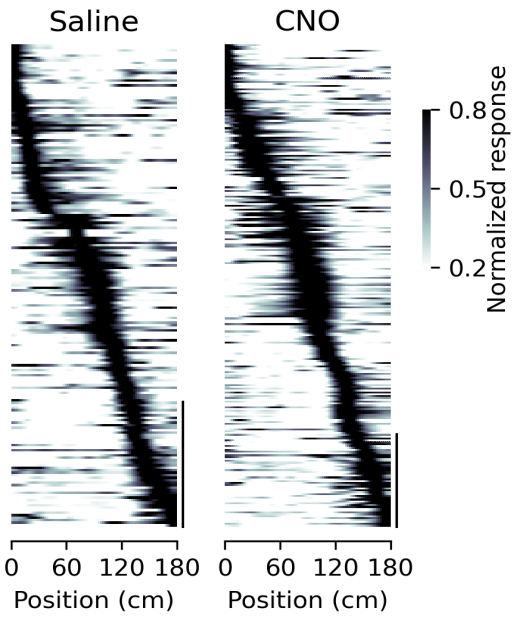

Figure 4.11: Normalized calcium responses as a function of position for neurons that contain significant amount of spatial information. Left panel, responses from recordings in which the animal was injected with saline solution (n = 193 informative ROIs out of 1192 total ROIs, 10 imaging sessions from 7 animals). Right panel, responses from recordings in which the animal was injected with CNO solution (n = 261 informative ROIs out of 1001 total ROIs, 10 imaging sessions from 7 animals). Responses are ordered according to the position of the center of the response field (from minimum to maximum). As described in the results, the FOV which was imaged in the saline condition was different from the one recorded in the CNO condition (nonlongitudinal recordings).

To study the effect of CNO injection on the information content about animal position in CA1 neuronal calcium activity, we calculated and compare the bias-corrected

MI distributions for all cells, that is, considering also non-place cells (Figure 4.12), and for place cell only populations (Figure 4.15), in each condition. In the first case (Figure 4.12) we first compared the distribution of MI values after saline or CNO injection for each animal. Boxplots and statistical testing are reported in each of the 7 panels. Here, both place cells and nonspatial encoding cells are pooled together; thus, the distributions are centered close to zero and heavy tailed towards positive values. To obtain a better sense of the the impact of the manipulation, we normalized the MI values to the maximal amount of MI possibly conveyable by the neurons, that is, dividing the MI values by the smallest between the stimulus and response entropies:

$$MI_{norm} = \frac{MI_{unbiased}}{\min(H(F), H(P))} \tag{4.1}$$

And performed the same comparisons (Figure 4.13). Tendencies and statistical significance for each animal are analogous to those without normalization (Figure 4.12). All future comparisons between MI values were performed separately after normalization and general tendencies were maintained (data not shown). Although not all

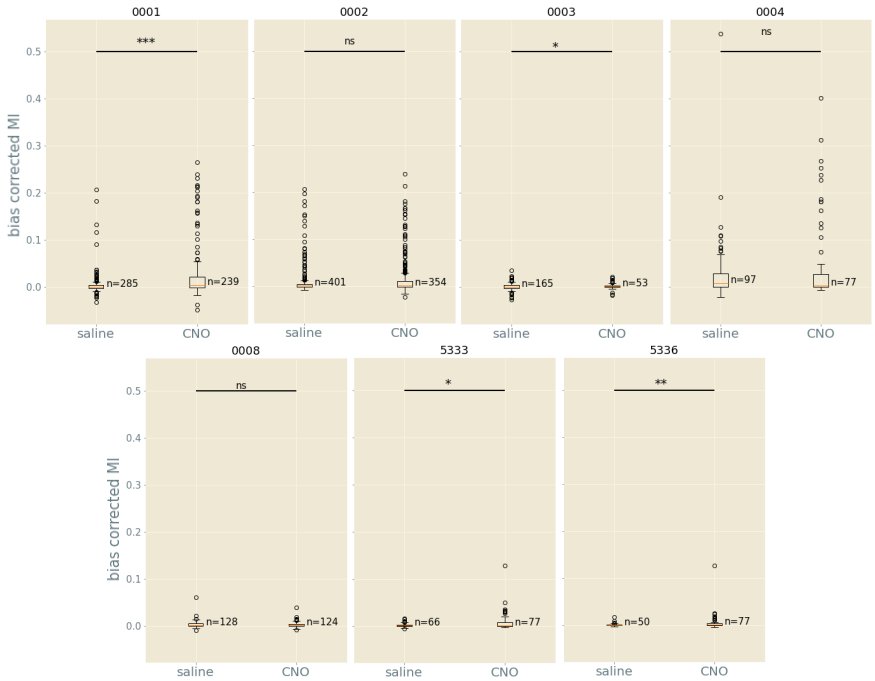

Figure 4.12: Difference in information content about animals position in neuronal cells after CNO application for each animal. Box plots of bias corrected MI values for each animal (each panel represents an animal) after saline or CNO injection. Not all animals have significantly different information content, and there's heterogeneity in the overall trends for each animal, in 4 out of 6 animals cells increase their mean information content.

animals had significantly different MI distributions (Mann-Whitney U test was performed in each case), when comparing averages across animals, we observed a significant increase in information content in experiments following CNO injection for bias

corrected values (Wilcoxon paired test, $p = 0.028$, Figure 4.14 left panel), normalized values (Wilcoxon paired test, $p = 0.028$, Figure 4.14 right panel) and for the percentage of variation (Wilcoxon paired test, $p = 0.028$, Figure 4.14 middle panel).

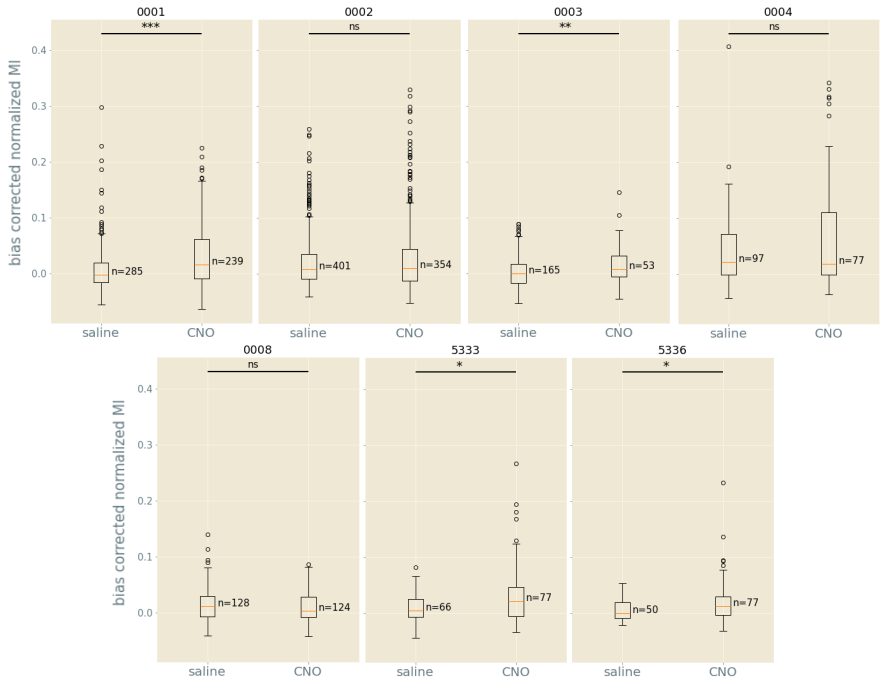

Figure 4.13: Tendencies in information content difference after CNO application for each animal persist when normalizing MI values. Box plots of bias corrected normalized MI values for each animal (each panel represents an animal) after saline or CNO injection. Tendencies and significance in treatment differences are maintained for all animals after normalization of MI values.

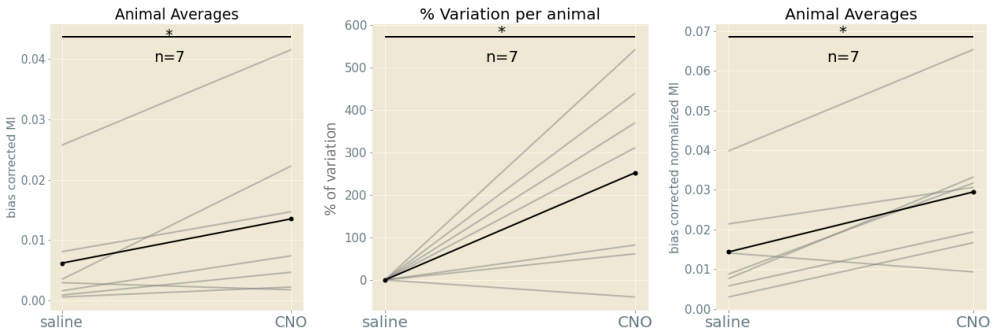

Figure 4.14: Higher information content about animals position in neuronal cells after CNO application. Not all animals have significantly different information content, but they do when averaged together (left panel, Wilcoxon paired test, $p = 0.028$). To get a better sense of the impact of the manipulation we computed the percentage of variation per animal in CNO compared to saline condition (middle panel, Wilcoxon paired test, $p = 0.028$). The increase of MI was still significant when comparing average normalized mutual information (right panel, $p = 0.028$).

Variability between data from different animals could bring differences across distributions that might mask the effect of CNO treatment. To account for this effect, we used a linear mixed effect (LME) model, taking the treatment (CNO or saline injection) as a fixed effect and the animal identity as a random effect (see methods 3.8). In each case, we compared 2 models-one with a random intercept (LME1, eq. 3.9) and another with a random intercept and a random slope (LME2, eq. 3.10). If the model that included the random slope explained significantly more variance, then this model was preferred (ANOVA test for model comparison). If, in contrast, the models were not significantly different, the simpler test was used. When comparing all cells from all animals, the LME2 model was used (LME2 explained significantly more variance than did LME1, using ANOVA for model comparison, $p = 6 \cdot 10^{-4}$). The fitted slope of the LME2 model was -0.01 (negative values implied a decrease in information for saline conditions), and the effect of the treatment was found to be statistically significant (Type II Wald chi-square tests, $p = 0.005$).

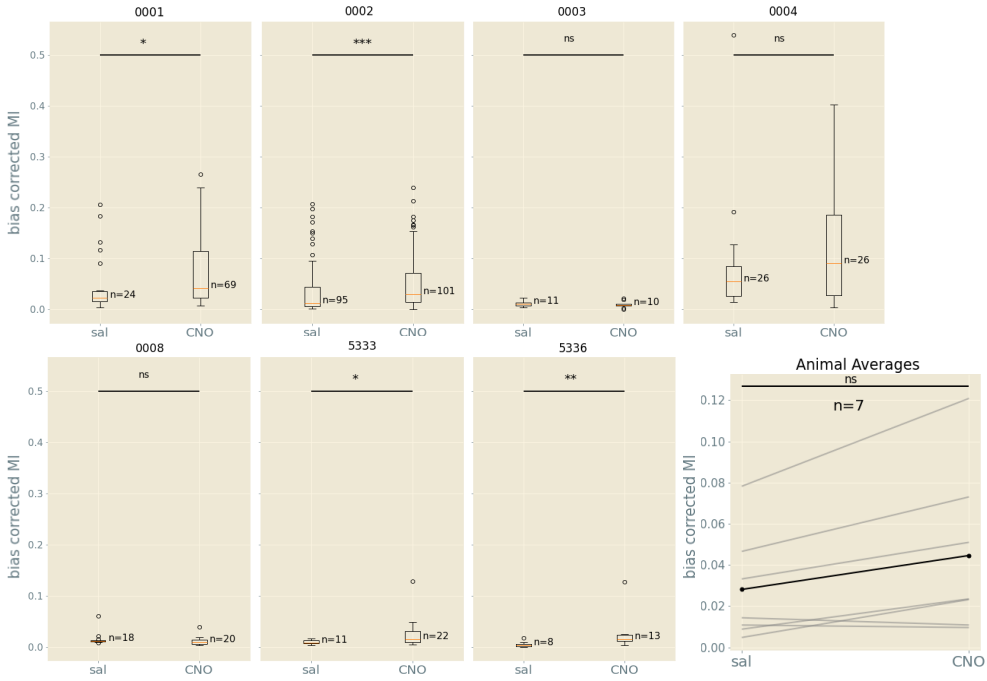

Figure 4.15: Difference in information content about animals position in place cells after CNO application. Box plots of bias corrected MI values for each animal (each panel represents an animal) after saline or CNO injection for place cells populations. Not all animals have significantly different information content, when averaged together there is an increase tendency close to significance (bottom right panel, Wilcoxon paired test, $p = 0.063$, but see main text for LMEM statistical testing).

Because place cells contributed the most to the information content about the animal position, we asked whether changes in MI values were observed when comparing CNO and saline conditions and when only place cells were considered (Figure 4.15). We fitted LME1 considering only place cells (note that this is a test on a subsample of

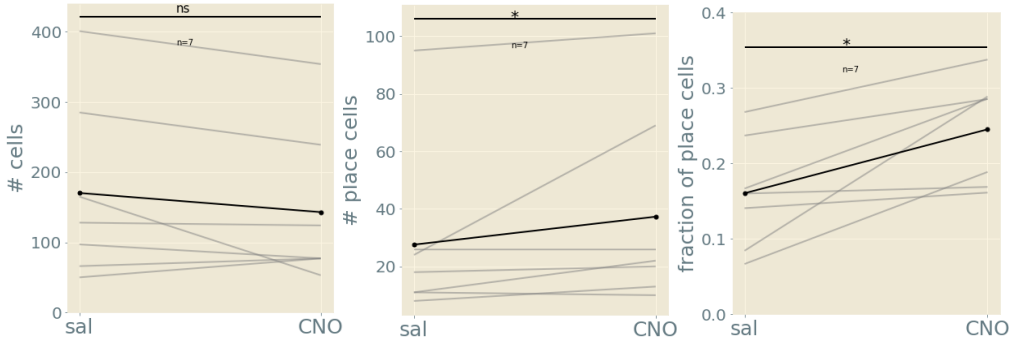

Figure 4.16: Increased number of place cells after CNO injection. The number of cells segmented per animal was not significantly different between conditions (Left panel, Wilcoxon paired test $p = 0.18$). The number of place cells and fraction of place cells from the total number of cells was significantly higher following CNO injection (center panel $p = 0.046$, and right panel $p = 0.017$ respectively).

the previous distribution), obtaining a slope of -0.026 and an even more significant effect ($p = 4 \cdot 10^{-6}$). These results showed that the increase in the information content after CNO injection was higher when considering only place cells. On the other hand, when performing a Wilcoxon test on animal averages, the difference was not significant (Figure 4.15 bottom right panel), this evidenced the importance of performing adequate and sufficiently powerful statistical tests considering the full extent of the data.

To determine whether the effect could be influenced by the number of cells in each condition or whether CNO injection could have an effect on the number of cells detected, we compared the number of cells found in each condition (Figure 4.16 left panel) and found no significant difference (Wilcoxon paired test, $p = 0.18$). We then quantified the number of place cells in each case (Figure 4.16 center panel) and found a small but significant increase after CNO injection (Wilcoxon paired test, $p = 0.046$). We then computed the ratio between the number of place cells and the total number of cells for each animal (Figure 4.16 right panel), which was found to be significantly higher for the CNO condition (Wilcoxon paired test, $p = 0.017$).

We further explored whether CNO application changed other properties of neuronal place cells. We compared the center and width of response profiles and/or place fields after saline injection and after CNO injection (Figure 4.17). When considering all cells, the response profile width was slightly but significantly higher after CNO injection (Figure 4.17 top left panel, Kolmogorov-Smirnov test, $p = 0.005$), as evidenced by a small shift to the right in the empirical distribution function (EDF). The distributions of response profile centers were significantly different (Figure 4.17 top right panel, $p = 9 \cdot 10^{-4}$). We then considered the same comparisons for place field widths and centers, taking into account exclusively place cells (Figure 4.17 center left and right panels, respectively). In both cases, the difference between distributions was not significant ($p = 0.1$ for PF width and $p = 0.13$ for PF centers), however, median PF width was significantly higher in CNO condition (Mann-Whitney U test $p = 0.024$). Finally we

compared response profile widths and centers for non-place cells (Figure 4.17 bottom left and right panels, respectively). Distribution of both, response profile widths and centers, were significantly different ($p = 0.03$ and $p = 10^{-4}$)

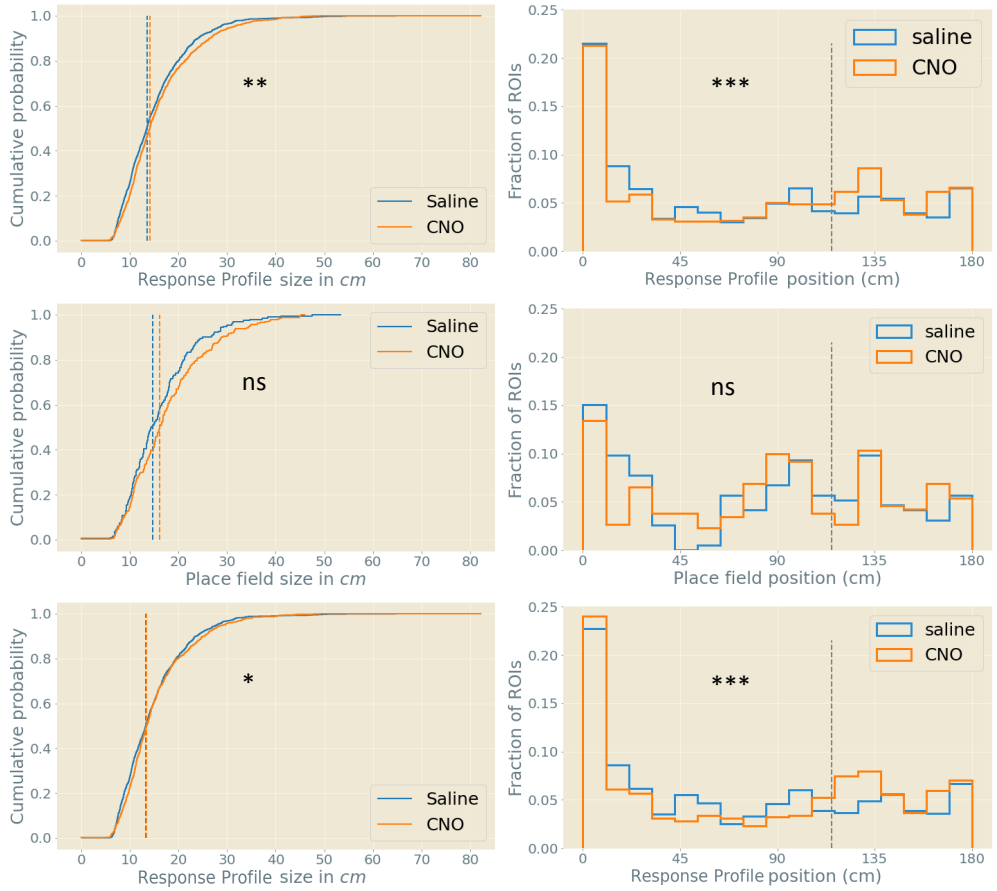

Figure 4.17: Difference in response profiles and place fields width and center distributions after CNO injection and after saline injection. Distribution of response profiles width (top left panel, Kolmogorov-Smirnov test on distributions $p = 0.005$) and centers (top right panel, $p = 9 \cdot 10^{-4}$) for all cells detected ($n = 1192$ saline, $n = 1001$ CNO). Distribution of place fields width (center left panel, $p = 0.10$, but a Mann-Whitney U test showed significantly higher median place field size for CNO $p = 0.024$) and centers (center right panel, $p = 0.13$) for place cells ($n = 193$ saline, $n = 261$ CNO). Distribution function of response profiles width (bottom left panel, $p = 0.03$) and centers (bottom right panel, $p = 10^{-4}$) for non-place cells ($n = 999$ saline, $n = 740$ CNO). All comparisons and tests were performed between full distributions with the exception of the median test for place field width.

Taken together, these results suggest that CNO application, and, consequently, the modification of calcium signaling in astrocytes significantly affected the neuronal representation of space and some aspects of neuronal response properties in the hippocampus of mice navigating in a unidimensional virtual corridor. There are, however, two aspects of the data presented that should be considered. First, the dataset presented above had large differences in the number of cells detected across FOVs. This could in

principle introduce biases in the comparisons, with FOVs with a higher number of cells having a larger influence on the result. Second, in the dataset described above, different FOVs were imaged under each experimental condition. Thus, statistical testing of the effect of the treatment (CNO vs. saline injection) was always performed on different sets of neurons, precluding a paired comparison. To address these limitations, we developed a more accurate protocol to repetitively position the animal under a two-photon microscope, allowing imaging of the same FOV over different experimental sessions (longitudinal recordings) and leading to a larger number of imaged neurons. The analysis of this new dataset is presented in the next section.

4.3 Imaging neuronal place cells during pharmacogenetic manipulation of astrocytes in vivo: longitudinal recordings

To study the same population of cells across conditions and across days, we performed longitudinal 2-photon imaging recordings in three sessions: day 0 - saline injection, day 1 - CNO injection, and day 3 - saline injection (see methods 3.1.4). The new experimental protocol (see methods 3.1.4) allowed us to successfully image the same FOV across sessions, as seen in the representative median projections of the acquired t-series in Figure 4.18. Segmentation was performed in the t-series concatenated across days (Figure 4.19A) and in individual t-series (Figure 4.19B). To compare segmentations of concatenated vs. individual t-series, we computed the F-1 score, which is defined as:

$$\frac{tp}{tp + \frac{1}{2}(fp + tn)}$$

where tp, fp and tn are the true positives, false positives, and true negatives, respectively. The F-1 score ranges between 0 and 1. In each case, to compute these values, the

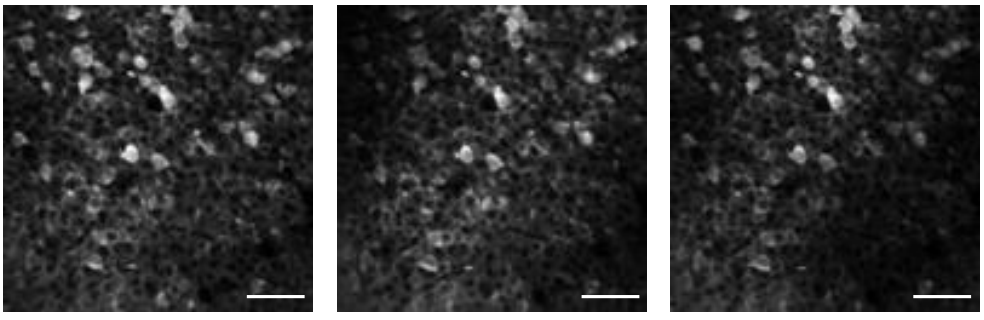

Figure 4.18: Fields of view were successfully tracked and recorded across days. From left to right, median projection of first day of saline, CNO and second day of saline injections of a representative FOV (scale 60 μm)

segmentation of one of the t-series was considered the ground truth, and the other was

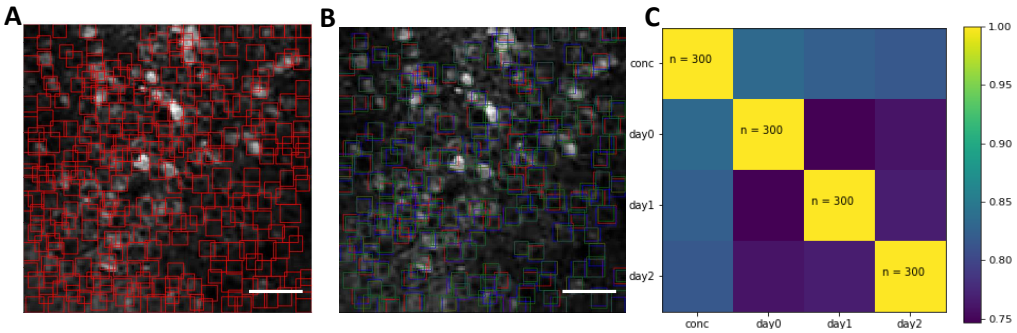

Figure 4.19: Segmentation and ROI tracking in longitudinal recordings. A) Segmented boxes (red) performed on the concatenated recording median projection of a two-photon t-series (scale 60 μm). B) Segmentation from different recording days are shown superimposed. Identities successfully tracked across days are shown in red, green and blue for each day respectively (190 tracked identities out of 300 total, scale as in A). C) F-1 matrix for detections performed in the concatenated t-series and the 3 different days.

used for comparison. The closer to 1 the F-1 score was, the larger was the overlap between segmentations in different t-series. In the example shown in Figure 4.18, the F-1 score varied between 0.75 and 1 for all pairs of recordings (Figure 4.19C), meaning that for any pair of t-series, the overlap between segmentation was higher than 75%. Identities shared across all 3 recording days (saline, CNO, and saline) and segmentations were considered successfully tracked.

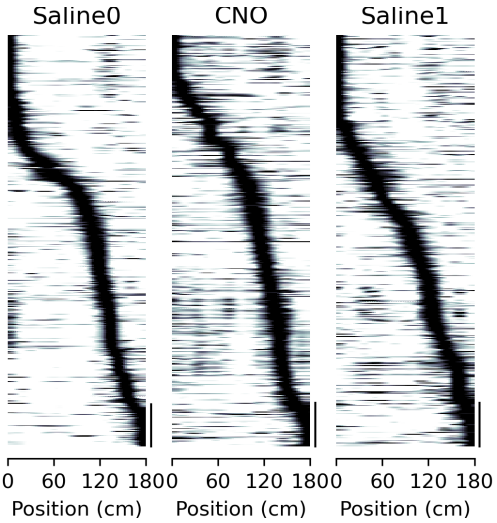

Figure 4.20: Normalized calcium responses as a function of position for neurons that contain significant amount of spatial information. Left panel, responses from recordings in which the animal was injected with saline solution (n = 488 informative ROIs out of 1740 total ROIs, 6 imaging sessions from 6 FOVs). Center panel, responses from recordings in which the animal was injected with CNO solution (n = 476 informative ROIs out of 1708 total ROIs, 6 imaging sessions from 6 FOVs). Right panel, responses from recordings in which the animal was injected with saline solution after the CNO day (n = 472 informative ROIs out of 1758 total ROIs, 6 imaging sessions from 6 FOVs). Responses are ordered according to the position of the center of the response field (from minimum to maximum), scale = 50 ROIs.

We computed the normalized calcium responses of all neurons with significant information content about space, as shown in Figure 4.11, for each of the 3 days of

recordings (Figure 4.20). Identities were ordered according to the position of the center of the response field in increasing order. The first day of saline injection recordings is shown in the left panel, CNO injection recordings are shown in the middle panel, and the second day of saline recordings is shown in the right panel (488, 476 and 472 informative ROIs out of 1740, 1708 and 1758 total, respectively). As in the nonlongitudinal recordings, in every condition, PF spans the whole trace, allowing for the complete mapping of space regardless of treatment. Recordings from 3 animals were analyzed.

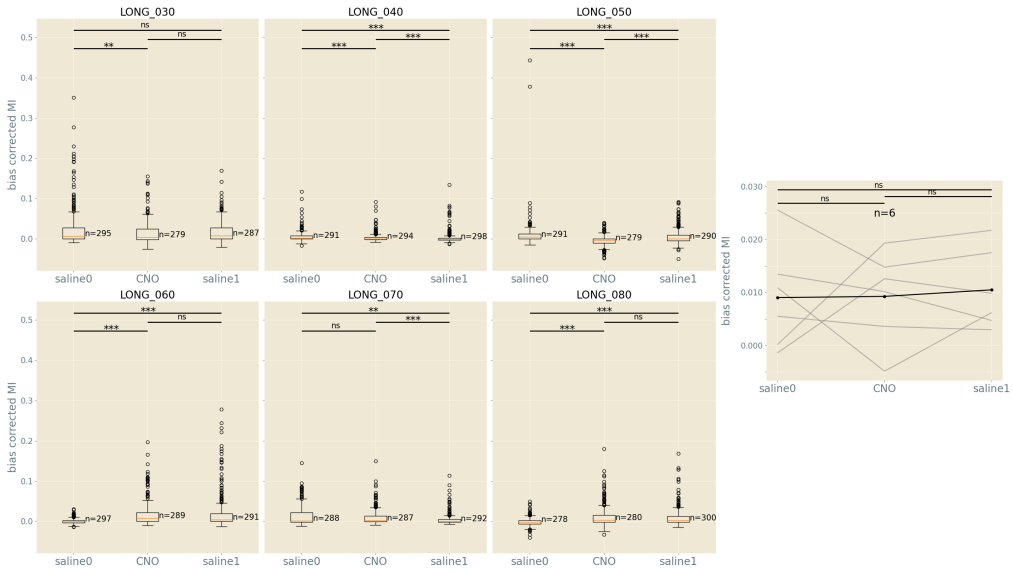

Figure 4.21: Bias corrected MI distributions under the different experimental conditions. Each panel represents a different FOV, with the box plots of MI distributions for first saline injection day, CNO injection day, and second saline injection day. Panels in the same column correspond to the same animal. Right-most panel shows the difference between MI values averages for each FOV (gray lines) and the overall average (black line), with no significant difference between different days (Wilcoxon paired test with Bonferroni correction, saline 0 vs CNO $p = 0.91$; saline 0 vs saline 1 $p = 0.91$; CNO vs saline 1 $p = 0.34$)

Although the procedure to track neurons was successful, the sets of neurons in each session were not entirely overlapping: not all cells from each recording had a corresponding one in the following sessions. For this reason, we first studied how alterations in astrocytic calcium activity influenced spatial mapping in the same population of neurons, by comparing the distributions of MI values after saline (first and second saline days) or CNO injection for each animal, considering the set of neurons in each FOV as independent from the others, analogously to the nonlongitudinal recordings (section 4.2), and then we compared only the tracked identitities (see bellow). Boxplots and statistical tests for the nonlongitudinal-like analysis are reported in each of the 6 panels of Figure 4.21.

Figure 4.22: Response profiles, place field widths, and place field centers in CNO and saline for longitudinal recordings. Distribution of response profiles width (top left panel, kolmogorov-smirnov test $p = 0.62$) and centers (top right panel, $p = 0.009$) for all cells detected. Distribution of place fields width (bottom left panel, $p = 8.8 \cdot 10^{-6}$) and centers (bottom right panel, $p = 0.001$) for place cells.

Both place cells and nonspatial encoding cells were pooled together; thus, the distributions were centered close to zero and heavy tailed towards positive values. Distributions of MI across conditions showed heterogeneous behavior across animals, and in contrast to observations for nonlongitudinal recordings, the difference in the averages was not significantly different for any of the comparisons between conditions (4.21 right-most panel, Wilcoxon paired test with Bonferroni correction; saline 0 vs. CNO, $p = 0.91$; saline 0 vs. saline 1, $p = 0.91$; CNO vs. saline 1, $p = 0.34$).

To account for FOV variability and asymmetries in the number of elements per condition per animal, we again used an LMEM with treatment as a fixed effect and FOV as a random effect with either a random intercept (LME1) or a random intercept and a random slope (LME2). First, we fitted an LME2 model, considering only treatment as the fixed effect. The fitted slope of the LME2 model was small, at $5 \cdot 10^{-4}$, and positive, which implies a small increase in the information content on saline days. In contrast to observations for nonlongitudinal recordings, the effect of treatment was found to be statistically nonsignificant (Type II Wald chi-square tests, $p = 0.87$). We then examined the effect of CNO injection when considering only place cell information content. We fitted an LME1 model with similar results-the fitted slope was 0.001, and the effect was nonsignificant ($p = 0.87$).

In doing this analysis, we pooled together two different days of saline injection, with one taking place before and one after the CNO injection day. To better compare the results of the analysis of this dataset with those of the nonlongitudinal recording (wherein only one saline condition was available), we limited the analysis to the first

day of saline injection and the following CNO injection day. We fitted an LME2 model for all cells and found that the effect of the treatment was not significant ($p = 0.96$) and that the slope was negative, at $-2 \cdot 10^{-}4$. We then fitted an LME1 model, taking into consideration only place cells from the first two days and obtained a fitted slope of -0.001 (10% decrease on saline day, $p = 0.57$). Finally, we fitted the LME2 model to compare the two saline days, and again, we found no statistically significant difference ($p = 0.74$).

We then compared the center and width of the response profiles and/or place fields for the first day of the saline injection and CNO injection experiments (Figure 4.22), again, in the same way as with the nonlongitudinal dataset: considering all cells from each FOV (including not tracked cells) and taking each FOV as independent from the rest. When considering all cells, the response profile width was not significantly different after CNO injection (Figure 4.22 top left panel, Kolmogorov-Smirnov test, $p = 0.62$). The distributions of response profile centers were significantly different (Figure 4.22 top right panel, $p = 0.009$). When considering the subset formed by only place cells and observing place field widths and centers (Figure 4.22 bottom left and right panels, respectively), we observed a statistically significant increase in PF width ($p = 8.8 \cdot 10^{-6}$) and a significant difference between PF center distributions ($p = 0.001$).

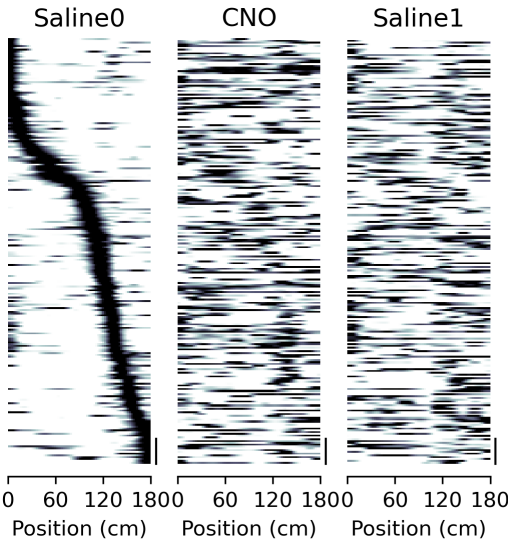

Figure 4.23: Normalized calcium responses as a function of position for all tracked ROIs. Left panel, responses from recordings in which the animal was injected with saline solution ordered according to the position of the center of the response field (from minimum to maximum). Center panel, responses from recordings in which the animal was injected with CNO solution, ordered as in left panel. Right panel, responses from recordings in which the animal was injected with saline solution after the CNO day, ordered as in left panel (n = 851 tracked ROIs, 6 imaging sessions from 6 FOVs, scale = 50 ROIs).

We then analyzed the effect of CNO injection **on the same cells**. For this, we tracked cell identities belonging to the same FOV across days (see methods 3.4). We computed the normalized calcium responses of all tracked ROIs with and without significant information content about space, for each of the 3 days of recordings (Figure 4.23). In this latter case, because identities were tracked, and therefore each ROIs had a corresponding one in the following days, we could compare the change in response profile center for each day. We did so by computing the order according to the maximum response for the first day (saline 0) and maintaining the order for the CNO and Saline 1 days. We observed that some cells maintained a similar response profile center

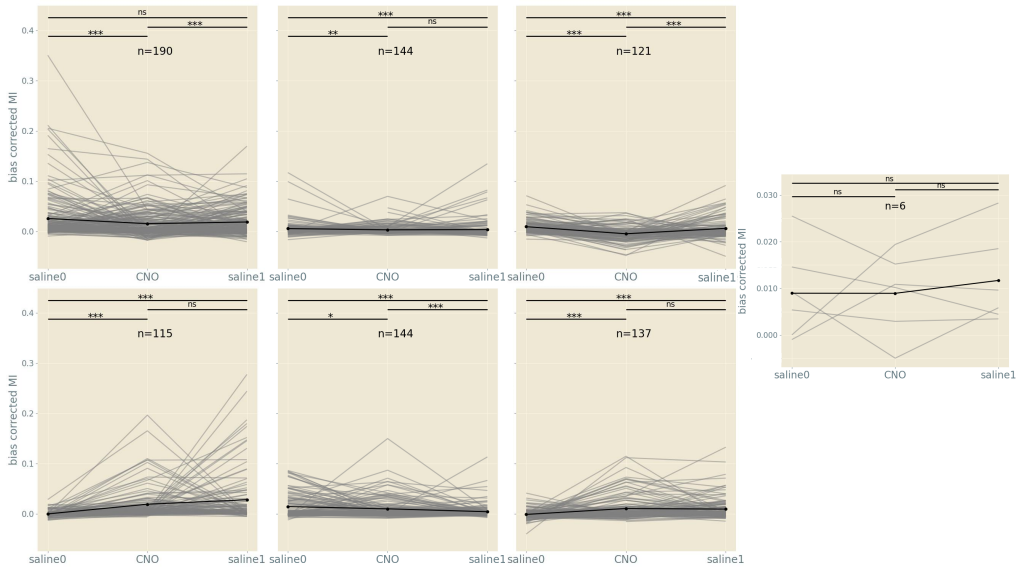

Figure 4.24: Bias corrected MI values for tracked cells across days. Each gray line corresponds to a tracked ROI and black lines to averages. Missing points (interrupted lines) correspond to cells that were silent in one of the days (paired Wilcoxon tests with Bonferroni correction where performed in each case). Information could not be computed in sessions in which neurons did not show activity. Right-most panel shows the difference between MI values averages for each FOV (gray lines) and the overall average (black line), with no significant difference between different days (Wilcoxon paired test with Bonferroni correction, saline 0 vs CNO $p = 0.91$; saline 0 vs saline 1 $p = 0.91$; CNO vs saline 1 $p = 0.34$)

in the following day while other do not. The order got even more scrambled for the 3rd recording day. This result is consistent with normal remapping of CA1 neurons as reported in literature [Ziv et al., 2013] and does not allow us to infer a causal relation with the CNO pharmacological manipulation.

We compared the MI values for each cell across days (Figure 4.24). The differences and results were heterogeneous and did not show statistically significant differences across days on average (Figure 4.24 right-most panel, Wilcoxon paired test with Bonferroni correction, saline 0 vs. CNO, $p = 0.91$; saline 0 vs. saline 1, $p = 0.91$; CNO vs. saline 1, $p = 0.34$). Note that these values are a subset of the data shown in figure 4.21, but here, each line represents one cell that has been tracked across all 3 days. It is important to note that the paired analysis could not be done while considering only place cells because cells changed their state across days: e.g., some cells that were defined as place cells in the first day of saline were not in the CNO application day (consistently with what is reported in Ziv et al., 2013).

Finally, we studied cell-wise variation in the place field and response profile widths and centers. We computed the difference between CNO and saline (first application) response profile centers for all tracked cells in all FOVs. The histogram of the differences showed an approximately symmetric distribution with respect to zero (Figure 4.25 top

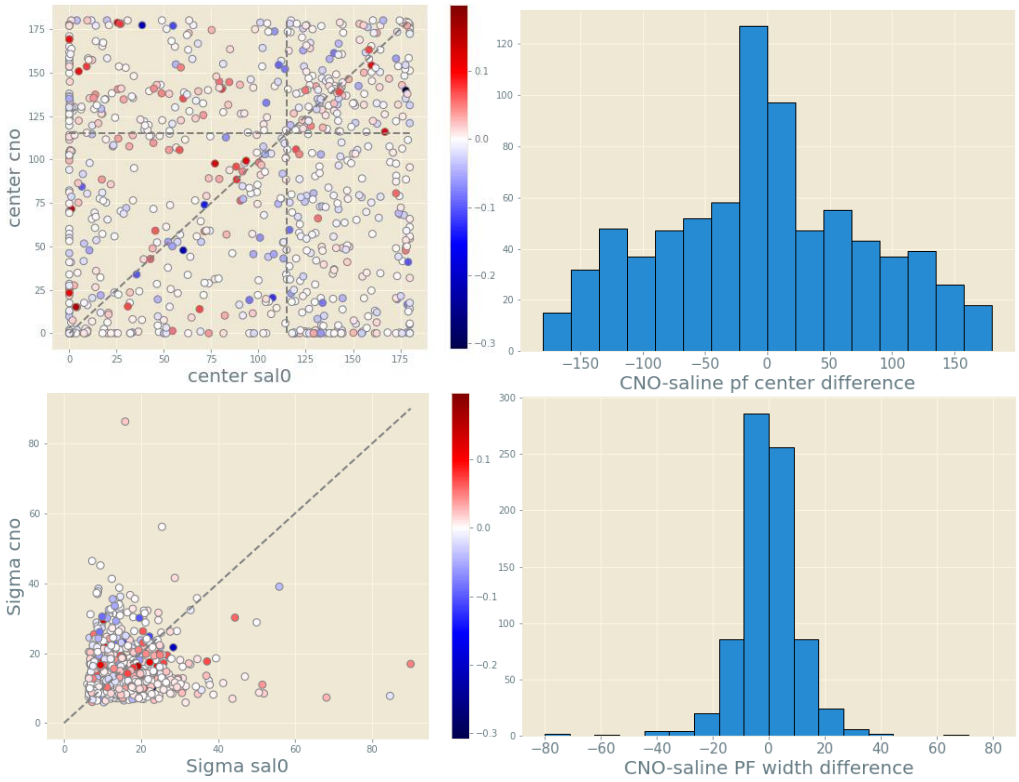

Figure 4.25: Place field width and center difference for tracked cells between first day of saline injection vs CNO injection. Top left panel shows position of PF centers in CNO day vs Saline 0 day, each dot is a cell and the color of the dot represents the difference in MI values between CNO minus Saline 0, dotted gray lines are the diagonal (representing equal centers position) and the reward location for each day. Top right panel, histogram of the difference between CNO minus Saline 0 days PF centers. Bottom panels as top panels for width of place fields.

right panel), with a higher number of cells in the two central bins, meaning that a high percentage of cells tended to maintain their response profile centers. We asked whether variations in response centers could be related to differences in information content. In the top lef panel of Figure 4.25, we can see the distributions of tracked cells in the plain defined by the centers of the response profile in each day. Each circle represents a tracked cell, and its color represents the difference in the MI value (CNO minus saline 0). No clear asymmetry in the distribution of cells in the plane or relationship with the change in information content was observed, besides the higher number of dots on the diagonal (as expected from the histogram), regardless of the variation in the MI content. Similarly, we computed the differences in the response profile width, with the vast majority of cells having a variation of less than 20cm (Figure 4.25 bottom right panel). This was further confirmed by the distribution in the plain defined by the width on different days (Figure 4.25 bottom left panel), which also had no clear relationship with the difference in MI values.

Taken together, the analysis of the longitudinal recordings showed that CNO application did not have major effects on the content of information or on the features of neuronal place cells, in contrast to the results of the nonlongitudinal recordings. We discuss these contrasting results in the following section.

Chapter 5

Discussion

Unpublished work from my mentor's laboratory in collaboration with Jacopo Bonato and Stefano Panzeri indicate that hippocampal astrocytes encode spatial information in their calcium dynamics during virtual navigation (see introduction 1.3.2). Given that calcium signals in astrocyte has downstream effects on synaptic transmission [Panatier, Theodosis, et al., 2006; Henneberger et al., 2010; Fellin, 2009] and neuronal excitability [Jourdain et al., 2007; J. Kang et al., 1998; Liu et al., 2004], this observation raises the hypothesis that space-encoding calcium dynamics into astrocytes may modulate the neuronal representation of space. In this thesis work, we developed an analytical pipeline to study the effects of manipulating astrocytic calcium activity on spatial information encoding in CA1 neurons of the mouse hippocampus during virtual navigation. To manipulate astrocytic calcium signals, we used pharmacogenetic interventions [B. L. Roth, 2016; B. Armbruster and B. Roth, 2005; B. N. Armbruster et al., 2007] using astrocyte-specific expression of DREADDs in combination with intraperitoneal CNO injection [Adamsky et al., 2018]. We found that CNO injection induced an initial synchronous increase of calcium activity in the majority of imaged astrocytes followed by a prolonged period of synchronously decreased calcium signals (Figure 4.4). To image neuronal representation of space during virtual navigation, we expressed the fluorescent functional indicator GCaMP6f [T.-W. Chen et al., 2013] in neurons and we compared neuronal spatial information encoding under control conditions (after saline injection) and after CNO injection using two-photon GCaMP6f imaging (Figure 4.12). Initially, we used nonlongitudinal recordings of neurons, meaning that different FOV were imaged across experimental conditions (e.g., control vs. CNO) similarly to D. A. Dombeck, Harvey, et al., 2010. In this first data set, we found that CNO injection resulted in a significant increase in the average information content in neurons. Importantly, using a LME model [Pinheiro and Bates, 2000] to compare full distributions of mutual information values and excluding animal variability produced similar result. The effect was stronger when comparing place cells subpopulations for each animal. Moreover, the ratio of place cells *per* field of view increased after CNO injection (Figure 4.16). We compared width and centers of response profiles for all cells and found a significant increase in response profile width after CNO injection (Figure 4.17). Response profiles centers were also significantly different across the two conditions (saline vs.

control). However, when considering only place cells, the distribution of place field width and place field centers were not significantly different. On the other hand, when considering only non-spatial encoding cells, the distribution of response profile width and centers were significantly different.

The results of this preliminary set of experiments (non-longitudinal recordings) suggested that CNO application (i.e., manipulation of calcium signalling in astrocytes) significantly affected neuronal representation of space in the hippocampus of mice navigating in a virtual corridor. However, to correctly interpret these preliminary findings two aspects of the data should be taken into consideration. First, there was a large variability in the number of cells detected across FOV and conditions. This could, in principle, introduce biases in the statistical comparison. For example, conditions with larger number of cells could influence more the result. Moreover, the low number of detected cells under certain conditions could represent a biased estimate of the full distribution because of subsampling. Second, different FOVs were imaged under each experimental condition. Thus, the effect of the treatment was assessed on different sets of neurons in each conditions, preventing pairwise statistical comparison.

To overcome these limitations, we developed and implemented a protocol to reliably image the same FOV over different experimental sessions across days (longitudinal recordings). At the same time, the recording protocol was modified to image more neurons *per* FOV. We succeeded in imaging the same FOV across sessions. However, the sets of neurons in each session were not entirely overlapping: not all cells from each recording had a corresponding one in the following sessions. This could be due to different activity levels leading to different basal fluorescence across conditions [T.-W. Chen et al., 2013]. As with the non-longitudinal recordings, we first compared the distribution of MI values after saline (two saline injections were performed in the longitudinal recordings, one preceding and one following the day of CNO application) and after CNO injection for each animal considering all cells from each session (Figure 4.21). In contrast to what we observed in the nonlongitudinal recordings, the mutual information averages were, in this second data set, not significantly different for any pair of days (first vs. second day of saline; first day of saline vs. CNO day; CNO day vs. second day of saline). To account for animal variability, we fitted a LME model with treatment as fixed effect and FOV as random effect with either a random intercept or a random intercept and a random slope. The fitted slope was small and positive, suggesting a small but not significant decrease of information content after CNO injection. Similar results were found when comparing only the subset of neurons that displayed significant amount of spatial information (i.e., place cells). To make the analysis more comparable with the one performed in the nonlongitudinal recordings, we fitted a LME model considering only the first day of saline injection and discarding the day of saline injection which followed CNO application. The fitted slope was negative, showing the general tendency of the nonlongitudinal recordings. However, the effect was statistically non significant. Comparing only place cells for these two days increased the absolute value of the negative slope, but the effect was still statistically

not significant. We fitted a LME model to compare the two saline days and found no significant difference. We then compared the center and width of response profiles and place fields for the first day of saline and CNO injection sessions (Figure 4.22). We observed a significant increase in place field width (i.e. considering only place cells), but no significant difference in response profile width when considering all cells. Field center distributions were, instead, significantly different in both cases.

The richness of this data set relies, however, on the possibility to compare single cells activity across conditions. To this end, we developed an analytical pipeline to detect and track identities across experimental sessions. We then compared mutual information values for each cell across session, with heterogeneous results across FOV, and no significant difference on distribution averages (Figure 4.24). While it is true that this is a comparison between subsets of the full distributions for each FOV, the statistical advantage of this comparison lies on the possibility of performing pairwise testing. This allowed us to compare not only trends in population values but single cell differences across days. To further exploit the longitudinal aspect of these recordings, we compared response profile and place field properties for each cell (Figure 4.25). We observed a symmetric distribution of both response profile centers and width differences between treatments, meaning that cells tended to increase their response width and center upon CNO application as much as they tended to decrease it. Moreover, a large proportion of cells maintained their values across conditions, evidenced by a high number of counts in the central bins of the difference histograms in figure 4.25 (right panels). To uncover possible relationships between changes in response profile centers and width with variations in information content *per* cell, we plotted each cell in the plane defined by either centers or widths in each day, and colored it according to the cell's variation in information content (Figure 4.25 left panels). Beyond a higher density of points in the diagonal, representing the aforementioned high percentage of cells that tended to maintain their properties across days, no other asymmetry in the distribution of dots or colors was observed. Moreover, dots along the diagonal had different colors, meaning that cells that preserved their response properties did not necessarily preserve also their information content.

The observation that CNO application changes the neuronal representation of space in the hippocampus in the non-longitudinal recordings is suggestive of a role of astrocytes in the control of neuronal place cells. However, the preliminary nature of this data set and the contrasting results coming out from the longitudinal recordings, imposes us to critically discuss limitations and biases that may affect the analysis of these recordings. First, the observation that in the nonlongitudinal recordings neurons after CNO injection have higher overall information content could be explained by the fact that the ratio of place cells increased upon pharmacological treatment. Given that, in some cases, the number of cells detected was small, this poses the question of whether we may have recorded signal from a biased set of neurons. For example, highly active and informative cells. However, the segmentation analysis that we performed on these 2-photon imaging data set does not favour highly active cells (see CITE-On in

appendix B) under normal GCaMP6f expression conditions, making this explanation unlikely. Nevertheless, it is possible that in FOV characterized by low GCaMP6f expression levels, recorded neurons did have a bias towards high activity regimes [Harris et al., 2016]. Low expression of GCaMP6f was not clearly observed in the recordings presented here, but more quantitative evaluation of the indicator expression should be performed in our data set to address this issue. Second, in the non-longitudinal recordings we found an increase of information content after CNO injection, and at the same time an increase in response profile and place field width. These two observations might be counter-intuitive: higher widths account for blunter responses, which in turn could induce a reduction in information content (see section 1.8). However, the variance of the response is not the only source of information content changes. The way we calculated the width of the response considered only the principal place field for place cells and the area of highest response for non place cells (see methods 3.7.1). This approach does not take into consideration secondary place fields, or responses far from the main response area [Danielson et al., 2016; Zaremba et al., 2017]. Thus, a reduction in the activity outside the main response area could account for the observed increase in information content. Further analytical characterization of cell activity is needed to clarify this point and will be performed in the near future. In figure 4.17, we discussed width differences more in detail. We found that the difference in place field width upon CNO application was not statistically significant when considering only place cells, while the difference was significant when considering only non place cells (bottom panel). A possible interpretation for these results is that the difference we observed in the response profile width when considering all cells was mostly due to the contribution of non place cells. However, the visual inspection of the plots in figure 4.17 and the fact that a Mann–Whitney U test, which compared medians instead of full distributions, came as significant suggested a second interpretation. That is that the difference was due to both place and non place cells, but the changes in numerosity between the two experimental groups (1739 vs 454 for non place cells and place cells, respectively) strongly influenced the output of the statistical test.

To overcome some of the aforementioned limitations, we performed longitudinal recordings. Surprisingly, we found that mutual information values were not significantly different upon CNO application compared to controls. Although both data sets and their analyses are preliminary, the contrasting results obtained from the two data sets could be due to a number of reasons that will be discussed in the following text. As mentioned above, one possible explanation is that the apparent significant effects we observed in the nonlongitudinal recordings were due to different numerosity of the samples under the two conditions or to the fact that we compared different FOVs across conditions. There are, however, other possible reasons that could justify the observed discrepancy. If we observe the comparisons for the first day of saline and the CNO injection recordings for the tracked cells in the longitudinal recordings, (Figure 4.24), the difference in mutual information is significant for each FOV individually but it is not when we average across FOVs. This is because the effects have different signs in

different FOVs, with some increasing and some decreasing mutual information upon CNO application. The different signs of the effect could be due to hidden variables such as running speed, number of trials, arousal, thirst/satiety [Allen et al., 2019], that could affect the output of the analysis. Refinement of the experimental protocol to measure some of these behavioral variables could help clarifying this issue. The use of more refine methods to include further levels of complexity in the analysis could also address some of these limitations. For example, using a generalized linear model [Saleem, Diamanti, et al., 2018; Saleem, Ayaz, et al., 2013] including several behavioral variables as well as treatment to analyze cell activity could partially address this issue. Another possibility would be to normalize mutual information values by the sum of the response and stimulus entropies [Kvålseth, 2017; Timme and Lapish, 2018]. In this latter way, the variability due to asymmetries in number of trials and cell activity could be accounted for. Future analytical work will be needed to clarify this point.

A second discrepancy between the nonlongitudinal and longitudinal recordings was observed in the place field width comparison. In nonlongitudinal recordings, significance in the difference place field width was found when comparing all cells, but not when comparing only place cells. In contrast, in longitudinal recordings place field width was significantly different when considering only place cells, but not when considering all cells (Figure 4.22). However, it should be noted that the tendency in the data was the same in both data sets (i.e., an increase in place field width upon CNO injection). Moreover, the absolute value of the difference and the range of the medians in each case was similar for longitudinal and nonlongitudinal recordings, but the number of cells was much larger for longitudinal recordings (964 cells under both conditions in longitudinal recordings vs 454 in nonlongitudinal recordings). It is thus possible that the different sample numerosity accounted for the observed results and future experimental work is needed to increase sample size.

Part of the richness of the longitudinal dataset lies on the possibility of comparing changes between CNO and first saline days with the second saline day. However the effect of CNO in astrocytic calcium activity has proven to be more complex than what's reported in literature and we cannot rule out long term effects of the pharmacological manipulation. Moreover, preliminary analysis has shown some similarities between Saline 1 and CNO days neuronal activity (data not shown). Whether these similarities are due to normal dynamics of spacial mapping across days or due to the CNO injection is a question that we cannot answer in the current dataset. For this reason we preferred not to deepened into Saline 1 day comparisons. We are currently performing control experiments to better elucidate the effect of CNO injection in time, and across days.

The goal of this thesis was to develop and implement an analytical workflow for the analysis of combined two-photon imaging and pharmacogenetic experiments in awake mice navigating in virtual reality. We developed the analytical package based on information theory [Shannon, 1948] and applied it to the the two presented hippocampal data sets. The results of the analysis did not provide a conclusive answer to

the question whether manipulation of astrocytic calcium activity changed information content about space in neuronal hippocampal circuits. As discussed in the previous paragraphs, several experimental and analytical improvements are necessary to fully test this hypothesis. However, it should be underlined that CNO injection similarly increased place field width and similarly modified the distribution of place field centers in the two data sets. This result suggested that alteration in astrocytic calcium activity might indeed induce reliable changes in neuronal position encoding by changing neuronal response properties. A higher width of place fields and response profiles would be compatible with a less accurate response at the single cell level. However, the increase or non significant change in information content in single neurons may suggest different interpretations. For example, one possibility is that upon CNO injection place cells became less accurate but more reliable in their responses, indicating a role of astrocytes in sharpening neuronal responses. Changes in reliability can be studied within the current dataset, although the notion of reliability in place cells is not uniformly defined in the literature [E. J. Markus et al., 1994; Trimper et al., 2017]. We could, for example, compute the percentage of trials in which the cell fires in its response field, or the difference between response fields computed with different subsets of trials. These possibilities will be explored in the near future. More reliable responses imply less variability on trial-by-trial bases, which could be due to changes in neuronal plasticity properties. Astrocytes play a prominent role in the modulation of neuronal plasticity [Pascual et al., 2005; Serrano et al., 2006; Henneberger et al., 2010; Min and Nevian, 2012], thus changes in their calcium activity could induce variations in the ability of neuronal networks to adapt to varying environmental conditions. This hypothesis cannot be tested in the current data set, but it is an experimental and theoretical direction we are willing to pursue in the next future.

Astrocytic calcium dynamics has been observed to play a role not only in the modulation of single cells, but also in the regulation of neuronal networks [Fellin, Halassa, et al., 2009; Szabó et al., 2017; Bellot-Saez et al., 2018; Mederos et al., 2020]. In the analytical work presented in this thesis, we analyzed neuronal population, but always based on measurement of single cell properties (e.g., information content, width and center of response *per* cell). However, population coding may arise on higher order properties of neuronal networks [Stefanini et al., 2020] that are not captured by single cell properties and that had not been analyzed here. Thus future analytical effort could be focused on addressing this important question. For example, studying the dynamics of neuronal CA1 populations in lower dimensional spaces, by using dimensionality reduction techniques [Marshel et al., 2019], could unmask differences in population coding of space under the different experimental conditions analyzed here (saline vs. CNO). Moreover, analyzing the sum (or averages) of information content *per* cell can potentially mask information-rich population properties, as cells can synergically work to encode or represent information about space [Stefanini et al., 2020]. Various other methods to unravel synergic information content in the network could also be used to further compare treatments at the population level [Pola et al., 2003; Magri et al., 2009]. Finally,

alterations in astrocytic calcium activity might change the way population activity is used to decode the animal's position. To test this hypothesis, bayesian or other types of decoders [K. Zhang et al., 1998; Shuman et al., 2020] could be used to compare decoding accuracy under control conditions and after CNO injection.

To correctly interpret the experimental design presented in this thesis, a more detailed understanding of the CNO effect on astrocytic calcium dynamics is also needed. CNO concentrations used in this work induced complex calcium dynamics in astrocytes, with an early increase of calcium activity, which was synchronous across astrocytes and which was followed by a prolonged silencing of astrocytic calcium signaling (see Figure 4.4). This observation is reminiscent of the effects observed in astrocytic calcium dynamics upon pharmacological stimulation of endogenous receptors [D'Ascenzo et al., 2007; Fellin, Pascual, Gobbo, et al., 2004; Perea and Araque, 2005; Fellin, Pozzan, and Carmignoto, 2006]. It is also important to note that in the two data sets presented in this thesis, two-photon imaging of neuronal activity was performed in the temporal window after CNO application (30-90 minutes after injection) when calcium signaling was largely suppressed in astrocytes. This was because the initial increase in calcium dynamics was confined to a short temporal window (approximately 10 minutes after injection) and that the time necessary to reposition the awake animal under the microscope objective after CNO injection was longer than 10 minutes. Thus under the current experimental conditions we cannot conclude whether the effects we observed on neuronal representation of space upon CNO application were due to astrocytic calcium signaling being silenced, being activated, or to a non trivial combination of both effects. To address this fundamental question, further characterization of CNO effect in astrocytic networks is needed. In future experiments, we will proceed with lowering the concentration of CNO and built a detailed dose-response curve. Ideally, CNO should induce dynamic changes in calcium signaling in astrocytes for prolonged time (about 1 hour), avoid oversynchronous responses across astrocytic cells, and prevent long lasting dampening of calcium activity.

The virtual navigation task implemented in the presented experiments had several advantages. It allowed 2-photon imaging and it enabled precise control of environmental cues. However, the head-fixed virtual reality approach also came with limitations [Minderer et al., 2016]: navigation in the hippocampus involves the delicate interplay of several neuronal types (see 1.1.2), including head direction cells. In head fixed experiments this degree of complexity is constrained and there is no engagement of the vestibular system [Minderer et al., 2016]. Thus, performing experiments in freely moving animals, while imaging the neuronal place cells with 1-photon mini-endoscopes [Flusberg et al., 2008; Aharoni et al., 2019] will allow to extend the importance of the presented data to a more physiologically-relevant context.

As mentioned above, recent work done at my supervisor's laboratory in collaboration with Jacopo Bonato and Stefano Panzeri (see 1.3) shows that information about space in the hippocampus is not only encoded in neuronal networks, but also in the

glial cell astrocyte. The possibility that neurons and astrocytes could synergisticly contribute to spatial navigation has several important implications in the way we understand how higher cognitive functions stem from the coordinated activity of populations of different cell types in the brain. Importantly, the synergistic interplay between neuronal and astrocytic networks can only be understood by specifically perturbing each of the involved cell type [Panzeri, Harvey, et al., 2017] and by combining this complex experimental approaches with advanced analysis methods. This thesis work aimed to be an initial and preliminary step in this direction. We believe the presented work contributes to open the door to new and profound questions that we aspire to fully tackle from an experimental and theoretical point of view in the near future.

Bibliography

[1] S. B. Achour and O. Pascual. "Astrocyte–neuron communication: functional consequences". In: *Neurochemical research* 37.11 (2012), pp. 2464–2473.

[2] A. Adamsky, A. Kol, T. Kreisel, A. Doron, N. Ozeri-Engelhard, T. Melcer, R. Refaeli, H. Horn, L. Regev, M. Groysman, et al. "Astrocytic activation generates de novo neuronal potentiation and memory enhancement". In: *Cell* 174.1 (2018), pp. 59–71.

[3] W. R. Adey. "An experimental study of the hippocampal connections of the cingulate cortex in the rabbit". In: *Brain* 74 (1951), pp. 233–247. DOI: https://doi.org/10.1093/brain/74.2.233.

[4] W. R. Adey and M. Meyer. "An experimental study of hippocampal afferent pathways from prefrontal and cingulate areas in the monkey". In: *J. Anat.* 86 (1952), pp. 58–74.

[5] G. Agarwal, I. H. Stevenson, A. Berényi, K. Mizuseki, G. Buzsáki, and F. T. Sommer. "Spatially distributed local fields in the hippocampus encode rat position." In: *Science* 344 (2014), pp. 626–630.

[6] D. Aharoni, B. S. Khakh, A. J. Silva, and P. Golshani. "All the light that we can see: a new era in miniaturized microscopy". In: *Nature methods* 16.1 (2019), pp. 11–13.

[7] J. Akerboom, N. Carreras Caldéron, L. Tian, S. Wabnig, M. Prigge, J. Tolö, A. Gordus, M. B. Orger, K. E. Severi, J. J. Macklin, R. Patel, S. R. Pulver, T. J. Wardill, E. Fischer, C. Schüler, T. W. Chen, K. S. Sarkisyan, J. S. Marvin, C. I. Bargmann, D. S. Kim, S. Kügler, P. Lagnado L.and Hegemann, A. Gottschalk, E. R. Schreiter, and L. L. Looger. "Genetically encoded calcium indicators for multi-color neural activity imaging and combination with optogenetics." In: *Front. Mol. Neurosci.* 6 (2013), p. 2.

[8] J. Akerboom, T.-W. Chen, T. J. Wardill, L. Tian, J. S. Marvin, S. Mutlu, N. Carreras Caldéron, F. Esposti, B. G. Borghuis, X. R. Sun, A. Gordus, M. B. Orger, R. Portugues, F. Engert, J. J. Macklin, A. Filosa, A. Aggarwal, R. A. Kerr, R. Takagi, S. Kracun, E. Shigetomi, B. S. Khakh, H. Baier, L. Lagnado, S. S.-H. Wang, C. I. Bargmann, B. E. Kimmel, V. Jayaraman, K. Svoboda, D. S. Kim, E. R. Schreiter, and L. L. Looger. "Optimization of a GCaMP Calcium Indicator for Neural Activity Imaging". In: *J. Neurosci.* 40 (2012), pp. 13819–13840.

[9] W. E. Allen, M. Z. Chen, N. Pichamoorthy, R. H. Tien, M. Pachitariu, L. Luo, and K. Deisseroth. "Thirst regulates motivated behavior through modulation of brainwide neural population dynamics". In: *Science* 364.6437 (2019).

[10] M. M. Almutairi, C. Gong, Y. G. Xu, Y. Chang, and H. Shi. "Factors controlling permeability of the blood–brain barrier". In: *Cellular and molecular life sciences* 73.1 (2016), pp. 57–77.

[11] P. Andersen, T. W. Blackstad, and T. Lomo. "Location and identification of excitatory synapses on hippocampal pyramidal cells". In: *Exp. Brain Res.* 1 (1966), pp. 236–248.

[12] P. Andersen, J. C. Eccles, and Y. Loyning. "Location of postsynaptic inhibitory synapses on hippocampal pyramids". In: *J. Neurophysiol.* 27 (1964), pp. 592–607. DOI: https://doi.org/10.1152/jn.1964.27.4.592.

[13] P. Andersen, J. C. Eccles, and Y. Loyning. "Pathway of postsynaptic inhibition in the hippocampus". In: *J. Neurophysiol.* 27 (1964), pp. 608–619. DOI: https://doi.org/10.1152/jn.1964.27.4.608.

[14] M. Anderson and K. Jeffery. "Heterogeneous modulation of place cell firing by changes in context." In: *Neurosci* 23 (2003), pp. 8827–8835.

[15] M. Andersson, F. Blomstrand, and E. Hanse. "Astrocytes play a critical role in transient heterosynaptic depression in the rat hippocampal CA1 region". In: *The Journal of physiology* 585.3 (2007), pp. 843–852.

[16] M. C. Angulo, A. S. Kozlov, S. Charpak, and E. Audinat. "Glutamate released from glial cells synchronizes neuronal activity in the hippocampus". In: *Journal of Neuroscience* 24.31 (2004), pp. 6920–6927.

[17] A. Araque, G. Carmignoto, and P. G. Haydon. "Dynamic signaling between astrocytes and neurons". In: *Annual review of physiology* 63.1 (2001), pp. 795–813.

[18] A. Araque, G. Carmignoto, P. G. Haydon, S. H. Oliet, R. Robitaille, and A. Volterra. "Gliotransmitters travel in time and space". In: *Neuron* 81.4 (2014), pp. 728–739.

[19] A. Araque, R. P. Sanzgiri, V. Parpura, and P. G. Haydon. "Calcium elevation in astrocytes causes an NMDA receptor-dependent increase in the frequency of miniature synaptic currents in cultured hippocampal neurons". In: *Journal of Neuroscience* 18.17 (1998), pp. 6822–6829.

[20] B. Armbruster and B. Roth. "Creation of designer biogenic amine receptors via directed molecular evolution". In: *Neuropsychopharmacology*. Vol. 30. NATURE PUBLISHING GROUP MACMILLAN BUILDING, 4 CRINAN ST, LONDON N1 9XW, ENGLAND. 2005, S265–S265.

[21] B. N. Armbruster, X. Li, M. H. Pausch, S. Herlitze, and B. L. Roth. "Evolving the lock to fit the key to create a family of G protein-coupled receptors potently activated by an inert ligand". In: *Proceedings of the National Academy of Sciences* 104.12 (2007), pp. 5163–5168.

[22] D. Attwell, A. M. Buchan, S. Charpak, M. Lauritzen, B. A. MacVicar, and E. A. Newman. "Glial and neuronal control of brain blood flow". In: *Nature* 468.7321 (2010), pp. 232–243.

[23] D. Attwell and S. B. Laughlin. "An energy budget for signaling in the grey matter of the brain". In: *Journal of Cerebral Blood Flow & Metabolism* 21.10 (2001), pp. 1133–1145.

[24] L. Bareket-Keren and Y. Hanein. "Carbon nanotube-based multi electrode arrays for neuronal interfacing: progress and prospects." In: *Front. Neural Circuits* 6 (2012), p. 122.

[25] C. Barry, R. Hayman, N. Burgess, and K. Jeffery. "Experience-dependent rescaling of entorhinal grids." In: *Nat. Neurosci.* 10 (2007), pp. 682–684.

[26] C. Barry, C. Lever, R. Hayman, T. Hartley, S. Burton, J. O'Keefe, K. Jeffery, and N. Burgess. "The boundary vector cell model of place cell firing and spatial memory." In: *Rev. Neurosci.* 17 (2006), pp. 71–97.

[27] M. Y. Batiuk, A. Martirosyan, J. Wahis, F. de Vin, C. Marneffe, C. Kusserow, J. Koeppen, J. F. Viana, J. F. Oliveira, T. Voet, et al. "Identification of region-specific astrocyte subtypes at single cell resolution". In: *Nature communications* 11.1 (2020), pp. 1–15.

[28] N. Bazargani and D. Attwell. "Astrocyte calcium signaling: the third wave". In: *Nature neuroscience* 19.2 (2016), pp. 182–189.

[29] A. Bellot-Saez, G. Cohen, A. van Schaik, L. Ooi, J. W. Morley, and Y. Buskila. "Astrocytic modulation of cortical oscillations". In: *Scientific reports* 8.1 (2018), pp. 1–13.

[30] D. E. Bergles, J. D. B. Roberts, P. Somogyi, and C. E. Jahr. "Glutamatergic synapses on oligodendrocyte precursor cells in the hippocampus". In: *Nature* 405.6783 (2000), pp. 187–191.

[31] P. J. Best, A. M. White, and A. Minai. "Spatial processing in the brain: the activity of hippocampal place cells". In: *Annual review of neuroscience* 24.1 (2001), pp. 459–486.

[32] P. Bezzi, G. Carmignoto, L. Pasti, S. Vesce, D. Rossi, B. L. Rizzini, T. Pozzan, and A. Volterra. "Prostaglandins stimulate calcium-dependent glutamate release in astrocytes". In: *Nature* 391.6664 (1998), pp. 281–285.

[33] T. Bjerknes, E. Moser, and M.-B. Moser. "Representation of geometric borders in the developing rat." In: *Neuron* 82 (2014), pp. 71–78.

[34] C. Boccara, F. Sargolini, V. Thoresen, T. Solstad, M. Witter, E. Moser, and M.-B. Moser. "Grid cells in pre- and parasubiculum." In: *Nat. Neurosci.* 13 (2010), pp. 987–994.

[35] S. Bovetti, C. Moretti, and T. Fellin. "Mapping brain circuit function in vivo using two-photon fluorescence microscopy". In: *Microsc. Res. Tech.* 7 (2014), pp. 492–501.

[36] C. L. Bowman and H. K. Kimelberg. "Excitatory amino acids directly depolarize rat brain astrocytes in primary". In: *Nature* 311 (1984), pp. 656–659.

[37] V. Brun, S. T., K. Kjelstrup, M. Fyhn, M. Witter, E. Moser, and M. Moser. "Progressive increase in grid scale from dorsal to ventral medial entorhinal cortex." In: *Hippocampus* 18 (2008), pp. 1200–1212. DOI: 10.1002/hipo.20504..

[38] J. Bruttger, K. Karram, S. Wörtge, T. Regen, F. Marini, N. Hoppmann, M. Klein, T. Blank, S. Yona, Y. Wolf, et al. "Genetic cell ablation reveals clusters of local self-renewing microglia in the mammalian central nervous system". In: *Immunity* 43.1 (2015), pp. 92–106.

[39] N. Burgess, J. Donnett, K. Jeffery, and J. O'Keefe. "Robotic and neuronal simulation of the hippocampus and rat navigation." In: *Trans. R. Soc. Lond. B Biol. Sci.* 352 (1997), pp. 1535–1543.

[40] E. A. Bushong, M. E. Martone, Y. Z. Jones, and M. H. Ellisman. "Protoplasmic astrocytes in CA1 stratum radiatum occupy separate anatomical domains". In: *Journal of Neuroscience* 22.1 (2002), pp. 183–192.

[41] C. Buzsáki, C. A. Anastassiou, and C. Koch. "The origin of extracellular fields and currents– EEG, ECoG, LFP and spikes." In: *Nat. Rev. Neurosci.* 13 (2012), pp. 407–420.

[42] G. Buzsáki. "Theta Oscillations in the Hippocampus". In: *Neuron* 33 (2002), pp. 325–340. DOI: https://doi.org/10.1016/S0896-6273(02)00586-X.

[43] G. Buzsáki and A. Draguhn. "Neuronal Oscillations in Cortical Networks". In: *Science* 304 (2004), pp. 1926–1929. DOI: 10.1126/science.1099745.

[44] K. L. Casey, M. Cuenod, and P. D. Maclean. "Unit analysis of visual input to posterior limbic cortex. II. Intracerebral stimuli". In: *J. Neurophysiol* 28 (1965), pp. 1118–1131. DOI: https://doi.org/10.1152/jn.1965.28.6.1118.

[45] H. Chai, B. Diaz-Castro, E. Shigetomi, E. Monte, J. C. Octeau, X. Yu, W. Cohn, P. S. Rajendran, T. M. Vondriska, J. P. Whitelegge, et al. "Neural circuit-specialized astrocytes: transcriptomic, proteomic, morphological, and functional evidence". In: *Neuron* 95.3 (2017), pp. 531–549.

[46] A. C. Charles, J. E. Merrill, E. R. Dirksen, and M. J. Sandersont. "Intercellular signaling in glial cells: calcium waves and oscillations in response to mechanical stimulation and glutamate". In: *Neuron* 6.6 (1991), pp. 983–992.

[47] J. Chen, Z. Tan, L. Zeng, X. Zhang, Y. He, W. Gao, X. Wu, Y. Li, B. Bu, W. Wang, et al. "Heterosynaptic long-term depression mediated by ATP released from astrocytes". In: *Glia* 61.2 (2013), pp. 178–191.

[48] T.-W. Chen, T. J. Wardill, Y. Sun, S. R. Pulver, S. L. Renninger, A. Baohan, E. R. Schreiter, R. A. Kerr, M. B. Orger, V. Jayaraman, et al. "Ultrasensitive fluorescent proteins for imaging neuronal activity". In: *Nature* 499.7458 (2013), pp. 295–300.

[49] S. Coco, F. Calegari, E. Pravettoni, D. Pozzi, E. Taverna, P. Rosa, M. Matteoli, and C. Verderio. "Storage and release of ATP from astrocytes in culture". In: *Journal of Biological Chemistry* 278.2 (2003), pp. 1354–1362.

[50] A. H. Cornell-Bell, S. M. Finkbeiner, M. S. Cooper, and S. J. Smith. "Glutamate induces calcium waves in cultured astrocytes: long-range glial signaling". In: *Science* 247 (1990), pp. 470–473.

[51] M. L. Cotrina, J. H.-C. Lin, A. Alves-Rodrigues, S. Liu, J. Li, H. Azmi-Ghadimi, J. Kang, C. C. Naus, and M. Nedergaard. "Connexins regulate calcium signaling by controlling ATP release". In: *Proceedings of the National Academy of Sciences* 95.26 (1998), pp. 15735–15740.

[52] A. Covelo and A. Araque. "Neuronal activity determines distinct gliotransmitter release from a single astrocyte". In: *Elife* 7 (2018), e32237.

[53] B. G. Cragg. "Afferent connexions of the allocortex". In: *J. Anat.* 99 (1965), pp. 339–357.

[54] B. G. Cragg. "Olfactory and other afferent connections of the hippocampus in the rabbit, rat and cat". In: *Experimental Neurology* 3 (1961), pp. 588–600. DOI: https://doi.org/10.1016/S0014-4886(61)80007-1.

[55] B. G. Cragg. "Responses of the hippocampus to stimulation of the olfactory bulb and of various afferent nerves in five mammals". In: *Experimental Neurology* 2 (1960), pp. 547–572. DOI: https://doi.org/10.1016/0014-4886(60)90031-5.

[56] J. C. Cronk and J. Kipnis. "Microglia–the brain's busy bees". In: *F1000prime reports* 5 (2013).

[57] E. C. Crosby, B. R. DeJonge, and R. Schneider. "Evidence for some of the trends in the phylogenetic development of the vertebrate telencephalon. In Evolution of the Forebrain (eds R. Hassler and H. Stephan)". In: *Georg Thieme Verlag, Stuttgart* (1966), pp. 117–135.

[58] M. Cuenod, K. L. Casey, and P. D. MACLEAN. "Unit analysis of visual input to posterior limbic cortex. I. Photic stimulation". In: *J. Neurophysiol.* 28 (1965), pp. 1101–17. DOI: https://doi.org/10.1152/jn.1965.28.6.1101.

[59] K. E. Cullen and J. S. Taube. "Our sense of direction: progress, controversies and challenges". In: *Nature Neuroscience* 20.11 (2017), p. 1465.

[60] M. D'Ascenzo, T. Fellin, M. Terunuma, R. Revilla-Sanchez, D. F. Meaney, Y. P. Auberson, S. J. Moss, and P. G. Haydon. "mGluR5 stimulates gliotransmission in the nucleus accumbens". In: *Proceedings of the National Academy of Sciences* 104.6 (2007), pp. 1995–2000.

[61] H. Dana, B. Mohar, Y. Sun, S. Narayan, A. Gordus, J. P. Hasseman, G. Tsegaye, G. T. Holt, A. Hu, D. Walpita, R. Patel, J. J. Macklin, C. I. Bargmann, M. B. Ahrens, E. R. Schreiter, V. Jayaraman, L. L. Looger, K. Svoboda, and D. S. Kim. "Sensitive red protein calcium indicators for imaging neural activity". In: *Elife* 5 (2016), pp. 2738–2750.

[62] H. Dana, Y. Sun, B. Mohar, B. K. Hulse, A. M. Kerlin, J. P. Hasseman, G. Tsegaye, A. Tsang, A. Wong, R. Patel, et al. "High-performance calcium sensors for imaging activity in neuronal populations and microcompartments". In: *Nature methods* 16.7 (2019), pp. 649–657.

[63] N. C. Danbolt. "Glutamate uptake". In: *Progress in neurobiology* 65.1 (2001), pp. 1–105.

[64] J. W. Dani, A. Chernjavsky, and S. J. Smith. "Neuronal activity triggers calcium waves in hippocampal astrocyte networks". In: *Neuron* 8.3 (1992), pp. 429–440.

[65] N. B. Danielson, J. D. Zaremba, P. Kaifosh, J. Bowler, M. Ladow, and A. Losonczy. "Sublayer-specific coding dynamics during spatial navigation and learning in hippocampal area CA1". In: *Neuron* 91.3 (2016), pp. 652–665.

[66] L. M. De Biase, A. Nishiyama, and D. E. Bergles. "Excitability and synaptic communication within the oligodendrocyte lineage". In: *Journal of Neuroscience* 30.10 (2010), pp. 3600–3611.

[67] W. Denk, K. R. Delaney, A. Gelperin, D. Kleinfeld, B. W. Strowbridge, D. W. Tank, and R. Yuste. "Anatomical and functional imaging of neurons using 2-photon laser scanning microscopy." In: *J. Neurosci. Methods* 54 (1994), pp. 151–162.

[68] W. Denk, J. H. Strickler, and W. W. Webb. "Two-photon laser scanning fluorescence microscopy". In: *Science* 248.4951 (1990), pp. 73–76.

[69] M. A. Di Castro, J. Chuquet, N. Liaudet, K. Bhaukaurally, M. Santello, D. Bouvier, P. Tiret, and A. Volterra. "Local Ca 2+ detection and modulation of synaptic release by astrocytes". In: *Nature neuroscience* 14.10 (2011), pp. 1276–1284.

[70] L. Dimou, C. Simon, F. Kirchhoff, H. Takebayashi, and M. Götz. "Progeny of Olig2-expressing progenitors in the gray and white matter of the adult mouse cerebral cortex". In: *Journal of Neuroscience* 28.41 (2008), pp. 10434–10442.

[71] F. Ding, J. O'Donnell, A. S. Thrane, D. Zeppenfeld, H. Kang, L. Xie, F. Wang, and M. Nedergaard. "α1-Adrenergic receptors mediate coordinated Ca2+ signaling of cortical astrocytes in awake, behaving mice". In: *Cell calcium* 54.6 (2013), pp. 387–394.

[72] D. A. Dombeck, C. D. Harvey, L. Tian, L. L. Looger, and D. W. Tank. "Functional imaging of hippocampal place cells at cellular resolution during virtual navigation." In: *Nat. Neurosci.* 13 (2010), pp. 1433–1440.

[73] D. A. Dombeck, A. N. Khabbaz, F. Collman, T. L. Adelman, and D. W. Tank. "Imaging Large-Scale Neural Activity with Cellular Resolution in Awake, Mobile Mice". In: *Neuron* 56 (2007), pp. 43–57. DOI: https://doi.org/10.1016/j.neuron.2007.08.003..

[74] M. R. Elmore, R. J. Lee, B. L. West, and K. N. Green. "Characterizing newly repopulated microglia in the adult mouse: impacts on animal behavior, cell morphology, and neuroinflammation". In: *PloS one* 10.4 (2015), e0122912.

[75] M. R. Elmore, A. R. Najafi, M. A. Koike, N. N. Dagher, E. E. Spangenberg, R. A. Rice, M. Kitazawa, B. Matusow, H. Nguyen, B. L. West, et al. "Colony-stimulating factor 1 receptor signaling is necessary for microglia viability, unmasking a microglia progenitor cell in the adult brain". In: *Neuron* 82.2 (2014), pp. 380–397.

[76] T. Fellin. "Communication between neurons and astrocytes: relevance to the modulation of synaptic and network activity". In: *Journal of neurochemistry* 108.3 (2009), pp. 533–544.

[77] T. Fellin, M. M. Halassa, M. Terunuma, F. Succol, H. Takano, M. Frank, S. J. Moss, and P. G. Haydon. "Endogenous nonneuronal modulators of synaptic transmission control cortical slow oscillations in vivo". In: *Proceedings of the National Academy of Sciences* 106.35 (2009), pp. 15037–15042.

[78] T. Fellin, O. Pascual, S. Gobbo, T. Pozzan, P. G. Haydon, and G. Carmignoto. "Neuronal synchrony mediated by astrocytic glutamate through activation of extrasynaptic NMDA receptors". In: *Neuron* 43.5 (2004), pp. 729–743.

[79] T. Fellin, O. Pascual, and P. G. Haydon. "Astrocytes Coordinate Synaptic Networks: Balanced Excitation and Inhibition". In: *Physiology* 21 (2006), pp. 208–215.

[80] T. Fellin, T. Pozzan, and G. Carmignoto. "Purinergic receptors mediate two distinct glutamate release pathways in hippocampal astrocytes". In: *Journal of Biological Chemistry* 281.7 (2006), pp. 4274–4284.

[81] C. Ffrench-Constant and M. C. Raff. "Proliferating bipotential glial progenitor cells in adult rat optic nerve". In: *Nature* 319.6053 (1986), pp. 499–502.

[82] A. J. Filiano, S. P. Gadani, and J. Kipnis. "Interactions of innate and adaptive immunity in brain development and function". In: *Brain research* 1617 (2015), pp. 18–27.

[83] B. A. Flusberg, A. Nimmerjahn, E. D. Cocker, E. A. Mukamel, R. P. Barretto, T. H. Ko, L. D. Burns, J. C. Jung, and M. J. Schnitzer. "High-speed, miniaturized fluorescence microscopy in freely moving mice". In: *Nature methods* 5.11 (2008), pp. 935–938.

[84] A. Forli, D. Vecchia, N. Binini, F. Succol, S. Bovetti, C. Moretti, F. Nespoli, M. Mahn, C. A. Baker, M. M. Bolton, et al. "Two-photon bidirectional control and imaging of neuronal excitability with high spatial resolution in vivo". In: *Cell reports* 22.11 (2018), pp. 3087–3098.

[85] Y. Fujita and H. Sakata. "Electrophysiological properties of CA1 and CA2 apical dendrites of rabbit hippocampus". In: *J. Neurophysiol.* 25 (1962), pp. 209–222. DOI: https://doi.org/10.1152/jn.1962.25.2.209.

[86] M. Fyhn, T. Hafting, A. Treves, M. Moser, and E. Moser. "Hippocampal remapping and grid realignment in entorhinal cortex." In: *Nature* 446 (2007), pp. 190–194.

[87] M. Fyhn, S. Molden, M. Witter, E. Moser, and M. Moser. "Spatial representation in the entorhinal cortex." In: *Science* 305 (2004), pp. 1258–1264.

[88] M. Fyhn, T. Solstad, and T. Hafting. "Entorhinal grid cells and the neural basis of navigation." In: *Hippocampal Place Fields* (2008), pp. 237–252.

[89] J. L. Gauthier and D. W. Tank. "A Dedicated Population for Reward Coding in the Hippocampus". In: *Neuron* 99 (2018), pp. 179–193.

[90] C. Genoud, C. Quairiaux, P. Steiner, H. Hirling, E. Welker, and G. W. Knott. "Plasticity of astrocytic coverage and glutamate transporter expression in adult mouse cortex". In: *PLoS Biol* 4.11 (2006), e343.

[91] A. Giovannucci, J. Friedrich, P. Gunn, J. Kalfon, B. L. Brown, S. A. Koay, J. Taxidis, F. Najafi, J. L. Gauthier, P. Zhou, B. S. Khakh, D. W. Tank, D. B. Chklovskii, and E. A. Pnevmatikakis. "CaImAn an open source tool for scalable calcium imaging data analysis". In: *Elife* 8:e38173 (2019). DOI: 10.7554/eLife.38173.

[92] P. Gloor, C. L. Vera, and L. Sperti. "Electrophysiological studies of hippocampal neurons. I. Configuration and laminar analysis of the 'resting' potential gradient, of the main-transient response to perforant path, fimbrial and mossy fibre volleys, and of 'spontaneous' activity". In: *Electroencephalogr. clin. Neurophysiol.*

15 (1963), pp. 353–378. DOI: https://doi.org/10.1016/0013-4694(63)90060-9.

[93] M. Gómez-Gonzalo, T. Zehnder, L. M. Requie, P. Bezzi, and G. Carmignoto. "Insights into the release mechanism of astrocytic glutamate evoking in neurons NMDA receptor-mediated slow depolarizing inward currents". In: *Glia* 66.10 (2018), pp. 2188–2199.

[94] J. Goodridge and J. Taube. "Preferential use of the landmark navigational system by head direction cells in rats." In: *Behav. Neurosci.* 109 (1995), pp. 49–61.

[95] M. Göppert-Mayer. "Über Elementarakte mit zwei Quantensprüngen". In: *Ann. Phys.* 401 (1931), pp. 273–294.

[96] C. Grienberger and A. Konnerth. "Imaging calcium in neurons". In: *Neuron* 73.5 (2012), pp. 862–885.

[97] R. M. Grieves and K. J. Jeffery. "The representation of space in the brain". In: *Behavioural Processes* 135 (2017), pp. 113–131.

[98] R. Grieves, S. Jedidi-Ayoub, K. Mishchanchuk, A. Liu, S. Renaudineau, and K. J. Jeffery. "The place-cell representation of volumetric space in rats". In: *Nat Commun* 11 (2020), p. 789. DOI: https://doi.org/10.1038/s41467-020-14611-7.

[99] T. Hafting, M. Fyhn, S. Molden, M.-B. Moser, and E. Moser. "Microstructure of a spatial map in the entorhinal cortex." In: *Nature* 436 (2005), pp. 801–806.

[100] M. M. Halassa, T. Fellin, H. Takano, J.-H. Dong, and P. G. Haydon. "Synaptic islands defined by the territory of a single astrocyte". In: *Journal of Neuroscience* 27.24 (2007), pp. 6473–6477.

[101] M. M. Halassa, C. Florian, T. Fellin, J. R. Munoz, S.-Y. Lee, T. Abel, P. G. Haydon, and M. G. Frank. "Astrocytic modulation of sleep homeostasis and cognitive consequences of sleep loss". In: *Neuron* 61.2 (2009), pp. 213–219.

[102] K. D. Harris, R. Q. Quiroga, J. Freeman, and S. L. Smith. "Improving data quality in neuronal population recordings". In: *Nature neuroscience* 19.9 (2016), pp. 1165–1174.

[103] T. Hartley, H. Tom, N. Burgess, C. Lever, F. Cacucci, and J. O'Keefe. "Modeling place fields in terms of the cortical inputs to the hippocampus." In: *Hippocampus* 10 (2000), pp. 369–379.

[104] M. D. Haustein, S. Kracun, X.-H. Lu, T. Shih, O. Jackson-Weaver, X. Tong, J. Xu, X. W. Yang, T. J. O'Dell, J. S. Marvin, et al. "Conditions and constraints for astrocyte calcium signaling in the hippocampal mossy fiber pathway". In: *Neuron* 82.2 (2014), pp. 413–429.

[105] Y. Hayashi, M. Nomura, S.-I. Yamagishi, S.-I. Harada, J. Yamashita, and H. Yamamoto. "Induction of various blood-brain barrier properties in non-neural endothelial cells by close apposition to co-cultured astrocytes". In: *Glia* 19.1 (1997), pp. 13–26.

[106] P. Heier. *Fundamental Principles in the structure of the brain: A study of the brain of petromyzon fluviatilis*. Vol. 5. Karger, 1948.

[107] L. Heimer. "Synaptic distribution of centripetal and centrifugal nerve fibres in the olfactory system of the rat. An experimental anatomical study". In: *J. Anat.* 103 (1968), pp. 413–432.

[108] F. Helmchen and W. Denk. "Deep tissue two-photon microscopy". In: *Nat. Methods* 2 (2005), pp. 932–940.

[109] F. Helmchen and J. Waters. "Ca2+ imaging in the mammalian brain in vivo." In: *Eur. J. Pharmacol.* 447 (2002), pp. 119–129.

[110] C. Henneberger, T. Papouin, S. H. Oliet, and D. A. Rusakov. "Long-term potentiation depends on release of D-serine from astrocytes". In: *Nature* 463.7278 (2010), pp. 232–236.

[111] S. Herculano-Houzel. "Scaling of brain metabolism with a fixed energy budget per neuron: implications for neuronal activity, plasticity and evolution". In: *PloS one* 6.3 (2011), e17514.

[112] S. Herculano-Houzel. "The glia/neuron ratio: how it varies uniformly across brain structures and species and what that means for brain physiology and evolution". In: *Glia* 62.9 (2014), pp. 1377–1391.

[113] M. A. Herman and C. E. Jahr. "Extracellular glutamate concentration in hippocampal slice". In: *Journal of Neuroscience* 27.36 (2007), pp. 9736–9741.

[114] A. Hill. "First occurrence of hippocampal spatial firing in a new environment". In: *Exp. Neurol.* 62 (1978), pp. 282–297. DOI: https://doi.org/10.1016/0014-4886(78)90058-4.

[115] H. Hirase, L. Qian, P. Barthó, and G. Buzsáki. "Calcium dynamics of cortical astrocytic networks in vivo". In: *PLoS Biol* 2.4 (2004), e96.

[116] A. Hjorth-Simonsen. "Some intrinsic connections of the hippocampus in the rat: An experimental analysis". In: *J. Comp. Neurol.* 147.2 (1973), pp. 145–161. DOI: 10.1002/cne.901470202.

[117] A. Hjorth-Simonsen and B. Jeune. "Origin and termination of the hippocampal perforant path in the rat studied by silver impregnation". In: *J. Comp. Neurol.* 144.2 (1972), pp. 215–232. DOI: https://doi.org/10.1002/cne.901440206.

[118] K. Horikawa, Y. Yamada, T. Matsuda, K. Kobayashi, M. Hashimoto, T. Matsuura, A. Miyawaki, T. Michikawa, K. Mikoshiba, and T. Nagai. "Spontaneous network activity visualized by ultrasensitive Ca2+ indicators, yellow Cameleon-Nano". In: *Nat. Methods, vol.* 7 (2010), pp. 729–732.

[119] D. H. Hubel and T. N. Wiesel. "Receptive fields of single neurones in the cat's striate cortex." In: *J. Physiol.* 148 (1959), pp. 574–591.

[120] E. G. Hughes, S. H. Kang, M. Fukaya, and D. E. Bergles. "Oligodendrocyte progenitors balance growth with self-repulsion to achieve homeostasis in the adult brain". In: *Nature neuroscience* 16.6 (2013), pp. 668–676.

[121] J. Huxter, N. Burgess, and J. O'Keefe. "Independent rate and temporal coding in hippocampal pyramidal cells". In: *Nature* 425 (2003), pp. 828–832. DOI: https://doi.org/10.1038/nature02058.

[122] S. Jäkel and L. Dimou. "Glial cells and their function in the adult brain: a journey through the history of their ablation". In: *Frontiers in cellular neuroscience* 11 (2017), p. 24.

[123] M. Jankowski and S. O'Mara. "Dynamics of place, boundary and object encoding in rat anterior claustrum." In: *Front. Behav. Neurosci.* 9 (2015), p. 250.

[124] M. Jankowski, J. Passecker, M. Islam, S. Vann, J. Erichsen, J. Aggleton, and S. O'Mara. "Evidence for spatially-responsive neurons in the rostral thalamus." In: *Front. Behav. Neurosci.* 9 (2015), p. 256.

[125] K. Jeffery. "Integration of the sensory inputs to place cells: what, where, why, and how?" In: *Hippocampus* 17 (2007), pp. 775–783.

[126] P. Jourdain, L. H. Bergersen, K. Bhaukaurally, P. Bezzi, M. Santello, M. Domercq, C. Matute, F. Tonello, V. Gundersen, and A. Volterra. "Glutamate exocytosis from astrocytes controls synaptic strength". In: *Nature neuroscience* 10.3 (2007), pp. 331–339.

[127] J. J. Jun, N. A. Steinmetz, and J. H. Siegle. "Fully integrated silicon probes for high-density recording of neural activity". In: *Nature* 551 (2017), pp. 232–236.

[128] J. B. Kacerovsky and K. Murai. "Stargazing: Monitoring subcellular dynamics of brain astrocytes". In: *Neuroscience* 323 (2016), pp. 84–95.

[129] E. R. Kandel, W. A. Spencer, and F. J. Brinley. "Electrophysiology of hippocampal neurons. I. Sequential invasion and synaptic organization". In: *J. Neurophysiol.* 24 (1961), pp. 225–242. DOI: https://doi.org/10.1152/jn.1961.24.3.225.

[130] J. Kang, L. Jiang, S. A. Goldman, and M. Nedergaard. "Astrocyte-mediated potentiation of inhibitory synaptic transmission". In: *Nature neuroscience* 1.8 (1998), pp. 683–692.

[131] N. Kang, J. Xu, Q. Xu, M. Nedergaard, and J. Kang. "Astrocytic glutamate release-induced transient depolarization and epileptiform discharges in hippocampal CA1 pyramidal neurons". In: *Journal of neurophysiology* 94.6 (2005), pp. 4121–4130.

[132] S. Kang, S.-I. Hong, J. Lee, L. Peyton, M. Baker, S. Choi, H. Kim, S.-Y. Chang, and D.-S. Choi. "Activation of astrocytes in the dorsomedial striatum facilitates transition from habitual to goal-directed reward-seeking behavior". In: *Biological psychiatry* 88.10 (2020), pp. 797–808.

[133] C. U. A. Kappers, G. C. Huber, and E. C. Crosby. *The comparative anatomy of the nervous system of vertebrates*. Vol. 2. Macmillan, 1936, pp. 1248–1255.

[134] R. Káradóttir, P. Cavelier, L. H. Bergersen, and D. Attwell. "NMDA receptors are expressed in oligodendrocytes and activated in ischaemia". In: *Nature* 438.7071 (2005), pp. 1162–1166.

[135] D. I. B. Kerr and B. J. Dennis. "Collateral projection of the lateral olfactory tract to entorhinal cortical areas in the cat". In: *Brain Res.* 36 (1972), pp. 399–403. DOI: https://doi.org/10.1016/0006-8993(72)90743-3.

[136] H. Kettenmann, K. Backus, and M. Schachner. "Aspartate, glutamate and γ-aminobutyric acid depolarize cultured astrocytes". In: *Neuroscience Letters* 52 (1984), pp. 25–29. DOI: https://doi.org/10.1016/0304-3940(84)90345-8.

[137] H. Kettenmann, K. Backus, and M. Schachner. "Aspartate, glutamate and γ-aminobutyric acid depolarize cultured astrocytes". In: *Neuroscience letters* 52.1-2 (1984), pp. 25–29.

[138] H. Kettenmann, U.-K. Hanisch, M. Noda, and A. Verkhratsky. "Physiology of microglia". In: *Physiological reviews* 91.2 (2011), pp. 461–553.

[139] B. S. Khakh and B. Deneen. "The emerging nature of astrocyte diversity". In: *Annual review of neuroscience* 42 (2019), pp. 187–207.

[140] K. Kierdorf, M. Prinz, et al. "Microglia in steady state". In: *The Journal of clinical investigation* 127.9 (2017), pp. 3201–3209.

[141] S. U. Kim and J. de Vellis. "Microglia in health and disease". In: *Journal of neuroscience research* 81.3 (2005), pp. 302–313.

[142] J. Knierim, H. Kudrimoti, and B. McNaughton. "Place cells, head direction cells, and the learning of landmark stability." In: *Neurosci* 15 (1995), pp. 1648–1659.

[143] T. Knöpfel, J. Díez-García, and W. Akemann. "Optical probing of neuronal circuit dynamics: genetically encoded versus classical fluorescent sensors". In: *Trends Neurosci.* 29 (2006), pp. 160–166.

[144] A. Kozlov, M. Angulo, E. Audinat, and S. Charpak. "Target cell-specific modulation of neuronal activity by astrocytes". In: *Proceedings of the National Academy of Sciences* 103.26 (2006), pp. 10058–10063.

[145] J. E. Krettek and J. L. Price. "Projections from the amygdala to the perirhinal and entorhinal cortices and to the subiculum". In: *Brain Res.* 71 (1974), pp. 150–154. DOI: https://doi.org/10.1016/0006-8993(74)90199-1.

[146] T. O. Kvålseth. "On normalized mutual information: measure derivations and properties". In: *Entropy* 19.11 (2017), p. 631.

[147] R. M. Lebovitz, M. Dichter, and W. A. Spencer. "Recurrent excitation in the CA3 region of cat hippocampus". In: *Int. J. Neurosci.* 2 (1971), pp. 99–108. DOI: https://doi.org/10.3109/00207457109146996.

[148] G. R. Leichnetz and J. Astruc. "Preliminary evidence for a direct projection of the prefrontal cortex to the hippocampus in the squirrel monkey". In: *Brain Behav. Evol.* 11 (1975), pp. 355–364. DOI: https://doi.org/10.1159/000123645.

[149] C. Lever, S. Burton, A. Jeewajee, J. O'Keefe, and N. Burgess. "Boundary vector cells in the subiculum of the hippocampal formation." In: *J. Neurosci.* 29 (2009), pp. 9771–9777.

[150] T. Y. Lin, P. Goyal, R. Girshick, K. He, and P. Dollar. "Focal Loss for Dense Object Detection". In: *IEEE Trans. Pattern. Anal. Mach. Intell.* 42 (2020), pp. 318–327. DOI: 10.1109/TPAMI.2018.2858826.

[151] B. L. Lind, A. R. Brazhe, S. B. Jessen, F. C. Tan, and M. J. Lauritzen. "Rapid stimulus-evoked astrocyte Ca2+ elevations and hemodynamic responses in mouse somatosensory cortex in vivo". In: *Proceedings of the National Academy of Sciences* 110.48 (2013), E4678–E4687.

[152] B. L. Lind, S. B. Jessen, M. Lønstrup, C. Joséphine, G. Bonvento, and M. Lauritzen. "Fast Ca2+ responses in astrocyte end-feet and neurovascular coupling in mice". In: *Glia* 66.2 (2018), pp. 348–358.

[153] Q.-s. Liu, Q. Xu, G. Arcuino, J. Kang, and M. Nedergaard. "Astrocyte-mediated activation of neuronal kainate receptors". In: *Proceedings of the National Academy of Sciences* 101.9 (2004), pp. 3172–3177.

[154] L. L. Looger and O. Griesbeck. "Genetically encoded neural activity indicators". In: *Curr. Opin. Neurobiol.* 22 (2012), pp. 18–23.

[155] R. Lorente De Nó. "Studies on the structure of the cerebral cortex. II. Continuation of the study of the ammonic system". In: *Journal für Psychologie und Neurologie* (1934), pp. 113–177.

[156] I. Lundgaard, M. J. Osório, B. Kress, S. Sanggaard, and M. Nedergaard. "White matter astrocytes in health and disease". In: *Neuroscience* 276 (2014), pp. 161–173.

[157] B. A. MacVicar and E. A. Newman. "Astrocyte regulation of blood flow in the brain". In: *Cold Spring Harbor perspectives in biology* 7.5 (2015), a020388.

[158] C. Magri, K. Whittingstall, V. Singh, N. K. Logothetis, and S. Panzeri. "A toolbox for the fast information analysis of multiple-site LFP, EEG and spike train recordings". In: *BMC neuroscience* 10.1 (2009), pp. 1–24.

[159] E. Mankin, G. Diehl, F. Sparks, L. Stefan, and J. Leutgeb. "Hippocampal CA2 activity patterns change over time to a larger extent than between spatial contexts". In: *Neuron* 85 (2015), pp. 190–201. DOI: https://doi.org/10.1016/j.neuron.2014.12.001.

[160] T. W. Margrie, A. Meyer A. H.and Caputi, H. Monyer, M. T. Hasan, A. T. Schaefer, W. Denk, and M. Brecht. "Targeted whole-cell recordings in the mammalian brain in vivo." In: *Neuron* 39 (2003), pp. 911–918.

[161] L. Mariotti, G. Losi, A. Lia, M. Melone, A. Chiavegato, M. Gómez-Gonzalo, M. Sessolo, S. Bovetti, A. Forli, M. Zonta, L. M. Requie, I. Marcon, A. Pugliese, C. Viollet, B. Bettler, T. Fellin, F. Conti, and G. Carmignoto. "Interneuron-specific signaling evokes distinctive somatostatin-mediated responses in adult cortical astrocytes". In: *Nature Communications* 9 (2018). DOI: 10.1038/s41467-017-02642-6.

[162] C. Markus E.J.and Barnes, B. McNaughton, and W. Gladden V.L.and Skaggs. "Spatial information content and reliability of hippocampal CA1 neurons: effects of visual input." In: *Hippocampus* 4 (1994), pp. 410–421.

[163] E. J. Markus, C. A. Barnes, B. L. McNaughton, V. L. Gladden, and W. E. Skaggs. "Spatial information content and reliability of hippocampal CA1 neurons: effects of visual input". In: *Hippocampus* 4.4 (1994), pp. 410–421.

[164] J. H. Marshel, Y. S. Kim, T. A. Machado, S. Quirin, B. Benson, J. Kadmon, C. Raja, A. Chibukhchyan, C. Ramakrishnan, M. Inoue, et al. "Cortical layer–specific critical dynamics triggering perception". In: *Science* 365.6453 (2019).

[165] T. McLardy. "Anticipatory recall deficit after cingulumotomy in rats". In: *Exp. Neurol.* 32 (1971), pp. 141–151. DOI: https://doi.org/10.1016/0014-4886(71)90058-6.

[166] B. McNaughton, C. Barnes, and J. O'Keefe. "The contributions of position, direction, and velocity to single unit activity in the hippocampus of freely-moving

rats". In: *Exp. Brain Res.* 52 (1983), pp. 41–49. DOI: https://doi.org/10.1007/BF00237147.

[167] B. McNaughton, F. Battaglia, O. Jensen, E. Moser, and M.-B. Moser. "Path integration and the neural basis of the cognitive map." In: *Nat. Rev. Neurosci.* 7 (2006), pp. 663–678.

[168] S. Mederos, C. Sánchez-Puelles, J. Esparza, M. Valero, A. Ponomarenko, and G. Perea. "GABAergic signaling to astrocytes in the prefrontal cortex sustains goal-directed behaviors". In: *Nature Neuroscience* (2020), pp. 1–11.

[169] M. R. Metea and E. A. Newman. "Glial cells dilate and constrict blood vessels: a mechanism of neurovascular coupling". In: *Journal of Neuroscience* 26.11 (2006), pp. 2862–2870.

[170] R. Min and T. Nevian. "Astrocyte signaling controls spike timing–dependent depression at neocortical synapses". In: *Nature neuroscience* 15.5 (2012), pp. 746–753.

[171] M. Minderer, C. D. Harvey, F. Donato, and E. I. Moser. "Virtual reality explored". In: *Nature* 533.7603 (2016), pp. 324–325.

[172] A. Miyawaki, J. Llopis, R. Heim, J. M. McCaffery, M. Adams J. A.and Ikura, and R. Y. Tsien. "Fluorescent indicators for Ca2+based on green fluorescent proteins and calmodulin". In: *Nature* 388 (1997), pp. 882–887.

[173] S. Mizumori and J. Williams. "Directionally selective mnemonic properties of neurons in the lateral dorsal nucleus of the thalamus of rats." In: *Neurosci* 13 (1993), pp. 4015–4028.

[174] R. S. Morrison and J. De Vellis. "Growth of purified astrocytes in a chemically defined medium". In: *Proceedings of the National Academy of Sciences* 78.11 (1981), pp. 7205–7209.

[175] M.-B. Moser, D. C. Rowland, and E. I. Moser. "Place cells, grid cells, and memory". In: *Cold Spring Harbor perspectives in biology* 7.2 (2015), a021808.

[176] J.-P. Mothet, A. T. Parent, H. Wolosker, R. O. Brady, D. J. Linden, C. D. Ferris, M. A. Rogawski, and S. H. Snyder. "D-serine is an endogenous ligand for the glycine site of the N-methyl-D-aspartate receptor". In: *Proceedings of the National Academy of Sciences* 97.9 (2000), pp. 4926–4931.

[177] J.-P. Mothet, L. Pollegioni, G. Ouanounou, M. Martineau, P. Fossier, and G. Baux. "Glutamate receptor activation triggers a calcium-dependent and SNARE protein-dependent release of the gliotransmitter D-serine". In: *Proceedings of the National Academy of Sciences* 102.15 (2005), pp. 5606–5611.

[178] Y. Mu, D. V. Bennett, M. Rubinov, S. Narayan, C. T. Yang, M. Tanimoto, B. D. Mensh, L. L. Looger, and M. B. Ahrens. "Glia Accumulate Evidence that Actions Are Futile and Suppress Unsuccessful Behavior". In: *Cell* 178 (2019), pp. 27–43.

[179] Y. Mu, D. V. Bennett, M. Rubinov, S. Narayan, C.-T. Yang, M. Tanimoto, B. D. Mensh, L. L. Looger, and M. B. Ahrens. "Glia accumulate evidence that actions are futile and suppress unsuccessful behavior". In: *Cell* 178.1 (2019), pp. 27–43.

[180] C. M. Müller and J. Best. "Ocular dominance plasticity in adult cat visual cortex after transplantation of cultured astrocytes". In: *Nature* 342.6248 (1989), pp. 427–430.

[181] R. Muller and J. Kubie. "The effects of changes in the environment on the spatial firing of hippocampal complex-spike cells." In: *Neurosci* 7 (1987), pp. 1951–1968.

[182] R. Muller, J. Kubie, and J. Ranck Jr. "Spatial firing patterns of hippocampal complex-spike cells in a fixed environment". In: *J. Neurosci.* https://doi.org/10.1523/JNEUROSCI.07-07-01935.1987 (1987), pp. 1935–1950. DOI: 7.

[183] P. H. J. Nafstad. "An electron microscope study on the termination of the perforant path fibres in the hippocampus and the fascia dentata". In: *Z. Zellforsch. mikrosk. Anal.* 76 (1967), pp. 532–542.

[184] E. A. Nagelhus and O. P. Ottersen. "Physiological roles of aquaporin-4 in brain". In: *Physiological reviews* 93.4 (2013), pp. 1543–1562.

[185] A. Nagy, J. Wu, and K. M. Berland. "Observation volumes and gamma-factors in two-photon fluorescence fluctuation spectroscopy." In: *Biophys. J.* 89 (2005), pp. 2077–2090.

[186] M. Navarrete and A. Araque. "Endocannabinoids mediate neuron-astrocyte communication". In: *Neuron* 57.6 (2008), pp. 883–893.

[187] M. Navarrete and A. Araque. "Endocannabinoids potentiate synaptic transmission through stimulation of astrocytes". In: *Neuron* 68.1 (2010), pp. 113–126.

[188] K.-A. Nave. "Myelination and support of axonal integrity by glia". In: *Nature* 468.7321 (2010), pp. 244–252.

[189] M. W. Nestor, L.-P. Mok, M. E. Tulapurkar, and S. M. Thompson. "Plasticity of neuron-glial interactions mediated by astrocytic EphARs". In: *Journal of Neuroscience* 27.47 (2007), pp. 12817–12828.

[190] W. J. Nett, S. H. Oloff, and K. D. Mccarthy. "Hippocampal astrocytes in situ exhibit calcium oscillations that occur independent of neuronal activity". In: *Journal of neurophysiology* 87.1 (2002), pp. 528–537.

[191] E. A. Newman and K. R. Zahs. "Calcium waves in retinal glial cells". In: *Science* 275.5301 (1997), pp. 844–847.

[192] S. Nielsen, E. A. Nagelhus, M. Amiry-Moghaddam, C. Bourque, P. Agre, and O. P. Ottersen. "Specialized membrane domains for water transport in glial cells: high-resolution immunogold cytochemistry of aquaporin-4 in rat brain". In: *Journal of Neuroscience* 17.1 (1997), pp. 171–180.

[193] A. Nimmerjahn, F. Kirchhoff, and F. Helmchen. "Resting microglial cells are highly dynamic surveillants of brain parenchyma in vivo". In: *Science* 308.5726 (2005), pp. 1314–1318.

[194] A. Nimmerjahn, F. Kirchhoff, J. N. Kerr, and F. Helmchen. "Sulforhodamine 101 as a specific marker of astroglia in the neocortex in vivo". In: *Nature methods* 1.1 (2004), pp. 31–37.

[195] A. Nimmerjahn, E. A. Mukamel, and M. J. Schnitzer. "Motor behavior activates Bergmann glial networks". In: *Neuron* 62.3 (2009), pp. 400–412.

[196] S. E. Nwaobi, V. A. Cuddapah, K. C. Patterson, A. C. Randolph, and M. L. Olsen. "The role of glial-specific Kir4. 1 in normal and pathological states of the CNS". In: *Acta neuropathologica* 132.1 (2016), pp. 1–21.

[197] J. O'Keefe and L. Nadel. *The Hippocampus as a Cognitive Map*. Vol. 27. Oxford University Press, 1980.

[198] J. O'Keefe. "Place units in the hippocampus of the freely moving rat". In: *Neurol.* 51 (1976), pp. 78–109. DOI: https://doi.org/10.1016/0014-4886(76)90055-8.

[199] J. O'Keefe and N. Burgess. "Geometric determinants of the place fields of hippocampal neurons." In: *Nature* 381 (1996), pp. 425–428.

[200] J. O'Keefe and D. Conway. "Hippocampal place units in the freely moving rat: why they fire where they fire". In: *Exp. Brain Res* 31 (1978), pp. 573–590.

[201] J. O'Keefe and M. Recce. "Phase relationship between hippocampal place units and the EEG theta rhythm". In: *Hippocampus* 3 (1993), pp. 317–330. DOI: https://doi.org/10.1002/hipo.450030307.

[202] J. O'Keefe. "Spatial cells in the hippocampal formation". In: *Nobel Lecture on* 7 (2014).

[203] K. Ohki, S. Chung, Y. H. Ch'ng, P. Kara, and R. C. Reid. "Functional imaging with cellular resolution reveals precise micro-architecture in visual cortex." In: *Nature* 433 (2005), pp. 597–603.

[204] M. Ohkura, M. Matsuzaki, H. Kasai, K. Imoto, and J. Nakai. "Genetically Encoded Bright Ca 2+ Probe Applicable for Dynamic Ca 2+ Imaging of Dendritic Spines". In: *Anal. Chem.* 77 (2005), pp. 5861–5869.

[205] M. Ohkura, T. Sasaki, C. Kobayashi, Y. Ikegaya, and J. Nakai. "An Improved Genetically Encoded Red Fluorescent Ca2+ Indicator for Detecting Optically Evoked Action Potentials". In: *PLoS One* 7 (2010), e39933.

[206] Y. Otsu, K. Couchman, D. G. Lyons, M. Collot, A. Agarwal, J.-M. Mallet, F. W. Pfrieger, D. E. Bergles, and S. Charpak. "Calcium dynamics in astrocyte processes during neurovascular coupling". In: *Nature neuroscience* 18.2 (2015), pp. 210–218.

[207] A. E. Palmer, Y. Qin, J. G. Park, and J. E. McCombs. "Design and application of genetically encoded biosensors." In: *Trends Biotechnol.* 29 (2011), pp. 144–152.

[208] A. Panatier, D. T. Theodosis, J.-P. Mothet, B. Touquet, L. Pollegioni, D. A. Poulain, and S. H. Oliet. "Glia-derived D-serine controls NMDA receptor activity and synaptic memory". In: *Cell* 125.4 (2006), pp. 775–784.

[209] A. Panatier, J. Vallée, M. Haber, K. K. Murai, J.-C. Lacaille, and R. Robitaille. "Astrocytes are endogenous regulators of basal transmission at central synapses". In: *Cell* 146.5 (2011), pp. 785–798.

[210] D. N. Pandya and H. G. J. M. Kupyers. "Cortico-cortical connections in the rhesus monkey". In: *Brain Res.* 13 (1969), pp. 13–36. DOI: https://doi.org/10.1016/0006-8993(69)90141-3.

[211] D. N. Pandya and A. A. Vignolo. "Interhemispheric projections of the parietal lobe in the rhesus monkey". In: *Brain Res.* 15 (1969), p. 49. DOI: https://doi.org/10.1016/0006-8993(69)90309-6.

[212] S. Panzeri, R. Senatore, M. A. Montemurro, and R. S. Petersen. "Correcting for the sampling bias problem in spike train information measures". In: *J. Neurophysiol.* 98 (2007), pp. 1064–1072. DOI: 10.1152/jn.00559.2007..

[213] S. Panzeri and A. Treves. "Analytical estimates of limited sampling biases in different information measures". In: *Network* 7 (1996), pp. 87–107. DOI: 10.1080/0954898X.1996.11978656.

[214] S. Panzeri, C. D. Harvey, E. Piasini, P. E. Latham, and T. Fellin. "Cracking the neural code for sensory perception by combining statistics, intervention, and behavior". In: *Neuron* 93.3 (2017), pp. 491–507.

[215] C. N. Parkhurst, G. Yang, I. Ninan, J. N. Savas, J. R. Yates III, J. J. Lafaille, B. L. Hempstead, D. R. Littman, and W.-B. Gan. "Microglia promote learning-dependent synapse formation through brain-derived neurotrophic factor". In: *Cell* 155.7 (2013), pp. 1596–1609.

[216] V. Parpura, T. A. Basarsky, F. Liu, K. Jeftinija, S. Jeftinija, and P. G. Haydon. "Glutamate-mediated astrocyte–neuron signalling". In: *Nature* 369.6483 (1994), pp. 744–747.

[217] H. R. Parri, T. M. Gould, and V. Crunelli. "Spontaneous astrocytic Ca 2+ oscillations in situ drive NMDAR-mediated neuronal excitation". In: *Nature neuroscience* 4.8 (2001), pp. 803–812.

[218] O. Pascual, K. B. Casper, C. Kubera, J. Zhang, R. Revilla-Sanchez, J.-Y. Sul, H. Takano, S. J. Moss, K. McCarthy, and P. G. Haydon. "Astrocytic purinergic signaling coordinates synaptic networks". In: *Science* 310.5745 (2005), pp. 113–116.

[219] M. Paukert, A. Agarwal, J. Cha, V. A. Doze, J. U. Kang, and D. E. Bergles. "Norepinephrine controls astroglial responsiveness to local circuit activity". In: *Neuron* 82.6 (2014), pp. 1263–1270.

[220] J. B. Pawley. *Handbook Of Biological Confocal Microscopy.* 2006.

[221] L. Pellerin, A.-K. Bouzier-Sore, A. Aubert, S. Serres, M. Merle, R. Costalat, and P. J. Magistretti. "Activity-dependent regulation of energy metabolism by astrocytes: an update". In: *Glia* 55.12 (2007), pp. 1251–1262.

[222] L. Pellerin and P. J. Magistretti. "Glutamate uptake into astrocytes stimulates aerobic glycolysis: a mechanism coupling neuronal activity to glucose utilization". In: *Proceedings of the National Academy of Sciences* 91.22 (1994), pp. 10625–10629.

[223] G. Perea and A. Araque. "Astrocytes potentiate transmitter release at single hippocampal synapses". In: *Science* 317.5841 (2007), pp. 1083–1086.

[224] G. Perea and A. Araque. "Properties of synaptically evoked astrocyte calcium signal reveal synaptic information processing by astrocytes". In: *Journal of Neuroscience* 25.9 (2005), pp. 2192–2203.

[225] G. Perea, M. Sur, and A. Araque. "Neuron-glia networks: integral gear of brain function". In: *Frontiers in cellular neuroscience* 8 (2014), p. 378.

[226] J. M. Petras. "Connections of the parietal lobe". In: *J. Psychiat. Res.* 8 (1971), pp. 189–201. DOI: https://doi.org/10.1016/B978-0-08-017007-7.50008-2.

[227] J. C. Pinheiro and D. M. Bates. "Linear mixed-effects models: basic concepts and examples". In: *Mixed-effects models in S and S-Plus* (2000), pp. 3–56.

[228] E. A. Pnevmatikakis and A. Giovannucci. "NoRMCorre: An online algorithm for piecewise rigid motion correction of calcium imaging data". In: *Journal of Neuroscience Methods* 291 (2017), pp. 83–94. DOI: https://doi.org/10.1016/j.jneumeth.2017.07.031..

[229] G. Pola, A. Thiele, K. Hoffmann, and S. Panzeri. "An exact method to quantify the information transmitted by different mechanisms of correlational coding". In: *Network: Computation in Neural Systems* 14 (2003), pp. 35–60.

[230] T. P. S. Powell, W. M. Cowan, and G. Raisman. "The central olfactory connections". In: *J. Anat.* 99 (1965), pp. 791–813.

[231] J. L. Price and T. P. S. Powell. "Certain observations on the olfactory pathway". In: *Journal of anatomy* 110 (1971), pp. 105–26.

[232] K. Psachoulia, F. Jamen, K. M. Young, and W. D. Richardson. "Cell cycle dynamics of NG2 cells in the postnatal and ageing brain". In: *Neuron glia biology* 5.3-4 (2009), pp. 57–67.

[233] G. Quirk, R. Muller, and J. Kubie. "The firing of hippocampal place cells in the dark depends on the rat's recent experience." In: *Neurosci* 10 (1990), pp. 2008–2017.

[234] R. Q. Quiroga and S. Panzeri. *Principles of Neural Coding*. CRC Press, 2013.

[235] R Core Team. *R: A Language and Environment for Statistical Computing*. R Foundation for Statistical Computing. Vienna, Austria, 2017. URL: https://www.R-project.org/.

[236] G. Raisman, W. M. Cowan, and T. P. S. Powell. "The extrinsic afferent, commissural and association fibres of the hippocampus". In: *Brain* 88 (1965), pp. 963–95. DOI: https://doi.org/10.1093/brain/88.5.963.

[237] S. Ramón y Cajal. *Algunas conjeturas sobre el mecanismo anatómico de la ideación, asociación y atención*. 1895.

[238] J. Ranck Jr. "Head direction cells in the deep cell layer of dorsal presubiculum in freely moving rats." In: *In: Buzsaki, G., Vanderwolf, C.H. (Eds.), Electrical Activity of the Archicortex. Hungarian Academy of Sciences, Budapest* (1985), pp. 217–220.

[239] J. Ranck Jr. "Head direction cells in the deep layers of the dorsal presubiculum in freely moving rats." In: *Society for Neuroscience* 10 (1984), p. 599.

[240] F. Raudies, R. Florian, M. Ennio, and M. Hasselmo. "Modeling the influence of optic flow on grid cell firing in the absence of other cues1." In: *J. Comput. Neurosci.* 33 (2012), pp. 475–493.

[241] F. Raudies and M. Hasselmo. "Modeling boundary vector cell firing given optic flow as a cue." In: *PLoS Comput. Biol.* 8 (2012), e1002553.

[242] B. J. Richmond and L. M. Optican. "Temporal encoding of two-dimensional patterns by single units in primate primary visual cortex. II. Information transmission". In: *Journal of Neurophysiology* 64.2 (1990), pp. 370–380.

[243] B. J. Richmond, L. M. Optican, and H. Spitzer. "Temporal encoding of two-dimensional patterns by single units in primate primary visual cortex. I. Stimulus-response relations". In: *Journal of Neurophysiology* 64.2 (1990), pp. 351–369.

[244] P. del Río Hortega. *El Tercer elemento de los centros nerviosos. Histogénesis y evolución normal: éxodo y distribución regional de la microglía*. Museo Nacional de Ciencias Naturales, 1921.

[245] W. C. Risher, R. D. Andrew, and S. A. Kirov. "Real-time passive volume responses of astrocytes to acute osmotic and ischemic stress in cortical slices and in vivo revealed by two-photon microscopy". In: *Glia* 57.2 (2009), pp. 207–221.

[246] L. E. Rivers, K. M. Young, M. Rizzi, F. Jamen, K. Psachoulia, A. Wade, N. Kessaris, and W. D. Richardson. "PDGFRA/NG2 glia generate myelinating oligodendrocytes and piriform projection neurons in adult mice". In: *Nature neuroscience* 11.12 (2008), pp. 1392–1401.

[247] E. Rolls. "Spatial view cells and the representation of place in the primate hippocampus." In: *Hippocampus* 9 (1999), pp. 467–480.

[248] E. Rolls and S. O'Mara. "View-responsive neurons in the primate hippocampal complex." In: *Hippocampus* 5 (1995), pp. 409–424.

[249] E. Rolls, R. Robertson, and G.-F. Pierre. "Spatial view cells in the primate hippocampus." In: *Neurosci* 9 (1997), pp. 1789–1794.

[250] B. L. Roth. "DREADDs for neuroscientists". In: *Neuron* 89.4 (2016), pp. 683–694.

[251] D. Rowland, Y. Yanovich, and C. Kentros. "A stable hippocampal representation of a space requires its direct experience". In: *Proc. Natl. Acad. Sci. U. S. A.* 108 (2011), pp. 14654–14658.

[252] A. Rubin, N. Geva, L. Sheintuch, and Y. Ziv. "Hippocampal ensemble dynamics timestamp events in long-term memory". In: *Elife* 4 (2015), e12247.

[253] A. Rubin, N. Geva, L. Sheintuch, and Y. Ziv. "Hippocampal ensemble dynamics timestamp events in long-term memory". In: *eLife* 4:e12247 (2015). DOI: 10.7554/eLife.12247.

[254] C. A. Runyan, E. Piasini, S. Panzeri, and C. D. Harvey. "Distinct timescales of population coding across cortex". In: *Nature* 548.7665 (2017), pp. 92–96.

[255] A. B. Saleem, A. Ayaz, K. J. Jeffery, K. D. Harris, and M. Carandini. "Integration of visual motion and locomotion in mouse visual cortex". In: *Nature neuroscience* 16.12 (2013), pp. 1864–1869.

[256] A. B. Saleem, E. M. Diamanti, J. Fournier, K. D. Harris, and M. Carandini. "Coherent encoding of subjective spatial position in visual cortex and hippocampus". In: *Nature* 562.7725 (2018), pp. 124–127.

[257] E. Save, L. Nerad, and B. Poucet. "Contribution of multiple sensory information to place field stability in hippocampal place cells". In: *Hippocampus* 10 (2000), pp. 64–76.

[258] F. Savelli, D. Yoganarasimha, and J. Knierim. "Influence of boundary removal on the spatial representations of the medial entorhinal cortex." In: *Hippocampus* 18 (2008), pp. 1270–1282.

[259] K. Schulz, A. Kroner, and S. David. "Iron efflux from astrocytes plays a role in remyelination". In: *Journal of Neuroscience* 32.14 (2012), pp. 4841–4847.

[260] J. Schummers, H. Yu, and M. Sur. "Tuned responses of astrocytes and their influence on hemodynamic signals in the visual cortex". In: *Science* 320.5883 (2008), pp. 1638–1643.

[261] A. Serrano, N. Haddjeri, J.-C. Lacaille, and R. Robitaille. "GABAergic network activation of glial cells underlies hippocampal heterosynaptic depression". In: *Journal of Neuroscience* 26.20 (2006), pp. 5370–5382.

[262] C. E. Shannon. "A Mathematical Theory of Communication". In: *The Bell System Technical Journal* 27 (1948), pp. 379–423. DOI: 10.1002/j.1538-7305.1948.tb01338.x.

[263] M. Sheffield and D. Dombeck. "Calcium transient prevalence across the dendritic arbour predicts place field properties". In: *Nature* 517 (2015), pp. 200–204. DOI: https://doi.org/10.1038/nature13871.

[264] M. Shein-Idelson, L. Pammer, M. Hemberger, and G. Laurent. "Large-scale mapping of cortical synaptic projections with extracellular electrode arrays". In: *Nat. Methods* 14 (2017), pp. 882–890.

[265] L. Sheintuch, A. Rubin, N. Brande-Eilat, N. Geva, N. Sadeh, O. Pinchasof, and Y. Ziv. "Tracking the Same Neurons across Multiple Days in Ca2+ Imaging Data". In: *Cell Reports* 21 (2017), pp. 1102–1115. DOI: https://doi.org/10.1016/j.celrep.2017.10.013..

[266] L. Sheintuch, A. Rubin, N. Brande-Eilat, N. Geva, N. Sadeh, O. Pinchasof, and Y. Ziv. "Tracking the same neurons across multiple days in Ca2+ imaging data". In: *Cell reports* 21.4 (2017), pp. 1102–1115.

[267] M. W. Sherwood, M. Arizono, C. Hisatsune, H. Bannai, E. Ebisui, J. L. Sherwood, A. Panatier, S. H. R. Oliet, and K. Mikoshiba. "Astrocytic IP3Rs: Contribution to Ca2+ signalling and hippocampal LTP". In: *Glia* 65.3 (2017), pp. 502–513.

[268] E. Shigetomi, D. N. Bowser, M. V. Sofroniew, and B. S. Khakh. "Two forms of astrocyte calcium excitability have distinct effects on NMDA receptor-mediated slow inward currents in pyramidal neurons". In: *Journal of Neuroscience* 28.26 (2008), pp. 6659–6663.

[269] E. Shigetomi, X. Tong, K. Y. Kwan, D. P. Corey, and B. S. Khakh. "TRPA1 channels regulate astrocyte resting calcium and inhibitory synapse efficacy through GAT-3". In: *Nature neuroscience* 15.1 (2012), p. 70.

[270] D. Shoham, D. E. Glaser, A. Arieli, T. Kenet, C. Wijnbergen, Y. Toledo, R. Hildesheim, and A. Grinvald. "Imaging cortical dynamics at high spatial and temporal resolution with novel blue voltage-sensitive dyes." In: *Neuron* 24 (1999), pp. 791–802.

[271] T. Shuman, D. Aharoni, D. J. Cai, C. R. Lee, S. Chavlis, L. Page-Harley, L. M. Vetere, Y. Feng, C. Y. Yang, I. Mollinedo-Gajate, et al. "Breakdown of spatial coding and interneuron synchronization in epileptic mice". In: *Nature neuroscience* 23.2 (2020), pp. 229–238.

[272] J. Sibille, U. Pannasch, and N. Rouach. "Astroglial potassium clearance contributes to short-term plasticity of synaptically evoked currents at the tripartite synapse". In: *The Journal of physiology* 592.1 (2014), pp. 87–102.

[273] C. Simon, M. Götz, and L. Dimou. "Progenitors in the adult cerebral cortex: cell cycle properties and regulation by physiological stimuli and injury". In: *Glia* 59.6 (2011), pp. 869–881.

[274] W. Skaggs, J. Knierim, and B. Kudrimoti H.S. andMcNaughton. "A model of the neural basis of the rat's sense of direction." In: *Adv. Neural Inf. Process. Syst.* 7 (1995), pp. 173–180.

[275] W. E. Skaggs, B. L. McNaughton, K. M. Gothard, and E. J. Markus. "An information-theoretic approach to deciphering the hippocampal code". In: *Proceedings of the 5th International Conference on Neural Information Processing Systems*. 1992, pp. 1030–1037.

[276] T. Solstad, C. Boccara, E. Kropff, M.-B. Moser, and E. Moser. "Representation of geometric borders in the entorhinal cortex." In: *Science* 322 (2008), pp. 1865–1868.

[277] W. A. Spencer and E. R. Kandel. "Hippocampal neuron responses to selective activation of recurrent collaterals of hippocampofugal axons". In: *Exp. Neurol.* 4 (1961), pp. 149–161. DOI: https://doi.org/10.1016/0014-4886(61)90037-1.

[278] M. E. Spira and A. Hai. "Multi-electrode array technologies for neuroscience and cardiology". In: *Nat. Nanotechnol.* 8 (2013), pp. 83–94.

[279] R. Srinivasan, B. S. Huang, S. Venugopal, A. D. Johnston, H. Chai, H. Zeng, P. Golshani, and B. S. Khakh. "Ca 2+ signaling in astrocytes from Ip3r2-/- mice in brain slices and during startle responses in vivo". In: *Nature neuroscience* 18.5 (2015), pp. 708–717.

[280] F. Stefanini, L. Kushnir, J. C. Jimenez, J. H. Jennings, N. I. Woods, G. D. Stuber, M. A. Kheirbek, R. Hen, and S. Fusi. "A distributed neural code in the dentate gyrus and in CA1". In: *Neuron* 107.4 (2020), pp. 703–716.

[281] D. Stellwagen and R. C. Malenka. "Synaptic scaling mediated by glial TNF-α". In: *Nature* 440.7087 (2006), pp. 1054–1059.

[282] H. Stensola, T. Stensola, T. Solstad, K. Frøland, M.-B. Moser, and E. Moser. "The entorhinal grid map is discretized." In: *Nature* 492 (2012), pp. 72–78.

[283] J. L. Stobart, K. D. Ferrari, M. J. Barrett, C. Glück, M. J. Stobart, M. Zuend, and B. Weber. "Cortical circuit activity evokes rapid astrocyte calcium signals on a similar timescale to neurons". In: *Neuron* 98.4 (2018), pp. 726–735.

[284] C. Stosiek, O. Garaschuk, K. Holthoff, and A. Konnerth. "In vivo two-photon calcium imaging of neuronal networks". In: *Proc. Natl. Acad. Sci. U. S. A.* 100 (2003), pp. 7319–7324.

[285] W. Sun and D. Dietrich. "Synaptic integration by NG2 cells". In: *Frontiers in cellular neuroscience* 7 (2013), p. 255.

[286] K. Svoboda and R. Yasuda. "Principles of Two-Photon Excitation Microscopy and Its Applications to Neuroscience". In: *Neuron* 50 (2006), pp. 823–839.

[287] L. W. Swanson, E. Newman, A. Araque, and J. M. Dubinsky. *The beautiful brain: the drawings of Santiago Ramón y Cajal*. Abrams, 2017.

[288] Z. Szabó, L. Héja, G. Szalay, O. Kékesi, A. Füredi, K. Szebényi, Á. Dobolyi, T. I. Orbán, O. Kolacsek, T. Tompa, et al. "Extensive astrocyte synchronization advances neuronal coupling in slow wave activity in vivo". In: *Scientific reports* 7.1 (2017), pp. 1–18.

[289] N. Takata, T. Nagai, K. Ozawa, Y. Oe, K. Mikoshiba, and H. Hirase. "Cerebral blood flow modulation by basal forebrain or whisker stimulation can occur independently of large cytosolic Ca 2+ signaling in astrocytes". In: *PloS one* 8.6 (2013), e66525.

[290] Y. N. Tallini, M. Ohkura, B.-R. Choi, G. Ji, K. Imoto, R. Doran, J. Lee, P. Plan, J. Wilson, H.-B. Xin, A. Sanbe, J. Gulick, J. Mathai, J. Robbins, G. Salama, J. Nakai, and M. I. Kotlikoff. "Imaging cellular signals in the heart in vivo: Cardiac expression of the high-signal Ca2+ indicator GCaMP2". In: *Proc. Natl. Acad. Sci.* 103 (2006), pp. 4753–4758.

[291] N. Tamamaki and Y. Nojyo. "Preservation of topography in the connections between the subiculum, field CA1, and the entorhinal cortex in rats". In: *Journal of Comparative Neurology* 353.3 (1995), pp. 379–390.

[292] W. Tang, K. Szokol, V. Jensen, R. Enger, C. A. Trivedi, Ø. Hvalby, P. J. Helm, L. L. Looger, R. Sprengel, and E. A. Nagelhus. "Stimulation-evoked Ca2+ signals in astrocytic processes at hippocampal CA3–CA1 synapses of adult mice are modulated by glutamate and ATP". In: *Journal of Neuroscience* 35.7 (2015), pp. 3016–3021.

[293] J. Taube. "Head direction cells recorded in the anterior thalamic nuclei of freely moving rats." In: *Neurosci* 15 (1995), pp. 70–86.

[294] J. Taube, R. Muller, R. Jr., and J.B. "A quantitative analysis of head-direction cells in the postsubiculum". In: *Society for Neuroscience* 13 (1987), p. 1332.

[295] J. Taube, R. Muller, R. Jr., and J.B. "Head-direction cells recorded from the postsubiculum in freely moving rats: I. Description and quantitative analysis." In: *Neurosci.* 10 (1990), pp. 420–435.

[296] J. Taube, R. J. Muller R.U., and J.B. "Head-direction cells recorded from the postsubiculum in freely moving rats: II. Effects of environmental manipulations." In: *Neurosci.* 10 (1990), pp. 436–447.

[297] L. Thompson and P. Best. "Long-term stability of the place-field activity of single units recorded from the dorsal hippocampus of freely behaving rats". In: *Brain Res.* 509 (1990), pp. 299–308.

[298] L. Tian, S. A. Hires, T. Mao, D. Huber, M. E. Chiappe, S. H. Chalasani, L. Petreanu, J. Akerboom, S. A. McKinney, E. R. Schreiter, C. I. Bargmann, V. Jayaraman, K. Svoboda, and L. L. Looger. "Imaging neural activity in worms, flies and mice with improved GCaMP calcium indicators". In: *Nat. Methods* 6 (2009), pp. 875–881.

[299] N. M. Timme and C. Lapish. "A tutorial for information theory in neuroscience". In: *eneuro* 5.3 (2018).

[300] E. C. Toleman. "Cognitive maps in rats and men." In: *Psychol Rev* 55 (1948), pp. 189–208.

[301] L. Torres, J. Danver, K. Ji, J. T. Miyauchi, D. Chen, M. E. Anderson, B. L. West, J. K. Robinson, and S. E. Tsirka. "Dynamic microglial modulation of spatial learning and social behavior". In: *Brain, behavior, and immunity* 55 (2016), pp. 6–16.

[302] A. Treves and S. Panzeri. "The Upward Bias in Measures of Information Derived from Limited Data Samples". In: *Neural Computation* 7.2 (1995), pp. 399–407. DOI: 10.1162/neco.1995.7.2.399.

[303] J. B. Trimper, S. G. Trettel, E. Hwaun, and L. L. Colgin. "Methodological caveats in the detection of coordinated replay between place cells and grid cells". In: *Frontiers in systems neuroscience* 11 (2017), p. 57.

[304] R. Y. Tsien. "A non-disruptive technique for loading calcium buffers and indicators into cells". In: *Nature* 290.5806 (1981), pp. 527–528.

[305] G. F. Turi, W.-K. Li, S. Chavlis, I. Pandi, J. O'Hare, J. B. Priestley, A. D. Grosmark, Z. Liao, M. Ladow, J. F. Zhang, et al. "Vasoactive intestinal polypeptide-expressing interneurons in the hippocampus support goal-oriented spatial learning". In: *Neuron* 101.6 (2019), pp. 1150–1165.

[306] G. W. Van Hoesen, D. N. Pandya, and N. Butters. "Cortical afferents to the entorhinal cortex of the rhesus monkey". In: *Science* 175.4029 (1972), pp. 1471–1473. DOI: 10.1126/science.175.4029.1471.

[307] G. W. Van Hoesen and D. N. Pandya. "Some connections of the entorhinal (area 28) and perirhinal (area 35) cortices of the rhesus monkey III. Efferent connections". In: *Brain Res.* 95 (1975), pp. 39–59. DOI: https://doi.org/10.1016/0006-8993(75)90206-1.

[308] A. Verkhratsky, M. Nedergaard, and L. Hertz. "Why are astrocytes important?" In: *Neurochemical research* 40.2 (2015), pp. 389–401.

[309] J. Viventi and J. A. Blanco. "Development of high resolution, multiplexed electrode arrays: Opportunities and challenges". In: *Annual International Conference of the IEEE Engineering in Medicine and Biology Society* (2012), pp. 1394–1396.

[310] A. Volterra, N. Liaudet, and I. Savtchouk. "Astrocyte Ca 2+ signalling: an unexpected complexity". In: *Nature Reviews Neuroscience* 15.5 (2014), pp. 327–335.

[311] X. Wang, N. Lou, Q. Xu, G.-F. Tian, W. G. Peng, X. Han, J. Kang, T. Takano, and M. Nedergaard. "Astrocytic Ca 2+ signaling evoked by sensory stimulation in vivo". In: *Nature neuroscience* 9.6 (2006), pp. 816–823.

[312] L. E. White. "Ipsilateral afferents to the hippocampal formation in the albino rat. I. Cingulum projections". In: *J. comp. Neurol.* 113 (1959), pp. 1–41. DOI: https://doi.org/10.1002/cne.901130102.

[313] L. E. White. "Olfactory bulb projections of the rat". In: *Anat. Rec.* 152 (1965), pp. 465–80. DOI: https://doi.org/10.1002/ar.1091520406.

[314] G. Y. Wiederschain. "The Molecular Probes handbook. A guide to fluorescent probes and labeling technologies". In: *Biochem.* 76 (2011), p. 1276.

[315] T. N. Wiesel and D. H. Hubel. "Single-cell responses in striate cortex of kittens deprived of vision in one eye". In: *Journal of neurophysiology* 26.6 (1963), pp. 1003–1017.

[316] M. A. Wilson and B. L. McNaughton. "Reactivation of hippocampal ensemble memories during sleep". In: *Science* 265 (1994), pp. 676–679. DOI: 10.1126/science.8036517.

[317] I. R. Winship, N. Plaa, and T. H. Murphy. "Rapid astrocyte calcium signals correlate with neuronal activity and onset of the hemodynamic response in vivo". In: *Journal of Neuroscience* 27.23 (2007), pp. 6268–6272.

[318] M. P. Witter et al. "Organization of the entorhinal-hippocampal system: a review of current anatomical data". In: *HIPPOCAMPUS-NEW YORK-CHURCHILL LIVINGSTONE-* 3 (1993), pp. 33–33.

[319] H. Wolosker, D. T. Balu, and J. T. Coyle. "The rise and fall of the d-serine-mediated gliotransmission hypothesis". In: *Trends in neurosciences* 39.11 (2016), pp. 712–721.

[320] W. Yang and R. Yuste. "In vivo imaging of neural activity". In: *Nat Methods* 14 (2017), pp. 349–359.

[321] M. M. Yartsev and N. Ulanovsky. "Representation of three-dimensional space in the hippocampus of flying bats". In: *Science* 340 (2013), pp. 367–372. DOI: 10.1126/science.1235338.

[322] R. Yoder, B. Clark, J. Brown, M. Lamia, S. Valerio, M. Shinder, and J. Taube. "Both visual and idiothetic cues contribute to head direction cell stability during navigation along complex routes". In: *Neurophysiol.* 105 (2011), pp. 2989–3001.

[323] R. Yoder, B. Clark, and J. Taube. "Origins of landmark encoding in the brain". In: *Trends Neurosci.* 34 (2011), pp. 561–571.

[324] D. Yoganarasimha and J. Knierim. "Coupling between place cells and head direction cells during relative translations and rotations of distal landmarks". In: *Exp. Brain Res* 160 (2005), pp. 344–359.

[325] R. Yuste and L. C. Katz. "Control of postsynaptic Ca2+ influx in developing neocortex by excitatory and inhibitory neurotransmitters." In: *Neuron* 6 (1991), pp. 333–344.

[326] J. L. Zamanian, L. Xu, L. C. Foo, N. Nouri, L. Zhou, R. G. Giffard, and B. A. Barres. "Genomic analysis of reactive astrogliosis". In: *Journal of neuroscience* 32.18 (2012), pp. 6391–6410.

[327] J. D. Zaremba, A. Diamantopoulou, N. B. Danielson, A. D. Grosmark, P. W. Kaifosh, J. C. Bowler, Z. Liao, F. T. Sparks, J. A. Gogos, and A. Losonczy. "Impaired hippocampal place cell dynamics in a mouse model of the 22q11. 2 deletion". In: *Nature neuroscience* 20.11 (2017), p. 1612.

[328] K. Zhang, I. Ginzburg, B. L. McNaughton, and T. J. Sejnowski. "Interpreting neuronal population activity by reconstruction: unified framework with application to hippocampal place cells". In: *Journal of neurophysiology* 79.2 (1998), pp. 1017–1044.

[329] Q. Zhang, T. Pangršič, M. Kreft, M. Kržan, N. Li, J.-Y. Sul, M. Halassa, E. Van Bockstaele, R. Zorec, and P. G. Haydon. "Fusion-related release of glutamate from astrocytes". In: *Journal of Biological Chemistry* 279.13 (2004), pp. 12724–12733.

[330] S. Zhang, F. Schönfeld, L. Wiskott, and D. Manahan-Vaughan. "Spatial representations of place cells in darkness are supported by path integration and border information". In: *Front. Behav. Neurosci* 88 (2014), p. 222.

[331] K. Zheng, L. Bard, J. P. Reynolds, C. King, T. P. Jensen, A. V. Gourine, and D. A. Rusakov. "Time-resolved imaging reveals heterogeneous landscapes of nanomolar Ca2+ in neurons and astroglia". In: *Neuron* 88.2 (2015), pp. 277–288.

[332] J. Zimmer. "Ipsilateral afferents to the commissural zone of the fascia dentata, demonstrated in decommissurated rats by silver impregnation". In: *J. comp. Neurol.* 142 (1971), pp. 393–416. DOI: https://doi.org/10.1002/cne.901420402.

[333] W. R. Zipfel, R. M. Williams, and W. W. Webb. "Nonlinear magic: multiphoton microscopy in the biosciences." In: *Nat. Biotechnol.* 21 (2003), pp. 1369–1377.

[334] Y. Ziv, L. Burns, E. Cocker, E. Hamel, K. Ghosh, L. Kitch, A. El Gamal, and M. Schnitzer. "Long-term dynamics of CA1 hippocampal place codes". In: *Nat. Neurosci.* 16 (2013), pp. 264–266.

[335] M. Zonta, M. C. Angulo, S. Gobbo, B. Rosengarten, K.-A. Hossmann, T. Pozzan, and G. Carmignoto. "Neuron-to-astrocyte signaling is central to the dynamic control of brain microcirculation". In: *Nature neuroscience* 6.1 (2003), pp. 43–50.

[336] M. Zugaro, E. Tabuchi, and S. Wiener. "Influence of conflicting visual, inertial and substratal cues on head direction cell activity." In: *Exp. Brain Res.* 133 (2000), pp. 198–208.

Appendix A

Thalamic Drive of Cortical Parvalbumin-Positive Interneurons during Down States in Anesthetized Mice

In the study presented in Appendix A, I was responsible for the analysis of Local Field Potential (LFP) recordings in anesthetized mice (Figure 4). I developed the algorithm for detection of slow waves and up and down states in the LFP measurements (Supplementary Figure 4). I measured the latency of down-to-up state transitions after optogenetic inhibitory manipulation of Parvalvumin postive interneurons under control condition and after silencing the thalamus via muscimol injection (Figure 4). I also used a Linear Mixed Effects model to study the interaction between pharmacological (muscimol) treatment and optogenetic stimulation in slow waves transitions (Figure 4).

Article

Current Biology

Thalamic Drive of Cortical Parvalbumin-Positive Interneurons during Down States in Anesthetized Mice

Graphical Abstract

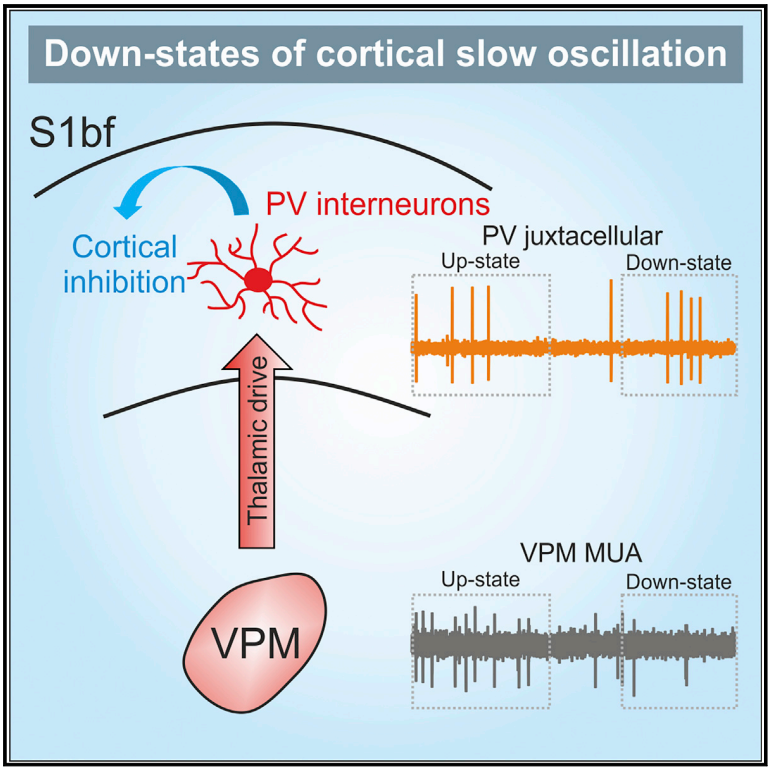

Highlights

- Thalamic activity in VPM is associated with longer down states in S1bf
- Thalamic inactivation decreases spikes of PV cells in S1bf during down states
- Thalamic suppression delays network response to PV cell silencing in down states
- Thalamus suppresses S1bf during down states through activation of PV cells

Authors

Stefano Zucca, Valentina Pasquale, Pedro Lagomarsino de Leon Roig, Stefano Panzeri, Tommaso Fellin

Correspondence

tommaso.fellin@iit.it

In Brief

Using a combination of electrophysiology, local pharmacology, and cell-specific optogenetic perturbations, Zucca et al. provide evidence that spontaneous thalamic activity inhibits cortex during down states through the suprathreshold activation of PV-positive interneurons.

Zucca et al., 2019, Current Biology *29*, 1481–1490
May 6, 2019
https://doi.org/10.1016/j.cub.2019.04.007

CellPress

Thalamic Drive of Cortical Parvalbumin-Positive Interneurons during Down States in Anesthetized Mice

Stefano Zucca,[1,2,4] Valentina Pasquale,[1,2,4] Pedro Lagomarsino de Leon Roig,[1,2] Stefano Panzeri,[2,3] and Tommaso Fellin[1,2,5,*]

[1]Optical Approaches to Brain Function Laboratory, Department of Neuroscience and Brain Technologies, Istituto Italiano di Tecnologia, Via Morego 30, 16163 Genova, Italy

[2]Neural Coding Laboratory, Istituto Italiano di Tecnologia, Via Morego 30, 16163 Genova, Italy

[3]Neural Computation Laboratory, Center for Neuroscience and Cognitive Systems at UniTn, Istituto Italiano di Tecnologia, Corso Bettini 31, 38068 Rovereto, Italy

[4]These authors contributed equally

[5]Lead Contact

*Correspondence: tommaso.fellin@iit.it

https://doi.org/10.1016/j.cub.2019.04.007

SUMMARY

Up and down states are among the most prominent features of the thalamo-cortical system during non-rapid eye movement (NREM) sleep and many forms of anesthesia. Cortical interneurons, including parvalbumin (PV) cells, display firing activity during cortical down states, and this GABAergic signaling is associated with prolonged down-state durations. However, what drives PV interneurons to fire during down states remains unclear. We here tested the hypothesis that background thalamic activity may lead to suprathreshold activation of PV cells during down states. To this aim, we performed two-photon guided juxtasomal recordings from PV interneurons in the barrel field of the somatosensory cortex (S1bf) of anesthetized mice, while simultaneously collecting the local field potential (LFP) in S1bf and the multi-unit activity (MUA) in the ventral posteromedial (VPM) thalamic nucleus. We found that activity in the VPM was associated with longer down-state duration in S1bf and that down states displaying PV cell firing were associated with increased VPM activity. Moreover, thalamic inhibition through application of muscimol reduced the fraction of spikes discharged by PV cells during cortical down states. Finally, we inhibited PV interneurons using optogenetics during down states while monitoring cortical LFP under control conditions and after thalamic muscimol injection. We found increased latency of the optogenetically triggered down-to-up transitions upon thalamic pharmacological blockade compared to controls. These findings demonstrate that spontaneous thalamic activity inhibits cortex during down states through the activation of PV interneurons.

INTRODUCTION

Slow-wave oscillations represent the dominant cortical rhythm observed during deep stages of non-rapid eye movement (NREM) sleep and under several types of anesthesia [1–6]. These oscillations are characterized by the rhythmic alternation (0.2–1 Hz) of silent (down) and active (up) network states, which can be captured in the local field potential (LFP) signal as depth-positive and depth-negative waves, respectively [7]. Down and up states occur in the cortex and in many subcortical regions, including the thalamus [1, 8], and they are believed to be crucial in the regulation of several processes, such as memory consolidation, sensory responses, and synaptic plasticity [9–18]. During up states, most types of cortical neurons display depolarized membrane potential and, in some cases, action potential firing. In contrast, down states are characterized by hyperpolarized membrane potential and no action potential firing in most cortical cells, including principal cells [19, 20]. However, some types of GABAergic interneurons, e.g., parvalbumin (PV)-positive fast spiking cells, were found to spike during down states [21, 22], and the speed of the LFP phase was observed to decrease after PV cell spikes during down states [22]. Moreover, optogenetic inhibitory manipulation of PV interneurons during down states reliably triggered swift up-state transitions, indicating that the spiking activity of PV cells during these cortical silent states was crucial to prolong down-state duration [22] and to maintain cortical networks in the silent state. However, what drives PV interneurons to spike during cortical down states remains unknown.

Here, we combined electrophysiological recording together with cell-specific optogenetic manipulation and pharmacology in anesthetized mice to demonstrate that thalamic activity significantly contributes to drive PV cells spiking during cortical down states. We found that activity in the thalamic ventral posteromedial (VPM) nucleus was associated with longer down-state duration in S1bf and that down states during which PV cells fired were associated with increased VPM spiking. Importantly, injection of muscimol in the thalamus decreased spikes of PV cells in the cortex during down states. Moreover, it increased the latency

of up-state transitions triggered by optogenetic inhibition of PV cells during down states. Altogether, our data demonstrate that spontaneous thalamic firing causes cortical silencing through the recruitment of PV interneurons during cortical silent states.

RESULTS

Simultaneous Recording of VPM and Cortical PV Cell Activity during Up and Down States

To simultaneously monitor cortical PV cells and VPM network activity, we performed two-photon-targeted juxtasomal recordings of PV interneurons in S1bf of anesthetized transgenic animals while collecting the LFP in S1bf and the multi-unit activity (MUA) in the VPM thalamic nucleus (Figure 1A). Transgenic animals were obtained by crossing the PV-cre mouse line and the TdTomato reporter line (see STAR Methods). We identified up and down states (Figure 1B), combining information about the LFP phase in the delta (<4 Hz) frequency band [7] and the power in higher bandwidths (i.e., beta and low gamma [10, 50] Hz) [23]. This method reliably detects up and down states from the LFP (false positive rates ~4%) [22]. In Figure 1B and in all other figures, time periods identified as up or down states are shown as pink or purple shaded areas, respectively.

PV-positive interneurons were mainly active during up states but also fired during down states (Figure 1C), in agreement with previous reports [21, 22]. The ratio of PV-active up states (i.e., the number of up states in which the interneuron fired divided by the total number of detected up states) was higher than the ratio of PV-active down states (Figure 1D), and the mean spike count per active up state was higher than the mean spike count per active down state (Figure 1E). In the VPM, we also observed a higher fraction of spikes during up states compared to down states (Figure 1F), although the difference in VPM activity between up and down states was smaller compared to that observed for PV interneurons (difference between fraction of up and down-state spikes: PV 0.459 ± 0.028, VPM 0.160 ± 0.035, paired Student's t test, $p = 1.42E{-}7$, n = 18 in 7 animals). The ratios of VPM-active up and down states were also different (Figure 1G). The mean VPM spike count per active state was higher in up states compared to down states (Figure 1H). PV spikes were not uniformly distributed during the up and down-state cycle (Rayleigh test for non-uniformity of phase-of-firing distributions; $p < 0.01$) with most spikes distributed in the up state phase range ([95, 255] degrees; Figures 1I and 1J) and less spikes in the down-state phases ([295, 75] degrees; Figures 1I and S1A). VPM MUA was phase locked to the up and down-state cycle in 6 out of 7 animals, corresponding to 16 out of 18 PV-cell recordings (Rayleigh test for non-uniformity of circular data; $p < 0.01$; Figures 1K and 1L), although the locking strength of VPM was lower than that of PV interneurons (paired Student's t test; $p = 1.47E{-}6$; n = 16 in 6 animals). Figure S1 shows the normalized phase of firing distributions limited to either up (Figures S1C and S1D) or down (Figures S1E and S1F) states for PV (Figures S1A, S1C, and S1E) and VPM (Figures S1B, S1D, and S1F) recordings with the corresponding relative time of firing distributions (mean ± SEM; n = 18 cells in 7 animals; see STAR Methods).

VPM Activity Correlates with Down-State Duration and PV Firing in Down States

Given that VPM neurons were active during down states, we asked whether VPM contributes driving cortical PV interneurons spiking during cortical down states. To this aim, we first correlated VPM MUA with the duration of simultaneously recorded cortical down states. We found that down-state duration was longer when the VPM was active (VPM active; Figure 2A) compared to down-state duration recorded when the VPM was silent (VPM silent; Figure 2A). Moreover, firing of PV interneurons during down states was associated to higher VPM spike count (Figure 2B), supporting the idea that VPM may promote interneuron spiking during cortical down states.

We next characterized the temporal relationship between VPM spikes and PV spikes during down states. If VPM neurons contribute to drive PV cells to fire, then VPM neurons should tend to fire earlier than PV cells, whereas a causal effect of PV firing on VPM MUA signal would lead to the opposite temporal relationship. To address this issue, we computed the instantaneous firing rate (IFR) of VPM MUA triggered on the timing of PV spikes in down states (Figure 2C). To investigate whether PV cell firing probability in down states can be correlated to an increase of VPM firing rate, we compared the spike-triggered VPM IFR with the one computed from randomly sampled time instants taken from PV-silent down states ("surrogate" PV spikes; Figure 2C). Surrogates were constructed preserving the phase of firing distribution in the down state, the maximal number of spikes per down state, and the total number of sampled down states (see STAR Methods for details). We examined the temporal relationship between VPM and PV firing for each individual PV cell. Figures S2A–S2R report the real (mean ± SEM) and surrogate (mean ± [5–95] percentile range) spike-triggered VPM IFR functions for all recorded PV interneurons (n = 18 from 7 animals). In Figure 2D, we reported the *Z* scores of VPM firing rate with respect to surrogate data distribution in 100-ms time windows preceding and following PV spikes in down state for each experiment. In 10 out of 18 PV cells, VPM firing frequency in the pre-spike window was significantly higher than expected by chance (false discovery rate [FDR] correction applied). Although heterogeneity of response was observed in different cells, the finding that 10 significant cells out of 18 at $p < 0.05$ was highly significant at the population level (binomial test; $p = 1.12E{-}10$; n = 18 recordings from 7 animals). Moreover, at the single-PV cell level, the pre-spike VPM mean firing rate was higher (one-tailed Wilcoxon signed-rank test; FDR corrected) than the post-spike VPM mean firing rate (see STAR Methods) in 6 out of 18 recordings (see Figure 2E for a representative cell), and no experiment showed a post-spike VPM firing rate higher than the pre-spike firing rate. Although heterogeneity was present across cells, the finding that 6 individual cells had significantly higher VPM firing rate in the pre-spike time window was highly significant (binomial test; $p = 1.1E{-}6$; n = 18 recordings from 7 animals). Finally, we normalized both pre- and post-spike VPM firing rate to the overall mean VPM firing rate triggered by surrogate spikes to account for different baseline VPM firing across experiments. We found higher percentages of variations in the pre-spike window compared to the post-spike time window (Figure 2F). Taken together, all results suggest

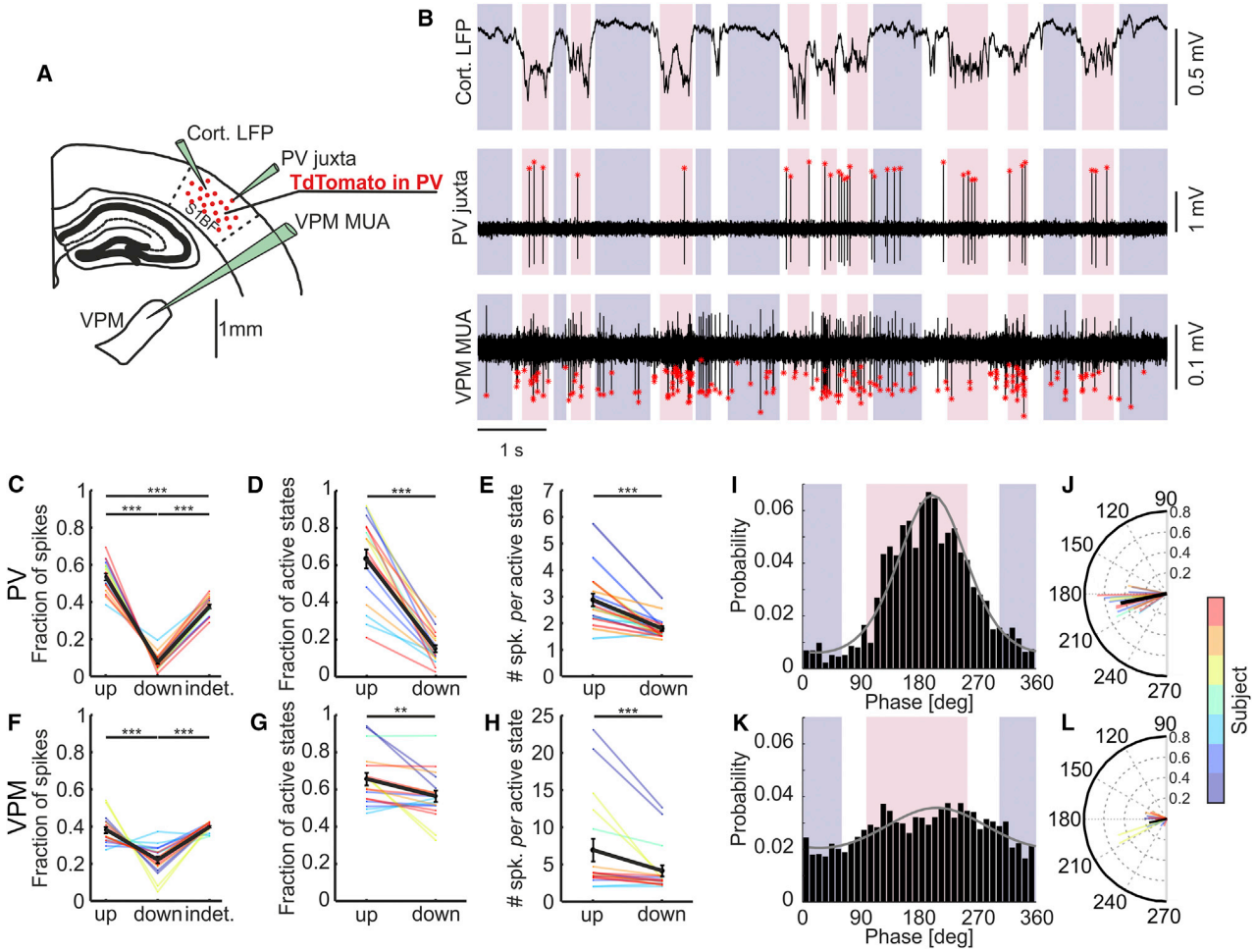

Figure 1. Firing of Cortical PV Interneurons and Thalamic VPM Nucleus during Up and Down States

(A) Schematic of the experimental configuration. Two-photon guided juxtasomal recordings of PV interneurons in S1bf were conducted while recording the LFP in S1bf and the MUA in the VPM.

(B) Representative traces of cortical LFP (top), single-unit activity from a PV interneuron (middle), and thalamic MUA (bottom) during up and down states. Pink and purple in the background indicate up and down states identified from the LFP, respectively. White indicates indeterminate states (see STAR Methods). Red asterisks mark detected spikes.

(C) Fraction of action potentials fired by PV cells in up, down, and indeterminate periods (up-down $p = 2.8E{-}11$; up-indeterminate $p = 0.00015$; down-indeterminate $p < 2E{-}16$; paired Student's t test; Bonferroni corrected; n = 18 cells from 7 animals) relative to the total number of PV spikes. In this as well in other figures, colored dots and lines identify individual cells. Black dots and lines indicate the average value across cells. Error bars indicate SEM. Not significant (n.s.), $p > 0.05$; *$p < 0.05$; **$p < 0.01$; ***$p < 0.001$.

(D) Fraction of active up states and active down states relative to the total number of up and down states, respectively ($p = 4.65E{-}9$; paired Student's t test; n = 18 cells from 7 animals).

(E) Average number of spikes fired by PV cells per single up or down state ($p = 2.82E{-}5$; paired Student's t test; n = 18 cells from 7 animals).

(F–H) Same as in (C)–(E) but for thalamic MUA. In (F), up-down $p = 0.00086$, up-indeterminate $p = 0.95020$, down-indeterminate $p = 4.7E{-}7$; paired Student's t test; Bonferroni corrected; n = 18 recordings from 7 animals. In (G), $p = 0.008$; paired Student's t test; n = 18 recordings from 7 animals. In (H), $p = 7.98E{-}4$; Wilcoxon signed-rank test; n = 18 recordings from 7 animals.

(I) Phase of firing distribution for one representative PV interneuron. Pink and purple indicate the range of phases corresponding to up and down states, respectively. The gray line shows the von Mises fit (see STAR Methods; $\mu = 188^{\circ}$ and $\kappa = 1.38$). The preferred phase of firing (see STAR Methods) was 192 ± 13 degrees (circular mean ± angular deviation; n = 18 cells in 7 animals) and the locking strength 0.461 ± 0.006 (n = 18 cells in 7 animals).

(J) Circular plot of the mean phase of firing of PV interneurons. The thick black line indicates the overall mean phase of firing and average locking strength (n = 18 cells from 7 animals).

(K and L) Phase of firing distribution for one representative VPM MUA (K) and circular plot of the mean phase of firing for all recorded VPM MUA signals (L). VPM MUA was simultaneously recorded together with the cortical PV interneuron. The preferred phase of firing of the 16 out of 18 phase-locked VPM MUA recordings was 191 ± 23 degrees (n = 16 cells in 6 animals), not different from that of simultaneously recorded PV interneurons (Watson-Williams test; $p = 0.92$; n = 16 in 6 animals).

See also Figure S1.

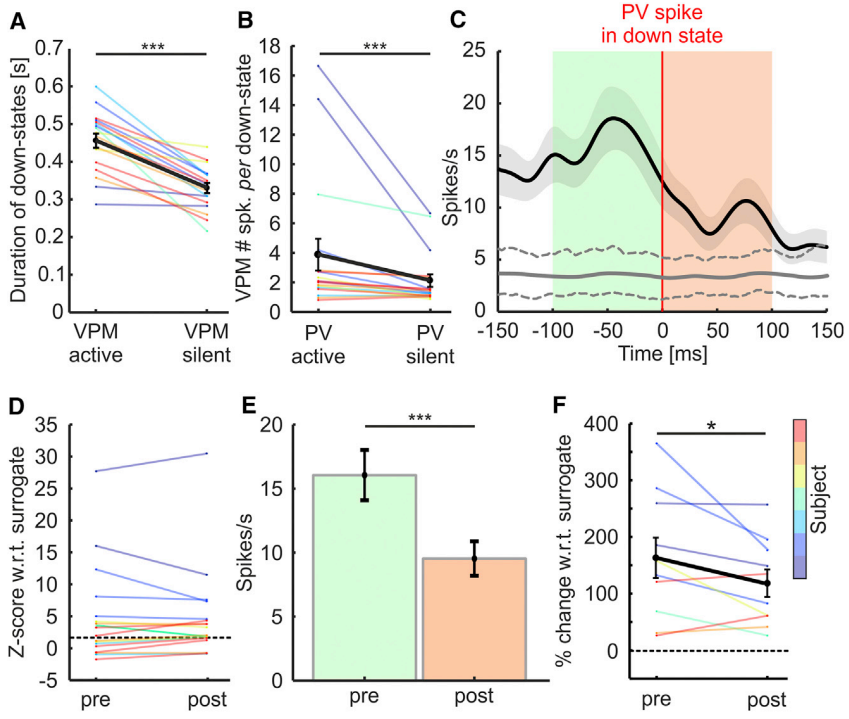

Figure 2. VPM Firing Correlates with Cortical Down-State Duration and PV Firing in Down States

(A) Duration of cortical down states associated with detected VPM activity (VPM-active) and VPM inactivity (VPM-silent; p = 4.5E−7; one-tailed paired Student's t test; n = 18 recordings from 7 animals).

(B) VPM spike count in PV-active and PV-silent cortical down states (p = 2.5E−4; one-tailed Wilcoxon signed rank test; n = 18 cells in 7 animals).

(C) Spike-triggered VPM IFR based on the timing of PV spikes recorded during cortical down states for one representative recording (Gaussian kernel SD, 12.5 ms; the thick black line indicates the mean; the shaded area the SEM). The VPM IFR triggered by "surrogate" spikes is displayed with the thick gray line. Dotted gray lines indicate the 5th and 95th percentiles of the distribution of the mean surrogate spike-triggered VPM IFR (100 surrogates).

(D) *Z* scores in the pre- and post-time windows of the PV-spike-triggered VPM mean firing rate with respect to surrogate data: 10 out of 18 recordings showed a significant difference between actual and surrogate data in the pre-spike window (one-tailed z-test). The dashed line indicates significance at p = 0.05. Cells with *Z* scores corresponding to p > 0.05 lie above the dashed line and are marked with asterisks in Figure S2.

(E) Mean firing rate of the VPM before and after PV spikes in down states (pre: [−100, 0] ms; post: [0, 100 ms]; mean ± SEM; p = 3E−4; two-sided Wilcoxon signed rank test; n = 116 spikes for the same recording as in C).

(F) Variation of VPM mean firing rate relative to the overall mean surrogate firing rate in the pre- and post- windows (p = 0.032; one-tailed Student's t test; n = 10 cells from 6 animals) for those cells showing a firing rate significantly higher than that of the surrogate data.

See also Figure S2.

that the occurrence of VPM spikes in the down state increases the probability of PV spikes in down states shortly after.

To check whether the observed temporal relationship between VPM and PV spikes is specific to the down state, we also computed the VPM IFR triggered on the timing of PV spikes in the up state (Figure S2S). We compared the pre- and post-spike VPM mean firing rate for each PV cell (one-tailed Wilcoxon signed-rank test; FDR corrected) during up states, and we found 1 cell out of 18 in which the pre-spike VPM firing rate was higher than the post-spike (binomial test; p = 0.2265; n = 18 recordings from 7 animals). We also found 2 cells out of 18 in which the pre-spike VPM firing rate was lower than the post-spike one (binomial test; p = 0.0581; n = 18 recordings from 7 animals). Therefore, in contrast to what we observed during down state, no temporal relationship between VPM and PV spikes emerges during up states at the population level.

Thalamic Inactivation Reduces PV Spikes during Down States

The observation of a statistical dependency between the firing of different cells (VPM neurons and PV cells in this case; Figure 2) is not enough to prove a causal relationship between firing of the corresponding two cellular populations [24]. To directly test for the causal necessity of the thalamus in the regulation of PV cell firing during down states, we used a perturbative pharmacological approach to silence the thalamus. We applied the GABA receptor agonist muscimol locally in the thalamus, and we performed two-photon-targeted juxtasomal recordings of PV interneurons in S1bf while collecting cortical LFP in S1bf and the MUA in the VPM thalamic nucleus before and after the pharmacological manipulation (Figure 3A). Muscimol application almost completely abolished spiking activity in the VPM MUA (10.12 ± 3.86 spikes/s under control conditions versus 0.03 ± 0.01 spikes/s after muscimol application; n = 11 animals; Wilcoxon signed-rank test; p = 9.77E−4; Figure 3B), and *a posteriori* observation in fixed tissue confirmed local application of muscimol in the thalamus (see STAR Methods). Muscimol application induced a reduction in the frequency of up states (Figure 3C) and an increase in down-state duration (Figure 3D), consistently with the previous literature [25]. Up-state duration (Figure S3A) and its coefficient of variation (Figure S3B) were also decreased. Down-state frequency (Figure S3C) and the coefficient of variation of down state duration (Figure S3D) were not significantly changed.

Most importantly, we found that the fraction of PV spikes in down states was decreased upon pharmacological inactivation of the thalamus (Figure 3E), in agreement with the hypothesis that the VPM contributes to drive PV cells spiking during down states. At the same time, the fraction of PV spikes in the up state increased (Figure S3E), the fraction of spikes in the indeterminate state decreased (Figure S3F), and the mean firing rate of PV cells remained constant (3.4 ± 1.0 spikes/s under control conditions, n = 8, versus 2.5 ± 0.5 spikes/s after muscimol application, n = 7; Student's t test; p = 0.47). The average preferred phase of firing of PV cells after muscimol injection was 201 ± 5 degrees (Figure S3G; n = 7 cells in 4 animals), not different from that under control conditions (192 ± 5 degrees; n = 8 cells in 4 animals;

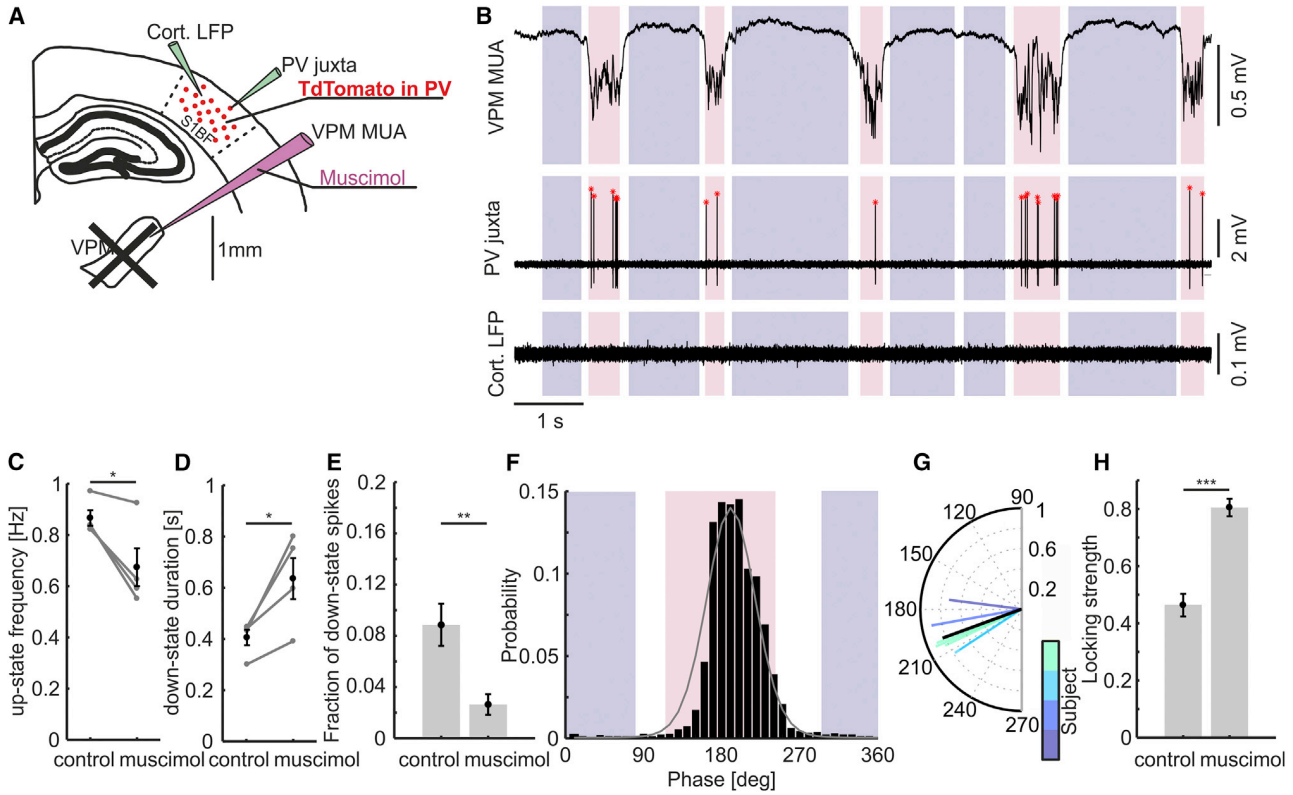

Figure 3. Thalamic Inactivation Significantly Reduces PV Spiking during Cortical Down States

(A) Schematic of the experimental configuration. Muscimol is injected in the thalamus while measuring cortical LFP, thalamic MUA, and one cortical PV interneuron.

(B) Representative traces of cortical LFP (top), juxtasomal recording from a PV interneuron (middle), and thalamic MUA (bottom) during up and down states after muscimol injection in the thalamus.

(C and D) Up-state frequency (C) and average down-state duration (D) under control conditions and after muscimol injection in the thalamus (paired Student's t test p = 0.0387 for C and p = 0.0367 for D; n = 4 animals).

(E) Fraction of PV spikes recorded during down states under control conditions and after muscimol injection in the thalamus (p = 6.24E−3, Student's t test; control, n = 8 cells; muscimol, n = 7 cells from 4 animals).

(F) Phase of firing distribution of one representative PV interneuron after muscimol injection in the thalamus. Pink and purple indicate the global range of up- and down-state phases after muscimol application, respectively. The gray line reports the corresponding von Mises fit (μ = 191° and κ = 4.30).

(G) Circular plot of the mean phase of firing of PV interneurons after muscimol application in the thalamus (n = 7 cells from 4 animals).

(H) Locking strength under control conditions and after muscimol injection (p = 1.25E−5, Student's t test; control, n = 8; muscimol, n = 7 from 4 animals).

See also Figure S3.

see Figure S3G legend). In contrast, the locking strength markedly increased upon thalamic inactivation (Figures 3F–3H), in agreement with the decreased occurrence of down-state spikes and increased probability of observing spikes in the up state. The phase of firing distribution for PV spikes during the up and down state was not changed after muscimol application with respect to control conditions (Figures S3H and S3I).

Down-to-Up Transitions Induced by Optogenetic Inhibition of PV Cells Show Increased Latency upon Thalamic Inactivation

Previous work demonstrated that the firing of PV interneurons during down states prolongs down-state durations [22]. More specifically, decreasing the probability of PV spiking in down states through optogenetic inhibitory manipulation reliably triggered short latency down-to-up-state transitions [22]. Here, we reasoned that, if the thalamus drives PV firing during down states, thalamic inactivation should prolong the latency of optogenetically induced down-to-up-state transitions. To test this hypothesis, we expressed the inhibitory opsin archaerhodopsin (Arch) [26] in PV cells while recording the LFP in S1bf before and after application of muscimol in the thalamus (Figure 4A). We confirmed that optical inhibition of PV cells during down states facilitated the up-state generation, resulting in a decrease of the latencies of down-to-up-state transitions compared to expected spontaneous transitions (latency: 0.11 ± 0.02 s for optically evoked transitions versus 0.32 ± 0.04 s for spontaneous transitions; n = 7 animals; p = 1.1E−3; paired Student's t test). Importantly, we found that pharmacological inhibition of the thalamus significantly prolonged the latencies of PV-inhibition-evoked down-to-up-state transitions when compared to PV-inhibition-evoked down-to-up-state transitions under control conditions (latency: 0.25 ± 0.4 s after muscimol application versus 0.11 ± 0.02 s under control conditions; n = 7 animals;

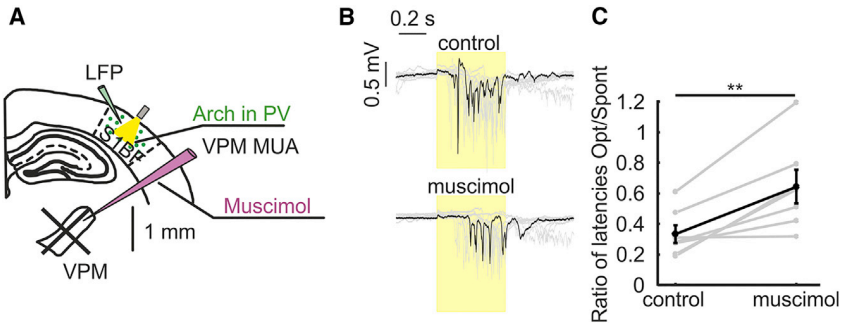

Figure 4. Increased Latency of Optogenetic-Evoked Down-to-Up Transitions upon Thalamic Inactivation

(A) Schematic of the experimental configuration. The inhibitory opsin Arch was expressed in PV cells located in S1bf (green circles). Cortical LFP was recorded via a glass electrode. Thalamic inhibition was achieved through local injection of muscimol.

(B) Representative cortical LFP traces under control conditions (top) and after muscimol injection in the thalamus (bottom), showing the effect of optogenetic inhibition of cortical PV interneurons (yellow bar).

(C) Ratio between light-evoked down-to-up transition latencies and spontaneous down-to-up transition latencies under control conditions and after muscimol application (n = 7 animals; p = 7.8E−3; Wilcoxon signed rank test).

See also Figure S4.

p = 1.7E−3; paired Student's t test; Figures 4B, 4C, and S4C). Moreover, the latency of optogenetically triggered down-to-up-state transitions was more similar to the latency of spontaneous down-to-up-state transitions upon thalamic inactivation, as demonstrated by the increase in the ratio between the latency of light-evoked transitions and the latency of spontaneous transitions after muscimol injection (Figure 4C). We confirmed the statistical significance of those results using a linear mixed effects model (see STAR Methods). We found that thalamic inactivation influenced the effect that the optogenetic manipulation had on up and down-state dynamics (p = 4E−3; type II Wald chi square tests for the interaction term between pharmacology and optogenetics).

Altogether, the results of these combined optogenetic and pharmacological experiments support the role of the thalamus in driving cortical PV interneuron spiking during down states.

DISCUSSION

Slow oscillations are the main oscillatory activity in the electroencephalogram (EEG), and they have long been considered of cortical origin. However, slow oscillations occur outside the cortex. For example, coordinated activity of cortical and thalamic networks is fundamental for their full expression [4, 27–30]. Early work [8] showed that thalamic neurons are active during slow oscillations. Moreover, thalamic spikes precede the initiation of an up state in the cortex [4, 21, 31, 32] and isolated thalamic slices displayed up and down states [33, 34]. Thalamic de-afferentation of the cortex significantly disrupted slow oscillations by reducing their frequency [25, 35]. Moreover, thalamic optogenetic stimulation reliably triggers up states and potentiates the EEG slow rhythms [4, 25, 36]. Sensory [10, 37, 38] or electrical thalamic [39] stimuli also triggered the generation of up states and slow oscillations in the cortex, suggesting that strong excitatory drive from the thalamus increases excitability in the cortex, ultimately favoring the appearance of a cortical up state.

Cortical inhibition is active during up and down states [40, 41], and inhibitory conductances have been shown to vary over the course of the up state [40, 42]. This inhibitory activity modulates up- and down-state transitions. Indeed, pharmacological blockade of the $GABA_A$ receptors [43] shortened up-state duration and pharmacological antagonism of the $GABA_B$ receptor prolonged it [44, 45]. A recent study combined cell-specific optogenetic manipulation targeted to cortical interneurons, including PV cells, with patch-clamp recordings *in vivo* to demonstrate that PV cell spiking controls both up-to-down and down-to-up-state transitions [22]. Specifically, PV cells were observed to fire during cortical down states and their spiking activity was associated with the prolongation of the down-state duration. Optogenetic inhibition of PV cells during cortical down states triggered a swift down-to-up-state transition, demonstrating that spiking of PV cells prolongs the duration of cortical down states [22]. However, what drives PV interneurons to fire during cortical down states remains unknown.

In this study, we provide a series of experimental evidences demonstrating that the thalamus contributes to drive PV cells to spike during cortical down states. Specifically, (1) the thalamic VPM nucleus is less phase locked to the up state of the slow oscillation compared to the S1bf and it is active during about half of cortical down states, (2) cortical down states have longer duration when the VPM is active compared to when the VPM is silent, (3) cortical down states, which display firing of PV cells, were associated with increased VPM activity, (4) the spike-triggered average of VPM activity based on the timing of PV spikes in down state showed increased VPM firing preceding the PV spike, (5) pharmacological blockade of the thalamus decreased PV spiking during down states, and (6) thalamic inactivation prolonged the latency of optogenetically induced down-to-up-state transitions. Remarkably, the involvement of the thalamus in driving interneurons was supported by non-perturbative experiments, in which we measured the spike activity of PV cells using two-photon guided juxtasomal electrophysiological recordings while recording network dynamics with the LFP and MUA, and pharmacological or optogenetic perturbative experiments, in which we modulated the firing of specific brain regions or specific cell types while recording network activity with electrophysiology.

In drawing these conclusions, it is important to underline that our results were obtained in anesthetized mice. Although recent studies investigating the role of specific cell types in the regulation of slow oscillation and up and down-state transitions found similar results in anesthetized and non-anesthetized mice [22, 46], future work will be needed to extend the findings presented in this study to sleeping animals [47].

VPM cells innervate both cortical principal neurons and GABAergic cells [48, 49], including PV interneurons [50–52]. If

VPM thalamic neurons fire during down states, they depolarize both cortical excitatory neurons and PV cells. However, a large body of previous work demonstrated that the firing of principal cells is largely silenced during cortical down states *in vivo* [3, 53, 54] (but see also [55–57]). In contrast, PV interneurons display spiking activity during these cortical silent states *in vivo* [21, 22, 56]. Thus, one possibility is that VPM directly drives PV cells during down states. This hypothesis implies that thalamo-cortical synapses are more efficient in driving suprathreshold response in PV cells compared to principal neurons, in agreement with previous work [58, 59]. It is important to underline, however, that regardless of whether the effect is direct (VPM → PV cell) or indirect (VPM → principal cell → PV cell), our data show that the VPM significantly drives PV cells to spike during cortical down states.

It is also important to note that down-to-up transitions in the cortex spontaneously occurred under conditions of largely reduced (but not suppressed; see Figure 3E) firing of PV cells during down states, as after muscimol application in the thalamus (Figure 3B). This suggests that PV interneurons are not necessary for the down-to-up transition to occur. Rather, through their spiking activity during down states, they prolong the cortical down-state duration and control the timing of the down-to-up transition, in agreement with previous observations [22].

In the framework of what was discussed above, it must be underlined that slow oscillations also occur in isolated cortical slices *in vitro* in the absence of the thalamus [42, 55] and *in vivo* following thalamic inactivation [25, 35] (see Figure 3) or cortical de-afferentation [35, 60]. Thus, the thalamic drive of cortical interneurons that we describe in this study is just one mechanism controlling state changes, which will likely be integrated with other fundamental cortical processes during spontaneous up and down-state transitions. Among these processes, activity-dependent K^+ currents, in particular Ca^{2+}-dependent K^+ current [61] and Na^+-dependent K^+ currents [62], are thought to play a critical role in cortical slow oscillations [55] powerfully contributing to the termination of the up state and generating prolonged hyperpolarization (down state) [63, 64]. Other cortical mechanisms controlling up- and down-state transitions may, for example, involve changes in the concentration of extracellular Ca^{2+} [65].

In our study, we restricted the investigation to PV cells. However, SOM interneurons have been shown to fire during the down state [22, 56, 66], and their perturbation has been demonstrated to profoundly modulate up- and down-state transitions [22] and slow oscillations [67]. Given that SOM interneurons, as well as other types of cortical GABAergic cells, also receive direct excitatory input from thalamo-cortical cells [51, 68], the thalamus may modulate state transitions through the active recruitment of interneuronal populations other than PV cells.

Our results demonstrate that thalamic spontaneous activity can have an overall inhibitory effect on cortical network dynamics during slow oscillations. This is in line with previous observations [69] suggesting that thalamo-cortical inputs to the neocortex may synchronize inhibitory interneurons, thus contributing to synchronous up-to-down-state transitions via feedforward inhibition. Although it is clear that strong thalamic activity induced by sensory [37], electrical [39], or optogenetic [25, 36] stimulation enhances excitation in the cortex, ultimately resulting in the generation of an up-state transition, the data presented in this study demonstrate that moderate level of spontaneous thalamic activity results in inhibitory (rather than excitatory) effects on cortical networks (i.e., prolongation of down-state duration). On the basis of the evidences presented in this study and of those described in the literature, we here propose a unifying view in which the thalamic firing level is seen as a control signal for cortical state transitions. According to this hypothesis, low spontaneous thalamic firing during cortical down states results in prevailing inhibitory effect onto cortex, e.g., prolonging silent cortical states through the action of PV interneurons. In contrast, progressively higher thalamic firing results in cortical networks excitation, thus promoting down-to-up-state transitions. This hypothesis is in agreement with the observation that thalamo-cortical connections form direct synapses onto cortical interneurons [70, 71] and that these connections are stronger and more effective than thalamo-cortical connections onto pyramidal excitatory neurons [58, 59, 68, 72].

One intriguing question is whether our findings in the somatosensory thalamo-cortical loop can be extended to other thalamo-cortical circuits, including those involving non-sensory areas (e.g., the centromedial thalamus [CMT] and the cingulate cortex), which are involved in the control up and down-state transitions [4]. Same similarities between different thalamo-cortical loops can be observed. For example, VPM thalamo-cortical neurons fire in advance of S1 cortical cells at up state start [21], and the firing of CMT neurons similarly precedes up-state generation in the cingulate cortex [4]. However, the spiking activity of CMT and VB neurons is differentially modulated during sleep-wake cycle, and optogenetic manipulation of CMT and VB neurons have different effects on sleep-wake transitions [4]. Thus, it is conceivable whether our findings can be extended to non-somatosensory thalamo-cortical circuits.

In summary, we demonstrated that the thalamus drives PV interneurons to fire during cortical down states, exerting an inhibitory control of cortical S1 network dynamics during down states. Given the role of up- and down-state transitions in memory consolidation [9], synaptic plasticity [15, 16], and the modulation of sensory responses [10, 12], these findings highlight the importance of precisely dissecting out the complex circuit mechanisms underlying the function of the thalamo-cortical system.

STAR★METHODS

Detailed methods are provided in the online version of this paper and include the following:

- KEY RESOURCES TABLE
- CONTACT FOR REAGENT AND RESOURCE SHARING
- EXPERIMENTAL MODEL AND SUBJECT DETAILS
- METHOD DETAILS
  - Viral Injections
  - Electrophysiology
  - Intrinsic optical imaging
  - Whisker stimulation
  - Pharmacology and optogenetics
- QUANTIFICATION AND STATISTICAL ANALYSIS
  - Data selection
  - Up- and down-state detection from LFP signal
  - Spike detection

SUPPLEMENTAL INFORMATION

Supplemental Information can be found online at https://doi.org/10.1016/j.cub.2019.04.007.

ACKNOWLEDGMENTS

This work was supported by ERC (NEURO-PATTERNS), NIH (U01 NS090576 and U19 NS107464), FP7 (DESIRE), and, in part, by Flag-Era JTC Human Brain Project (SLOW-DYN).

AUTHOR CONTRIBUTIONS

S.Z. performed experiments. V.P., P.L.d.L.R., S.Z., and S.P. performed analysis. T.F. conceived and coordinated the project. V.P., P.L.d.L.R., S.Z., S.P., and T.F. wrote the manuscript.

DECLARATION OF INTERESTS

The authors declare no competing interests.

Received: December 21, 2018
Revised: March 8, 2019
Accepted: April 3, 2019
Published: April 25, 2019

REFERENCES

1. Steriade, M., Contreras, D., Curró Dossi, R., and Nuñez, A. (1993). The slow (< 1 Hz) oscillation in reticular thalamic and thalamocortical neurons: scenario of sleep rhythm generation in interacting thalamic and neocortical networks. J. Neurosci. *13*, 3284–3299.
2. Steriade, M., Nuñez, A., and Amzica, F. (1993). A novel slow (< 1 Hz) oscillation of neocortical neurons in vivo: depolarizing and hyperpolarizing components. J. Neurosci. *13*, 3252–3265.
3. Steriade, M., Nuñez, A., and Amzica, F. (1993). Intracellular analysis of relations between the slow (< 1 Hz) neocortical oscillation and other sleep rhythms of the electroencephalogram. J. Neurosci. *13*, 3266–3283.
4. Gent, T.C., Bandarabadi, M., Herrera, C.G., and Adamantidis, A.R. (2018). Thalamic dual control of sleep and wakefulness. Nat. Neurosci. *21*, 974–984.
5. Massimini, M., Ferrarelli, F., Esser, S.K., Riedner, B.A., Huber, R., Murphy, M., Peterson, M.J., and Tononi, G. (2007). Triggering sleep slow waves by transcranial magnetic stimulation. Proc. Natl. Acad. Sci. USA *104*, 8496–8501.
6. Mukamel, E.A., Pirondini, E., Babadi, B., Wong, K.F.K., Pierce, E.T., Harrell, P.G., Walsh, J.L., Salazar-Gomez, A.F., Cash, S.S., Eskandar, E.N., et al. (2014). A transition in brain state during propofol-induced unconsciousness. J. Neurosci. *34*, 839–845.
7. Saleem, A.B., Chadderton, P., Apergis-Schoute, J., Harris, K.D., and Schultz, S.R. (2010). Methods for predicting cortical UP and DOWN states from the phase of deep layer local field potentials. J. Comput. Neurosci. *29*, 49–62.
8. Contreras, D., and Steriade, M. (1995). Cellular basis of EEG slow rhythms: a study of dynamic corticothalamic relationships. J. Neurosci. *15*, 604–622.
9. Marshall, L., Helgadóttir, H., Mölle, M., and Born, J. (2006). Boosting slow oscillations during sleep potentiates memory. Nature *444*, 610–613.
10. Petersen, C.C.H., Hahn, T.T.G., Mehta, M., Grinvald, A., and Sakmann, B. (2003). Interaction of sensory responses with spontaneous depolarization in layer 2/3 barrel cortex. Proc. Natl. Acad. Sci. USA *100*, 13638–13643.
11. Crochet, S., Chauvette, S., Boucetta, S., and Timofeev, I. (2005). Modulation of synaptic transmission in neocortex by network activities. Eur. J. Neurosci. *21*, 1030–1044.
12. Haider, B., Duque, A., Hasenstaub, A.R., Yu, Y., and McCormick, D.A. (2007). Enhancement of visual responsiveness by spontaneous local network activity in vivo. J. Neurophysiol. *97*, 4186–4202.
13. Reig, R., Zerlaut, Y., Vergara, R., Destexhe, A., and Sanchez-Vives, M.V. (2015). Gain modulation of synaptic inputs by network state in auditory cortex in vivo. J. Neurosci. *35*, 2689–2702.
14. Tononi, G., and Cirelli, C. (2014). Sleep and the price of plasticity: from synaptic and cellular homeostasis to memory consolidation and integration. Neuron *81*, 12–34.
15. Vyazovskiy, V.V., Cirelli, C., Pfister-Genskow, M., Faraguna, U., and Tononi, G. (2008). Molecular and electrophysiological evidence for net synaptic potentiation in wake and depression in sleep. Nat. Neurosci. *11*, 200–208.
16. Chauvette, S., Seigneur, J., and Timofeev, I. (2012). Sleep oscillations in the thalamocortical system induce long-term neuronal plasticity. Neuron *75*, 1105–1113.
17. Timofeev, I., and Chauvette, S. (2017). Sleep slow oscillation and plasticity. Curr. Opin. Neurobiol. *44*, 116–126.
18. Crunelli, V., Lőrincz, M.L., Connelly, W.M., David, F., Hughes, S.W., Lambert, R.C., Leresche, N., and Errington, A.C. (2018). Dual function of thalamic low-vigilance state oscillations: rhythm-regulation and plasticity. Nat. Rev. Neurosci. *19*, 107–118.
19. Timofeev, I., Grenier, F., and Steriade, M. (2001). Disfacilitation and active inhibition in the neocortex during the natural sleep-wake cycle: an intracellular study. Proc. Natl. Acad. Sci. USA *98*, 1924–1929.
20. Chauvette, S., Crochet, S., Volgushev, M., and Timofeev, I. (2011). Properties of slow oscillation during slow-wave sleep and anesthesia in cats. J. Neurosci. *31*, 14998–15008.
21. Ushimaru, M., and Kawaguchi, Y. (2015). Temporal structure of neuronal activity among cortical neuron subtypes during slow oscillations in anesthetized rats. J. Neurosci. *35*, 11988–12001.
22. Zucca, S., D'Urso, G., Pasquale, V., Vecchia, D., Pica, G., Bovetti, S., Moretti, C., Varani, S., Molano-Mazón, M., Chiappalone, M., et al. (2017). An inhibitory gate for state transition in cortex. eLife *6*, 1–31.
23. Mukovski, M., Chauvette, S., Timofeev, I., and Volgushev, M. (2007). Detection of active and silent states in neocortical neurons from the field potential signal during slow-wave sleep. Cereb. Cortex *17*, 400–414.
24. Panzeri, S., Harvey, C.D., Piasini, E., Latham, P.E., and Fellin, T. (2017). Cracking the neural code for sensory perception by combining statistics, intervention, and behavior. Neuron *93*, 491–507.
25. David, F., Schmiedt, J.T., Taylor, H.L., Orban, G., Di Giovanni, G., Uebele, V.N., Renger, J.J., Lambert, R.C., Leresche, N., and Crunelli, V. (2013). Essential thalamic contribution to slow waves of natural sleep. J. Neurosci. *33*, 19599–19610.
26. Chow, B.Y., Han, X., Dobry, A.S., Qian, X., Chuong, A.S., Li, M., Henninger, M.A., Belfort, G.M., Lin, Y., Monahan, P.E., and Boyden, E.S. (2010). High-performance genetically targetable optical neural silencing by light-driven proton pumps. Nature *463*, 98–102.
27. Crunelli, V., and Hughes, S.W. (2010). The slow (<1 Hz) rhythm of non-REM sleep: a dialogue between three cardinal oscillators. Nat. Neurosci. *13*, 9–17.
28. Crunelli, V., Errington, A.C., Hughes, S.W., and Tóth, T.I. (2011). The thalamic low-threshold Ca^{2+} potential: a key determinant of the local and global dynamics of the slow (<1 Hz) sleep oscillation in thalamocortical networks. Philos. Trans. A Math. Phys. Eng. Sci. *369*, 3820–3839.
29. Crunelli, V., David, F., Lőrincz, M.L., and Hughes, S.W. (2015). The thalamocortical network as a single slow wave-generating unit. Curr. Opin. Neurobiol. *31*, 72–80.

30. Gent, T.C., Bassetti, C., and Adamantidis, A.R. (2018). Sleep-wake control and the thalamus. Curr. Opin. Neurobiol. *52*, 188–197.
31. Slézia, A., Hangya, B., Ulbert, I., and Acsády, L. (2011). Phase advancement and nucleus-specific timing of thalamocortical activity during slow cortical oscillation. J. Neurosci. *31*, 607–617.
32. Sheroziya, M., and Timofeev, I. (2014). Global intracellular slow-wave dynamics of the thalamocortical system. J. Neurosci. *34*, 8875–8893.
33. Hughes, S.W., Cope, D.W., Blethyn, K.L., and Crunelli, V. (2002). Cellular mechanisms of the slow (<1 Hz) oscillation in thalamocortical neurons in vitro. Neuron *33*, 947–958.
34. Blethyn, K.L., Hughes, S.W., Tóth, T.I., Cope, D.W., and Crunelli, V. (2006). Neuronal basis of the slow (<1 Hz) oscillation in neurons of the nucleus reticularis thalami in vitro. J. Neurosci. *26*, 2474–2486.
35. Lemieux, M., Chen, J.-Y., Lonjers, P., Bazhenov, M., and Timofeev, I. (2014). The impact of cortical deafferentation on the neocortical slow oscillation. J. Neurosci. *34*, 5689–5703.
36. Poulet, J.F.A., Fernandez, L.M.J., Crochet, S., and Petersen, C.C.H. (2012). Thalamic control of cortical states. Nat. Neurosci. *15*, 370–372.
37. Civillico, E.F., and Contreras, D. (2012). Spatiotemporal properties of sensory responses in vivo are strongly dependent on network context. Front. Syst. Neurosci. *6*, 25.
38. Ngo, H.-V.V., Martinetz, T., Born, J., and Mölle, M. (2013). Auditory closed-loop stimulation of the sleep slow oscillation enhances memory. Neuron *78*, 545–553.
39. MacLean, J.N., Watson, B.O., Aaron, G.B., and Yuste, R. (2005). Internal dynamics determine the cortical response to thalamic stimulation. Neuron *48*, 811–823.
40. Neske, G.T. (2016). The slow oscillation in cortical and thalamic networks: mechanisms and functions. Front. Neural Circuits *9*, 88.
41. Puig, M.V., Ushimaru, M., and Kawaguchi, Y. (2008). Two distinct activity patterns of fast-spiking interneurons during neocortical UP states. Proc. Natl. Acad. Sci. USA *105*, 8428–8433.
42. Shu, Y., Hasenstaub, A., and McCormick, D.A. (2003). Turning on and off recurrent balanced cortical activity. Nature *423*, 288–293.
43. Sanchez-Vives, M.V., Mattia, M., Compte, A., Perez-Zabalza, M., Winograd, M., Descalzo, V.F., and Reig, R. (2010). Inhibitory modulation of cortical up states. J. Neurophysiol. *104*, 1314–1324.
44. Mann, E.O., Kohl, M.M., and Paulsen, O. (2009). Distinct roles of GABA(A) and GABA(B) receptors in balancing and terminating persistent cortical activity. J. Neurosci. *29*, 7513–7518.
45. Craig, M.T., and McBain, C.J. (2014). The emerging role of GABAB receptors as regulators of network dynamics: fast actions from a 'slow' receptor? Curr. Opin. Neurobiol. *26*, 15–21.
46. Beltramo, R., D'Urso, G., Dal Maschio, M., Farisello, P., Bovetti, S., Clovis, Y., Lassi, G., Tucci, V., De Pietri Tonelli, D., and Fellin, T. (2013). Layer-specific excitatory circuits differentially control recurrent network dynamics in the neocortex. Nat. Neurosci. *16*, 227–234.
47. Urbain, N., Fourcaud-Trocmé, N., Laheux, S., Salin, P.A., and Gentet, L.J. (2019). Brain-State-Dependent Modulation of Neuronal Firing and Membrane Potential Dynamics in the Somatosensory Thalamus during Natural Sleep. Cell Rep. *26*, 1443–1457.
48. Brecht, M. (2007). Barrel cortex and whisker-mediated behaviors. Curr. Opin. Neurobiol. *17*, 408–416.
49. Feldmeyer, D., Brecht, M., Helmchen, F., Petersen, C.C.H., Poulet, J.F.A., Staiger, J.F., Luhmann, H.J., and Schwarz, C. (2013). Barrel cortex function. Prog. Neurobiol. *103*, 3–27.
50. Ji, X.Y., Zingg, B., Mesik, L., Xiao, Z., Zhang, L.I., and Tao, H.W. (2016). Thalamocortical innervation pattern in mouse auditory and visual cortex: laminar and cell-type specificity. Cereb. Cortex *26*, 2612–2625.
51. Tan, Z., Hu, H., Huang, Z.J., and Agmon, A. (2008). Robust but delayed thalamocortical activation of dendritic-targeting inhibitory interneurons. Proc. Natl. Acad. Sci. USA *105*, 2187–2192.
52. Wall, N.R., De La Parra, M., Sorokin, J.M., Taniguchi, H., Huang, Z.J., and Callaway, E.M. (2016). Brain-wide maps of synaptic input to cortical interneurons. J. Neurosci. *36*, 4000–4009.
53. Sakata, S., and Harris, K.D. (2009). Laminar structure of spontaneous and sensory-evoked population activity in auditory cortex. Neuron *64*, 404–418.
54. Chauvette, S., Volgushev, M., and Timofeev, I. (2010). Origin of active states in local neocortical networks during slow sleep oscillation. Cereb. Cortex *20*, 2660–2674.
55. Sanchez-Vives, M.V., and McCormick, D.A. (2000). Cellular and network mechanisms of rhythmic recurrent activity in neocortex. Nat. Neurosci. *3*, 1027–1034.
56. Fanselow, E.E., and Connors, B.W. (2010). The roles of somatostatin-expressing (GIN) and fast-spiking inhibitory interneurons in UP-DOWN states of mouse neocortex. J. Neurophysiol. *104*, 596–606.
57. Senzai, Y., Fernandez-Ruiz, A., and Buzsáki, G. (2019). Layer-specific physiological features and interlaminar interactions in the primary visual cortex of the mouse. Neuron *101*, 500–513.e5.
58. Cruikshank, S.J., Lewis, T.J., and Connors, B.W. (2007). Synaptic basis for intense thalamocortical activation of feedforward inhibitory cells in neocortex. Nat. Neurosci. *10*, 462–468.
59. Hull, C., Isaacson, J.S., and Scanziani, M. (2009). Postsynaptic mechanisms govern the differential excitation of cortical neurons by thalamic inputs. J. Neurosci. *29*, 9127–9136.
60. Timofeev, I., Grenier, F., Bazhenov, M., Sejnowski, T.J., and Steriade, M. (2000). Origin of slow cortical oscillations in deafferented cortical slabs. Cereb. Cortex *10*, 1185–1199.
61. Schwindt, P.C., Spain, W.J., and Crill, W.E. (1992). Calcium-dependent potassium currents in neurons from cat sensorimotor cortex. J. Neurophysiol. *67*, 216–226.
62. Schwindt, P.C., Spain, W.J., and Crill, W.E. (1989). Long-lasting reduction of excitability by a sodium-dependent potassium current in cat neocortical neurons. J. Neurophysiol. *61*, 233–244.
63. Compte, A., Sanchez-Vives, M.V., McCormick, D.A., and Wang, X.-J. (2003). Cellular and network mechanisms of slow oscillatory activity (<1 Hz) and wave propagations in a cortical network model. J. Neurophysiol. *89*, 2707–2725.
64. Hill, S., and Tononi, G. (2005). Modeling sleep and wakefulness in the thalamocortical system. J. Neurophysiol. *93*, 1671–1698.
65. Massimini, M., and Amzica, F. (2001). Extracellular calcium fluctuations and intracellular potentials in the cortex during the slow sleep oscillation. J. Neurophysiol. *85*, 1346–1350.
66. Tahvildari, B., Wölfel, M., Duque, A., and McCormick, D.A. (2012). Selective functional interactions between excitatory and inhibitory cortical neurons and differential contribution to persistent activity of the slow oscillation. J. Neurosci. *32*, 12165–12179.
67. Funk, C.M., Peelman, K., Bellesi, M., Marshall, W., Cirelli, C., and Tononi, G. (2017). Role of somatostatin-positive cortical interneurons in the generation of sleep slow waves. J. Neurosci. *37*, 9132–9148.
68. Cruikshank, S.J., Urabe, H., Nurmikko, A.V., and Connors, B.W. (2010). Pathway-specific feedforward circuits between thalamus and neocortex revealed by selective optical stimulation of axons. Neuron *65*, 230–245.
69. Lemieux, M., Chauvette, S., and Timofeev, I. (2015). Neocortical inhibitory activities and long-range afferents contribute to the synchronous onset of silent states of the neocortical slow oscillation. J. Neurophysiol. *113*, 768–779.
70. Swadlow, H.A. (1995). Influence of VPM afferents on putative inhibitory interneurons in S1 of the awake rabbit: evidence from cross-correlation, microstimulation, and latencies to peripheral sensory stimulation. J. Neurophysiol. *73*, 1584–1599.
71. Feldmeyer, D., Qi, G., Emmenegger, V., and Staiger, J.F. (2018). Inhibitory interneurons and their circuit motifs in the many layers of the barrel cortex. Neuroscience *368*, 132–151.

72. Bagnall, M.W., Hull, C., Bushong, E.A., Ellisman, M.H., and Scanziani, M. (2011). Multiple clusters of release sites formed by individual thalamic afferents onto cortical interneurons ensure reliable transmission. Neuron *71*, 180–194.

73. Maccione, A., Gandolfo, M., Massobrio, P., Novellino, A., Martinoia, S., and Chiappalone, M. (2009). A novel algorithm for precise identification of spikes in extracellularly recorded neuronal signals. J. Neurosci. Methods *177*, 241–249.

74. Forli, A., Vecchia, D., Binini, N., Succol, F., Bovetti, S., Moretti, C., Nespoli, F., Mahn, M., Baker, C.A., Bolton, M.M., et al. (2018). Two-photon bidirectional control and imaging of neuronal excitability with high spatial resolution in vivo. Cell Rep. *22*, 3087–3098.

75. De Stasi, A.M., Farisello, P., Marcon, I., Cavallari, S., Forli, A., Vecchia, D., Losi, G., Mantegazza, M., Panzeri, S., Carmignoto, G., et al. (2016). Unaltered network activity and interneuronal firing during spontaneous cortical dynamics in vivo in a mouse model of severe myoclonic epilepsy of infancy. Cereb. Cortex *26*, 1778–1794.

76. Bovetti, S., Moretti, C., Zucca, S., Dal Maschio, M., Bonifazi, P., and Fellin, T. (2017). Simultaneous high-speed imaging and optogenetic inhibition in the intact mouse brain. Sci. Rep. *7*, 40041.

77. Harrison, T.C., Sigler, A., and Murphy, T.H. (2009). Simple and cost-effective hardware and software for functional brain mapping using intrinsic optical signal imaging. J. Neurosci. Methods *182*, 211–218.

78. Li, C.Y., Poo, M.M., and Dan, Y. (2009). Burst spiking of a single cortical neuron modifies global brain state. Science *324*, 643–646.

79. Barbaresi, P., Spreafico, R., Frassoni, C., and Rustioni, A. (1986). GABAergic neurons are present in the dorsal column nuclei but not in the ventroposterior complex of rats. Brain Res. *382*, 305–326.

80. Arcelli, P., Frassoni, C., Regondi, M.C., De Biasi, S., and Spreafico, R. (1997). GABAergic neurons in mammalian thalamus: a marker of thalamic complexity? Brain Res. Bull. *42*, 27–37.

81. Barthó, P., Slézia, A., Mátyás, F., Faradzs-Zade, L., Ulbert, I., Harris, K.D., and Acsády, L. (2014). Ongoing network state controls the length of sleep spindles via inhibitory activity. Neuron *82*, 1367–1379.

82. Eschenko, O., Magri, C., Panzeri, S., and Sara, S.J. (2012). Noradrenergic neurons of the locus coeruleus are phase locked to cortical up-down states during sleep. Cereb. Cortex *22*, 426–435.

83. Siapas, A.G., Lubenov, E.V., and Wilson, M.A. (2005). Prefrontal phase locking to hippocampal theta oscillations. Neuron *46*, 141–151.

84. Montemurro, M.A., Rasch, M.J., Murayama, Y., Logothetis, N.K., and Panzeri, S. (2008). Phase-of-firing coding of natural visual stimuli in primary visual cortex. Curr. Biol. *18*, 375–380.

85. Pinheiro, J.C., and Bates, D.M. (2000). Linear mixed-effects models: basic concepts and examples. Mixed-Effects Models in S and S-PLUS (Springer-Verlag), pp. 3–56.

86. Fox, J. (1997). Applied Regression Analysis, Linear Models, and Related Methods (SAGE Publications).

STAR★METHODS

KEY RESOURCES TABLE

REAGENT or RESOURCE	SOURCE	IDENTIFIER
Bacterial and Virus Strains		
AAV1.CBA.Flex.Arch-GFP.WPRE.SV40	Penn Vector Core	RRID:Addgene_22222; Addgene viral prep # 22222-AAV1
Chemicals, Peptides, and Recombinant Proteins		
Muscimol, BODIPY TMR-X Conjugate	Thermo Fisher Scientific	Cat#:M23400
Urethane, > 99%	Sigma-Aldrich	Cat#:U2500; CAS: 51-79-6
Alexa 488 Fluor Hydrazide	Thermo Fisher Scientific	Cat#:A10436
Deposited Data		
Raw electrophysiological recordings (datasets 1 & 2)	Zenodo	DOI: https://www.doi.org/10.5281/zenodo.2609157
Experimental Models: Organisms/Strains		
Mouse: B6;129S6-*Gt(ROSA)26Sor*$^{tm14(CAG-TdTomato)Hze}$/*J*	Jackson Laboratory	RRID:IMSR_JAX:007908
Mouse: B6;129P2-*Pvalb*$^{tm1(cre)Arbr}$/*J*	Jackson Laboratory	RRID:IMSR_JAX:008069
Software and Algorithms		
MATLAB R2017a	Mathworks	RRID:SCR_001622; URL: http://www.mathworks.com/products/matlab/
Origin 2016 64bit	OriginLab	RRID:SCR_002815; URL: https://www.originlab.com/
RStudio	RStudio	RRID:SCR_000432; URL: http://www.rstudio.com/
Spike detection	See [73]	https://doi.org/10.1016/j.jneumeth.2008.09.026
Custom MATLAB code (up/down state detection, phase locking, spike-triggered IFR, evoked transitions latencies algorithms)	This paper; Zenodo	DOI: https://www.doi.org/10.5281/zenodo.2609157

CONTACT FOR REAGENT AND RESOURCE SHARING

Further information and requests for resources and reagents should be directed to and will be fulfilled by the Lead Contact, Tommaso Fellin (tommaso.fellin@iit.it).

EXPERIMENTAL MODEL AND SUBJECT DETAILS

Experimental procedures involving animals have been approved by the IIT Animal Welfare Body and by the Italian Ministry of Health (authorization # 34/2015-PR and 125/2012-B), in accordance with the National legislation (D.Lgs. 26/2014) and the European legislation (European Directive 2010/63/EU). The mouse lines B6;129S6-*Gt(ROSA)26Sor*$^{tm14(CAG-TdTomato)Hze}$/*J*, id #007908, (otherwise called TdTomato line) and B6;129P2-*Pvalb*$^{tm1(cre)Arbr}$/*J*, id #008069, (called PV-cre line) were purchased from the Jackson Laboratory (Bar Harbor, USA). The animals were housed in a 12:12 hr light-dark cycle in individually ventilated cages, with access to food and water *ad libitum*.

METHOD DETAILS

Viral Injections

The adeno-associated virus AAV1.CBA.Flex.Arch-GFP.WPRE.SV40 (Arch) was purchased from the University of Pennsylvania Viral Vector Core. PV-Cre transgenic mice (both males and females) were injected between postnatal day 0 (P0) and P2. Pups were anesthetized using hypothermia, placed on a custom-made stereotaxic apparatus and kept at approximately 4°C for the entire duration of

the surgery. A small skin incision was used to expose the skull and ~250 nL of viral suspension were injected using a micropipette at stereotaxic coordinates of 0 mm from bregma, 2 mm lateral of the sagittal sinus, and 0.25–0.3 mm depth. Following injection, the micropipette was held in place for 1–2 min before retraction. After pipette removal, the skin was sutured, and the pup was revitalized under an infrared heating lamp.

Electrophysiology

Electrophysiological recordings were performed at postnatal day P24-P28 for PV-cre and PV-cre x TdTomato mice. Urethane anesthesia (16.5%, 1.65 g/kg) was used to induce cortical spontaneous up- and down-states transitions. The body temperature was monitored using a rectal probe and maintained at 37°C with a heating pad. Oxygen saturation was controlled by a pulse oximeter (MouseOx, Starr Life Sciences, Oakmont, PA). The depth of anesthesia throughout the surgery and the experiments was controlled by monitoring respiration rate, heartbeat, eyelid reflex, vibrissae movements, reactions to tail and toe pinching. Simultaneous cortical LFP and two-photon-guided PV juxtasomal recordings (Figures 1 and 3) were performed as in [22] and centered on top of the barrel cortex. Briefly, a low resistance (0.3-0.6 MΩ) pipette, filled with HEPES-buffered artificial cerebrospinal solution (ACSF), was lowered at ~300 μm depth from the pial surface to monitor superficial LFP activity. Juxtasomal recordings were performed with a second high resistance (5-8 MΩ) pipette, filled with ACSF and 2 mM Alexa 488 Fluor (Thermo Fisher Scientific, Waltham, MA, USA) [74, 75]. Superficial (80-350 μm below the pial surface) PV interneurons were identified by imaging TdTomato fluorescence with an Ultima II laser scanning two-photon microscope (Bruker, Billerica, MA, former Prairie Technologies, Madison, WI, USA) coupled to a Chameleon Ultra II (Coherent Santa Clara, CA, λ_{exc} = 720 nm) [76]. In addition, a third craniotomy was performed at specific coordinates (AP: 3.8, ML: 1.7) which allows to selectively target the thalamic VPM nucleus by lowering a glass pipette.

For LFP recordings during optogenetic manipulation of PV interneurons (Figure 4), Arch expression was first controlled by looking at GFP fluorescence through the mouse skull under a fluorescence stereo microscope. The skull was thinned on top of the barrel cortex where Arch expression was higher. In a subset of experiments, intrinsic optical imaging (IOI) was then performed by stimulating a single whisker (usually B2 or C2). The selected whisker or neighboring ones (e.g., C1, C3 if C2 was used for IOI) were later used to control for whisker-evoked responses in the VPM. A small craniotomy (0.5 mm x 0.5 mm) was performed on top of the identified area and a low resistance (0.5-1 MOhm) glass pipette was lowered to collect the LFP signals from superficial layers (~350 μm from cortical surface). At the same time a second craniotomy was performed at the following coordinates (AP = 3.8, ML = 1.8) and a tilted glass capillary was placed at a depth of about 3.2-3.5 mm in order to target the VPM and to collect its multi-unit activity (MUA) signal.

In all the experiments the cortical surface was kept moist with ACSF. LFP signal displayed in Figures 1 and 3 was filtered in the bandwidth 0.1 – 1 kHz, amplified by an AM-amplifier (AM-system, Carlsborg, WA, USA) and digitized at 10 kHz with a Digidata 1440 (Axon Instruments, Union City, CA). MUA and juxtasomal signals were acquired using a Multiclamp 700B amplifier, filtered at 2.2 kHz and 6 kHz respectively, digitized at 10 kHz with a Digidata 1440. For experiments displayed in Figure 4, all the signals were filtered at 0.1 – 2 kHz, acquired using a Multiclamp 700B, and digitized at 50 kHz. All data were stored with pClamp 10 (Axon Instruments, Union City, CA, USA).

Intrinsic optical imaging

IOI was performed with a customized set-up. The skin was cut to expose the skull and the area above the primary somatosensory cortex was thinned. A single whisker (usually B2 or C2) was introduced in a glass capillary tube glued to a piezoelectric bender actuator (Physik Instrumente, Milan, IT), and then stimulated at 18 Hz for 1.1 s at intervals of 20 s for a total of 40 trials. Illumination upon the skull was done with red light (630 ± 10 nm) and a CCD camera (Hamamatsu, Milan, IT) was used to acquire time series images during whisker stimulation. The analysis of the images was performed with a custom MATLAB script based on [77]. The region that showed lower reflectance compared to baseline was used to identify the principal barrel corresponding to that whisker. Blood vessels were used as reference by acquiring an image under green light (546 ± 10 nm). Once the area of interest was identified by IOI, a small craniotomy (~1 mm^2) was performed over that region.

Whisker stimulation

To assess the position of pipettes used for recording and pharmacological application in the thalamic VPM nucleus, we stimulated the mouse whiskers with a single pulse of compressed air delivered through a glass capillary and, at the same time, we recorded the MUA activity in the VPM. The pulses were 20-ms long and presented at 0.25 Hz. We evaluated the responsiveness of the recorded region by detecting extracellular spikes as described before and calculating the spike rate in 100-ms windows before and after the onset of the stimulation (pre- and post-stimulation windows). Under control conditions, we found a significant increase in the spike rate after whisker stimulation with respect to the preceding time period (pre stimulation: 8.14 ± 2.62 spikes/s, post stimulation: 24.09 ± 3.10 spikes/s, mean ± s.e.m., n = 7 animals, p = 0.0074, paired Student's t test). After muscimol injection VPM was largely suppressed with no significant difference between activity preceding and following whisker stimulation (no detected spikes in pre-stimulation windows versus 2.38 ± 2.30 spikes/s in post-window, mean ± sem, n = 7 animals, p = 0.34, one-sample Student's t test). We computed the spike rate of the complete recordings averaged across animals during spontaneous activity, obtaining: 5.71 ± 1.65 spikes/s under control condition and 0.02 ± 0.01 spikes/s after muscimol injection.

Pharmacology and optogenetics

To induce pharmacological block of thalamic activity, a glass pipette was filled with a solution containing fluorescent muscimol (Muscimol, BODIPY TMR-X Conjugate, Thermo Fisher) 0.5 mM dissolved in 1% DMSO and ACSF. A small positive pressure was applied to infuse between 250-500 nL into the thalamus. Using the same pipette, we collected the MUA and the effect of muscimol silencing was controlled for by looking at the almost complete loss of MUA spikes. The muscimol diffused for about 20 - 40 minutes and the effect on whisker stimulation was further confirmed by the dramatic decreased of MUA spikes in the thalamic activity following whisker deflection. The animal was then sacrificed and correct positioning of the glass pipette for pharmacological application was confirmed by imaging the fluorescent conjugate of muscimol in fixed tissue using the upright fluorescent microscope Olympus BX51 coupled with Neurolucida software.

A continuous wave solid-state laser source (Cobolt, Vretenvägen, Sweden) was used to deliver yellow (λ = 594 nm, stimulus duration of 500 ms) light illumination through an optical fiber (diameter 200 μm, NA: 0.22, AMS Technologies, Milan, Italy). Laser power was measured at the fiber tip and set at $\sim$30 mW.

QUANTIFICATION AND STATISTICAL ANALYSIS

Data selection

To ensure that our analysis was restricted to synchronized periods of activity, in consecutive 5 s trials we computed the synchronization index, i.e., the ratio between the LFP signal power in low-frequency ([0.1, 4] Hz) over high-frequency bandwidth ([4, 100] Hz) [23, 78]. We ran our analysis only on those trials showing synchronization index > 4 [78].

Up- and down-state detection from LFP signal

Up- and down-states were detected from the cortical LFP signal using the same method described in [22]. Briefly, the raw LFP signal was first low-pass filtered below 500 Hz (using an elliptic filter) and then down-sampled to 1 kHz. Up- and down-states were then detected from the filtered LFP using a method based on combining the approach of Saleem and colleagues [7] (based on the instantaneous phase of the LFP in the low-frequency < 4 Hz band), with a modified version of the algorithm proposed by Mukovski [23] (exploiting differences in beta and gamma-band power between up- and down-states). As described in [22] we optimized the parameters of the algorithm for our experimental conditions by using six simultaneous LFP and patch-clamp recordings on pyramidal neurons. The Saleem method depends on the choice of a few low-frequency bands, whose instantaneous phase is used for state detection, as well as on the corresponding angular parameters that may vary according to the specific recording configuration. We found that under our conditions the optimal LFP bands for state detection were [0 – 1 Hz] and [1 – 2 Hz]. This choice allowed us to maximize the performance of the detection algorithm (data not shown). The output of the Saleem method is a decision (or evidence) variable $S_{delta}(t)$, computed by combining the differential likelihood of observing an up- or down-state from the chosen bands, which varies between 0 and 1 and can be used to determine the instantaneous state. To also take advantage of the information about the state given by higher frequencies, following [23] we combined $S_{delta}(t)$ with another decision variable extracted from the LFP in the 10 – 50 Hz range including the beta and low gamma bands ($S_{beta-gamma}(t)$). To calculate $S_{beta-gamma}(t)$, we first processed the filtered signal to calculate the standard deviation (i.e., root mean square) of the filtered signal in the [10, 51] Hz band in a running frame of 5 ms. We then smoothed the obtained trace with a 50 ms running frame linear filter [23]. Finally, the resulting signal was normalized between 0 and 1, excluding the top 5^{th} percentile, and averaged with $S_{delta}(t)$ to obtain $S_{comb}(t)$. Since the performances of the algorithm considering $S_{comb}(t)$ were slightly higher than when using $S_{delta}(t)$ alone [22], we decided to use $S_{comb}(t)$ instead of $S_{delta}(t)$ to estimate the state at each time instant. To determine the thresholds for the detection of up/down-states, the distribution of $S_{comb}(t)$ (excluding the top 5^{th} percentile) was fitted by a mixture of three Gaussians using an expectation maximization algorithm [7, 22]. Each Gaussian represents a different cortical state: up (highest values of S_{comb}), down (lowest), and indeterminate (intermediate). Time samples corresponding to $S_{comb}(t) > \mu_{UP} - 2\sigma_{UP}$ were assigned to up-states, and samples corresponding to $S_{comb}(t) < \mu_{DOWN} + 2\sigma_{DOWN}$ to down-states (where means and variances of the Gaussians were represented as μ_{UP}, μ_{DOWN}, and σ_{UP}, σ_{DOWN} for the up- and down-states, respectively). The remaining samples were considered as indeterminate state. We set the minimum state duration equal to 100 ms and the minimum inter-state interval equal to 50 ms [22].

After muscimol injection in the thalamus, we re-fitted $S_{comb}(t)$ distributions and determined new up/down-state detection thresholds. We ensured that thresholds in the control condition were not significantly different from thresholds in the muscimol condition for the same animals (data not shown). All the analyses were performed by using custom-made software implemented in MATLAB (The Mathworks, Natick, MA, USA).

Spike detection

We detected action potentials in cortical PV interneurons from juxtasomal recordings by applying a hard-threshold algorithm to the high-pass filtered signal (elliptic filter, cut-off frequency 300 Hz). The threshold was computed as 6 times the estimated standard deviation of the signal. The time stamps of the detected spikes were assigned to the action potential positive peak. Extracellular spikes in the thalamic MUA were detected using a previously published spike detection algorithm known as precise timing spike detection (PTSD) [73]. Briefly, after band-pass filtering (elliptic filter, bandwidth [300, 3000 Hz]), the algorithm looked for pairs of relative maxima/minima in the filtered signal within a user-defined peak lifetime period (set at 3 ms) exceeding a differential threshold set at 8-9 times the estimated standard deviation of the noise. A refractory period of 1 ms was also applied to discard overlapping spikes.

The time stamps of the detected spikes were assigned to the negative voltage peaks. The VPM nucleus contains one type of excitatory neuron the thalamo-cortical cell [79] and virtually no local interneurons [80]. The MUA signal should thus provide a proxy of the integrated activity of VPM thalamo-cortical cells. However, previous work demonstrated that extracellular electrodes placed in the VPM can record narrow spikes generated by the axons of TRN inhibitory cells [81]. Thus, we cannot exclude that part of the VPM MUA signal recorded under our experimental conditions reflects TRN activity.

Phase locking analysis between cortical PV interneurons / thalamic activity and LFP

To investigate the temporal relationship between PV interneurons' spiking activity/thalamic MUA and up/down-state occurrence during spontaneous activity, we asked whether the LFP slow oscillation phase (which in turn reflected cortical state) was related to the occurrence of spikes by quantifying phase locking of recorded spikes. To do that, we applied a previously described method [22, 82, 83]. We computed the instantaneous low-frequency phase of the LFP as the angle of the Hilbert transform of the LFP trace filtered in the [0.1, 4] Hz band. The phase of firing distribution quantifies, for each cell, the phase values at which each spike was fired. Non-uniform phase of firing distributions meant that neurons fired preferentially at certain phases. Hence, phase locking can be detected by assessing departure from uniformity in the distribution of rescaled phases observed at spike times. To correct for the effect of possible non-uniformities in the phase distributions due to asymmetries in the LFP wave shape [83], we made the overall distribution of phase across all time points uniform by rescaling it by its cumulative distribution. The significance of phase locking was computed as departure from uniformity of the phase of firing distribution, using the Rayleigh's test [83]. As a measure of strength of locking, we considered one minus the circular variance, to quantify the concentration of the distribution of angles [82, 84]. We also determined the preferred phase of firing by calculating the circular mean of the phase of firing distribution. To quantify how spikes are distributed during the course of either up- or down-states, we also computed the phase of firing distribution of PV interneuron spikes separately for either up- or down-states. PV spikes recorded during up- (or down-) states were limited to the 5^{th}-95^{th} percentile up-state (or down-state) phase range, i.e., [95, 255] degrees for up-, and [295, 75] degrees for down-state, respectively. In this case, to account for the non-uniformity of the overall distribution of up-state (or down-state) phase, we rescaled it by its cumulative distribution in the above mentioned range. The phase of firing distribution during up- or down-states can be easily compared to the time of firing distribution when normalized to state extremes (0 = start of up/down-state; 1 = end of up/down-state). Point-wise comparison between the phase and time distributions demonstrated no significant difference between the phase and time domain with the exception of the last three bins at the end of the down-state for VPM (marked by asterisks in Figure S1F, paired Student's t test, FDR correction for multiple comparisons). When comparing relative time of firing distributions with the uniform distribution, we observed significant differences only in down-state for both PV interneurons and VPM, with the exception of one point at the end of the up-state for PV cell activity (marked by hashtags in Figures S1E and S1F, left- or right-tailed one-sample Student's t test, FDR corrected for multiple comparisons). Cortical PV interneurons tended to spike more than expected from a uniform distribution at the beginning and less in the middle of the down-state, showing a median time-of-firing of 0.39 ± 0.03 (significantly different from 0.5, one-sample Student's t test, p = 7.71E-4, n = 18 cells in 7 animals). The thalamus showed lower spiking probability in the middle of the down-state and symmetrically higher probability at the borders. Nonetheless, the VPM median time-of-firing was 0.48 ± 0.02 (n = 18 recordings in 7 animals), not significantly different from 0.5 (one-sample Student's t test, p = 0.30, n = 18 in 7 animals). During the up-state, both PV interneurons and the thalamic VPM nucleus fired uniformly, showing median time of firing of 0.49 ± 0.01 and 0.51 ± 0.01, respectively (not significantly different from 0.5, one-sample Student's t test, p = 0.43 and p = 0.45, n = 18 in 7 animals).

Spike-triggered thalamic instantaneous firing rate

To measure the temporal relationship between cortical PV interneuron spiking activity and thalamic MUA during cortical down-states, we computed the spike-triggered VPM instantaneous firing rate (IFR) based on the timing of PV spikes recorded during down-states (this analysis was also extended to PV spike times during up-states, see Results). To estimate the IFR function, we convolved VPM spike trains with Gaussian kernels of increasing standard deviations (1.25 ms – 12.5 ms). We averaged VPM IFR functions in time windows of corresponding increasing durations (10-100 ms) preceding (pre-spike) and following (post-spike) PV spikes in down-state. We finally selected those parameter values that maximized the correlation between VPM and PV activity in the pre-spike window (Gaussian kernel standard deviation of 12.5 ms, corresponding to low-pass filtering with 20-Hz cut-off frequency, and pre- / post-spike time windows of 100 ms). For each PV interneuron, to test whether the VPM mean firing rate preceding PV spikes in down-state was higher than expected by chance, we repeated the same analysis for "surrogate" PV spikes. We generated 100 surrogate datasets by randomly sampling PV-silent down-states while preserving the total number of spikes and the phase of firing distribution in down-state. We checked that, by doing this, also the time of firing distribution during down-state, when normalized to state extremes, was approximately preserved. We also fixed the maximum number of sampled down-states and the maximum number of spikes *per* down-state. This helped us to also mimic with our surrogate data the statistical distribution of the number of spikes *per* down-state. We then computed for each surrogate dataset the VPM IFR triggered by surrogate spikes and computed preceding and following VPM mean firing rates, as done for the actual PV spikes. For each PV interneuron, we computed the z-score of the average VPM firing rate in the pre-spike and post-spike windows with respect to the corresponding statistical distribution of surrogate mean firing rates to check for significant statistical differences between actual and surrogate data. Moreover, we asked whether the statistical distribution of VPM mean firing rate in the pre-spike window was significantly higher than in the post-spike

window, suggesting a possible temporal relationship directed from VPM to PV interneurons in down-state. The latter analysis was also performed for VPM mean firing rate preceding and following PV spikes in up-state.

Evoked down-to-up transition latency

We computed the latencies of down-to-up transitions evoked by optogenetic suppression of PV interneurons during cortical down-states both under control conditions and after muscimol injection in the thalamus in two steps. First, for finding putative down-state periods, we slightly modified the previously described detection algorithm by simplifying it, since we did not need to determine precisely up/down-state boundaries in this case. We observed a short polarization of the signal at the beginning of the optogenetic stimulation, which can be considered as an artifact of the illumination (duration $\sim$ 4 ms). To correct for this we substracted to the LFP signal the mean of all stimulation trials in which the artifact was visible and not superimposed to a fast evoked down-to-up state transition, and finally smoothed it using a 14-ms window moving average filter in a 60-ms window centered on the stimulation onset. We then computed the evidence (or decision) variable $S_{beta-gamma}(t)$ as previously described (using 10-ms windows for running standard deviation computation of the [10, 51] Hz filtered signal,) and we detected as putative down-states those time periods in which the processed signal was lower than its overall median (see Figure S4A, middle trace). The same thresholds computed under control conditions were used to detect putative down-states after thalamic pharmacological inhibition. We then selected those 5 s trials in which the onset of the optogenetic stimulation fell in a putative down-state and we computed the discrete temporal derivative of the LFP signal (Figure S4A, bottom trace). For each optogenetic stimulation falling in a down-state, we computed the mean μ and standard deviation σ of the LFP derivative in the corresponding down-state. We identified the evoked transition to an up-state as the time sample when the LFP derivative exceeded the threshold T defined as $T = \mu - k\sigma$, with k being an arbitrary multiplicative constant set at 4. The latency of the transition was therefore computed as the time interval between the onset of the illumination period and the first crossing of the threshold T (Figure S4A, top trace). To check whether light-evoked transition latencies were shorter than expected by chance due to optogenetic inhibition of PV cells, we selected periodically distributed points during spontaneous activity as ''surrogate'' stimulation onsets and performed the same analysis by computing the latencies to the next spontaneous down-to-up transitions (setting $k = 2$ to account for slower spontaneous transition slopes with respect to light-evoked ones). We considered as *spontaneous* the LFP activity occurring at least 50 ms before the onset and 550 ms after the offset of each illumination period in each 5 s trial. To control for possible long-term effects of the optogenetic PV inhibition in cortical activity, we compared the latencies of spontaneous down-to-up transitions obtained with this method with latencies calculated on longer recordings of fully spontaneous activity for 20 different random selection of the beginning of stimulation time instants in 3 animals under control conditions and after muscimol injection. The obtained results were not significantly different from previous ones (data not shown). Then, we compared the obtained results by using different thresholds for putative down-state identification from $S_{beta-gamma}(t)$ distribution, instead of using the signal's median. (i.e., the full-width-half-maximum of the first peak of $S_{beta-gamma}(t)$probability distribution function, and the mean plus standard deviation of the first Gaussian component of two-Gaussian mixture fitting of $S_{beta-gamma}(t)$ distribution). In both cases, we obtained statistically indistinguishable results compared to the median threshold (Figure S4B).

Finally, we developed a linear mixed effects model (LME) [85] to further explore the effects that pharmacological inhibition of the thalamus had on the down-to-up state transition regulatory function of PV cells. This statistical model allowed us to discriminate the contributions to the variance of the experimental variables of interest (fixed effects) from the ones due to animal variability (random effects). We defined as ''fixed effects'' pharmacological *treatment* (considering either control or muscimol conditions), and *stimulation* (considering either optogenetically induced transitions or spontaneous ones), and we also considered their interaction. To account for animal variability, we first included as ''random effects'' the *animal identity*, and variations in intercept among animals within both *treatment* and *stimulation*.

The model is described by the following equation:

$$Latency_{ijk} = \beta_0 + \beta_1(i) + \beta_2(j) + \beta_3(i,j) + \gamma_{0k} + \gamma_{1k}(i) + \gamma_{2k}(j) + \varepsilon_{ijk}$$

with β the fixed effects, γ the random effects, for *treatment* i, *stimulation* j and *animal* k. We first tested the statistical significance of each random effect by using a likelihood ratio test (LRT). The LRT compared the likelihood of the complete model with reduced ones dropping one effect at a time. The random intercepts corresponding to the interaction between animal and treatment and between animal and stimulation were significant (γ_{1k}; p = 0.02, γ_{2k}; p = 1.4E-8), but animal identity was not and we therefore excluded it from the model (γ_{0k}; p = 0.26). Then, after re-fitting the model, each fixed effect was evaluated using type II Wald chi-square test [86]. To evaluate the output of this model, we performed a pairwise contrast test between the means of the factorial groups adjusting the degrees of freedom using the Kenward-Roger method and the p values using the Tukey method for comparing a family of four estimates (Figure S4C).

Statistics

The Kolmogorov-Smirnov test was run on each experimental sample with N > 5 to test for normality. Two-tailed (unless otherwise stated) Student's t test (in case of normal distribution), and the Wilcoxon rank-sum or signed-rank (for unpaired and paired comparison of non-normal distributed data, respectively) tests were used when comparing two populations. For comparison of more than two populations, one-way ANOVA was used. We used Benjamini-Hochberg procedure to correct p values for FDR in case of multiple comparisons, and binomial test to combine p values resulting from several independent tests bearing upon the same overall

hypothesis. To study the significance of fixed effects in the LME model, we used the Type II Wald Chi-square test and a pairwise contrasts test adjusted with the Tukey method to compare the population means of the model. When not specified explicitly, the significance level for statistical testing was set at 0.05. Statistical analysis was performed using Origin 2016, RStudio, or MATLAB software.

DATA AND SOFTWARE AVAILABILITY

The raw datasets (i.e., electrophysiological recordings) and custom MATLAB code were deposited in Zenodo. The DOI to the deposited data and code reported in this paper is https://doi.org/10.5281/zenodo.2609157.

Current Biology, Volume *29*

Supplemental Information

Thalamic Drive of Cortical Parvalbumin-Positive Interneurons during Down States in Anesthetized Mice

Stefano Zucca, Valentina Pasquale, Pedro Lagomarsino de Leon Roig, Stefano Panzeri, and Tommaso Fellin

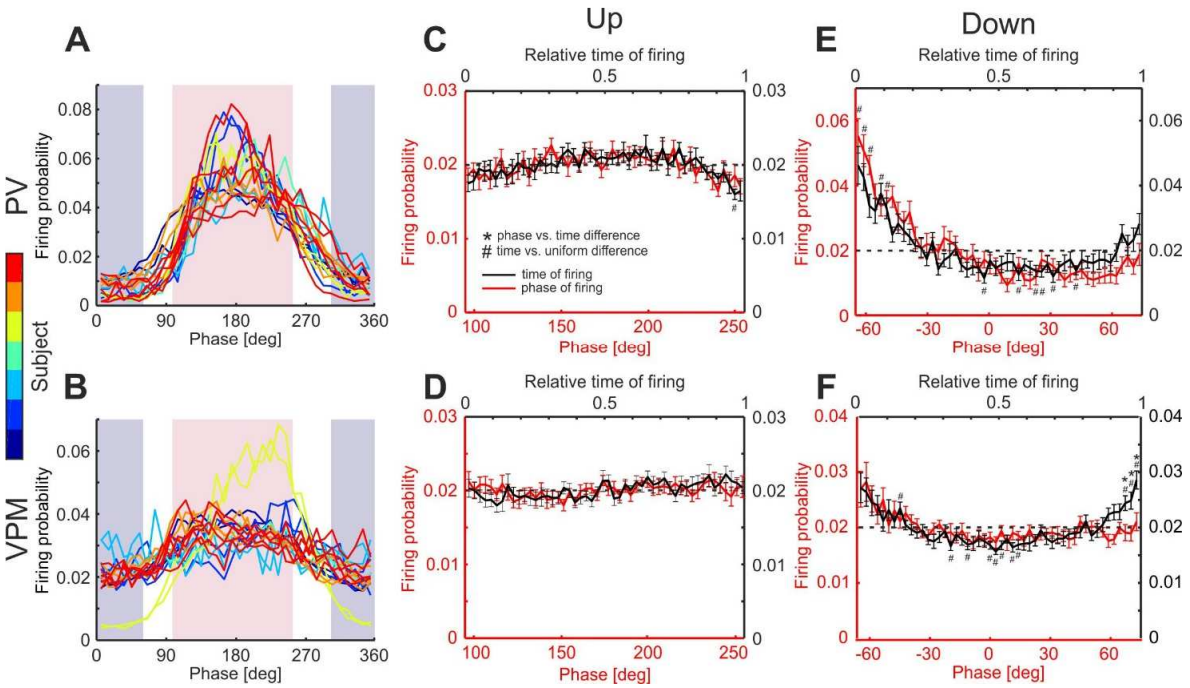

Figure S1. Phase-of-firing and relative time-of-firing distributions of PV cells and VPM MUA during cortical up- and down-states. Related to Figure 1. (A-B) Phase-of-firing distributions of all PV interneurons (color-coded by animal (A) and simultaneously recorded VPM MUA (B). **(C-D)** Phase-of-firing distribution (red, mean ± s.e.m., n = 18 cells in 7 animals) and relative time-of-firing distribution (black) for PV interneurons (C) and VPM MUA (D) during cortical up-states. **(E-F)** Same as for (C, D), but for cortical down-states (mean ± s.e.m., n = 18 recordings in 7 animals). For all panels: asterisks indicate point-wise significant statistical differences between the two curves (paired Student's t-test, FDR corrected for multiple comparisons, p-level = 0.05). Hashtags indicate point-wise significant statistical differences between time-of-firing distributions and the uniform distribution (one-sample Student's t-test, FDR corrected for multiple comparisons, p-level = 0.05).

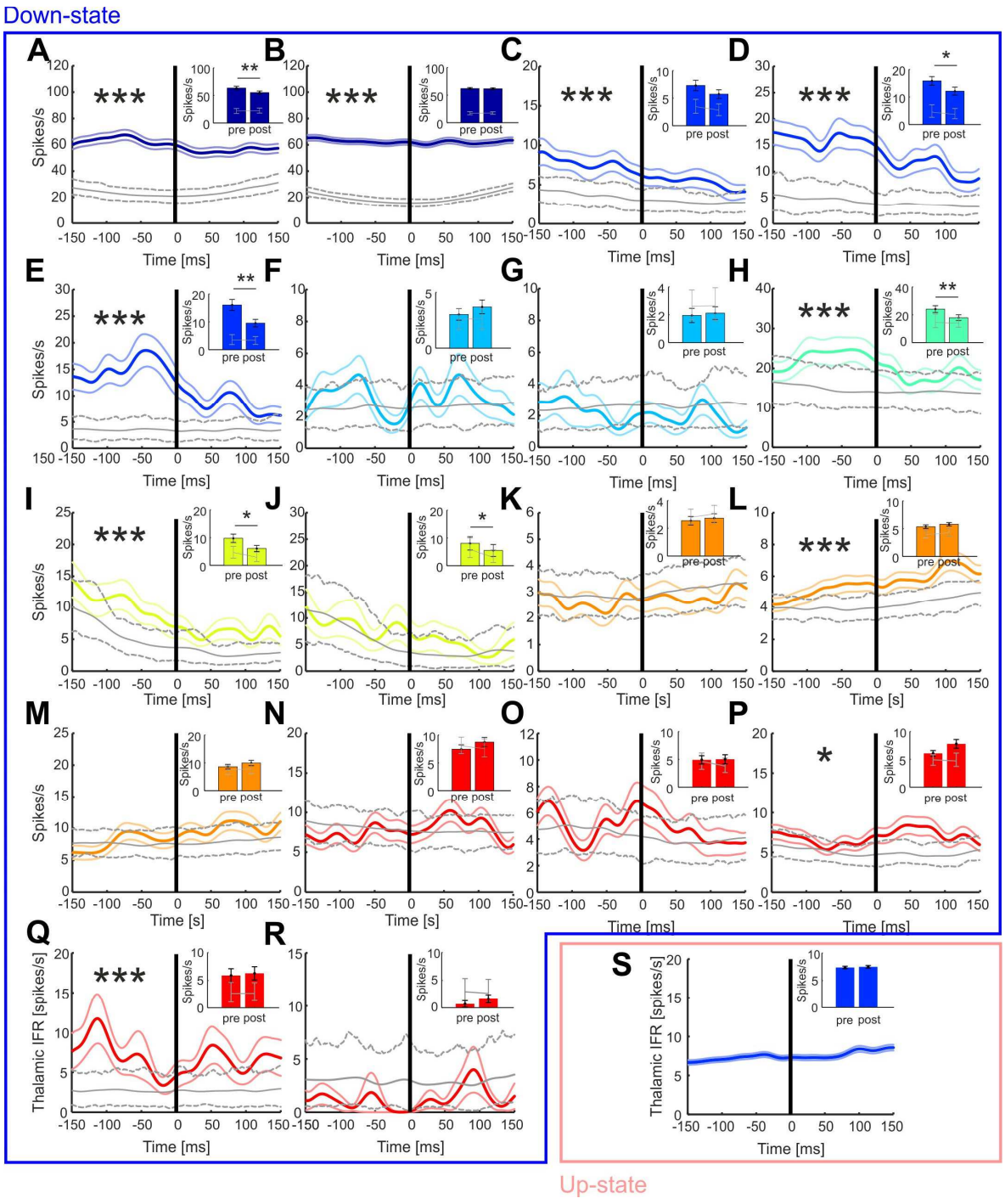

Figure S2. Spike-triggered average analysis across individual experiments. Related to Figure 2. (A-R) Spike-triggered VPM firing rate based on PV interneuron spike times during cortical down-states for all recorded cells (n = 18 from 7 animals, Gaussian kernel standard deviation 12.5 ms, mean ± s.e.m.). Statistical difference of the pre-spike VPM mean firing rate with respect to surrogate data is indicated by the asterisks (z-test, $p < 0.05$). Insets: VPM firing rate before and after a PV spike in down-state (pre: [-100, 0] ms; post: [0, 100 ms]; mean ± s.e.m.; Wilcoxon signed rank test). **(S)** Same as in (A-R**)** but for PV interneuron spike times during cortical up-states for one representative recorded cell.

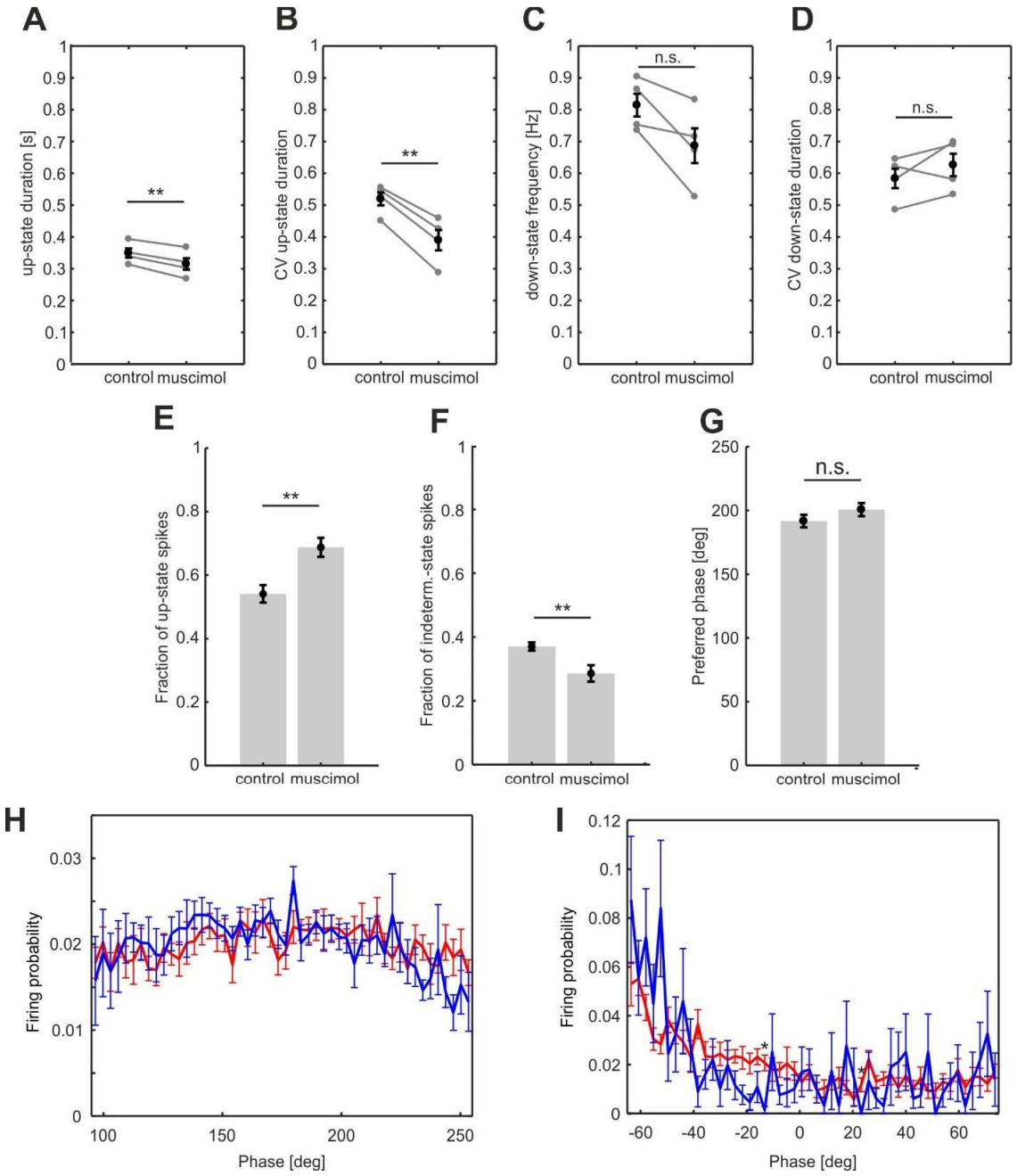

Figure S3. Effect of thalamic muscimol injection on cortical up and down-state dynamics and PV interneuron firing activity. **Related to Figure 3. (A-B**) Up-state duration (A) and its coefficient of variation (B) under control conditions and after muscimol injection in the thalamus (mean ± s.e.m., paired Student's t-test, p = 0.009 for A and p = 0.003 for B, n = 4 animals). **(C**) Down-state frequency under control conditions and after muscimol injection in the thalamus (mean ± s.e.m., p = 0.056, paired Student's t-test, n = 4 animals). **(D**) Coefficient of variation of down-state duration under control conditions and after muscimol injection in the thalamus (mean ± s.e.m., paired Student's t-test p = 0.27 for D, n = 4 animals). **(E-F**) Fraction of up (E) and indeterminate (F) state spikes under control conditions and after muscimol injection (mean ± s.e.m., Student's t-test, p = 0.003 for C and p = 0.008 for D, control: n = 8 cells, muscimol: n = 7 cells from 4 animals). **(G**) Mean phase of firing of PV interneurons under control conditions and after thalamic muscimol injection (circular mean ± s.e.m, p = 0.26, Watson-Williams test, control: n = 8, muscimol: n = 7 from 4 animals). **(H-I**) Phase-of-firing distribution of PV interneurons during cortical up (H) and down (I) states under control conditions (red, mean ± s.e.m., n = 8 cells in 4 animals) and after thalamic muscimol injection (blue, mean ± s.e.m., n = 7 cells in 4 animals). In both panels, the two curves do not show significant point-wise differences, except for two points (marked by asterisks, Student's t-test, FDR corrected for multiple comparisons, p-level = 0.05).

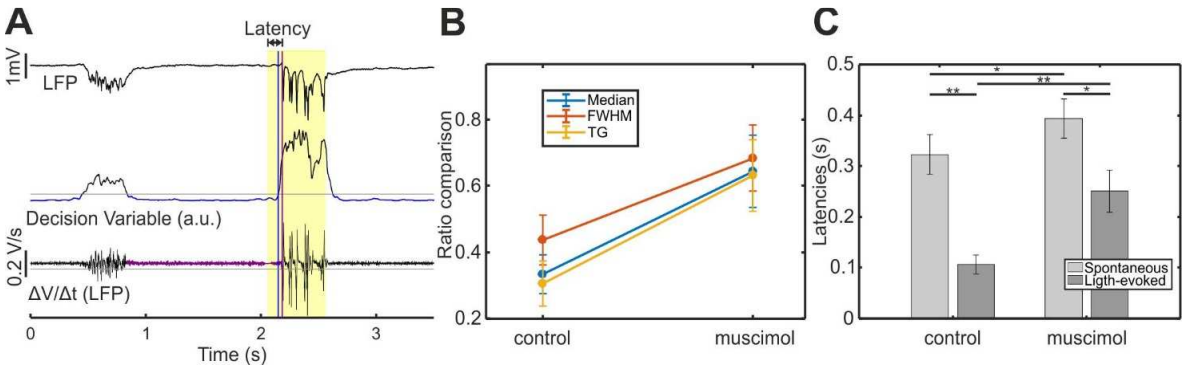

Figure S4. Latencies of down-to-up transitions upon inhibition of cortical PV interneurons under control condition and after thalamic pharmacological inactivation. Related to Figure 4. (A) Representative cortical LFP trace after muscimol injection in the thalamus (top) showing characteristic silent and active periods during slow oscillation network dynamics. The gamma-filtered signal (middle) is used to detect down-states (blue periods). This detection is then used to select the traces in which the beginning of the optogenetic inhibition of PV cells (yellow bar) occurred in a down-state. The transition to an up-state (purple vertical line) is defined as occurring when the LFP temporal derivative (bottom) crosses the threshold T (gray line). The latency of the transition is therefore the time interval between the beginning of the yellow bar and the purple vertical line. **(B**) Comparison of the average latency ratios calculated using three different thresholds (median, full-width-half-maximum and two-Gaussian mixture fitting, indicated by different colors) for down-state detection (see STAR Methods) (mean ± s.e.m., one-way ANOVA, $p = 0.36$ for control and $p = 0.94$ for muscimol, $n = 7$ animals). **(C**) Latencies of spontaneous and light-evoked down-to-up transitions under control conditions and after muscimol application in the thalamus (mean ± s.e.m., $n = 7$ animals).

Appendix B

CITE-On

In the study presented in Appendix B, I compared traces extracted by CITE-On with those extracted by CaImAn [Giovannucci et al., 2019], a state-of-the-art method based on constrain non-negative matrix factorization (Supplementary Figure 4 and 6). I compared different background extraction methods and the correlation between traces for each method (Supplementary Figure 4 and 6), as well as the relationship with signal-to-noise ratio of putative neurons and correlation between methods (Supplementary Figure 4 and 6).

CITE-On: a deep learning approach for online cell identification and trace extraction in functional two-photon calcium imaging

Luca Sità[1,*,#], Marco Brondi[1,*,#], Pedro Lagomarsino de Leon Roig [1,2], Sebastiano Curreli[1], Mariangela Panniello[1], Tommaso Fellin[1,#]

[1] Optical Approaches to Brain Function Laboratory, Istituto Italiano di Tecnologia, Genova, Italy

[2] University of Genova, Genova, Italy

* Equal contribution

Corresponding authors:

Luca Sità, Optical Approaches to Brain Function Laboratory, Istituto Italiano di Tecnologia, Via Morego 30, 16163 Genova, Italy, tel: +39 010 2896549, fax: +39 010 2896230, email: luca.sita@iit.it

Marco Brondi, Optical Approaches to Brain Function Laboratory, Istituto Italiano di Tecnologia, Via Morego 30, 16163 Genova, Italy, tel: +39 010 2896549, fax: +39 010 2896230, email: marco.brondi@iit.it

Tommaso Fellin, Optical Approaches to Brain Function Laboratory, Istituto Italiano di Tecnologia, Via Morego 30, 16163 Genova, Italy, tel: +39 010 2896549, fax: +39 010 2896230, email: tommaso.fellin@iit.it

Keywords: two-photon functional imaging, genetically encoded calcium indicators (GECI), deep neuronal networks, online image segmentation

Abstract

In vivo two-photon calcium imaging is a powerful approach in experimental neuroscience. However, processing two-photon calcium imaging data is computationally intensive and time-consuming, making online frame-by-frame analysis a challenge. This is especially true for large field-of-view (FOV) imaging. Here, we present CITE-On (Cell Identification and Trace Extraction Online), a convolutional neural network-based algorithm for fast automatic cell identification, segmentation, identity tracking, and trace extraction in two-photon calcium imaging data. CITE-On processes thousands of cells online, including data from mesoscopic two-photon imaging, and provides accurate functional measurements from most neurons in the FOV. Applied to publicly available datasets, CITE-On achieves performance similar to that of state-of-the-art methods for offline analysis. Moreover, CITE-On generalizes across calcium indicators, brain regions, and acquisition parameters in anesthetized and awake head-fixed mice. CITE-On represents a powerful new tool to speed up image analysis and facilitate closed-loop approaches, for example in combined all-optical imaging and manipulation experiments.

Introduction

Multi-photon imaging in combination with Genetically Encoded Calcium Indicators (GECI) allows the recording of population activity with high spatial resolution in the intact brain *in vivo* [1-6]. However, multi-photon imaging datasets, in the form of t-series, can be heavy (0.5 GB to > 1 TB) and their processing requires time and computational power. More specifically, the precise identification and segmentation of neuronal structures (typically somata) in a given FOV is critical to extract truthful and reliable information from raw imaging t-series [6]. This step can be complex because of dense GECI staining, low signal-to-noise ratio (SNR), presence of motion artifacts, and large number of neurons in the FOV (e.g., in the case of mesoscopic two-photon imaging [7, 8]).

130

Segmentation is typically performed in two ways: *i)* manually, based on visual inspection by an expert user and on selection of pixels into regions of interest (ROIs); *ii)* automatically, employing supervised or unsupervised methods leveraging on static and dynamic properties of the fluorescence signal in the t-series [9-23]. Manual segmentation [24, 25] is time consuming and impractical in case of large datasets and FOVs (e.g. mesoscopic imaging) or when real-time manipulation of experimental conditions is needed [26, 27]. State-of-the-art automatic approaches apply pixel correlation [15, 16, 19], principal/independent component analysis (PCA/ICA) [15, 16], constrained non-negative matrix factorization (CNMF) [10, 14, 17], and deep neural networks (DNN) [10, 20-22] to perform FOV segmentation. These approaches are usually applied offline and generally take advantage of both neuronal spatial footprints and the temporal dynamics of the fluorescence signal associated to the identified spatial footprints. Consequently, their performance benefits from long acquisitions [10, 16, 23], with highly active cells being more easily segmented than rarely active or inactive ones [10, 22]. Moreover, current methods often require the experimenter to set initialization parameters ahead of the segmentation process [10, 11, 15-17, 22]. While most of these parameters are generally easy to adjust (*e.g.* frame rate and indicator kinetics), some are inaccessible to the user online (*e.g.* number of expected ROIs in a FOV and spatial constraints on ROI shapes) and must be determined through multiple offline rounds of empirical tuning steps.

The quality of *in vivo* two-photon calcium imaging is also extremely sensitive to motion artifacts [6]. In particular, the shape and position of imaged cells may change due to motion artifacts correlated with the animal's locomotion, breathing, and heartbeat. In current approaches [10, 15-17, 22, 28], successful neuronal segmentation is typically achieved after correcting for motion artifacts: a process requiring additional time and computational power. The output of the segmentation process is thus a static

mask, representing the "average" shape and position of each cell throughout the t-series. This approach is impractical whenever cells should be tracked online on a frame-by-frame basis, for instance when a neuronal ensemble (i.e. a group of coactive neurons) must be optogenetically manipulated after being identified [29, 30]. In fact, neuronal ensembles are dynamic and different cells may belong to a given ensemble at a certain time instant, making it difficult to define *a priori* the neuronal identities belonging to future ensembles [31]. Finally, downstream of segmentation, the dynamic fluorescence signal from each cell must be extracted and "decontaminated" from background signal [6, 32]. Different approaches are available to this end [10, 11, 15-17, 32, 32, 33], all requiring additional computational time. As a result of all these analytical steps, a total processing time of 30 to 90 minutes was reported for most efficient methods when processing FOVs of about 500 x 500 μm^2 containing hundreds of cells imaged over tens of thousands frames [10, 11, 22]. Altogether, current analytical approaches are: *i)* still limited in their ability to perform online analysis, which is necessary for closed-loop experiments; *ii)* biased against the identification of rarely active or inactive cells, which could be as informative to target as more active neurons, for example, in longitudinal all-optical imaging and manipulation approaches; *iii)* not validated on large FOVs, such as those generated by mesoscopic imaging.

Here, we describe CITE-On, a CNN-based algorithm trained to perform neuronal somata identification in two-photon imaging recordings, combined with a light-weight dynamic segmentation and trace extraction pipeline. CITE-On identified hundreds to thousands of neuronal cell bodies on a frame-by-frame basis. Moreover, CITE-On also identified inactive neurons, removing biases towards highly active cells. CITE-On's light architecture and processing strategy allowed, for the first time, fast automatic segmentation, tracking, and trace extraction in mesoscopic two-photon imaging t-series.

Results

CITE-On: structure and analysis pipeline

CITE-On accepted individual frames from two-photon calcium imaging t-series (Fig. 1a) and it comprised two main parts: an image detector based on the publicly available convolutional neural network (CNN) RetinaNet [34] dedicated to the identification of neuronal somata and a custom-built downstream light-weight analysis pipeline, designed for functional trace extraction. The image detector and the analysis pipeline operate as asynchronous parallel processes, in order to provide discrete cell detection update (up to 10 Hz, see text below) and faster than real time functional traces (available at 100 Hz under all experimental conditions tested in this study, see text below). CITE-On required three pre-processing steps ahead of the CNN image detection: *i)* frame downsampling; *ii)* image upscaling; *iii)* replication of the input image into three identical channels (Fig. 1a). The frame downsampling value was set according to the image SNR, while the upscaling factor depended on the ratio between the FOV surface and the average surface of the neuronal somata (see Methods and text below). The length of the frame downsampling window, as well as the value of the upscaling factor, was defined *a priori* and adjusted according to the data to maximize performance. The three identical images were sent to the CNN for image detection (blue rectangle in Fig. 1). The output of the CNN (yellow highlights in Fig. 1) was a set of boxes tightly surrounding each detected cell soma ("bounding boxes", represented as green squares over the FOVs in Fig. 1a-d). Coordinates and surfaces of each bounding box were used in the analysis pipeline, to generate: *i)* cell identity assignment and tracking along the t-series; *ii)* dynamic segmentation of neuronal somata; *iii)* background subtraction procedure and extraction of neuronal functional trace.

CITE-On worked both offline, after the acquisition was completed and the whole t-series was available (Fig. 1b), or online, using individual imaging frames as inputs, continuously streamed from the experimental set-up during the acquisition of the imaging t-series (Fig. 1c-d). In the offline pipeline, a Fourier-transform approach [35] was used to correct for planar motion artifacts throughout the t-series (Fig. 1b). The frame downsampling corresponded to the projection of the entire t-series onto its temporal median calculated across all frames (Fig. 1b). Soma detection was then performed once on the pre-processed median image (detection in Fig. 1b), and bounding boxes were generated for each frame of the t-series (Fig. 1b, yellow highlights). Each bounding box was associated with a score, representing network confidence in cell detection. Bounding boxes with intersection over union (IoU) < 20 % were considered as separate neuronal identities. When IoU of two bounding boxes was > 20 %, the bounding box with the highest score was retained.

In the online pipeline, no motion correction was performed, and the user selected between two downsampling strategies depending on the SNR of the data, and on the required upscaling factor in the pre-processing step. In case of relatively high SNR and low upscaling factors (Fig. 1c), a sliding average was calculated on the first *n* frames of the t-series and updated with every new individual frame generated by the microscope. Neuronal detections were updated for each imaging frame starting from the $n+1^{th}$ frame. When the SNR was relatively low and the upscaling factor large (Fig. 1d), a step average approach was performed, where the input for the image detector was the average projection of blocks of *n* frames. Additional *n* frames were thus required for generating the next step average projection and the detections were updated every *n* frames. The maximum detection rate decreased with the upscaling factor, with a peak rate of 10 Hz with upscaling factor equal to 1 (Fig. 1e). Active detections (*i.e.* detections in the current sliding average or step average) and past detections (*i.e.* detections in any previous sliding or step average) were continuously tracked and

updated (Fig. 1c-d, detection update and I.D. tracking). Specifically, active detections were compared with past detections at each step of detection update and a new identity was added (and included in the tracking system) every time the surface of an actively detected bounding box had IoU < 25 % with any of the previously identified boxes. Bounding boxes from active detections with IoU > 25 % with those of past detections did not change identities of previously detected boxes, but their positions and shapes were updated according to the position in the most recent detection step. All past detections without updates were retained in the tracking system in the form of their last active detection for the remaining part of the t-series (Supplementary Movie 1).

For both the online and offline pipelines (Fig. 1f-g), bounding boxes were used to generate a dynamic segmentation of the t-series and to identify ROIs. The distribution of fluorescence values inside each bounding box was computed at each frame (Fig. 1f, left). Only pixels with values between the 80^{th} and the 95^{th} percentile of the box's fluorescence distribution were assigned to the ROI corresponding to the cell soma (white pixels of the binary mask in Fig. 1f, right). Since pixel assignment to cell somata in each individual box was updated at each frame, the resulting dynamic segmentation was updated online for every new frame. All the FOV pixels that were not included in any bounding box were assigned to a global background ROI. The fluorescence intensity of all pixels belonging to the global background ROI was averaged at each frame to obtain the background signal (*bg*). Moreover, at each frame, the *bg* was subtracted from the fluorescence of each segmented neuronal ROI, generating functional fluorescence traces (Fig. 1g). Since shape, number, and position of bounding boxes changed as the t-series progressed (according to active detections and tracking), the pixels assigned to *bg* also changed in number and identity across frames. Identity tracking, segmentation, and functional trace extraction required on average 10 ms *per* frame (either offline or online).

Ground truth generation and training of the image detector

The ResNet50 Feature Extractor CNN incorporated in CITE-On was not originally developed for detecting neuronal somata, rather for the analysis of natural images and it was trained on > 1 million RGB images across 80 classes (http://www.image-net.org/). We decided to use a transfer learning strategy [36] to adapt this efficient detection architecture to the identification of neuronal somata (*i.e.* a single class) in grey-scale two-photon images. This choice was dictated by the fact that available two-photon calcium imaging datasets (http://neurofinder.codeneuro.org/, http://help.brain-map.org/display/observatory/Data+-+Visual+Coding) are far too small for an *ab-initio* CNN training. Moreover, they are too homogeneous in terms of calcium indicator used, FOV dimensions, cell density, acquisition frame period, SNR and background signal contamination [22], making them suboptimal even for a transfer learning strategy. For example, no publicly available large dataset comprises imaging data collected using red-shifted GECIs, such as jRCaMP1a. We thus decided to use a dedicated dataset for training and internal validation. In this way, we employed publicly available datasets to test CITE-On performance and its generalization capability on never-before-seen data. The dedicated dataset included 197 t-series from 28 mice acquired using different acquisition parameters (see Methods). More specifically, we included 121 t-series from layer IV neurons of the somatosensory cortex expressing either GCaMP6f, GCaMP6s, or GCaMP7f (globally indicated as "LIV") and 76 t-series from the CA1 pyramidal neurons of the hippocampus expressing both GCaMP6f and jRCaMP1a (indicated as "CA1 GCaMP6f" and "CA1 jRCaMP1a", respectively). We included t-series with heterogeneous median fluorescence and SNR in order to reduce potential biases toward bright cells during the training process, while avoiding large differences between groups of data that could have generated better performance on specific subsets of t-series (Supplementary Fig. 1a, b).

136

To obtain a consensus Ground Truth (GT) annotation of the t-series used for training and validation of the CNN, two human graders manually annotated all t-series, defining the tightest rectangular box fitting each visible cell in each FOV. Manual GT annotation was preferred to automatic segmentation for two main reasons: *i)* available automatic segmentation approaches rely on both functional (i.e. fluorescence signal dynamics across frames) and morphological features [9-23], while we wanted the GT annotation to be exclusively based on morphological features (see below); *ii)* manual annotation is still frequently considered more accurate than automatic methods [10, 22]. Initially, manual annotation on single frames by two graders produced only few neuronal identities because cells were only visible in a minority of frames (Supplementary Fig. 1c, Supplementary Movie 2). This could be due to the low basal emission of some of the indicators used (e.g. GCaMP6f), to the variable expression level of the calcium indicator across cells, and to the sparse activity profile of the imaged cells. In order to increase the visibility of neurons, we created high contrast single images representative of each t-series. To this end, we first corrected each t-series for planar motion artifacts, and then collapsed each acquisition onto its median projection (Supplementary Fig. 1d). These images were sharpened (Supplementary Fig. 1e) and gamma corrected. Brightness and contrast were adjusted in order to obtain a distribution of intensity values spanning the whole bit range. The sharpened images, named enhanced median projection (EMP) (Supplementary Fig. 1f, g), were used for manual annotation (Supplementary Fig. 1h, Supplementary Movie 3). In training and validation datasets, grader #1 annotated 14,425 boxes, while grader 2 annotated 12,912 (Supplementary Table 1). The bounding boxes produced by grader #1 and grader #2 and their superposition in different experimental preparations are shown in Supplementary Fig. 2. Annotations from the two graders largely overlapped (weighted average precision or mAP, 0.77 ± 0.08; F-1 score, 0.93 ± 0.02; precision: 0.98 ± 0.01; recall: 0.88 ± 0.12, N = 197 EMPs, Supplementary Table 2). Given the high similarity of the independent annotations provided by the two graders, we defined the consensus GT for our entire

dataset as the union of the two sets of annotations. Given that our dataset contained partially overlapping FOVs and more than one t-series acquired on the same FOV, the dataset was manually split into training (160 t-series) and validation (37 t-series) subsets. To avoid data leakage and to decrease overfitting [37], t-series from the same or similar FOVs were included in either the training dataset or the validation dataset. We trained the CITE-On image detector on the training dataset and evaluated its performance on the validation dataset.

Performance of the image detector

We trained the CITE-On image detector on our consensus GT annotations achieving the best performance after 17 training epochs (mAP: 0.79 on the validation dataset). We first evaluated CITE-On performance using the offline pipeline on the validation dataset. A representative CITE-On output for a CA1-GCaMP6f, a CA1-jRCaMP1a, and a LIV t-series is shown in Fig. 2a-d and Fig. 2e, respectively. For the whole validation dataset, the mean ± s.d. F-1 score, Precision, and Recall are reported in Fig. 2f and Supplementary Table 3.

We then used the online pipeline and calculated the F-1 of CITE-On detections on the motion corrected validation dataset, which was used as input to CITE-On at the actual frame rate occurring during acquisition. Our validation data required an upscaling factor of 1, compatible with a maximum detection rate of 10 Hz, while acquisition frame rates varied between 1.5 Hz for LIV and 3 Hz for CA1 acquisitions. We empirically explored the effect of frame downsampling on detection performance using the sliding average approach with different numbers of frames (*n*). Our aim was to maximize F-1 and score threshold for detections, while minimizing *n*. F-1 increased with *n* between 1 and 20 frames, value at which the absolute maximum was observed (Fig. 3a). Using the sliding average, an initial delay of 6.6 s for LIV data and 14 s for CA1 data was necessary before CITE-On

processed each frame in real time at a detection rate of 10 Hz. F-1 values calculated on sliding averages of 20 frames are reported in Fig. 3a. Detections (green boxes) are displayed together with GT annotations (red boxes) for both the GCaMP6s (Fig. 3b, left) and the jRCaMP1a channels (Fig. 3b, middle). The superimposition of the detections from both channels is shown on Fig. 3b (right). Similarly, in Fig. 3c, we show GT and online detections (red and green boxes, respectively) for a representative LIV (GCaMP6s) t-series.

To quantify the impact of motion artifacts on online detection accuracy, we calculated the F-1 score on validation t-series that were not corrected for motion artifacts (Supplementary Table 4). To this end, we translated the GT annotations for each frame according to the shift vectors produced by the motion correction algorithm implemented when building the relative EMPs (see Methods). We observed no significant difference between the F-1 obtained on motion corrected and non-corrected validation t-series (Fig. 3d), suggesting that the motion correction step was not necessary to achieve higher performance with our approach. The F-1 values across frames for the non-motion-corrected data are reported in Fig. 3e. The distribution of motion displacements is shown in Supplementary Fig. 3.

Online data processing

We developed a fast method to dynamically segment each detected cell based on the corresponding bounding box, relying on the instantaneous (i.e. frame-wise) fluorescence statistics of the pixels inside each box (Fig. 4, Supplementary Movie 4). Specifically, the fluorescence intensity distribution of the pixels inside each bounding box was first computed frame-wise. Pixels with fluorescence values between the 80^{th} and 95^{th} percentile of the distribution were then selected as belonging to neuronal somata. The values of selected pixels were averaged, and the resulting fluorescence trace

was “denoised” by subtracting, at each frame, the *bg* signal. This simple method was computationally light, an important requirement to achieve fast frame-by-frame data processing (trace extraction rate, 100 Hz). Bounding boxes detected by CITE-On on a representative LIV t-series and a representative CA1 t-series are shown in Fig. 4a. Representative fluorescence traces extracted by CITE-On on the two t-series are displayed in Fig. 4b-c. Fig. 4d-e shows the cross correlation matrix (lower left triangle) and the dendrogram analysis (upper right triangle) of all the identified cells before (Fig. 4d-e left) and after (Fig. 4d-e, right) *bg* subtraction.

We compared traces extracted by CITE-On with those extracted by CaImAn, a state-of-the-art method based on CNMF [10]. We used the bounding boxes generated offline by CITE-On to build binary masks that were used as seeds to initialize the seeded-CNMF algorithm [10]. The spatial components of the CNMF were non-zero only inside the bounding boxes identified by CITE-On, therefore, the detected factors from seeded-CNMF had one-to-one correspondence with the detected boxes from CITE-On. We first observed very high pairwise cross correlations between the *bg* traces extracted with the two methods (Supplementary Fig. 4a). We then asked how the *bg* signal calculated over the whole FOV (*bg*) correlated with the ‘local *bg*’, that is, the background activity calculated for each cell from the pixels in the immediate surroundings of the relative bounding box (see Methods). The average correlation between *bg* and local *bg* traces was high (Supplementary Fig. 4b). Given the high correlation values observed between *bg* and local *bg* and the lower computational cost of *bg*, we decided to implement the *bg* method only. We then tested how the *bg*-subtracted functional traces calculated by CITE-On compared with those extracted with seeded-CNMF and we again observed high correlation values (Supplementary Fig. 4c).

Although the average correlation values for the cells extracted with the two methods were high, some neuronal pairs showed lower correlations. We asked whether the low correlation values emerged from pairs of cells with low SNR. We found that pairwise correlation values for traces extracted with the two methods increased with the SNR of the corresponding neuronal traces (Supplementary Fig. 4f), indicating that indeed the functional traces obtained with the two methods were more similar when the trace SNR was high.

Offline performance on never-before-seen recordings

To test the robustness of our image detection approach and its ability to generalize across experimental conditions, we tested CITE-On on three additional datasets, which were not used during the training and validation phases. The three datasets were: the Allen Brain Observatory repository (ABO, 19 t-series divided into 9 superficial, ABO_{sup}, t-series, acquired in visual cortex at depth 175 µm, and 10 deep, ABO_{deep}, t-series, acquired in visual cortex at depth 275 µm), the Neurofinder Challenge dataset (28 t-series, divided into 19 t-series, NF_{train}, 9 t-series, NF_{test}, from different preparations at different depths), and a dataset acquired in our laboratory using GRIN-based endoscopic two-photon imaging of the ventral posteromedial thalamic nucleus (VPM, 9 t-series). The three datasets were first manually annotated *de novo* to obtain the GT annotation (Supplementary Fig. 5, Supplementary Table 1-2). Because the ratios between FOV and cell surface were variable across the ABO, NF, and VPM datasets, and different from our validation dataset, we optimized the upscaling factor and used the one that maximized the F-1 score (Fig. 5a-e). The offline performance (Precision, Recall and F-1 score) obtained using optimized upscaling factors for each dataset is shown in Fig. 5f and Supplementary Table 3.

We compared the offline detection performance of CITE-On (Supplementary Table 3) with state-of-the-art alternative segmentation approaches such as STNeuroNET [22], $CaImAn_{online}$ [10], $CaImAn_{batch}$ [10], Suite2P [16], HNCcorr [19], UNet2DS [23] on the ABO and NF datasets provided in [22]. We used our GT annotations to test CITE-On and those reported in [22] to test the alternative methods. We found that the average CITE-On performance was equivalent to that computed with other methods (Fig. 6). Moreover, the background signals calculated using seeded CNMF and CITE-On presented high cross correlation values for all three datasets (Supplementary fig. 6a). Similarly, high cross correlation was measured between local *bg* and *bg* signals (Supplementary Fig. 6b), as well as between CITE-On extracted functional traces after global *bg* subtraction and CaImAn extracted traces (Supplementary Fig. 6c). As for our previous characterization on the validation dataset, cross correlation values of the extracted traces with CITE-On and CaImAn increased with SNR in all datasets (Supplementary Fig. 6f).

We compared true positive detections obtained with CITE-On with ABO true positive detections and with STNeuroNET true positive detections (Fig. 7a-c). Examples of cells identified by CITE-On and present in the true positive detections from both ABO and STNeuroNET are reported in Fig. 7 d, together with their relative background-subtracted traces extracted by CITE-On. We analyzed the functional traces of all the CITE-On true positives (i.e. including cells detected in ABO and STNeuroNET) after background subtraction (Fig. 7f). Similarly to what described for our validation dataset, the dendrogram sorting showed blocks with different cross correlation values for various subgroups of cells. On average, the number of CITE-On detected cells exceeded the number of identities available in public repositories (Supplementary Fig. 7, Supplementary Table 1).

Since state-of-the-art segmentation methods have a bias against inactive cells, we investigated whether CITE-On-only cells were inactive. We quantified the number of calcium events *per* detection in the ABO true positives (ABO TP), STNeuroNET true positives (STNuroNET TP), CITE-On true positives (CITE-On TP), and CITE-On-only true positives (CITE-On-only, Supplementary Fig. 7). The number of cells with few detected calcium events was larger for CITE-On TP (Supplementary Fig. 7). Moreover, although some of the CITE-On-only cells were silent (as expected), a large fraction of them displayed detectable activity (in the whole ABO dataset, 91 % displayed at least one calcium event and 69 % showed at least ten calcium events, Supplementary Fig. 7a-d). Moreover, the structure of the dendrogram built with CITE-On-only cells resulted similar to the one obtained with the complete set of CITE-On true positives (Fig. 7g), indicating that the group of active cells detected exclusively by CITE-On recapitulated the functional structure of most active neurons. The number of detected calcium events with CITE-On (all detections, true positives, false positives, and CITE-On-only identities), ABO (true and false positives), and with STNeuroNET (true and false positives) is reported in Supplementary Fig. 7e. The number of detections in the different datasets is reported in Supplementary Table 5.

Online performance on never-before-seen recordings

We ran CITE-On online using our GT annotation on each frame of the ABO, NF, and VPM datasets. When computing the F-1 score, we tested different sizes of the sliding average, in order to define the smallest number of frames required to achieve real-time processing. The absolute maximum F-1 score was achieved in 10 frames for the ABO dataset (both ABO_{sup}, and ABO_{deep}), 20 frames for the VPM dataset, and 200 frames for the NF (train and test) dataset (Fig. 8a-e). For the ABO dataset, 0.3 s were necessary to acquire 10 frames (0.00086 % of the whole time series of average duration 115,635 ± 130 frames) with a CITE-On detection rate of 5 Hz and an upscaling factor of 2. The NF dataset

required upscaling factors of 2.4 and 2.6 for NF_{train} and NF_{test}, respectively. A time window of 28.5 s was required to acquire the 200 frames necessary to reach peak F-1 value (5.4 % of the whole t-series of average duration 3,697 ± 1,874 frames) with a CITE-On detection rate of 4 Hz for NF_{train} and 3 Hz for NF_{test}. Given the relatively low online performance for these latter datasets, we decided to measure the F-1 score using an alternative frame downsampling strategy: step average. Using this approach, we found that detection performance remained high (Fig. 8i and Supplementary Table 4). The F-1 score calculated online as a function of the length of the t-series for ABO (ABO_{sup} and ABO_{deep} together), NF (NF_{train} and NF_{test}) and VPM data is shown in Fig. 8j. Stable F-1 scores were observed within 30 % of the total length of the t-series. Processing time required for running the online pipeline on the ABO, VPM, and NF datasets was not different from what described previously for our validation datasets.

Analysis of large FOV mesoscopic images

Given the speed and light-weight of the CITE-On architecture, we tested if it could be applied for detecting cells in the mesoscopic imaging t-series described in [7]. Because the dimensions of the input image were too large (1792 pixels x 1682 pixels, or 4.8 mm x 4.8 mm, 1 µm pixel size) to fit the CNN architecture using the appropriate upscaling factor based on the FOV/neuron surface ratio (upscaling factor for direct processing, 12.8), we tiled the entire mesoscopic FOV in 272 subfields (subfield dimension, 128 pixels x 128 pixels, 28 pixels overlap). Each subfield was appropriately upscaled (upscaling factor, 1; score threshold, 0.4; detection rate, 10 Hz). To increase speed, we multiplexed the CNN detector process and processed subfields in batches of 8 images in parallel, until completion. Identity duplicates were suppressed using a non-maximum suppression algorithm, where boxes having an IoU > 25% were considered duplicates and only the one with the highest score was retained (see Methods). Image detection outputs were finally recombined to reconstruct the entire FOV. In

Fig. 9a, we report CITE-On detected bounding boxes on the entire FOV obtained using the offline pipeline. Two FOV patches are magnified (Fig. 9b) to show the shape of the detected cells (total number of detected somata, 4,842). In Fig. 9c, we show representative fluorescence traces obtained with CITE-On from five cells from the whole mesoscopic FOV. Fig. 9d shows the cross correlation matrix (lower left triangle) of all the identified cells for the first 700 frames of the t-series. The dendrogram analysis (upper right triangle of Fig. 9d) highlighted several distinct functional modules observed in the identified neuronal population.

The single subfields were processed by the CITE-On detector at 10 Hz (upscaling factor, 1), while segmentation, tracking, and functional trace extraction were performed at 100 Hz (see previous results). Parallel processing of all the 272 sub-fields required 12.6 s for each detection step. Therefore, with a step average downsampling approach including 25 frames (13.2 s of mesoscopic imaging time since acquisition rate was 1.9 Hz), and while extracting traces faster than the incoming frames, we minimized the CITE-On detection lag with respect to the running acquisition. With this strategy, we achieved an online F-1 score of 0.54 with a score threshold of 0.25 (quantified on four patches from the entire FOV). CITE-On can thus be efficiently applied for fast processing of mesoscopic two-photon t-series.

Discussion

In this study, we developed a CNN-based algorithm, CITE-On, for fast analysis of two-photon imaging recordings. CITE-On performed online accurate identification of neuronal somata, tracking of identities across frames, dynamic segmentation, and functional trace extraction with background subtraction. CITE-On generalized across calcium indicators, brain regions, acquisition parameters, and it was successfully applied to data obtained using different surgical and optical preparations (e.g.

406 chronic superficial imaging window, chronic deep imaging window, and endoscopic GRIN lens-
407 based deep imaging).
408
409 Our image detection strategy was based on RetinaNET, a CNN originally developed to detect natural
410 images [34]. On one side, this choice was justified by RetinaNET's excellent performance in object
411 recognition and by its readiness. On the other hand, it required us to exploit RetinaNET on a set of
412 images, grey-scale two-photon fluorescence images of neurons, that were remarkably different from
413 those RetinaNET was originally trained on. To compensate for this difference, and to have a large
414 and heterogeneous dataset for training and validation of the detection algorithm, we built a dedicated
415 library of hundreds of two-photon imaging t-series acquired with different GECIs, in different regions
416 of the mouse brain, at different frame rates, using different surgical/optical preparations, and showing
417 variable image quality. In this dataset, a reliable GT consensus was reached using the annotations of
418 two human graders, which allowed us to evaluate CITE-On performance. To obtain a GT annotation
419 insensitive to the graders' biases, a potential alternative approach could have been to generate an *in*
420 *silico* dataset for network training and validation [38]. No online libraries of this kind are currently
421 available, but we foresee that this approach may represent an extremely useful method to optimize
422 future CNN-based approaches for the analysis of two-photon functional data. It is also worth noticing
423 that utilizing public datasets already used for training and validation of alternative processing
424 toolboxes [22] would have given us the possibility to take advantage of third-party GT annotations.
425 However, we decided not to do so because: *i)* CITE-On would have likely inherited the annotation
426 bias toward more active cells, which is shared by existing publicly available repositories; *ii)* by using
427 public datasets exclusively for the validation of the CITE-On image detector (rather than for training,
428 too), we avoided any chance of data leakage, and we demonstrated that CITE-On generalized well to
429 never-before-seen data.

CITE-On performed as state-of-the-art algorithms [10, 11, 16, 19, 22, 39] on publicly available datasets and, importantly, it did so in a much shorter time. In fact, only a few seconds were needed to have online, frame-by-frame, accurate ROI segmentation, identity tracking, *bg* subtraction, and functional trace extraction. Four main characteristics were crucial for CITE-On's high performance. First, CITE-On relied exclusively on morphological features to identify neurons. Second, neuronal identification was dynamic and it adapted to changes in shape, position, and activity of the detected cells frame-by-frame, avoiding time-expensive motion correction procedures. Third, once bounding boxes were identified in individual frames, we used a simple cost-effective strategy to extract pixels belonging to neuronal ROIs based on pixel's brightness. Fourth, we implemented a fast background subtraction strategy, limiting computational costs. When applied in the online modality, these characteristics were crucial to achieve real-time frame-by-frame trace extraction, something current approaches do not achieve [9-25], while maintaining high cell detection performance.

The most common automatic analytic pipelines for the analysis of two-photon imaging t-series typically rely on both spatial features and fluorescence signal fluctuations [9-23]. This necessarily requires the use of several, if not all, frames in a t-series, precluding efficient online analysis. In contrast, CITE-On was conceived such that the analysis pipeline was performed frame-by-frame based on morphological features. This dynamic analytical process was continuously updated over time allowing the algorithm to cope with planar motion artifacts, a feature that, unlike other available methods, enabled us to bypass the motion correction pre-processing step and to save further computational time. Importantly, neuronal identities identified frame-by-frame were reliably tracked over the t-series. To extract pixels belonging to neuronal ROIs within a bounding box, we used a criterion based on pixel brightness and to correct for background contamination we devised a global

rather than local neuropil computation. These procedures had the advantage of being simply and simultaneously implementable for thousands of cells, allowing the extraction of functional traces at low computation cost. The observation that functional fluorescence traces extracted by CITE-On were highly correlated with those extracted on the same bounding boxes by a state-of-the-art method, i.e. CaImAn [10], confirmed the validity of our computationally effective approach.

Thanks to the features described above, CITE-On efficiently processed full mesoscopic two-photon t-series (FOV dimension, 5 mm x 5 mm). CITE-On analyzed full mesoscopic images dividing each image in subfields and processing subfields in parallel. CITE-On's detector processed single subfields at 10 Hz, while segmentation, tracking, and functional trace extraction were performed at 100 Hz. Parallel processing of all the 272 sub-fields generating a whole mesoscopic FOV required 12.6 s for each detection step. Thus after 12.6 s, trace extraction could be performed at 100 Hz on thousands cells. Besides it application online, the offline application of CITE-On is also going to be extremely powerful for the identification of the thousands neurons imaged in mesoscopic two-photon functional imaging.

Closed-loop all-optical experiments are fundamental to investigate whether models of network dynamics, circuit connectivity, and causality are accurate [26]. Recently, all-optical closed-loop experiments have been validated [27]. For example, using this approach specific groups of neurons were activated based on the readout of ongoing activity in a reference cell. However, the closed-loop strategy described in [27] was based on *a priori* identification of the reference cell. Because CITE-On allows efficient frame-by-frame cell identification and trace extraction, it will enable a new type of experiment in which the loop is closed based on real time identification and readout of any neuron or group of neurons in the FOV.

CITE-On differs in several main features from OnACID [11], a recent method that combines CNMF and fast deconvolution for the online analysis of calcium data. First, CITE-On does not need any initialization step in the online pipeline. In contrast, OnACID requires the user to provide the expected number of cells to be identified, and it starts the online analysis based on the CNMF output of an initial portion of the t-series (typically 1000-3000 frames), generating an initial temporal lag of 2-4 minutes [11]. Second, CITE-On does not require the correction of motion artifacts in the online pipeline, saving further computational time. Third, CITE-On performs tracking, dynamic segmentation, and functional trace extraction processes at 100 Hz independently of the number of detected neurons and their activity. This feature allows maintaining high online performance on FOVs characterized by large number of neurons (e.g., those obtained with mesoscopic two-photon imaging) and sparse activity. Four, CITE-On does not use local pixel correlation for cell identification, which may be advantageous to separate nearby synchronous cells. In contrast, the OnACID fast deconvolution approach may be more efficient in separating adjacent cells with different temporal profiles of fluorescence emission [11]. Finally, OnACID was tested on two datasets with rather homogenous acquisition parameters [11]. Here, we demonstrate that CITE-On generalizes across indicators (e.g., GCaMP6s, GCaMP6f, GCaMP7f, and jRCaMP1a) and across data acquired with different pixel size, SNR, and frame rate. This property adds flexibility in the application of online analysis tools to different experimental conditions.

Because cell identification was based only on spatial features, CITE-On identified both active and silent cells. This unique characteristic of CITE-On is important because it adds further flexibility in designing imaging experiments. Neurons that are silent in a t-series may change their level of activity in subsequent acquisitions depending on the behavioral state of the animal or because of external

manipulations [40-42]. Thus, being able to track cells regardless of their activity level is key, for instance, for investigating the sensory information beard by neurons that dramatically change their activity throughout longitudinal imaging experiments. Biasing the analysis toward active neurons, as currently done by most approaches, intrinsically skews the proportion of cells that are responsive to a given stimulation in a certain brain region. In this regard, it is also interesting to note that neurons that were detected only by CITE-On and not by other state-of-the-art approaches comprised silent cells but, unexpectedly, also active cells. Active CITE-On only cells may be associated with low SNR of fluorescence signals and they may be missed by current approaches [10].

In summary, we developed CITE-On, a new tool to effectively process two-photon imaging data frame-by-frame, while maintaining similar cell detection and trace extraction performance of existing offline state-of-the-art methods. Future developments of CITE-On will likely include its optimization for one-photon imaging [43, 44], its application to genetically encoded voltage indicators [45] as well as to volumetric two-photon imaging [46].

Author contributions

LS, MB, PL developed software and performed analysis. MB, SC performed experiments. LS, MB, TF conceived the project. TF coordinated the project. LS, MB, MP, TF wrote the paper with inputs from other authors. All authors approved the final version of the manuscript.

Acknowledgments

We thank Dr. C. Arlt and Dr. C. Harvey for sharing mesoscopic imaging data, Dr. A. Sattin for sharing VPM recordings, Dr. S. Fiorini and Dr. A. Barla for discussion and comments on algorithm development, Dr. D.S. Kim and the GENIE project and Dr. J.M. Wilson for constructs, Dr. S. Succol

for technical support, and Dr. D. Vecchia for help with the figures. This work was supported by the European Research Council (ERC, NEURO-PATTERNS) and NIH Brain Initiative (U19 NS107464).

Declaration of interest

The authors declare no competing interests.

References

1. Helmchen,F. & Denk,W. Deep tissue two-photon microscopy. *Nat Methods* 2, 932-940 (2005).
2. Wang,T. *et al.* Three-photon imaging of mouse brain structure and function through the intact skull. *Nat. Methods* 15, 789-792 (2018).
3. Chen,T.W. *et al.* Ultrasensitive fluorescent proteins for imaging neuronal activity. *Nature* 499, 295-300 (2013).
4. Dana,H. *et al.* Sensitive red protein calcium indicators for imaging neural activity. *Elife.* 5, 12727 (2016).
5. Svoboda,K. & Yasuda,R. Principles of two-photon excitation microscopy and its applications to neuroscience. *Neuron* 50, 823-839 (2006).
6. Harris,K.D., Quiroga,R.Q., Freeman,J., & Smith,S.L. Improving data quality in neuronal population recordings. *Nat Neurosci.* 19, 1165-1174 (2016).
7. Sofroniew,N.J., Flickinger,D., King,J., & Svoboda,K. A large field of view two-photon mesoscope with subcellular resolution for in vivo imaging. *Elife.* 5, (2016).
8. Tsai,P.S. *et al.* Ultra-large field-of-view two-photon microscopy. *Opt. Express* 23, 13833-13847 (2015).

9. Diego,F. & Hamprecht,F. Sparse space-time deconvolution for Calcium image analysis. *Prooceedings of the 27th International Conference on Neural Information Processing Systems* 1, 64-72 (2014).

10. Giovannucci,A. *et al.* CaImAn an open source tool for scalable calcium imaging data analysis. *Elife.* 8, (2019).

11. Giovannucci,A. *et al.* OnACID: Online analysis of calcium imaging data in real time. *Advances in Neural Information Processing Systems*(2017).

12. Guan,J. *et al.* NeuroSeg: automated cell detection and segmentation for in vivo two-photon Ca(2+) imaging data. *Brain Struct. Funct.* 223, 519-533 (2018).

13. Kaifosh,P., Zaremba,J.D., Danielson,N.B., & Losonczy,A. SIMA: Python software for analysis of dynamic fluorescence imaging data. *Front Neuroinform.* 8, 80 (2014).

14. Maruyama,R. *et al.* Detecting cells using non-negative matrix factorization on calcium imaging data. *Neural Netw.* 55, 11-19 (2014).

15. Mukamel,E.A., Nimmerjahn,A., & Schnitzer,M.J. Automated analysis of cellular signals from large-scale calcium imaging data. *Neuron* 63, 747-760 (2009).

16. Pacitariu,M. *et al.* Suite2p: beyond 10,000 neurons with standard two-photon microscopy. *BioRxiv*(2017).

17. Pnevmatikakis,E.A. *et al.* Simultaneous Denoising, Deconvolution, and Demixing of Calcium Imaging Data. *Neuron* 89, 285-299 (2016).

18. Reynolds,S. *et al.* ABLE: An Activity-Based Level Set Segmentation Algorithm for Two-Photon Calcium Imaging Data. *eNeuro.* 4, (2017).

19. Spaen,Q. *et al.* HNCcorr: A Novel Combinatorial Approach for Cell Identification in Calcium-Imaging Movies. *eNeuro.* 6, (2019).

20. Stringer,C., Wang,T., Michaelos,M., & Pachitariu,M. Cellpose: a generalist algorithm for cellular segmentation. *Nat. Methods*(2020).

21. Apthorpe,N.J. *et al.* Automatic Neuron Detection in Calcium Imaging Data Using Convolutional Networks. *arXiv*(2016).

22. Soltanian-Zadeh,S., Sahingur,K., Blau,S., Gong,Y., & Farsiu,S. Fast and robust active neuron segmentation in two-photon calcium imaging using spatiotemporal deep learning. *Proc. Natl. Acad. Sci. U. S. A* 116, 8554-8563 (2019).

23. Ronneberger,O., Fischer,P., & Brox,T. U-net:Convolution networks for Biomedical Image Segmentation. *arXiv*(2015).

24. Ohki,K., Chung,S., Ch'ng,Y.H., Kara,P., & Reid,R.C. Functional imaging with cellular resolution reveals precise micro-architecture in visual cortex. *Nature* 433, 597-603 (2005).

25. Smith,S.L. & Hausser,M. Parallel processing of visual space by neighboring neurons in mouse visual cortex. *Nat. Neurosci.* 13, 1144-1149 (2010).

26. Grosenick,L., Marshel,J.H., & Deisseroth,K. Closed-loop and activity-guided optogenetic control. *Neuron* 86, 106-139 (2015).

27. Zhang,Z., Russell,L.E., Packer,A.M., Gauld,O.M., & Hausser,M. Closed-loop all-optical interrogation of neural circuits in vivo. *Nat. Methods* 15, 1037-1040 (2018).

28. Dombeck,D.A., Khabbaz,A.N., Collman,F., Adelman,T.L., & Tank,D.W. Imaging large-scale neural activity with cellular resolution in awake, mobile mice. *Neuron* 56, 43-57 (2007).

29. Bovetti,S. & Fellin,T. Optical dissection of brain circuits with patterned illumination through the phase modulation of light. *J. Neurosci. Methods* 241, 66-77 (2015).

30. Panzeri,S., Harvey,C.D., Piasini,E., Latham,P.E., & Fellin,T. Cracking the Neural Code for Sensory Perception by Combining Statistics, Intervention, and Behavior. *Neuron* 93, 491-507 (2017).

31. Carrillo-Reid,L., Yang,W., Kang Miller,J.E., Peterka,D.S., & Yuste,R. Imaging and Optically Manipulating Neuronal Ensembles. *Annu. Rev. Biophys.* 46, 271-293 (2017).

32. Lecoq,J., Orlova,N., & Grewe,B.F. Wide. Fast. Deep: Recent Advances in Multiphoton Microscopy of In Vivo Neuronal Activity. *J. Neurosci.* 39, 9042-9052 (2019).

33. Keemink,S.W. *et al.* FISSA: A neuropil decontamination toolbox for calcium imaging signals. *Sci. Rep.* 8, 3493 (2018).

34. Lin,T.Y., Goyal,P., Girshick,R., He,K., & Dollar,P. Focal Loss for Dense Object Detection. *IEEE Trans. Pattern. Anal. Mach. Intell.* 42, 318-327 (2020).

35. Dubbs,A., Guevara,J., & Yuste,R. moco: Fast Motion Correction for Calcium Imaging. *Front Neuroinform.* 10, 6 (2016).

36. Weiss,K., Khoshgoftaar,T.M., & Wang.D.D. A survey of transfer learning. *Journal of Big Data* 3, (2016).

37. Cogswell,M., Ahmed,F., Girshick,R., Zitnick,L., & Batra,D. Reducing overfitting in deep networks by decorrelating representations. *ICLR Conference Track Proceedings*(2016).

38. Charles,A.S., Song,A., Gauthier,J.L., Pillow,J.W., & Tank,D.W. Neuronal Anatomy and Optical Microscopy (NAOMi) Simulation for evaluating calcium imaging methods. *BioRxiv*(2019).

39. Cicek,O., Abdulkadir,A., Lienkamp,S.S., Brox,T., & Ronneberger,O. 3D U-net: learning dense columetric segmentation from sparse annotation. *Proceedings of the*

International Conference on Medical Image Computing and Computer-Assisted Intervention(2016).

40. Goard,M. & Dan,Y. Basal forebrain activation enhances cortical coding of natural scenes. *Nat. Neurosci.* 12, 1444-1449 (2009).

41. Vinck,M., Batista-Brito,R., Knoblich,U., & Cardin,J.A. Arousal and locomotion make distinct contributions to cortical activity patterns and visual encoding. *Neuron* 86, 740-754 (2015).

42. Jacobs,E.A.K., Steinmetz,N.A., Peters,A.J., Carandini,M., & Harris,K.D. Cortical State Fluctuations during Sensory Decision Making. *Curr. Biol.*(2020).

43. Grewe,B.F. *et al.* Neural ensemble dynamics underlying a long-term associative memory. *Nature* 543, 670-675 (2017).

44. Shuman,T. *et al.* Breakdown of spatial coding and interneuron synchronization in epileptic mice. *Nat. Neurosci.* 23, 229-238 (2020).

45. Villette,V. *et al.* Ultrafast Two-Photon Imaging of a High-Gain Voltage Indicator in Awake Behaving Mice. *Cell* 179, 1590-1608 (2019).

46. Weisenburger,S. *et al.* Volumetric Ca(2+) Imaging in the Mouse Brain Using Hybrid Multiplexed Sculpted Light Microscopy. *Cell* 177, 1050-1066 (2019).

47. Pluta,S.R., Telian,G.I., Naka,A., & Adesnik,H. Superficial Layers Suppress the Deep Layers to Fine-tune Cortical Coding. *J. Neurosci.* 39, 2052-2064 (2019).

48. Antonini,A. *et al.* Extended field-of-view ultrathin microendoscopes for high-resolution two-photon imaging with minimal invasiveness. *Elife.* 9, (2020).

49. Brondi,M. *et al.* High-Accuracy Detection of Neuronal Ensemble Activity in Two-Photon Functional Microscopy Using Smart Line Scanning. *Cell Rep.* 30, 2567-2580 (2020).

642 50. Forli,A. *et al.* Two-Photon Bidirectional Control and Imaging of Neuronal Excitability
643 with High Spatial Resolution In Vivo. *Cell Rep.* 22, 3087-3098 (2018).
644 51. Vecchia,D. *et al.* Temporal Sharpening of Sensory Responses by Layer V in the Mouse
645 Primary Somatosensory Cortex. *Curr. Biol.*(2020).
646 52. Mori,T. *et al.* Inducible gene deletion in astroglia and radial glia--a valuable tool for
647 functional and lineage analysis. *Glia* 54, 21-34 (2006).
648 53. Castello-Waldow,T.P. *et al.* Hippocampal neurons with stable excitatory connectivity
649 become part of neuronal representations. *PLoS. Biol.* 18, e3000928 (2020).
650 54. Dombeck,D.A., Harvey,C.D., Tian,L., Looger,L.L., & Tank,D.W. Functional imaging
651 of hippocampal place cells at cellular resolution during virtual navigation. *Nat. Neurosci.*
652 13, 1433-1440 (2010).
653 55. Moretti,C., Antonini,A., Bovetti,S., Liberale,C., & Fellin,T. Scanless functional
654 imaging of hippocampal networks using patterned two-photon illumination through GRIN
655 lenses. *Biomed. Opt. Express* 7, 3958-3967 (2016).
656 56. He,K., Zhang,X., Ren,S., & Sun,J. Deep residual learning for image recognition.
657 *Proceedings of the IEEE Computer Society Conference on Computer Vision and Pattern*
658 *Recognition*(2016).
659 57. Kingma,D.P. & Ba,J.L. Adam: a method for stochastic optimization. *arXiv*(2015).
660 58. Herlihy,M. & Shavit,N. *The art of multiprocessor programming*(Elsevier,2006).
661 59. Malisiewicz,T., Gupta,A., & Efros,A.A. Ensemble of exemplar-SVMs for object
662 detection and beyond. *Proceedings of the IEEE International Conference on Computer*
663 *Vision*(2011).
664 60. Abadi,M. *et al.* TensorFlow: a system for large-scale machine learning. *arXiv*(2016).
665 61. Van Rossum,G. & Drake,F.L. *Python 3 Reference Manual*(CreateSpace,2009).

62. Miller,J.E., Ayzenshtat,I., Carrillo-Reid,L., & Yuste,R. Visual stimuli recruit intrinsically generated cortical ensembles. *Proc. Natl. Acad. Sci. U. S. A* 111, E4053-E4061 (2014).

Methods

Animals

All experiments were carried out in accordance with the guidelines of the European Communities Council Directive, and were approved by the National Council on Animal Care of the Italian Ministry of Health (authorization #34/2015-PR, #1134/2015-PR, and #61/2019-PR).

Wild type (wt) C57BL/6J mice were purchased from Charles River Laboratories (Calco, Italy; strain code #632), transgenic *Scnn1a-cre* (B6;C3-Tg(Scnn1a-cre)3Aibs/J; JAX #009613), and *Ai95D* (B6;129S-*Gt(ROSA)26Sor*$^{tm95.1(CAG-GCaMP6f)Hze}$/J; JAX #024105) were purchased from Jackson Laboratories (Bar Harbor, USA). *Scnn1a-cre* mice express the enzyme Cre in a subpopulation of layer IV neurons [47] and of VPM cells [48]. Animals were housed in individually ventilated cages under a 12-hr light:dark cycle. A maximum of five animals per cage was allowed with *ad libitum* access to food and water. Mice of both sexes were used for experiments.

Viral injections and surgical procedures

We expressed GCaMP6 or GCaMP7 through the following viral vectors AAV1.Syn.Flex.GCaMP6s.WPRE.SV40 (Addgene viral prep # 100845-AAV1), AAV1.Syn.Flex.GCaMP6f.WPRE.SV40 (Addgene viral prep # 100833-AAV1) purchased from the University of Pennsylvania Viral Vector Core, or AAV1.Syn.Flex.GCaMP7f.WPRE.SV40 (Addgene viral prep #104492-AAV1) purchased from Addgene. For CA1 imaging, we expressed jRCaMP1a using co-injection of AAV1.CAG.Flex.NES-jRCaMP1a.WPRE.SV40 (Addgene viral prep # 100846-AAV1) and AAV1.CamKII 0.4.Cre.SV40 (Addgene viral prep # 105558-AAV1) purchased from the University of Pennsylvania Viral Vector Core.

For LIV imaging, we used a total of 29 mice. Specifically, 17 *Scnn1a-cre* mice injected with a viral vector transducing GCaMP6s, 6 *Scnn1a-cre* mice injected with a virus transducing GCaMP6f, 3 *Scnn1a-cre* mice injected with a virus transducing GCaMP7s, and 3 *Scnn1a-cre* crossed with *Ai95D* mice. Mice between post-natal days 30 and 33 were anesthetized with 2% isoflurane (IsoFlu, Zoetis, IT) in 0.8 % oxygen, placed into a stereotaxic apparatus (Stoelting Co, Wood Dale, IL), and maintained on a warm platform at 37°C for the whole duration of the anesthesia. Viral injection in mice used for LIV imaging was carried out similarly to [49] and [50]. Briefly, a scalp incision was performed after local administration of lidocaine (2 %) and then two small holes were drilled on the skull above the right/left somatosensory cortex at 1.2 mm and 2 mm posterior (P) to the bregma suture, 2.8 mm and 3 mm lateral (L) to the sagittal sinus. A micropipette was slowly inserted into the cortical tissue until the tip reached a depth of 0.3 mm below the pia mater. 200 nL of GCaMP6 virus were injected at 20 - 60 nl/min by means of a hydraulic injection apparatus driven by a syringe pump (UltraMicroPump, WPI, Sarasota, FL). The pipette was then further lowered to reach 0.4 mm below the *pia mater*, and a second injection was performed. This procedure was repeated for the second injection site. The injected solution contained 10^{12} viral genomes/ml diluted 1:1 in artificial cerebro-spinal fluid (aCSF: 127 mM NaCl, 3.2 mM KCl, 2 mM $CaCl_2$, 1 mM $MgCl_2$ and 10 mM HEPES, pH 7.4). The exposed skull was then cleaned, and the skin sutured and cleansed with Iodopovidone (Betadine®, Meda pharma, Milan, Italy). Mice were monitored until full recovery from the anesthesia. In mice used for imaging in awake conditions, a custom metal bar was sealed to the skull using Vetbond (3 M, St. Paul, MN, USA) and dental cement (Paladur, Kulzer GmbH, Hanau, Germany). The exposed bone was covered using the silicone elastomer KWIK-Cast (World Precision Instruments, Friedberg, DE) and an intraperitoneal injection of antibiotic (BAYTRIL, Bayer, DE) was performed. 2-4 weeks after virus injection, mice used for imaging in LIV during anesthesia were injected with urethane (1.65 g/kg, 16.5 % in saline solution, i-p.). A scalp incision was performed

after local administration of Lidocaine (2 %). A circular craniotomy was opened over the somatosensory cortex, in the area where green fluorescence was clearly visible using an epifluorescent microscope. The surface of the brain was kept moist with aCSF. A heating pad underneath the animal was set at 35.5-37°C. Respiration rate, eyelid reflex, vibrissae movements, and reactions to tail pinching were monitored throughout the surgery. Mice were then moved under the two-photon microscope, kept at 37 °C with a heating pad, and the brain surface irrigated with aCSF. Imaging began one hour after the end of the surgery. Before imaging LIV activity in awake animals, mice were habituated to head-fixation similarly to [51]. In brief, habituation lasted for 7 to 10 days, during which they were head restrained for increasing periods (from 15 minutes to one hour), while running or standing on a custom made treadmill. On the day of the experiment, the habituated mouse was anesthetized with a mixture of isoflurane and oxygen (0.8 – 2 %), and a craniotomy performed similarly to what described above. After surgery, the animal was head fixed and allowed to recover under the microscope for at least one hour before imaging.

For VPM imaging, we used a total of 4 mice. Viral injections and aberration-corrected microendoscopes insertion in mice used for VPM imaging were performed in Scnn1a-Cre mice as in [48]. Mice were anesthetized as previously described. A single craniotomy was performed at stereotaxic coordinates P 1.7 mm, L 1.6 mm. A micropipette was lowered to a depth of 3 mm below the brain surface. 0.5 - 1 µl of GCaMP6s virus containing solution (containing 10^{12} viral genomes/ml diluted 1:4 in aCSF) were injected at 30 - 50 nl/min. Following virus injection, a craniotomy (area: 600 µm x 600 µm) was performed at stereotaxic coordinates P 2.3 mm, L 2 mm. A thin column of brain tissue was displaced with a glass cannula (ID = 300 µm, OD = 500 µm; Vitrotubs, Vitrocom Inc., Mounting Lakes, NJ) and a microendoscope was slowly inserted into the cannula track using a custom holder,

down to 3 mm from the brain surface. The microendoscope was finally secured by acrylic adhesive and dental cement. Imaging was performed 2-4 weeks after endoscope implantation.

For CA1 imaging, we used a total of 2 mice. Before surgery, mice were medicated with an intramuscular bolus of Dexamethasone (Dexadreson, 4 gr/kg). After scalp incision, a 0.5 mm craniotomy was drilled at stereotaxic coordinates P 1.75 mm, L 1.35 mm. A micropipette was lowered 1.40 mm below the brain surface. 0.8 µl of viral solution (containing a mixture of CamKII-Cre and jRCaMP1a viruses at 10^{12} viral genomes/ml diluted 1:1 in aCSF) was injected at 100 nL/min in *Ai95* crossed with *Glast-cre-ERT2* mice [52]. Inducible Glast-cre was not activated after viral injection, resulting in CA1 neuronal staining with jRCaMP1a and GCaMP6f. A stainless-steel screw was attached to the skull, and a chronic hippocampal window was implanted as described in [53, 54]. A 3 mm craniotomy was opened, centered at coordinates P 2.00 mm, L1.80 mm. The *dura mater* was removed using fine forceps, and the cortical tissue overlaying the hippocampus slowly aspirated using a blunt needle coupled to a vacuum pump. During aspiration, the exposed tissue was continuously irrigated with aCSF. Aspiration was stopped once the fibers of the external capsule were exposed. A cylindrical optical window made of a thin-walled stainless-steel cannula (OD, 3 mm; ID, 2.77 mm; height, 1.50 - 1.60 mm) attached to a 3 mm diameter round coverslip, was fitted to the craniotomy in contact to the external capsule. A thin layer of silicone elastomer was used to surround the interface between the brain tissue and the steel surface of the optical window. A custom stainless-steel headplate was attached to the skull using epoxy glue. All the components were finally fixed in place using black dental cement and the scalp incision was sutured to adhere to the implant. All the animals received an intraperitoneal bolus of antibiotic (BAYTRIL, Bayer, DE) to prevent postsurgical infections.

762

763 *Functional two-photon imaging*

764 Two-photon imaging was performed using a chameleon ultra II pulsed laser (80 MHz pulse frequency,
765 Coherent Inc, Santa Clara, CA, USA) tuned at 920 nm for GCaMP6/7 imaging and at 990 nm for
766 dual color imaging. Excitation power was 30 - 110 mW as measured under the microscope objective
767 and controlled via a Pockel cell (Conoptics Inc, Danbury CT, USA,). An Ultima II scanhead (Bruker
768 Corporation, Milan, Italy) equipped with 3 mm raster scanning galvanometers (6215H, Cambridge
769 Technology, Bedford, MA) and standard photomultiplier tubes (Hamamatsu Photonics, Tokyo, Japan)
770 and an Ultima Investigator (Bruker Corporation, Milan, Italy), equipped with 6 mm raster scanning
771 galvanometers, movable objective mount, and multi-alkali photomultiplier tubes were used. The three
772 objectives were: 25x/1.05 N.A. (Olympus Corp., Tokyo, JP) for LIV imaging, 20x/0.5NA (Zeiss,
773 Oberkochen, Germany) for VPM endoscopic imaging, and 16x/0.8 N.A. (Nikon, Tokyo, Japan) for
774 CA1 experiments.

775

776 For LIV imaging, dwell time was 4.4 µs, photomultiplier voltage was 777 V, zoom factor was always
777 1, pixel size was 0.77 µm, acquisition frame rate ranged between 0.5 – 3 Hz for a 512 pixels x 512
778 pixels image. Fluorescence values spanned 95 % of the available dynamic range (16 bit). For dual
779 color CA1 imaging, pixel dwell-time was set at 4 µs, photomultiplier voltage was 777 V, zoom factor
780 was always 5, pixel size was 0.634 µm, acquisition frame rate was 3.03 Hz for a 256 pixels x 256
781 pixels image. For VPM imaging, the set up was similar to the one described in [48, 55], pixel dwell-time
782 was set at 4 µs, photomultiplier voltage was 810 V, zoom factor was always 1, pixel size was 2.19
783 µm, acquisition frame rate was 2.66 Hz for a 196 pixels x 196 pixels image. Imaging sessions lasted
784 1 hour for CA1, VPM, and awake LIV experiments. They lasted 4 hours for the anesthetized LIV
785 condition. After awake imaging sessions, animals were returned to their home cages.

Training and validation datasets

In the absence of a generally accepted wide-scale annotated dataset of two-photon calcium imaging, we built a dataset of *in vivo* t-series collected using raster scanning acquisitions. A total of 197 t-series (average frame number per time series: 597 ± 262, average frame rate: 2.3 ± 1.5 Hz) were included in the dataset: 76 t-series from CA1 imaging of principal neurons stained with both GCaMP6f (38 t-series) and jRCaMP1a (38 t-series); 121 t-series from cortical LIV imaging of principal neurons stained with virally injected GCaMP6s (107 t-series), GCaMP6f (4 t-series), GCaMP7f (5 t-series), GCaMP6f expressed in transgenic animals (Scnn1a-cre x Ai95; 5 t-series). Training and validation datasets contained 160 (118 from LIV, 21 from CA1 GCaMP6f, and 21 from CA1 jRCaMP1a) and 37 t-series (13 from LIV, 12 from CA1 GCaMP6f, and 12 from CA1 jRCaMP1a), respectively. To avoid data leakage between training and validation datasets, we manually split t-series including different FOVs in the datasets.

Additional datasets

Four additional datasets were selected and used for validation purposes only:

1) VPM microendoscopic imaging t-series in awake head restrained mice (9 t-series).

2) The publicly available Allen Brain Observatory (ABO) visual coding dataset (19 t-series, https://observatory.brain-map.org/visualcoding). T-series identification numbers: 501271265, 501484643, 501574836, 501704220, 501729039, 501836392, 502115959, 502205092, 502608215, 503109347, 504637623, 510214538, 510514474, 510517131, 527048992, 531006860, 539670003, 540684467, 545446482.

3) The publicly available Neurofinder (NF) challenge dataset (28 t-series, https://github.com/codeneuro/neurofinder). T-series identification numbers: neurofinder.00.00,

neurofinder.00.01, neurofinder.00.02, neurofinder.00.03, neurofinder.00.04, neurofinder.00.05, neurofinder.00.06, neurofinder.00.07, neurofinder.00.08, neurofinder.00.09, neurofinder.00.10, neurofinder.00.11, neurofinder.01.00, neurofinder.01.01, neurofinder.02.00, neurofinder.02.01, neurofinder.03.00, neurofinder.04.00, neurofinder.04.01, neurofinder.00.00.test, neurofinder.00.01.test, neurofinder.01.00.test, neurofinder.01.01.test, neurofinder.02.00.test, neurofinder.02.01.test, neurofinder.03.00.test, neurofinder.04.00.test, neurofinder.04.01.test.

4) A single t-series of mesoscopic full field imaging from [7].

No preprocessing was performed on the VPM, ABO, NF, and mesoscopic t-series. All t-series were manually annotated *de novo* by the two graders working independently. The consensus ground truth was obtained as described for the training and validation dataset (see also Supplementary Table 1-2).

Image processing and consensus labelling

The CITE-On image detector was based on purely morphological features extracted from imaging data. No information from the dynamic fluorescence signal in the t-series was used to detect putative cells. Each imaging t-series was corrected for lateral displacements using MOCO [35]. T-series were aligned using the first frame as reference, without downsampling and with a maximum possible shift of 13 pixels. The 8-bit median projection of each t-series was then computed on the motion-corrected t-series. The resulting images (one *per* t-series) were globally sharpened to better visualize cell shapes. A gamma correction of 0.3 was applied, and the dynamic range was linearly adjusted normalizing across the whole 8 bit depth. Processed images were named “enhanced median projections” (EMPs) and were used to define our GT labelling. Two graders independently labelled each EMP. LabelImg (http://github.com/tzutalin/labelImg) was used to define a single object class by manually drawing bounding boxes around every visible cell soma in the EMP. The surface of each bounding box was manually defined in order to tightly surround the cell shape. Boxes were allowed

to overlap. Coordinates and surface of each bounding box for all EMPs were saved in a standard VOC format where each file reported the top left and bottom right coordinates (in pixels) for each bounding box. The GT was defined as the union between the set of notations from the two graders.

Image detector training

CITE-On is based on a fully convoluted single-shot image detector, RetinaNet [34]. Briefly, a feature pyramid network was constructed from residual layers of the ResNet50 feature extractor [56]. This feature pyramid was then fed to two separate sets of convolution filters: one computing the label score (classification subnet), the second performing bounding box regression from priors (regression subnet). We used the open-source Keras implementation of this architecture (http://github.com/fizyr/keras-retinanet). Given the relatively small set of training data available, we could not perform *ab initio* training. Rather, we employed a transfer learning approach. Starting from the network trained on a large-scale dataset of natural images, we fine-tuned the weights of the classification and regression subnets, while freezing the weights of the feature pyramids. We used "plain" median projections obtained from the motion corrected t-series and linearly normalized across the bit range. The resulting projections were then upsampled in order to obtain images were the short side was 800 pixels long, while the long side did not exceed 1,333 pixels. Since the input layer of the network accepted a three-channel image, the same image was replicated for each channel without changing any parameter. These last two image conversions were necessary as the network was originally trained on RGB images, and the transfer learning approach did not allow input modifications to the image shape. The network was trained with a regression L1 loss function (Mean Absolute Errors, MAE, https://rishy.github.io/ml/2015/07/28/l1-vs-l2-loss/), with focal loss (http://arxiv.org/abs/1708.02002) and the Adam optimizer [57] with learning rate 10-5 and clipnorm 10-3 (http://github.com/keras-team/keras/issues/510) [34] modified by reducing the learning rate on loss

plateau with a factor of 0.1. The network was trained for 17 epochs, each consisting of 1000 training steps of batch size 1.

CITE-On offline pipeline

Two-photon calcium imaging t-series were first corrected for lateral artifacts using MOCO (as described above). The median projections were then computed, normalized, upscaled to the target input size, and converted to 8 bit RGB images. The resulting images were fed to the image detection network. Upscaling factor and score threshold were the only two parameters defined *a priori*. Upscaling factor was adjusted in order to have the smallest feature in each image inscribed in a 32 $pixels^2$ box. This was because the smallest prior box encoded in the network was 32 $pixels^2$. To avoid using a shallower convolutional residue that would have carried less information, we decided to adjust the up-scaling factor instead of reducing the size of the smallest prior box. After exploring the parameter space on different datasets, we defined an up-scaling factor of 1 for the training and validation datasets. The optimal up-scaling factors were 2.3 for the ABO dataset, and between 1.7 and 3.1 for the NF datasets (these datasets were heterogeneous in terms of FOV size and pixel size). In the VPM dataset, image projections were characterized by an altered magnification factor in the radial direction, due to the optical properties of the corrected microendoscopes used for imaging [48]. These images went through a further preprocessing step to correct for this field distortion. Up-scaling factor for the VPM dataset was 1.4. Each bounding box was associated with a score, representing network confidence in cell detection. Bounding boxes with intersection over union (IoU) < 20 % were considered as separate neuronal identities. When IoU of two bounding boxes was > 20 %, the bounding box with the highest score was retained. Results of the image detector were filtered by applying a threshold on the output score provided by the network and optimized for each dataset.

CITE-On online pipeline

In the online pipeline, individual raw imaging frames were continuously grabbed from a streaming source (e.g. live microscope output) and processed. To simulate this process, we individually imported in the CITE-On pipeline each frame of each raw t-series. Single frames were passed on to the trace extractor and to a buffer. The buffer stored the number of frames sufficient to produce an average projection. Once the buffer was filled, the projection was computed, sent to the image detector, and the buffer emptied.

Detections were performed using the same procedure described for the offline pipeline. Detection results were fed to a custom tracking algorithm detecting all the overlaps between current and previous detections, and designed in order to maximize overlap between putative matching boxes. For every detection matching a previous one, the coordinates of the relative bounding box were updated to the last one. For each new detection having an IoU < 0.25 % with all the previous detections, a new identity was created. In case of identities not actively detected in the current frame, relative coordinates were anyway updated using a rigid shift calculated as the mean shift obtained from the active identities. In this way, we aimed to minimize the effect of motion artifacts and identity switch without implementing online motion correction approaches. A simple dynamic segmentation was then performed for each identity. At each raw frame, the interval between the 80^{th} and the 95^{th} percentile of the pixel fluorescence intensity distribution inside each bounding box was averaged to extract the raw functional trace. At each frame, background signal corresponded to the average fluorescence of all the pixels in the FOV not belonging to any bounding box. This frame-wise value was subtracted from all the individual raw functional traces. In order to optimize real-time performance for high frame rate acquisitions (above 3 Hz, including all ABO and some NF t-series), the entire pipeline was implemented in a multiprocessing scheme where one process was responsible

for data loading, one for image preprocessing, and for sending its output to the CNN detector accelerated over GPU and tracking parts, while the remaining CPU cores were dedicated to real-time trace extraction given the parallel nature of the problem [58]. This implementation scheme allowed for cell detection update (up to 10 Hz) and functional trace extraction update from all identities (100 Hz) to operate as parallel and asynchronous processes.

Parameter exploration for the object detector

To find the best operating parameters for the object detector, we quantified offline CITE-On performance while systematically exploring various plausible values of score threshold and upscaling factor. For all datasets, we evaluated the F-1 across a set of net size multipliers between 0.6 and 3.4 in steps of 0.2. We also explored score thresholds between 0.05 and 0.95, in steps of 0.05. This mapping strategy allowed us to define the optimal combination of score threshold and upscaling factor for each input data. The upscaling factor was dependent on the ratio between the average box surface and the whole FOV surface, while the score threshold presented non obvious dependence on trivial image statistics. Therefore, we determined the upscaling factor according to the acquisition parameters and the relative score thresholds, in order to maximize the F-1 score for each dataset. For the online pipeline, we used appropriate upscaling factors and proceeded by exploring the dependency of F-1 from the score threshold and from the number of averaged frames in each detection.

Trace extraction: comparison between CITE-On and other methods

We compared CITE-On trace extraction with trace extraction performed with a popular state-of-the-art method based on CNMF, CaImAn [10]. Briefly, we provided binary masks corresponding to the CITE-On detected bounding boxes and used these masks to seed the CNMF algorithm. Seeded-CNMF first calculated the temporal background component using pixels that were not included in

any mask. We compared this background component to the CITE-On background traces used for trace correction. The subsequent step of the seeded-CNMF algorithm estimated temporal components and spatial footprints, constrained to be non-zero only at the location of the binary masks. Using this strategy, we obtained fluorescent traces from putative cells detected in the same locations as those detected by CITE-On, allowing for a one-to-one trace comparison between algorithms. It is important to note that, for this analysis, we set the order of the autoregressive model of the CNMF to zero because we were not interested in trace deconvolution, but only in correcting for background contamination.

Local vs. global background signal correlation

To compare local and global background noise contributions, we used the same approach for background noise subtraction, but considering only the pixels in the vicinity of each cell. The vicinity of a cell was defined as all the pixels in a concentric rectangular box double the size of the box detected by CITE-On, with no overlap with other bounding boxes. We then calculated the cross correlation at lag zero between the local noise for each cell and the global background trace.

Tiled detection on mesoscopic images

For large scale datasets (> 3000 pixel^2) as the mesoscopic imaging dataset [7] , requiring large amounts of GPU memory (> 500 GB), we implemented a tiled detection approach. We divided each mesoscopic FOV in a configurable number of tiles with configurable overlap factor, in order to batch process all tiles up to the limit of the available GPU memory. Once all detections were computed, they were appropriately shifted back to the original position in the FOV and a Non Maximum Suppression [59] was performed in order to remove duplicate boxes in regions of the FOV were overlap between tiles occurred.

954

955 *Performance and metrics*

956 Performance of the CITE-On object detector was calculated employing standard Precision, Recall
957 and F-1 metrics. In order to determine true or false positives, we computed the IoU between each
958 ground truth and detected boxes. A custom algorithm was used to match the two sets using a cut-off
959 threshold of 0.5.

960

961 *Hardware and software for data analysis*

962 All the data analysis procedures presented in this work were performed on a Dell Precision 7920
963 desktop with an Intel Xeon Silver 4110 @ 2.1 GHz 8 core CPU, 32 GB DDR4-2666 ECC RAM,
964 NVIDIA Quadro RTX5000 GPU, 512 GB NVMe SSD, and 2 TB 7200 rpm HDD.

965

966 All processing steps, including network training and validation, were carried out under
967 Keras/Tensorflow software libraries [60]. Image processing and data analysis were carried out using
968 Python Language Reference 3 [61].

969

970 *Statistics*

971 Values were expressed as mean ± sd, unless otherwise stated. The number of samples (N) and p values
972 are reported in the figure legends or in the text. No statistical methods were used to pre-determine
973 sample size, but sample size was chosen based on previous studies [3, 62]. All recordings with no
974 technical issues were included in the analysis and blinding was not used in this study. Statistical
975 analysis was performed with the scientific Python ecosystem (SciPy, NumPy 1.19) under Python 3,
976 Python Software Foundation, Python Language Reference 3 (available at https://www.python.org). A
977 Kolmogorov-Smirnov test was run on each experimental sample to test for normality. The

978 significance threshold was always set at 0.05. When comparing two paired populations of non-
979 normally distributed data, a two-sample Kolmogorov-Smirnov test. All tests were two-sided, unless
980 otherwise stated.
981
982 *Code availability*
983 The code is available from the corresponding authors on request and it will be shared upon
984 publication.

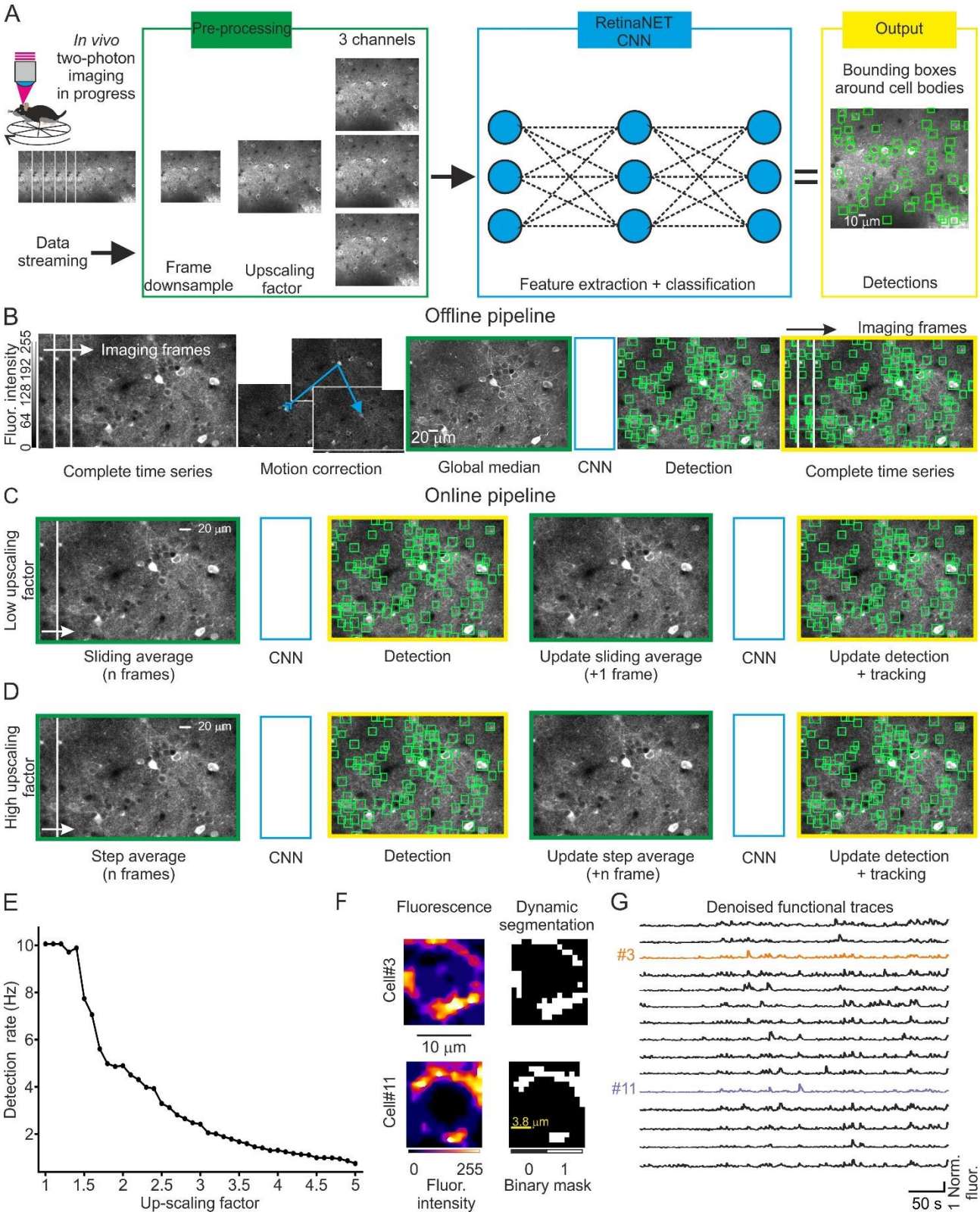

Figure 1. Structure and analysis pipeline of CITE-On. A) Schematic of the image detection process in CITE-On. During ongoing two-photon imaging acquisition, individual frames are

transferred to CITE-On as they are completed (left). A pre-processing step (green rectangle) is required ahead of image detection, comprising frame downsampling, image upscaling and triplication of the upscaled image. The result of the preprocessing is then used as input for the CNN (blue rectangle). The CNN output is the detection of neuronal somata in the form of bounding boxes (green squares black and white image on the right). **B)** CITE-On offline pipeline starts with the complete t-series and the correction of motion artifacts (blue arrow, motion correction). Frame downsampling is performed by computing the global median projection of the t-series. The upscaled and triplicated global median (green) is fed to the CNN (blue), a single detection is performed, and the bounding boxes (detection, green squares) are projected onto each frame of the complete t-series (yellow). **C)** In the online pipeline, for data requiring small upscaling factors, a sliding average projection of the first n frames of the ongoing t-series is calculated in the frame downsampling pre-processing step (green). This image is upscaled and triplicated, processed by the CNN (blue), producing the first detection (yellow). As the next frame of the t-series is acquired, a new sliding average is computed, again on *n* frames, but starting from the second frame of the acquisition and including the $n+1^{th}$ one. The CNN processes this image, updating the detections and starting the tracking system (yellow). The grayscale shown in this panel applies to all grayscale images in this figure. **D)** For data requiring high upscaling factors, the pipeline is similar to that in (C), but instead of a sliding average, a step average is calculated on *n* frames as the frame downsampling pre-processing step (green). Detections are updated every *n* new frames. **E)** Detection rates as a function of the magnitude of the upscaling factor. Maximum detection rate is 10 Hz for upscaling factor between 1 and 1.5. **F)** Representative average fluorescence of pixels inside the bounding box relative to two cells (cell #3 and cell #11), calculated in a single frame of the LIV dataset (GCaMP6s, pseudocolor, left). Associated dynamic segmentation mask in the same frame (binary mask, right). **G)** Functional traces from N = 15

representative cells extracted with online CITE-On pipeline. Traces of cells displayed in (F) are shown in green.

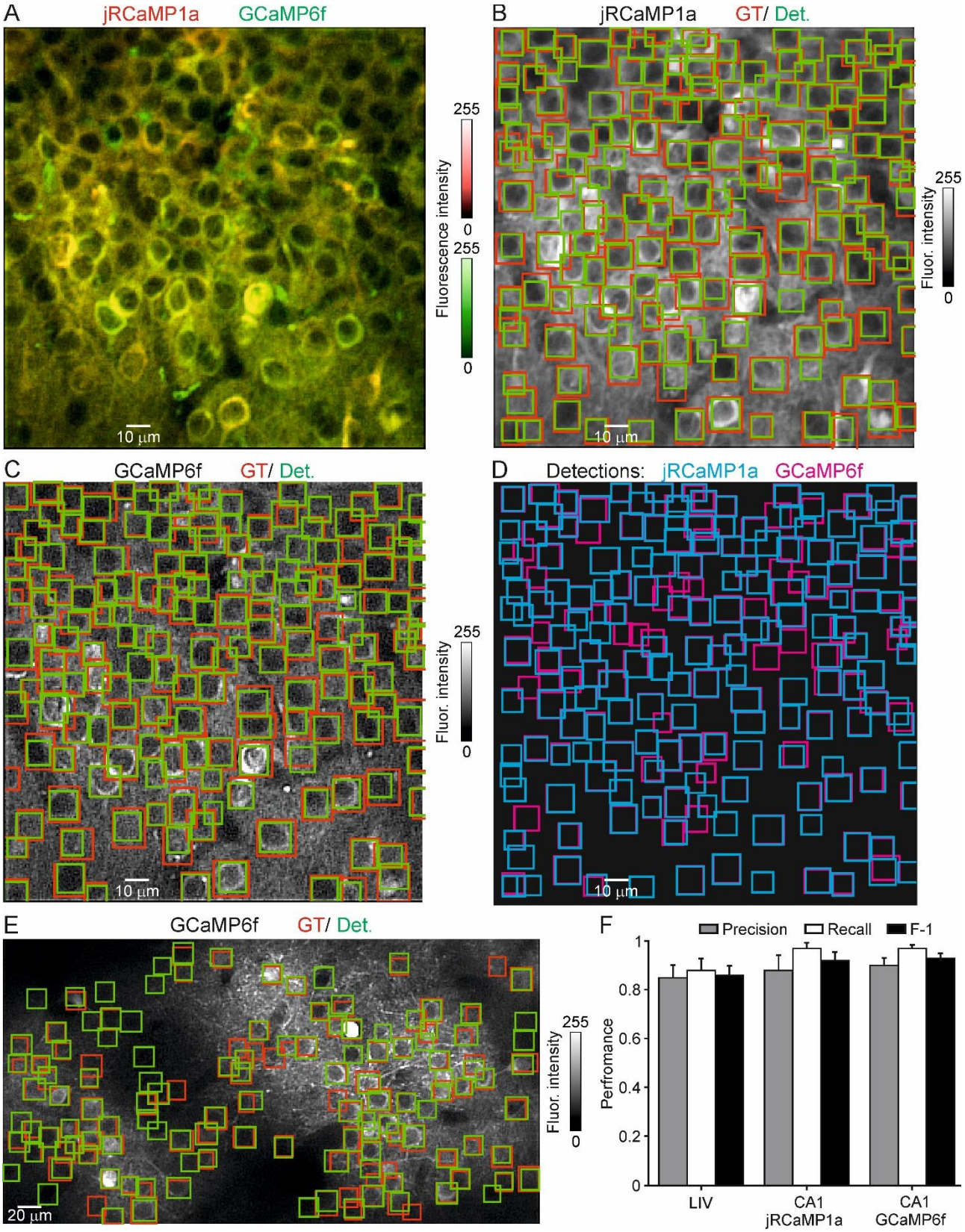

Figure 2. CITE-On offline performance. A) Representative median projection showing jRCaMP1a (red) and GCaMP6f (green) expressing CA1 neurons. **B)** GT (red) and CITE-On detections (green) for the jRCaMP1a channel of the image shown in A. **C)** same as in (B), but for the GCaMP6f channel. **D)** Superposition of CITE-On detections on jRCaMP1a (cyan) and GCaMP6f (magenta) channels. **E)** Representative median projection from the LIV dataset with GT (red) and CITE-On detections (green). **F)** Performance for precision (grey), recall (white), and F-1 (black) obtained with the offline CITE-On pipeline on the validation t-series of the LIV (N = 13), CA1 jRCaMP1a (N = 12), and CA1 GCaMP6f (N = 12) datasets. In this and in other figures values are expressed as means ± sd.

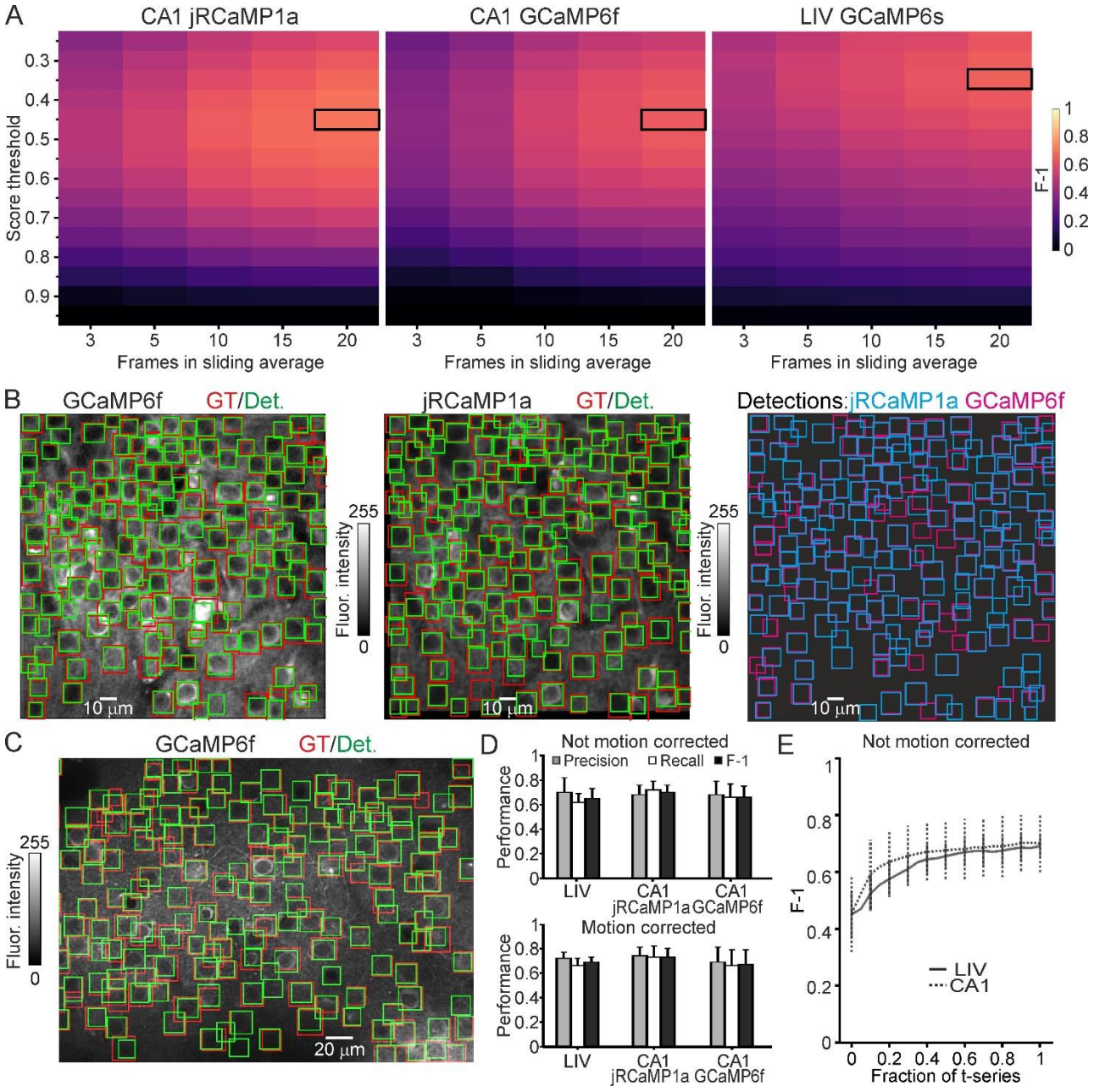

Figure 3. CITE-On online performance. A) Best parameter search for frame downsampling: F-1 score (pseudocolor) as a function of score threshold (vertical axis) and number of frames in the sliding average (horizontal axis) for LIV (left), CA1 GCaMP6f (middle) and CA1 jRCaMP1a (right). The maximal F-1 is indicated with the black rectangle. **B)** Median projections of one representative FOV for CA1 jRCaMP1a (left) and one FOV for CA1 GCaMP6f (middle). GT (red) and online detections (DET, green) are also shown. In the rightmost panel, the online detections of jRCaMP1a (cyan) and GCaMP6f (magenta) are shown. **C)** Same as in (B) but for a representative LIV t-series. **D)** Top:

online performance of Precision (grey), Recall (white), and F-1 (black) for all t-series in the validation LIV (N = 13), CA1 jRCaMP1a (N = 12), and CA1 GCaMP6f (N = 12) datasets. No motion correction was performed. Bottom: same as top, but for the motion corrected t-series. Results of Kolmogorov-Smirnov test for performance in not motion corrected t-series vs. motion corrected t-series from LIV: p = 0.54 for F-1, p = 0.15 for Precision, p = 0.38 for Recall, N = 13 t-series. Results of Kolmogorov-Smirnov test for performance in not motion corrected t-series vs. motion corrected t-series from CA1 jRCaMP1a: p = 0.16 for F-1, p = 0.20 for Precision, p = 0.20 for Recall, N = 12 t-series. Results of Kolmogorov-Smirnov test for performance in not motion corrected vs. motion corrected t-series from CA1 GCaMP6f: p = 0.18 for F-1, p = 0.28 for Precision, p = 0.22 for Recall, N = 12 t-series. **E)** F-1 values as a function of the fraction of the total length of the t-series for not-motion corrected data (N = 13 t-series for LIV, N = 24 t-series for CA1, including N = 12 t-series for CA1 jRCaMP1a and N = 12 t-series for CA1 GCaMP6f t-series).

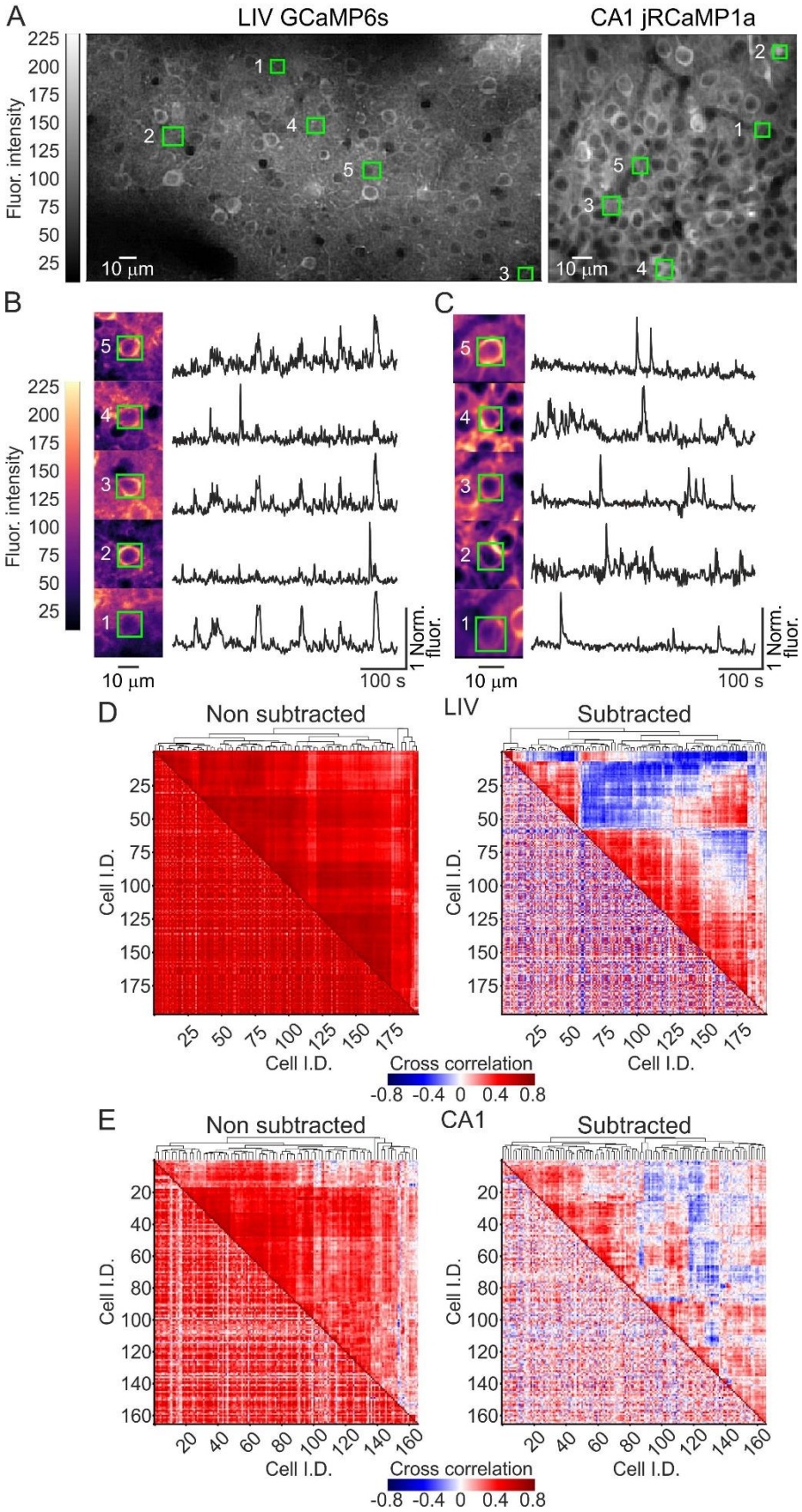
A
LIV GCaMP6s
CA1 jRCaMP1a
Fluor. intensity
225
200
175
150
125
100
75
50
25
10 µm
B
C
Norm. fluor.
1
100 s
D
Non subtracted
Subtracted
LIV
Cell I.D.
Cross correlation
-0.8 -0.4 0 0.4 0.8
E
CA1

Figure 4. Fast extraction of fluorescence traces using CITE-On. A) Median projection showing representative FOVs from the LIV GCaMP6s (left) and the CA1 jRCaMP1a (right) datasets. True positive bounding boxes for five CITE-On identified cells in each FOV are shown. **B)** Left: the five cells indicated in the LIV t-series displayed in (A) are shown at an expanded spatial scale. Right: corresponding background subtracted fluorescence traces. **C)** Same as in B but for the CA1 t-series in A. **D)** Lower-left triangle: cross correlation matrix for all functional traces extracted from true positive detection in the LIV GCaMP6s t-series displayed in (A). Upper-right triangle: corresponding dendrogram sorting. The left matrix shown signals before background subtraction. The right matrix after background subtraction. **E)** Same as in (D), but for the CA1 jRCaMP1a t-series shown in (A).

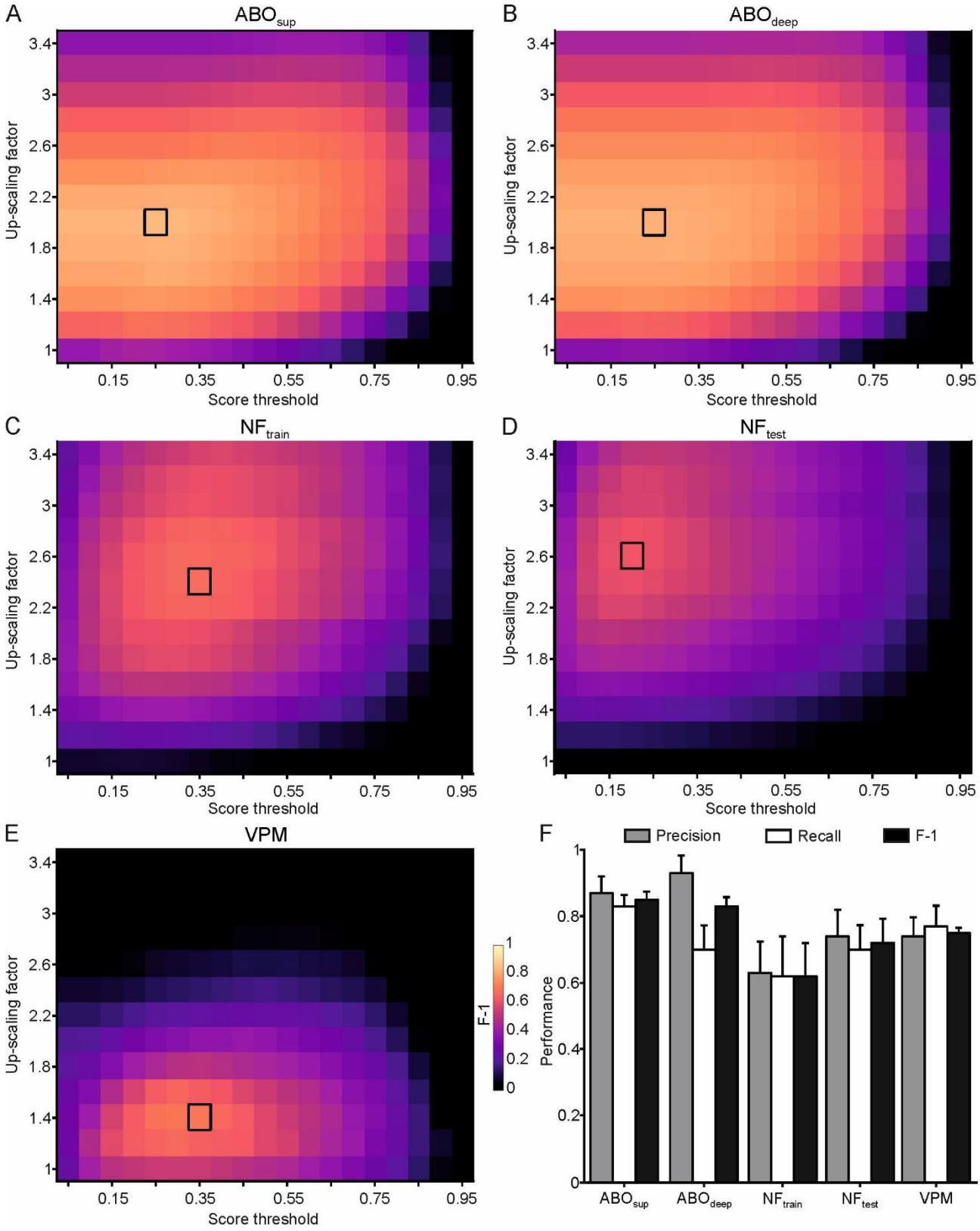

Figure 5. CITE-On offline performance on never-before-seen data. A-E) Best parameter search for frame upscaling: F-1 score (pseudocolor) as a function of upscaling factor (vertical axis) and score

threshold (horizontal axis) for the ABO_{sup} (A), ABO_{deep} (B), NF_{train} (C), NF_{test} (D) and VPM (E) datasets. The maximal F-1 is indicated with the black rectangle. The pseudocolor scale in (E) applies to (A-D). **F)** Performance of Precision (grey), Recall (white), and F-1 (black) for all t-series in the ABO_{sup} (N = 9), ABO_{deep} (N = 10), NF_{train} (N = 19), NF_{test} (N = 9), and VPM (N = 9) datasets.

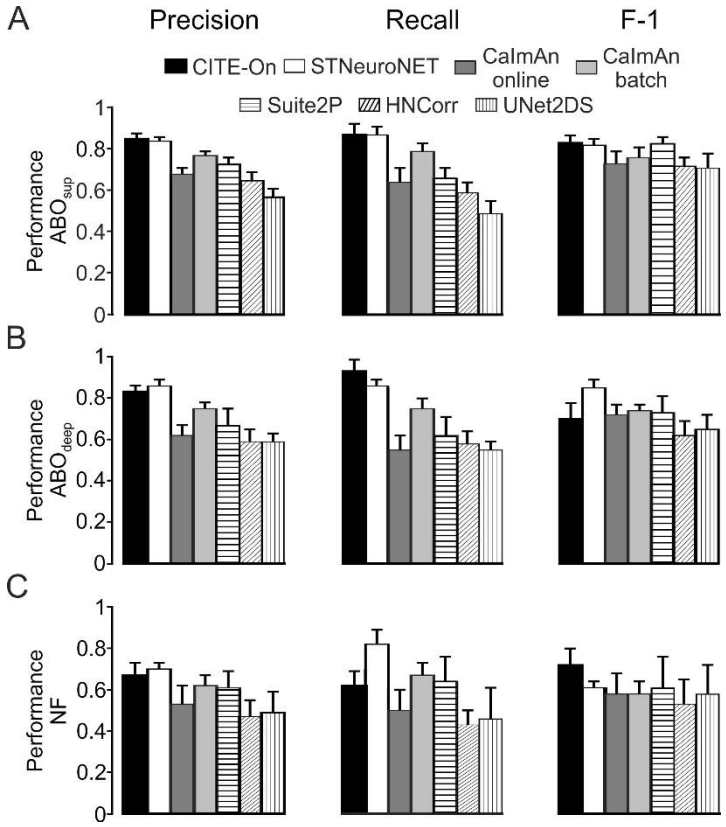

Figure 6. CITE-On offline performance compared with state-of-the-art methods. A-C) Offline performance of CITE-On (black) compared to STNeuroNET (white), CaImAn On Line (dark grey), CaImAn Batch (light grey), Suite2P (horizontal line), HNCorr (tilted line) and UNet2DS (vertical line). Precision (left), Recall (middle), and F-1 (right) are shown. Performance is evaluated on ABO_{sup} (A, N = 9 t-series), ABO_{deep} (B, N = 10 t-series), and NF_{train} + NF_{test} (NF, C, N = 28 t-series).

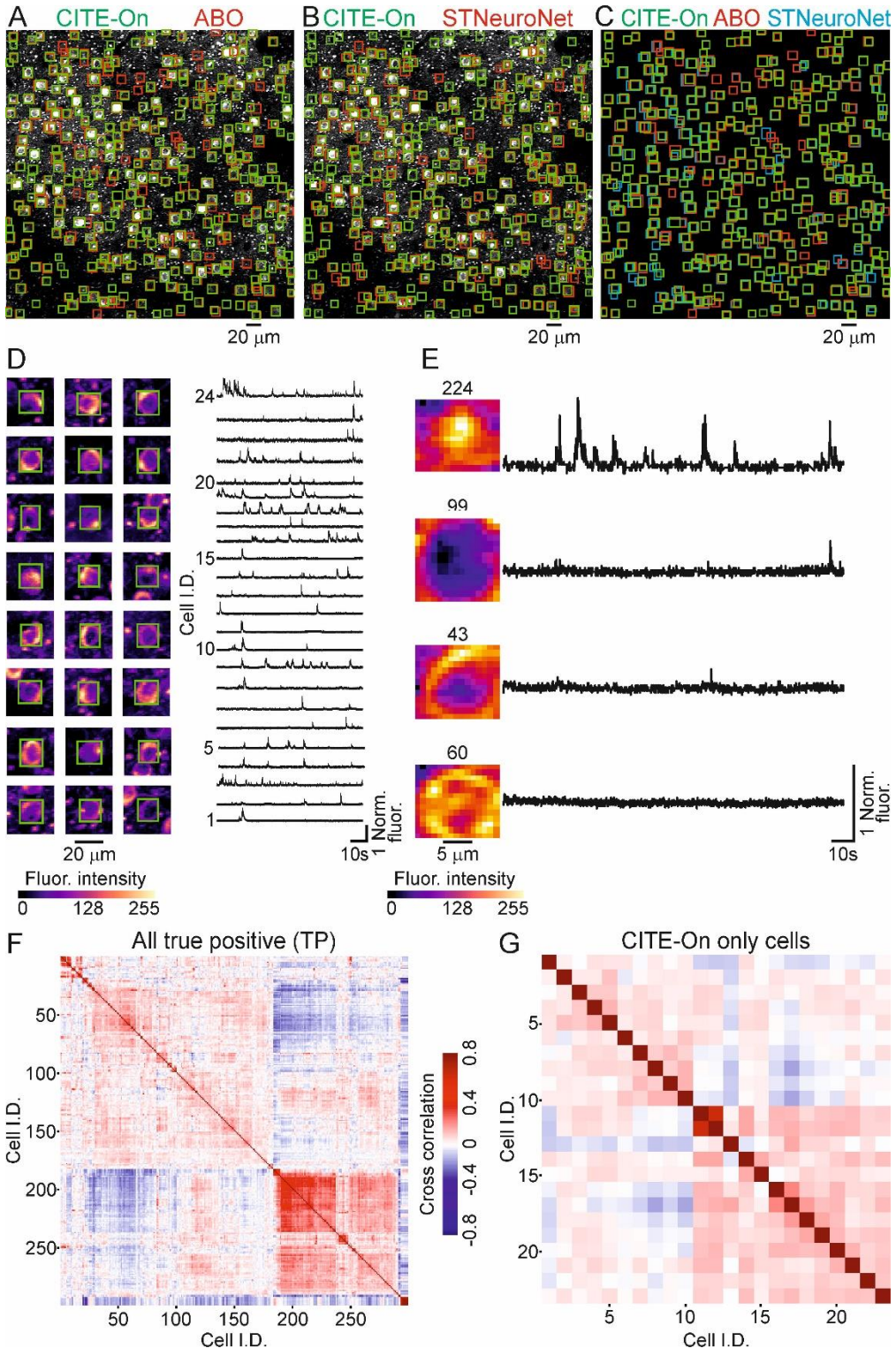

Figure 7. CITE-On data processing of never-before-seen recordings. A) Median projection of a representative t-series from the ABO dataset showing GCaMP6f expressing cortical neurons. CITE-On true positives (CITE-On, green) and true positives provided by the Allen Brain Observatory

(ABO, red) are shown. **B)** Same as in (A) with CITE-On true positives (green) and STNeuroNET true positives (red). **C)** Superposition of CITE-On (green), ABO (red), and STNeuroNET (cyan) true positives. **D)** Left: 24 representative cells detected by CITE-On and identified as true positives in ABO and STNeuroNET. The CITE-On-identified bounding box is represented in green. Right: corresponding CITE-On-extracted fluorescence traces. **E)** Same as in (D) for four representative CITE-On-only cells. These fours cells were not counted in the GT of ABO and STNeuroNET GT, either as true or false positives. **F)** Lower-left triangle: cross correlation matrix for all functional traces extracted from true positive detection in the t-series displayed in (A). Upper-right triangle: corresponding dendrogram sorting. The pseudocolor scale indicates the cross correlation value. **G)** same as in (F), but for the CITE-On-only true positive cells. Pseudocolor scale as in (F).

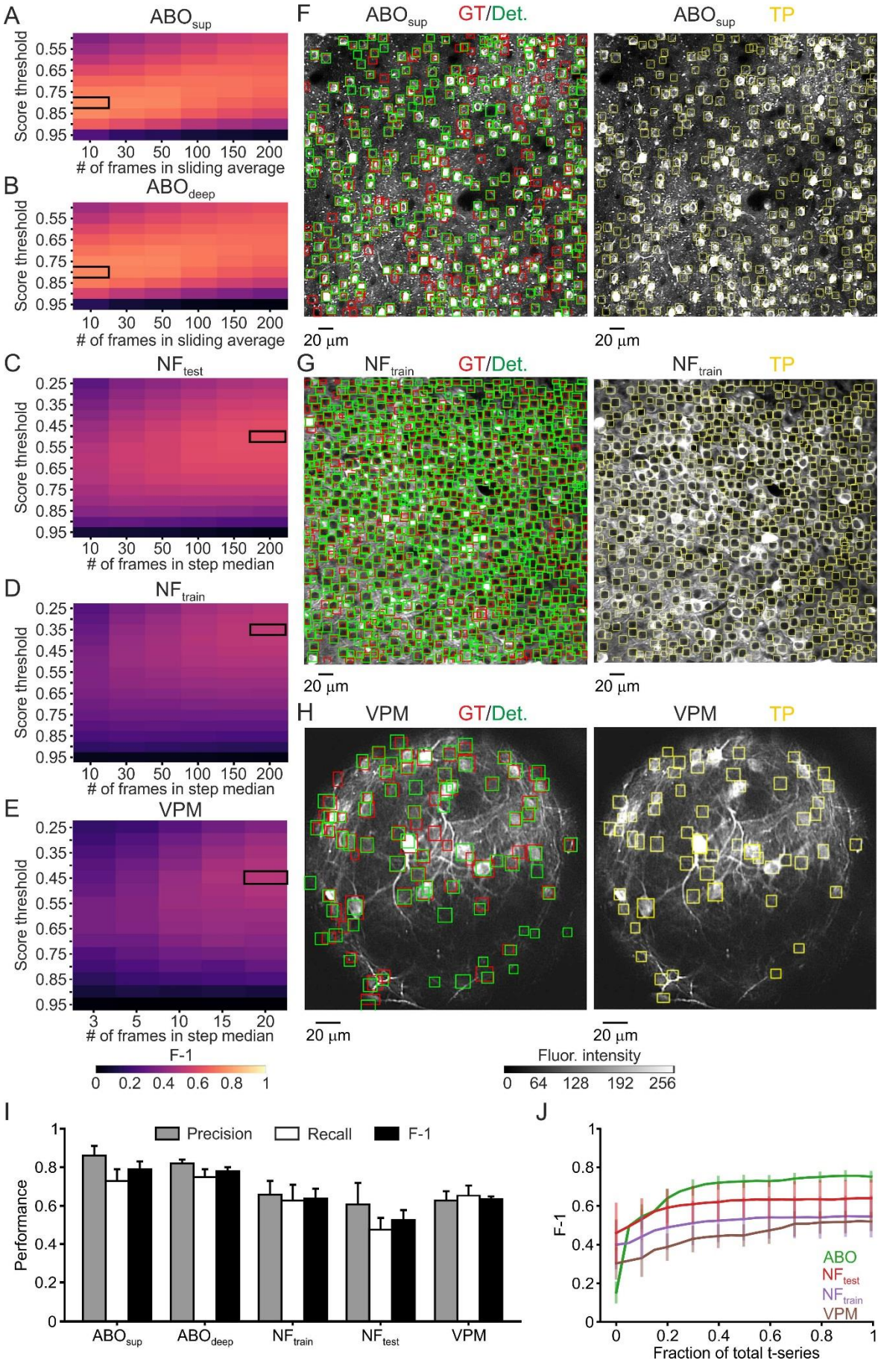
A
ABO sup
Score threshold
0.55
0.65
0.75
0.85
0.95
10 30 50 100 150 200
# of frames in sliding average
B
ABO deep
Score threshold
0.55
0.65
0.75
0.85
0.95
10 30 50 100 150 200
# of frames in sliding average
C
NF test
Score threshold
0.25
0.35
0.45
0.55
0.65
0.75
0.85
0.95
10 30 50 100 150 200
# of frames in step median
D
NF train
Score threshold
0.25
0.35
0.45
0.55
0.65
0.75
0.85
0.95
10 30 50 100 150 200
# of frames in step median
E
VPM
Score threshold
0.25
0.35
0.45
0.55
0.65
0.75
0.85
0.95
3 5 10 15 20
# of frames in step median
F-1
0 0.2 0.4 0.6 0.8 1
F
ABO sup GT/Det.
ABO sup TP
20 µm
20 µm
G
NF train GT/Det.
NF train TP
20 µm
20 µm
H
VPM GT/Det.
VPM TP
20 µm
20 µm
Fluor. intensity
0 64 128 192 256
I
Precision
Recall
F-1
Performance
0
0.2
0.4
0.6
0.8
1
ABO sup
ABO deep
NF train
NF test
VPM
J
F-1
0
0.2
0.4
0.6
0.8
1
ABO
NF test
NF train
VPM
0 0.2 0.4 0.6 0.8 1
Fraction of total t-series

1079

Figure 8. CITE-On online performance on never-before-seen datasets. A-E) Best parameter search for frame downsampling: F-1 score (pseudocolor) as a function of score threshold (vertical axis) and number of frames (horizontal axis) for the ABO_{sup} (A), ABO_{deep} (B), NF_{train} (C), NF_{test} (D) and VPM (E) datasets. The maximal F-1 is indicated with the black rectangle. The pseudocolor scale in (E) applies to (A-D). For the ABO_{sup}, ABO_{deep} datasets the sliding average frame downsampling approach was used, while for the NF_{test}, NF_{train}, and VPM datasets the step average approach was implemented. **F-H)** Left: median projection of a representative t-series from the ABO_{sup} (F), NF_{train} (G), and VPM (H) datasets. GT (red) and online CITE-On detections (green bounding boxes) are shown. Right: bounding boxes (yellow) corresponding to true positives are shown. The greyscale in H applies also to (F-G). **I)** Online detection performance of Precision (grey), Recall (white), and F-1 (black) for all t-series in the ABO_{sup} (N = 9), ABO_{deep} (N = 10), NF_{train} (N = 19), NF_{test} (N = 9), and VPM (N = 9) datasets. **J)** F-1 as a function of the fraction of processed t-series for ABO (green, N = 19 t-series), NF_{test} (red, N = 9 t-series), NF_{train} (purple, N = 19 t-series), and VPM (brown, N = 9 t-series) datasets. 10 frames sliding averages for ABO; detection rate, 5 Hz. Step median of 20 frames and 200 frames for VPM and NF datasets; detection rate, 0.3 Hz and 0.035 Hz for SPM and NF datasets, respectively.

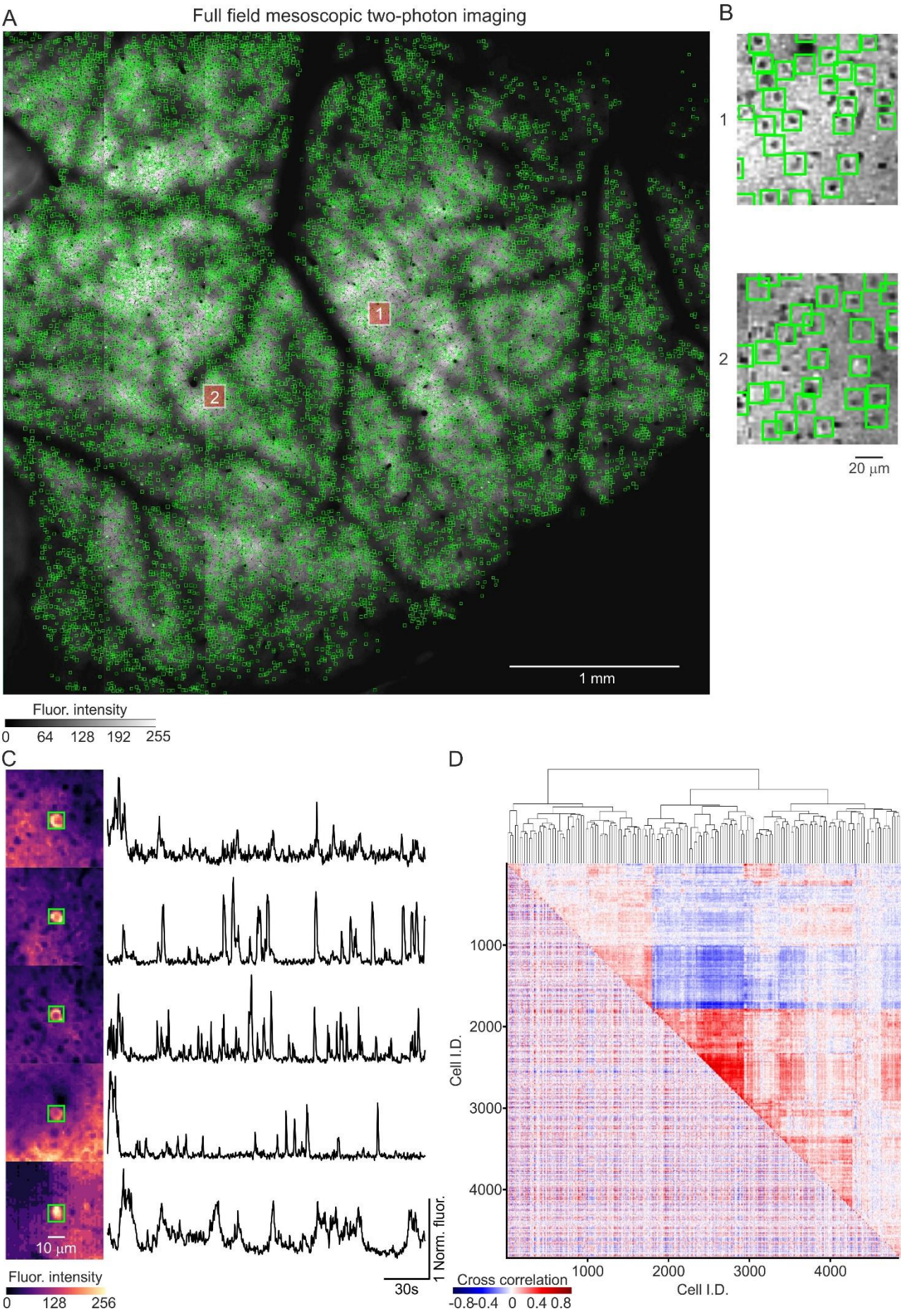
A
Full field mesoscopic two-photon imaging
1
2
1 mm
Fluor. intensity
0 64 128 192 255
B
1
2
20 μm
C
10 μm
Fluor. intensity
0 128 256
30s
1 Norm. fluor.
D
Cell I.D.
1000
2000
3000
4000
Cross correlation
-0.8-0.4 0 0.4 0.8

Figure 9. CITE-On analysis of mesoscopic two-photon imaging t-series. A-B) Median projection of a mesocopic imaging t-series showing GCaMP6s expressing neurons (mesoscopic data from [7]). Green boxes indicate cells detected by CITE-On (total: 4,842 cells). Two regions are highlighted by yellow squares and shown at an expanded spatial scale in (B). Greyscale in (A) applies also to (B). **C)** Left: five representative cells detected by CITE-On. Right: corresponding CITE-On-extracted fluorescence traces in the first 230 s of the t-series. **D)** Cross correlation matrix (bottom-left triangle) calculated on the background subtracted traces extracted by CITE-On on all detected cells in the first 7,000 frames and relative dendrogram (top-right triangle).

Supplementary material

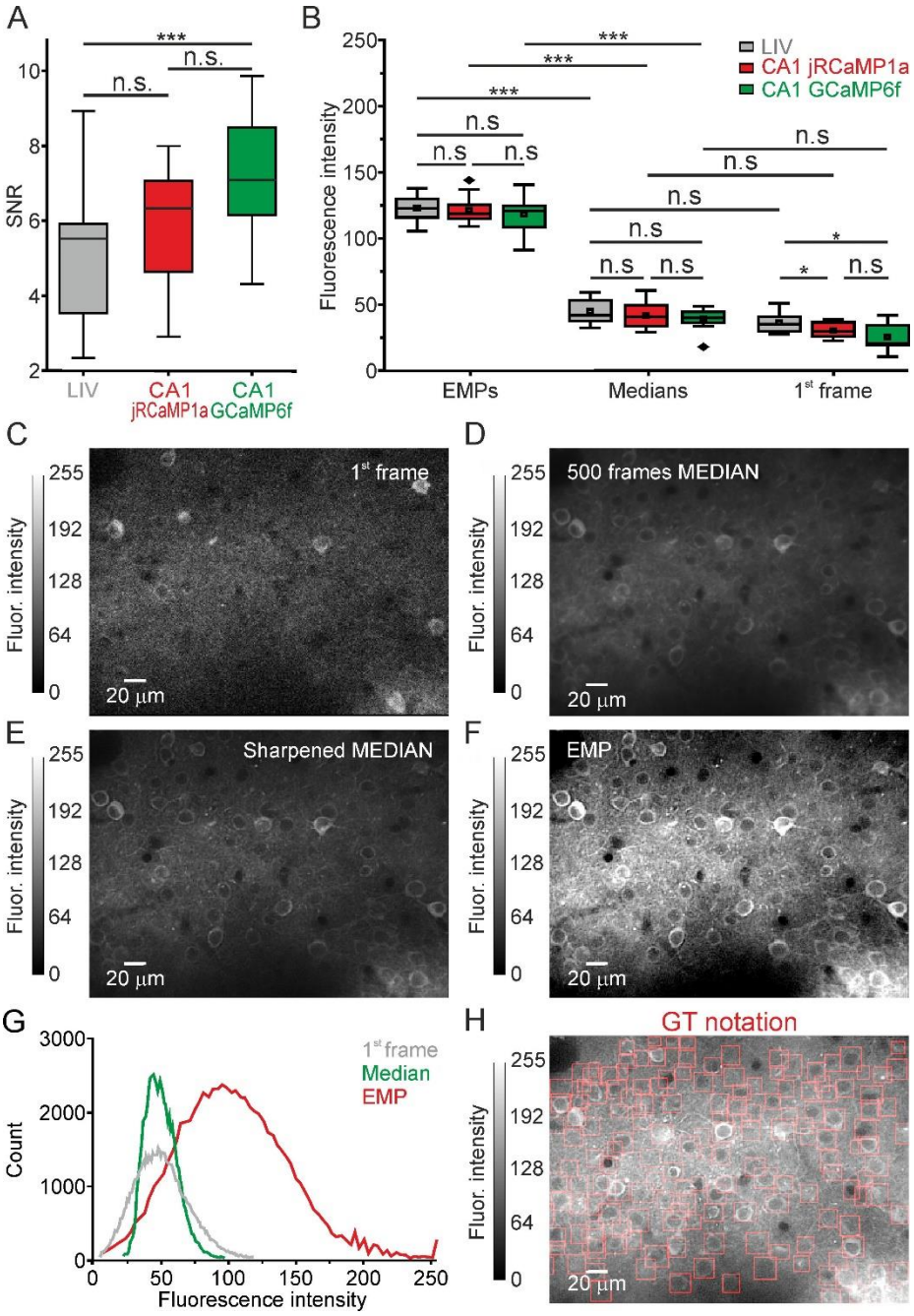

Supplementary Figure 1. Processing imaging t-series for GT annotation. A) SNR values across all dataset t-series (both training and validation). Unpaired Student's *t*-test, p = 0.17 between LIV vs. CA1 jRCaMP1a; p = 0.009 for LIV vs. CA1 GCaMP6f; p = 0.26 for CA1 GCaMP6f vs. CA1 jRCaMP1a. N = 121 for LIV, N = 38 for CA1 jRCaMP1a and for CA1 GCaMP6f. **B)** Fluorescence intensity for EMPs images, median projections of time series, and individual first frames of acquisitions for LIV (grey) and CA1 (GCaMP6f: green and jRCaMP1a: red) datasets. For EMPs, unpaired Student's *t*-test: p = 0.77 for LIV vs. CA1 jRCaMP1a; p = 0.62 for LIV vs. CA1 GCaMP6f; p = 0.78 for CA1 GCaMP6f vs. CA1 jRCaMP1a. For individual frames, Wilcoxon signed rank test: p = 0.38 for LIV vs. CA1 jRCaMP1a; p = 0.56 for LIV vs. CA1 GCaMP6f; p = 0.68 for CA1

jRCaMP1a vs. CA1 GCaMP6f. For EMPs vs. median values, median values for LIV were significantly larger compared with individual frames of CA1 jRCAMP1a and CA1 GCaMP6f: Wilcoxon signed rank test, p = 2.5E-5 for LIV median vs. 1st frame CA1 jRCaMP1a; p = 8.6E-6 for LIV median vs. 1st frame CA1 GCaMP6f; p = 0.082 for LIV median vs. LIV 1st frame. Wilcoxon signed rank test p = 3.5E-5 for LIV EMP vs. LIV median; p = 4.8E-8 for LIV EMP vs. LIV 1st frame; p = 5.6E-6 for LIV EMP vs. CA1 jRCaMP1a median; p = 4.8E-8 for LIV EMP Vs CA1 jRCaMP1a 1st frame; p = 5.6E-6 for LIV EMP vs. CA1 GCaMP6f median; p = 6.9E-8 for LIV EMP vs. CA1 GCaMP6f 1st frame). N = 121 for LIV, N = 38 for CA1 jRCaMP1a and for CA1 GCaMP6f. **C-F)** Individual frame (C), median projection (D), global sharpened image (E), and EMP (F) for a representative LIV t-series. **G)** Distribution of absolute fluorescence intensity values for individual frames (grey), median projection (green), sharpened median projection (cyan) and EMP images (red) for a representative LIV t-series. **H)** GT annotation on a representative EMP.

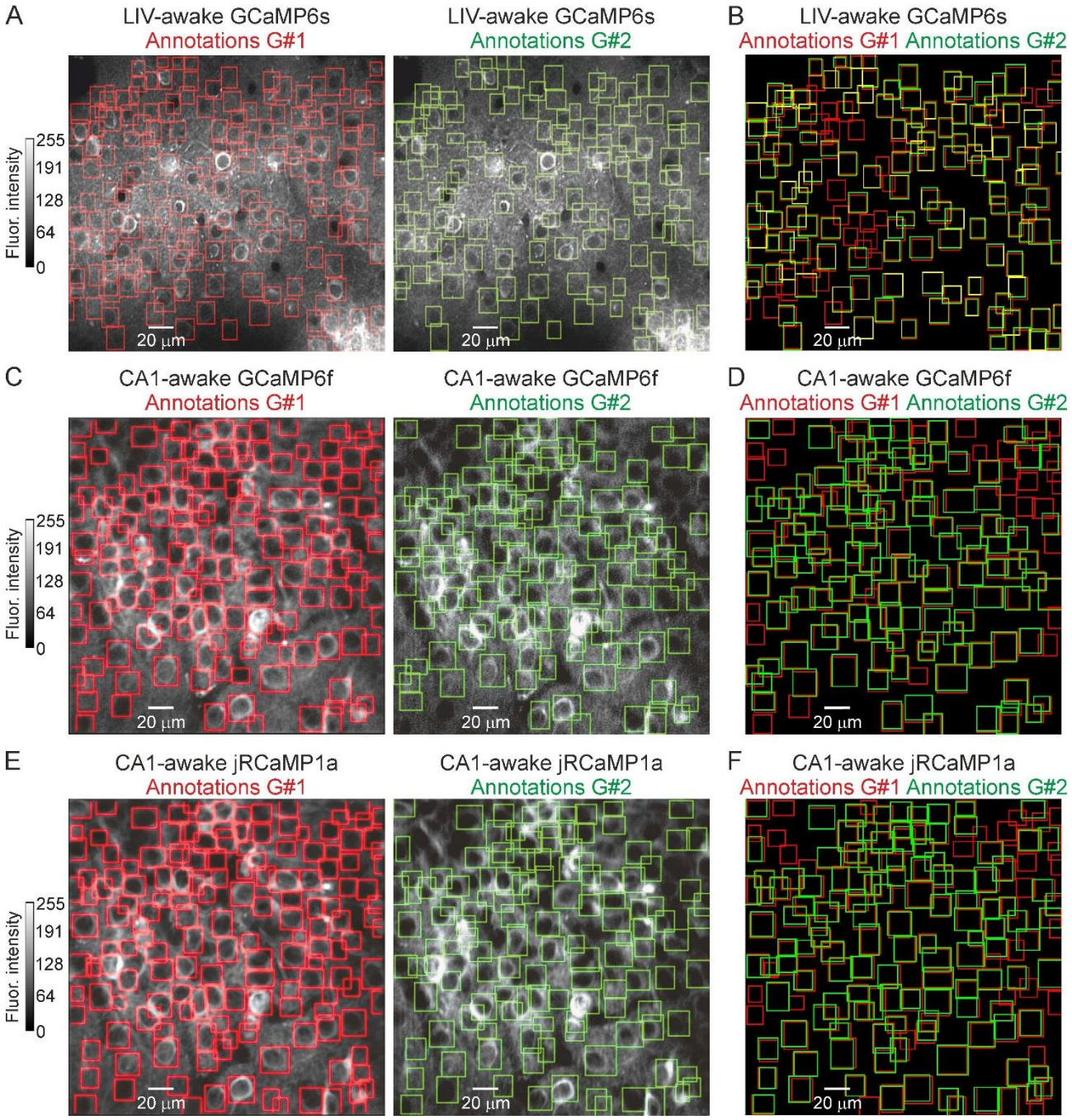

Supplementary Figure 2. Graders' annotations on LIV and CA1 validation t-series. A) EMP image from a representative LIV t-series. Bounding boxes generated by grader #1 are shown in red in the left panel. Those generated by grader #2 are shown in green in the right panel. **B)** Superposition of the bounding boxes generated by grader #1 (red) and grader #2 (green). **C-D)** Same as in (A-B) for a representative CA1 GCaMP6f t-series. **E-F)** Same as in (A-B) for a representative CA1 jRCaMP1a t-series.

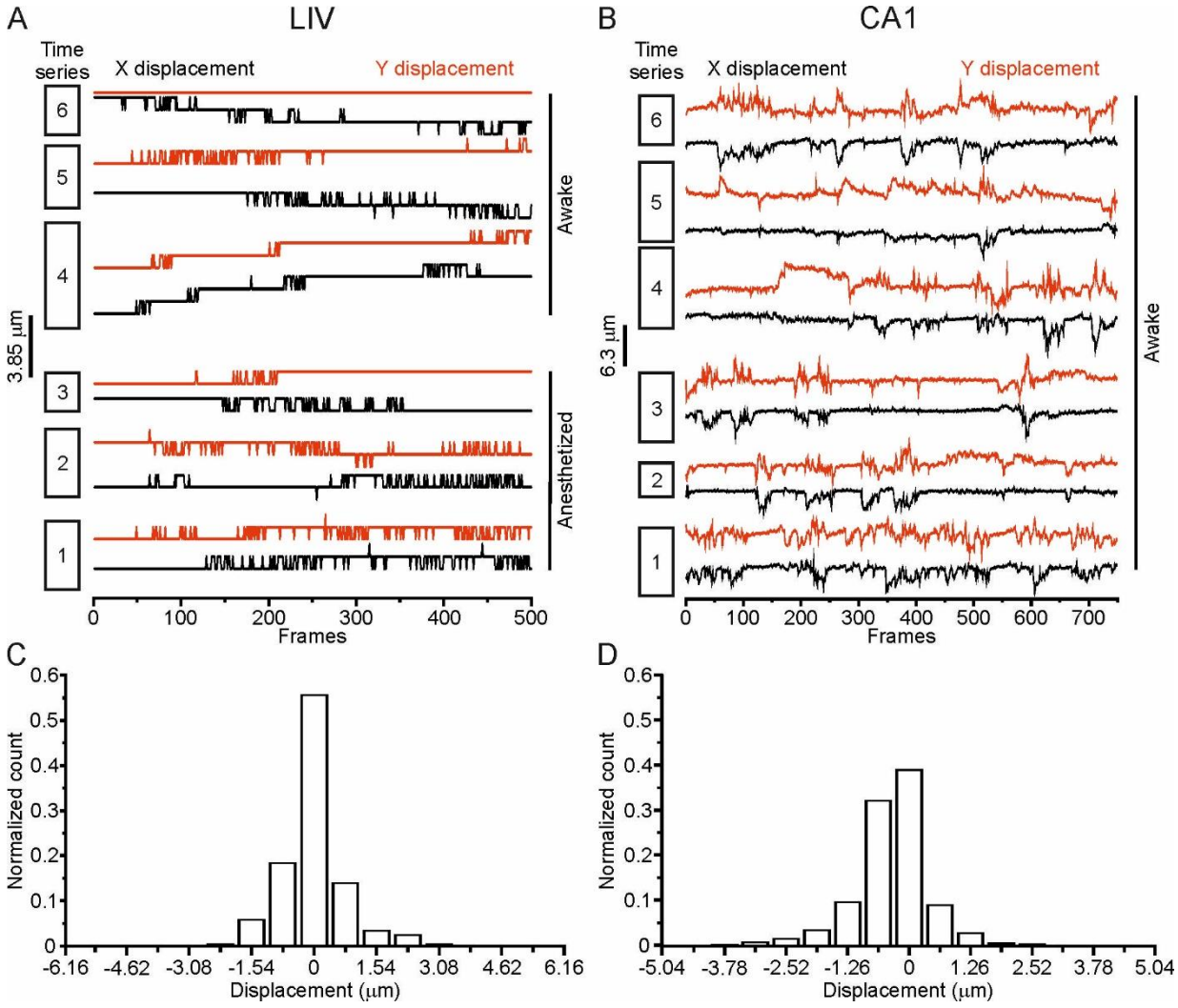

Supplementary Figure 3. **Motion artefacts in the LIV and CA1 validation datasets**. **A)** X, Y displacement of the FOV (black, X; red, Y) expressed in microns as observed across frames of six representative 500 frame-long LIV t-series (traces 1-3 from anesthetized animals, traces 4-6 from awake mice). **B)** Same as in (A) but for six representative 750 frame-long CA1 jRCaMP1a acquisitions. **C)** Percentage of total X, Y displacements in LIV validation t-series (N = 13). D) Same as in (C) for CA1 jRCaMP1a validation t-series (N = 12).

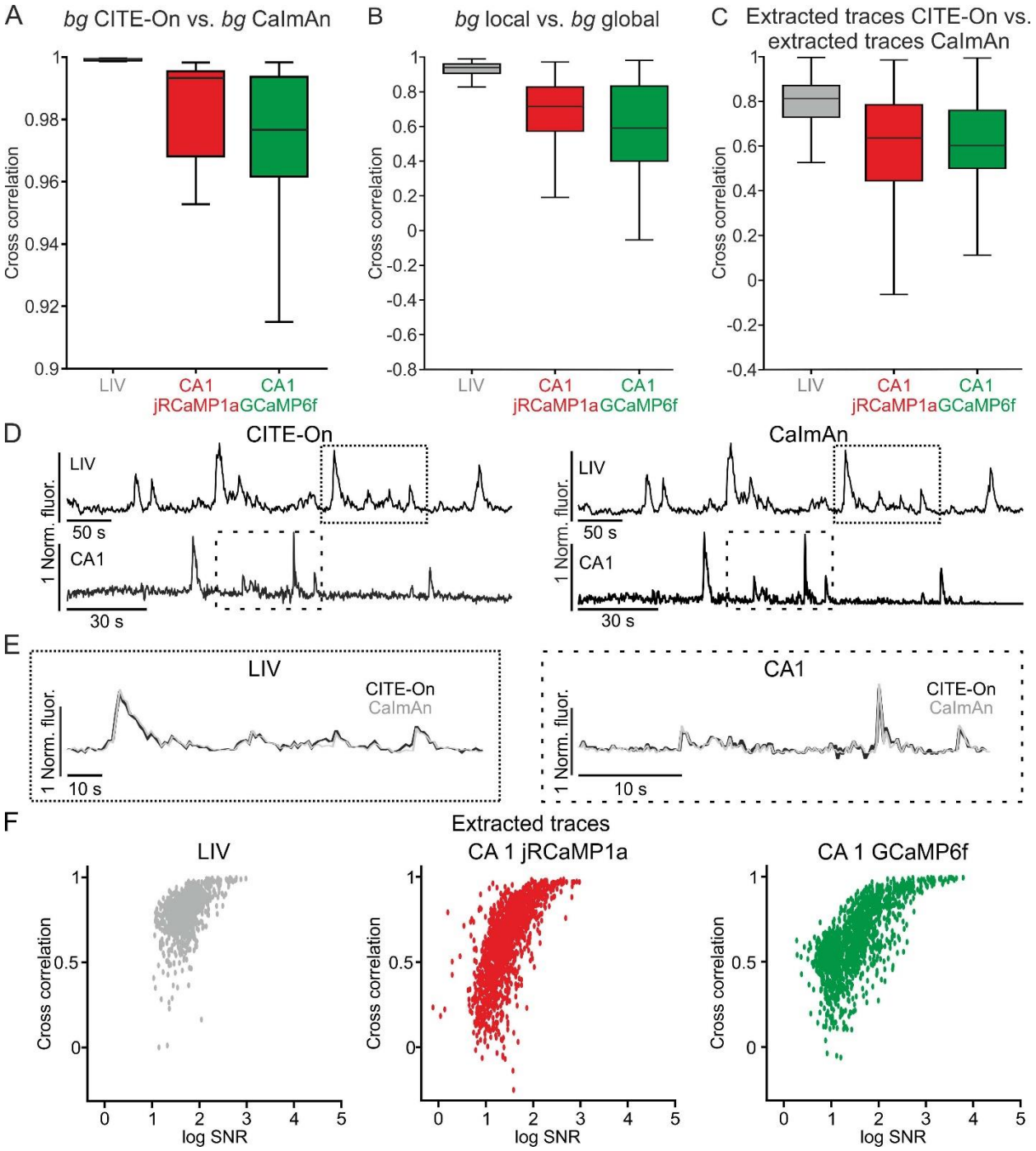

Supplementary Figure 4. Trace extraction from the validation dataset: CITE-On vs. seeded-CaImAn. A) Boxplots showing cross correlation values between the background obtained using CITE-On and seeded-CaImAn for the LIV, CA1 jRCaMP1a, and CA1 GCaMP6f datasets (N = 13, N = 12, and N = 12 t-series, respectively). **B)** Cross correlation values between global and local background signals computed with CITE-On. **C)** Cross correlation of background-subtracted functional traces extracted with CITE-On and with seeded-CaImAn for all true positive detected identities in the LIV, CA1 jRCaMP1a, and CA1 GCaMP6f datasets. **D)** Representative background subtracted functional traces extracted with CITE-On (left) and seeded-CaImAn (right) from LIV (top) and CA1 jRCaMP1a (bottom) t-series. **E)** Representative traces extracted with CITE-On (black) and CaImAn (grey) are shown superimposed for LIV (left) and CA1 (right). **F)** Cross correlation of

background-subtracted functional traces extracted with CITE-On and with seeded-CaImAn as a function of the cell's SNR for all true positive identities in the LIV (left), CA1 jRCaMP1a (middle), and CA1 GCaMP6f (right) datasets. Each dot represents a cell detected by CITE-On (see Supplementary Table 1).

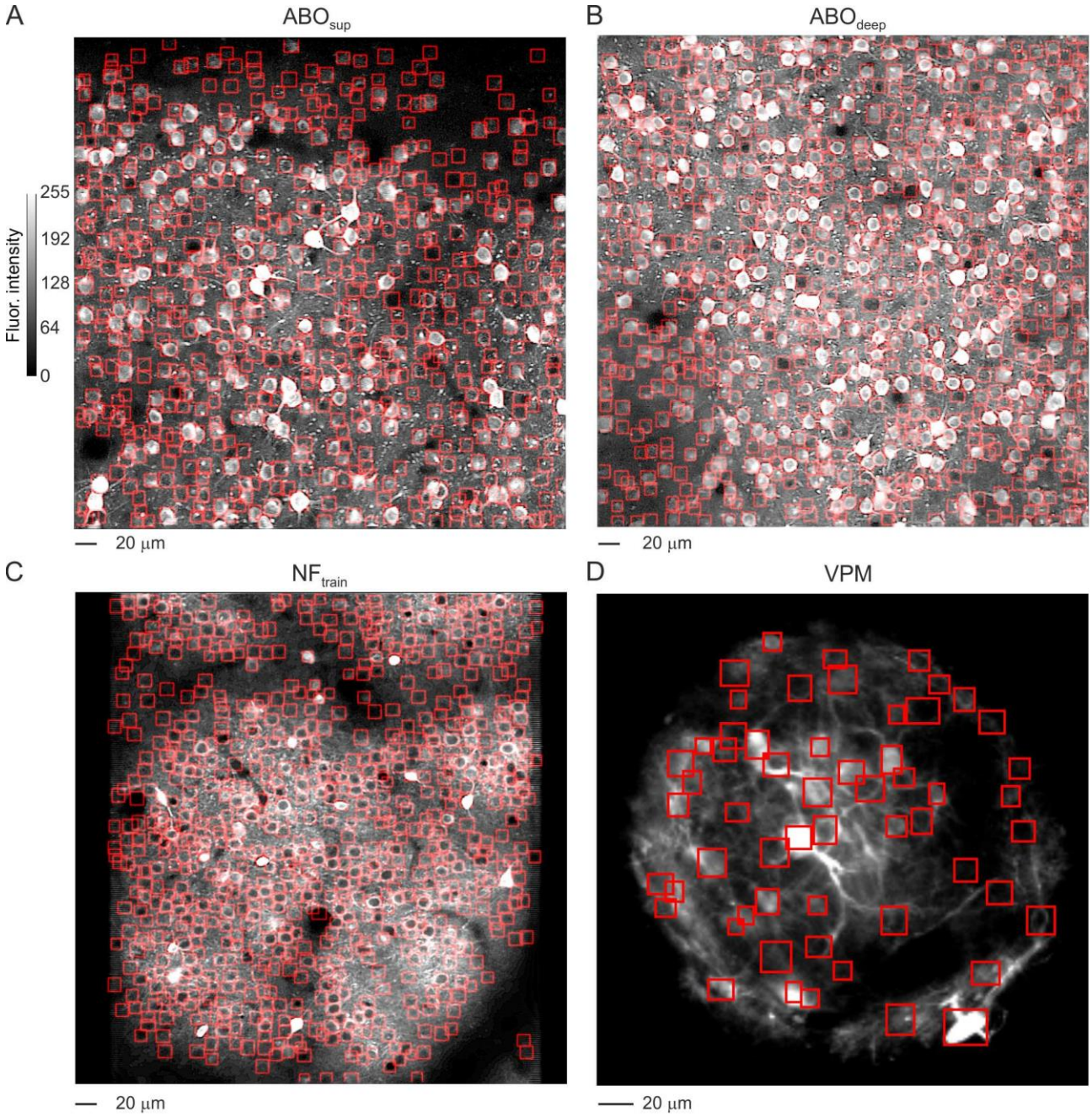

Supplementary Figure 5. GT bounding box annotation of publicly available datasets. A-D) Median projection of t-series from ABO_{sup} (A), ABO_{deep} (B), NF_{train} (C), and VPM (D) datasets. GT bounding boxes are shown in red.

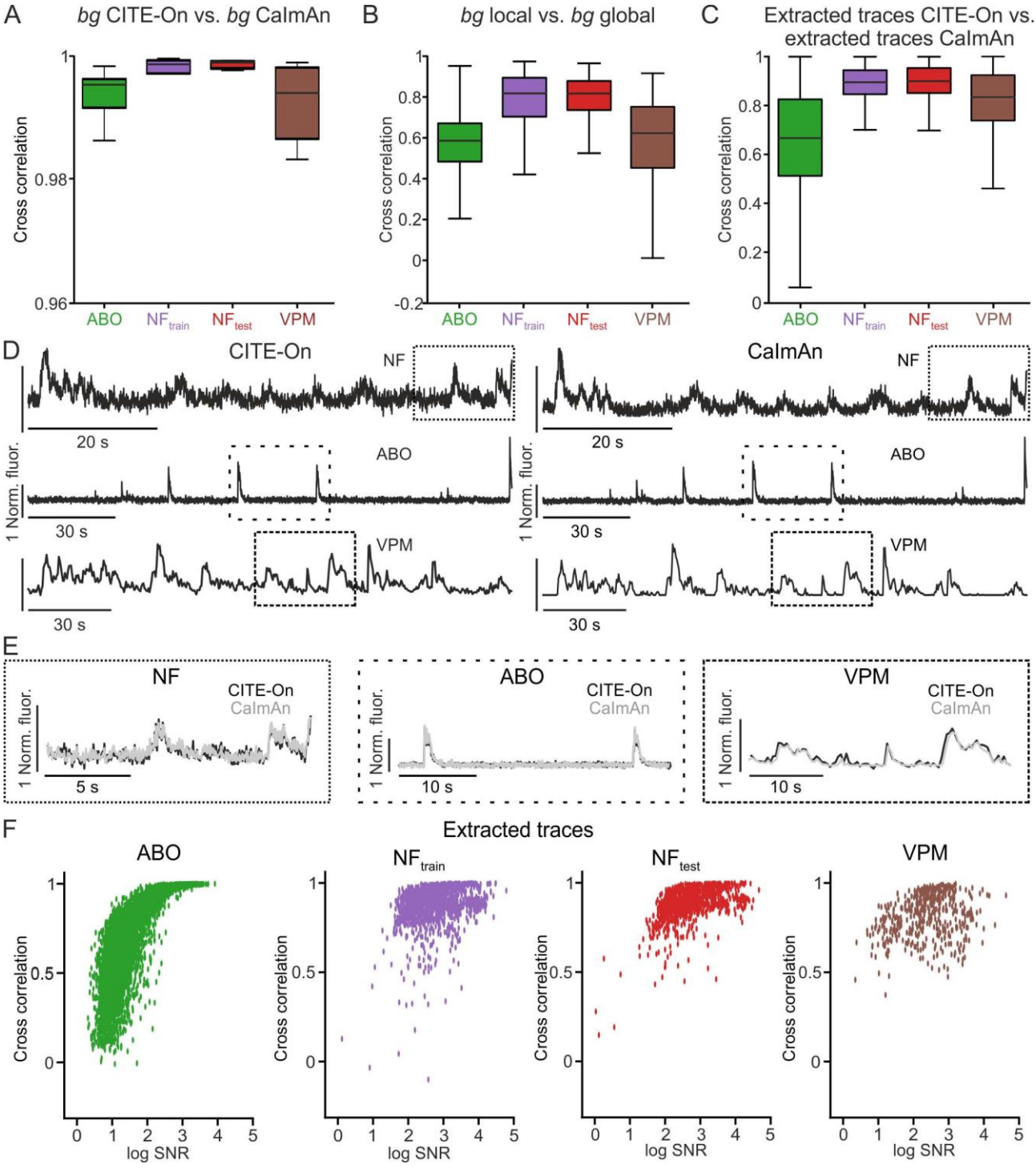

Supplementary Figure 6. Trace extraction from publicly available datasets: CITE-On vs. seeded-CaImAn. A) Boxplots showing cross correlation values between the background obtained using CITE-On and seeded-CaImAn for the for ABO, NF_{train}, NF_{test}, and VPM data (N = 19, N = 19, N = 9, and N = 9 t-series, respectively). **B)** Cross correlation values between global and local background signals computed with CITE-On. **C)** Cross correlation of background-subtracted functional traces extracted with CITE-On and with seeded-CaImAn for the various datasets. **D)** Representative background subtracted functional traces extracted with CITE-On (left) and seeded-CaImAn (right) for NF (top), ABO (middle) and VPM (bottom) acquisitions. **E)** Representative traces

extracted with CITE-On (black) and CaImAn (grey) are shown superimposed for NF (left), ABO (middle), and VPM (right). **F)** Cross correlation of background-subtracted functional traces extracted with seeded-CaImAn and CITE-On as a function of the cell's SNR for all true positive identities in the ABO (leftmost), NF_{train} (middle left), NF_{test} (middle right) and VPM (rightmost) acquisitions. Each dot represents a cell detected by CITE-On (see Supplementary Table 1).

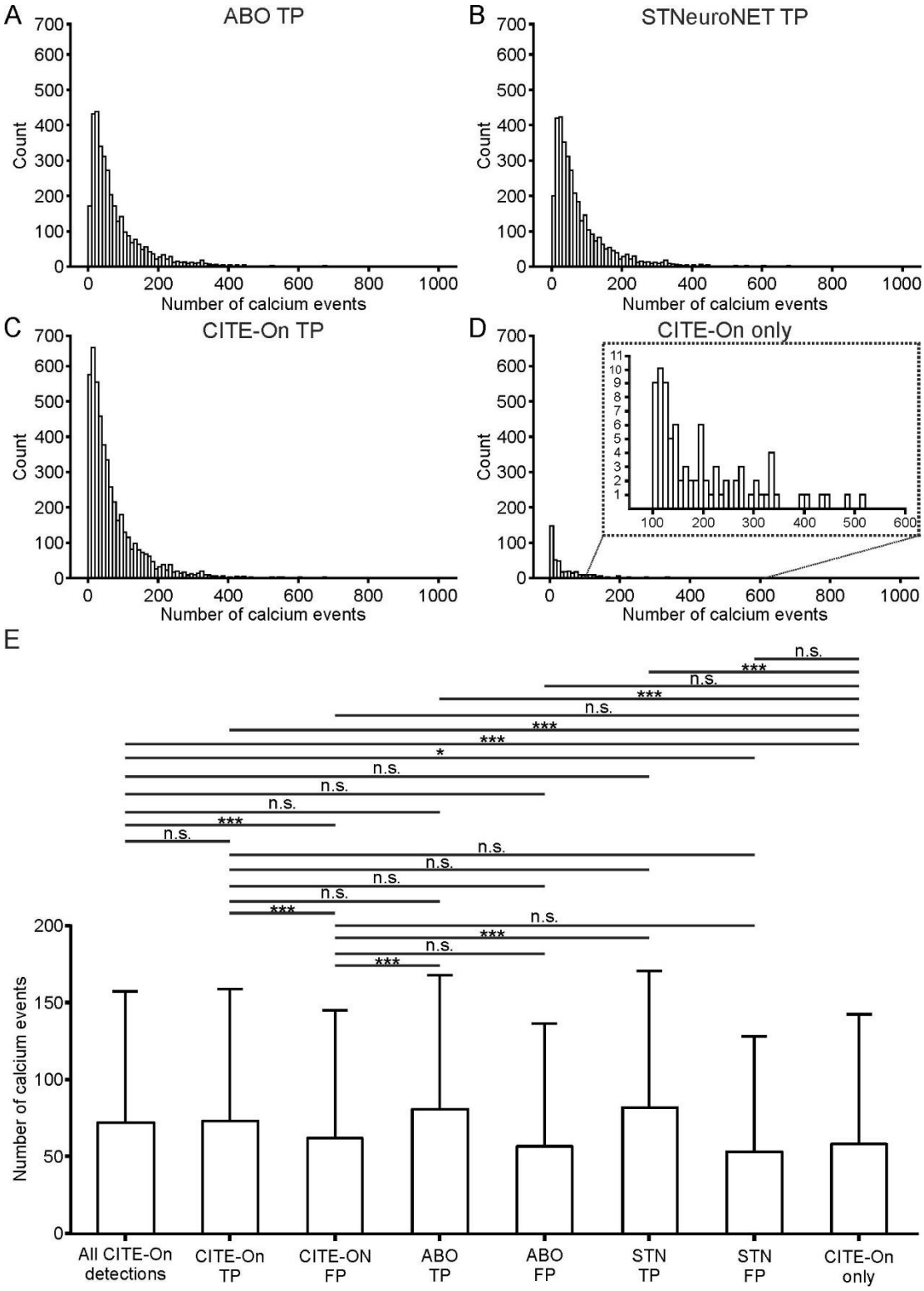

Supplementary Figure 7. Calcium activity in CITE-On, ABO, and STNeuroNET detections. A-D) Distribution of the number of calcium events in true positive detection in a representative ABO t-series analyzed by ABO (A), STNeuroNET (B), CITE-On (C). (D) shows the distribution of CITE-On-only true positive detections. Data refers to the corresponding GT annotation provided by the consensus GT for CITE-On, ABO, and STNeuroNET. **E)** Average (and s.d.) number of detected

calcium events *per* cell for all CITE-On detections, CITE-On true positives (CITE-On TP), CITE-On false positives (CITE-On FP), ABO true positives (ABO TP), ABO false positives (ABO FP), STNeuroNET true positives (STN TP), STNeuroNET false positives (STN FP), and CITE-On only detections. Data from N = 19 t-series of the ABO dataset. Results of Kolmogorov-Smirnov test: p = 0.00012 for All cells vs. CITE-On-only cells; p = 1.00 for All cells vs. CITE-On True Positives; p = 0.00022 for All cells vs. CITE-On False Positives; p = 0.99 for All cells vs. ABO True Positives; p = 0.078 for All cells vs. ABO False Positives; p = 0.99 for All cells vs. STN True Positives; p = 0.036 for All cells vs. STN False Positives; p =0.00041 for CITE-On-only Cells vs. CITE-On True Positives; p = 0.99 for CITE-On-only Cells vs. CITE-On False Positives; p = 0.0012 for CITE-On-only Cells vs. ABO True Positives; p = 0.28 for CITE-On-only Cells vs. ABO False Positives; p = 0.00073 for CITE-On-only Cells vs. STN True Positives; p = 0.36 for CITE-On-only Cells vs. STN False Positives; p = 0.00073 for CITE-On True Positives vs. CITE-On False Positives; p = 0.99 for CITE-On True Positives vs. ABO True Positives; p = 0.11 for CITE-On True Positives vs. ABO False Positives; p = 0.99 for CITE-On True Positives vs. STN True Positives; p = 0.078 for CITE-On True Positives vs. STN False Positives; p = 0.0022 for CITE-On False Positives vs. ABO True Positives; p = 0.46 for CITE-On False Positives vs. ABO False Positives; p = 0.0012 for CITE-On False Positives vs. STN True Positives; p = 0.70 for CITE-On False Positives vs. STN False Positives; p =0.28 for ABO True Positives vs. ABO False Positives; p = 1.00 for ABO True Positives vs. STN True Positives; p = 0.15 for ABO True Positives vs. STN False Positives; p = 0.21 for ABO False Positives vs. STN True Positives; p = 0.99 for ABO False Positives vs. STN False Positives; p =0.11 for STN True Positives vs. STN False Positives. Total number of detected cells: N = 5482, for All CITE-On detections; N = 4934, for CITE-On TP; N = 548, for CITE-On FP; N = 3516, for ABO TP; N = 1966, for ABO FP; N = 3606, for STN TP; N = 1876, for STN FP; N = 439, for CITE-On only.

Supplementary tables

Dataset	# of t-series	# of detections grader 1	# of detections grader 2	# of detections overlap	# of detections grader 1 only	# of detections grader 2 only	# of ground truth
ABO	19	6225	5456	5443	782	13	6238
NF_{train}	19	11171	9772	9630	1541	142	11313
NF_{test}	9	3187	2814	2793	394	21	3208
VPM	9	517	470	444	73	26	543
LIV_{test}	13	979	868	861	118	7	986
$CA1_{test}$ jRCaMP1a	12	884	809	795	89	14	898
$CA1_{test}$ GCaMP6s	12	1000	927	916	84	11	1011
LIV_{train}	118	7221	6489	6356	865	133	7354
$CA1_{train}$ jRCaMP1a	21	2123	1856	1833	290	23	2146
$CA1_{train}$ GCaMP6s	21	2218	1963	1940	278	23	2241

Supplementary table 1. Dataset annotation and ground truth generation. Two graders manually annotated the LIV, CA1, ABO, NF, and VPM datasets. The table reports the number of t-series, the

number of detections by grader 1 and 2, the number of overlapping detections, the number of detections exclusively produced by grader 1 and grader 2, and the number of detections in the consensus ground truth.

Dataset	mAP	s.d	N	F-1	s.d	N	Precision	s.d	N	Recall	s.d	N
ABO	0.80	0.10	19	0.93	0.02	19	0.998	0.004	19	0.87	0.04	19
NF_{train}	0.71	0.14	19	0.92	0.03	19	0.99	0.02	19	0.86	0.05	19
NF_{test}	0.72	0.10	9	0.93	0.02	9	0.99	0.01	9	0.88	0.04	9
VPM	0.64	0.13	9	0.90	0.03	9	0.95	0.03	9	0.86	0.04	9
LIV_{test}	0.81	0.11	13	0.93	0.03	13	0.99	0.01	13	0.88	0.05	13
$CA1_{test}$ jRCaMP1a	0.76	0.07	12	0.94	0.03	12	0.98	0.02	12	0.90	0.04	12
$CA1_{test}$ GCaMP6s	0.82	0.08	12	0.95	0.01	12	0.99	0.01	12	0.92	0.03	12
LIV_{train}	0.73	0.09	118	0.93	0.02	118	0.98	0.02	118	0.88	0.05	118
$CA1_{train}$ jRCaMP1a	0.74	0.08	21	0.92	0.02	21	0.99	0.01	21	0.87	0.04	21
$CA1_{train}$ GCaMP6s	0.76	0.07	21	0.93	0.02	21	0.99	0.01	21	0.87	0.04	21

Supplementary table 2. Evaluation of consensus GT. The table reports the average (and relative s.d.) of the mean average precision (mAP), the F-1 score, the precision and recall across the t-series of the various datasets annotated by the different graders.

Offline												
Dataset	F-1	s.d	N	Precision	s.d	N	Recall	s.d	N	# of TP	# of FP	# of FN
ABO	0.84	0.03	19	0.90	0.06	19	0.80	0.07	19	4934	548	1303
NF_{train}	0.63	0.1	19	0.63	0.09	19	0.62	0.12	19	6849	3932	4120
NF_{test}	0.74	0.08	9	0.70	0.07	9	0.51	0.06	9	2286	716	911
VPM	0.75	0.02	9	0.74	0.06	9	0.77	0.06	9	398	140	123
LIV_{test}	0.86	0.04	13	0.85	0.05	13	0.88	0.05	13	1486	257	205
$CA1_{test}$ jRCaMP1a	0.92	0.04	12	0.88	0.06	12	0.97	0.02	12	1618	222	55
$CA1_{test}$ GCaMP6s	0.93	0.02	12	0.91	0.03	12	0.97	0.02	12	1638	170	56

Supplementary table 3. CITE-On offline performance. Average (and relative s.d.) F-1, Precision, Recall, and number of true positives (TP), false positives (FP), and false negatives (FN) for LIV, CA1, ABO, NF and VPM datasets generated by the CITE-On offline pipeline.

Online

Dataset	F-1	s.d	N	Precision	s.d	N	Recall	s.d	N	# of TP	# of FP	# of FN
ABO	0.77	0.03	19	0.83	0.04	19	0.83	0.04	19	4573	978	1664
NF_{train}	0.55	0.11	19	0.56	0.11	19	0.56	0.11	19	6164	4906	5026
NF_{test}	0.64	0.10	9	0.68	0.12	9	0.68	0.12	9	2096	921	1101
VPM	0.52	0.50	9	0.60	0.11	9	0.60	0.11	9	244	181	277
LIV_{test}	0.69	0.04	13	0.72	0.05	13	0.72	0.05	13	1127	437	564
$CA1_{test}$ jRCaMP1a	0.73	0.07	12	0.74	0.07	12	0.74	0.07	12	1233	439	440
$CA1_{test}$ GCaMP6s	0.67	0.12	12	0.69	0.12	12	0.69	0.12	12	1145	493	549

Supplementary table 4. CITE-On online performance. Average (and relative s.d.) F-1, Precision, Recall, and number of true positives (TP), false positives (FP), and false negatives (FN) for LIV, CA1, ABO, NF and VPM datasets generated by the CITE-On online pipeline.

ABO Dataset	# of detections	s.d	N
All CITE-On	289	21	19
CITE-On TP	260	28	19
CITE-On FP	29	16	19
ABO TP	185	36	19
ABO FP	103	31	19
STNeuroNET TP	190	33	19
STNeuroNET FP	99	24	19
CITE-On only	23	15	19

Supplementary table 5. Detections in the ABO dataset. Average (and relative s.d.) number of detections in the ABO dataset reported by CITE-On, ABO, and STNeuroNET. TP, true positives; FP, false positives. Data relative to CITE-On were calculated online as the number of identities obtained at the end of the processing of each t-series then averaged across all t-series.

Supplementary movie legends

Supplementary movie 1. Online tracking of detected identities across the t-series. A representative t-series (# of frames, 750; frame rate, 3 Hz; no motion correction) from the CA1 validation dataset was processed online for cell detection (detection update rate, 10 Hz). Bounding boxes (colored squares) for active detections (i.e. neurons identified by CITE-On in the current frame) and past detections (i.e. neurons identified by CITE-On in previous frames) are represented with or without a central dot, respectively. Each identity was associated with a bounding box color which was retained across the t-series. The position and shape of each bounding box was updated in each frame according to the procedure described in the Results section.

Supplementary movie 2. Frame-by-frame manual annotation. Representative t-series (# of frames, 500; frame rate, 1.5 Hz) from the LIV training dataset (awake head-fixed *Scnn1a-cre* mouse expressing GCaMP6s) used for manual annotation of individual frames. The t-series was motion corrected. Brightness and contrast of each displayed frame of the t-series could be adjusted. Bounding boxes were manually positioned around each visible cell in each frame. Only a minority of neurons were identified in the frame-by-frame annotation process.

Supplementary movie 3. Manual annotation of EMP images. EMP image corresponding to the same t-series as in Supplementary movie 2. Brightness and contrast of the EMP image could be regulated to better visualize bright and dim cells. Bounding boxes (green) were manually defined around identified neurons.

Supplementary movie 4. Online dynamic segmentation and functional trace extraction. Top left: raw fluorescence of a representative cell from a t-series in the ABO dataset. The displayed cell was detected online using CITE-On. Top right: binary mask generated by CITE-On on each frame of the t-series displayed on the left. The white pixels represent the segmented pixels, black pixels are discarded. Bottom: functional fluorescence trace extracted online for the cell displayed on top.